# On the Design of Structural Glazing Joints under Seismic Loading

Paul Jakob Müller

Vollständiger Abdruck der von der Fakultät für Bauingenieurwesen und Umweltwissenschaften der Universität der Bundeswehr München zur Erlangung des akademischen Grades eines

Doktor-Ingenieurs (Dr.-Ing.)

angenommene Dissertation.

**Gutachter:**

1. Univ.-Prof. Dr.-Ing. Geralt Siebert
   Universität der Bundeswehr München
2. Prof. Dr.-Ing. Christian Schuler
   Hochschule München

Die Dissertation wurde am 11.05.2026 bei der Universität der Bundeswehr München eingereicht und durch die Fakultät für Bauingenieurwesen und Umweltwissenschaften am 29.09.2026 angenommen. Die mündliche Prüfung fand am 29.09.2026 statt.

# Danksagung

Die vorliegende Arbeit wurde im Rahmen einer kooperativen Promotion im BayWISS-Verbundkolleg *Infrastruktur, Bauen und Urbanisierung* zwischen der Hochschule München (HM) und der Universität der Bundeswehr München (UniBw) während meiner Zeit als wissenschaftlicher Mitarbeiter am Labor für Stahl- und Leichtmetallbau der HM verfasst. Der Großteil der Ergebnisse entstand zunächst im Rahmen einer Qualifikationsstelle an der HM und anschließend im IGF-Forschungsprojekt *Dickschichtklebungen in Katastrophenszenarien (RISIKO)* (IGF-Nr. 01IF22888N), das vom Bundesministerium für Wirtschaft und Energie aufgrund eines Beschlusses des Deutschen Bundestages gefördert wurde.

Mein herzlichster Dank gilt Herrn Univ.-Prof. Dr.-Ing. Geralt Siebert (UniBw) und Herrn Prof. Dr.-Ing. Christian Schuler (HM) für die Betreuung dieser Arbeit sowie den gewährten Freiraum und das entgegengebrachte Vertrauen. Darüber hinaus danke ich Herrn Prof. Schuler besonders für die freundschaftliche und stets auf Augenhöhe geführte Zusammenarbeit. Herrn Univ.-Prof. Dr.-Ing. Max Spannaus danke ich für die Übernahme des Prüfungsvorsitzes.

Ganz herzlicher Dank gilt auch den Studierenden, Hilfskräften und allen voran meinen ehemaligen und aktuellen Kolleginnen und Kollegen, die den Arbeitsalltag bereichert und zum Erfolg dieser Arbeit beigetragen haben. Besonderer Dank gilt Dr.-Ing. Lena Efferz und Dr.-Ing. Steffen Dix für die tolle Zusammenarbeit und die vielen fachlichen Diskussionen und persönlichen Gespräche. Steffen Dix und Nicolas Wachter (seele GmbH) sowie Michael Rieß (sedak GmbH & Co. KG) danke ich zudem für die unkomplizierte Möglichkeit zur Fertigung meiner Probekörper und die wertvollen Anregungen aus der Praxis.

Abschließend möchte ich mich von ganzem Herzen bei meinen Freunden und meiner Familie bedanken. Mein innigster Dank gilt meiner Moni – für ihr grenzenloses Verständnis, ihre Geduld und ihre bedingungslose Unterstützung, die mir all die Jahre Halt gegeben haben. Und meinen Söhnen: Ihr startet jeden Tag mit einer Begeisterung und einem Lachen, die mich immer wieder motivieren – danke, dass ihr einfach ihr seid.

> I wanna thank me for believing in me. I wanna thank me for doing all this hard work. I wanna thank me for having no days off. I wanna thank me for never quitting. I wanna thank me for always being a giver and trying to give more than I receive. I wanna thank me for trying to do more right than wrong. I wanna thank me for just being me at all times.
>
> — Snoop Dogg, Hollywood Walk of Fame (2018)

# Abstract

Earthquakes represent a significant hazard to facade systems, with documented damage to glazing and facade components in numerous seismic events worldwide. Despite the increasing use of structural glazing (SG) joints in modern facade construction, current design standards provide no explicit provisions for seismic loading, representing a critical gap in engineering practice. This work investigates both the load-bearing and failure behavior of SG joints under seismic actions, as well as the characterization of seismic loading demands, with the objective of developing an engineering-oriented design approach.

Experimental investigations under low-cycle fatigue loading revealed that while initial load-bearing behavior was comparable to quasi-static conditions, failure behavior differed fundamentally with loading control type. Force-controlled tests, representative of all-glass constructions, produced sudden complete failure after steadily increasing deformations. Displacement-controlled tests, representative of conventional facade systems, resulted in gradual stress relaxation without complete failure at test termination. An energy-based failure criterion was introduced to consistently define the number of cycles to failure across both conditions. The classical Basquin model was extended by a linearly proportional frequency-dependent term, which captured the observed frequency dependence of fatigue life with high accuracy across different joint geometries and loading configurations.

Seismic loading was characterized through a parametric simulation framework using single-degree-of-freedom systems and a database of real ground motion records. Response histories were converted into equivalent load cycles via the frequency-dependent fatigue model, enabling derivation of frequency-dependent design parameters, including the seismic reserve factor $k_{\mathrm{sr}}$, which quantified the increased load-bearing capacity of SG joints under seismic conditions relative to quasi-static reference strengths.

Four verification methods of increasing complexity were developed, ranging from a simplified approach treating seismic loading as a variable action to an advanced method incorporating a frequency-dependent $k_{\mathrm{sr}}(f)$. For practical application, a fixed seismic reserve factor of $k_{\mathrm{sr}} = 1.25$ and a global safety factor for seismic loading $\gamma_{\mathrm{meth,s}} = 2.67$ were proposed.

The proposed framework directly links experimental fatigue characterization, seismic demand analysis, and engineering verification, providing, for the first time, a consistent and application-oriented design of SG joints subjected to seismic actions.

# Zusammenfassung

Erdbeben stellen eine erhebliche Gefährdung für Fassadensysteme dar, mit weltweit dokumentierten Schäden an Verglasungen. Obwohl Structural-Glazing-(SG)-Klebverbindungen im modernen Fassadenbau zunehmend eingesetzt werden, enthalten aktuelle Bemessungsnormen keine expliziten Regelungen für seismische Einwirkungen. Die vorliegende Arbeit untersucht das Trag- und Versagensverhalten von SG-Klebverbindungen unter seismischen Einwirkungen und entwickelt auf Basis einer Charakterisierung der seismischen Beanspruchungen einen praxisorientierten Bemessungsansatz.

Experimentelle Untersuchungen unter zyklischer Beanspruchung im Kurzzeitfestigkeitsbereich zeigten, dass das Tragverhalten in den ersten Lastzyklen mit dem quasi-statischen Verhalten vergleichbar war, das Versagensverhalten jedoch von der Art der Versuchssteuerung abhing. Kraftgeregelte Versuche, repräsentativ für Ganzglaskonstruktionen, führten zu plötzlichem Versagen nach stetiger Verformungszunahme, während weggeregelte Versuche, repräsentativ für konventionelle Fassadenkonstruktionen, eine allmähliche Spannungsrelaxation ohne vollständiges Versagen am Versuchsende zeigten. Ein energiebasiertes Versagenskriterium wurde eingeführt, um die Lastwechsel bis zum Versagen zu bestimmen. Das klassische Basquin-Modell wurde um einen frequenzabhängigen Term erweitert, der die Frequenzabhängigkeit der Ermüdungslebensdauer mit hoher Genauigkeit erfasste.

Die seismische Beanspruchung wurde durch ein parametrisches Simulationsmodell auf Basis von Einmassenschwingern und einer Datenbank realer Erdbebenzeitverläufe charakterisiert. Die Antwortverläufe wurden in äquivalente Lastzyklen umgerechnet, was die statistische Ableitung frequenzabhängiger Bemessungsparameter einschließlich des seismischen Reservefaktors $k_{\mathrm{sr}}$ ermöglichte, der die Tragfähigkeitsreserve von SG-Klebverbindungen unter Erdbebenbeanspruchung gegenüber der quasi-statischen Referenzfestigkeit quantifiziert.

Vier Nachweisverfahren mit zunehmendem Komplexitätsgrad wurden entwickelt, von einem vereinfachten Ansatz unter Behandlung als veränderliche Einwirkung bis hin zu einem erweiterten Verfahren mit frequenzabhängigem $k_{\mathrm{sr}}(f)$. Für die praktische Anwendung wurden ein fester seismischer Reservefaktor von $k_{\mathrm{sr}} = 1.25$ und ein globaler Sicherheitsfaktor für seismische Beanspruchungen von $\gamma_{\mathrm{meth,s}} = 2.67$ vorgeschlagen.

Das vorgeschlagene Konzept verbindet experimentelle Ermüdungsuntersuchungen, die Analyse der seismischen Einwirkung sowie ingenieurtechnische Nachweiskonzepte und ermöglicht hiermit erstmals eine praxisorientierte Bemessung von SG-Klebverbindungen unter seismischen Einwirkungen.

# Contents


**1 Introduction** . . . . . **1**
1.1 Motivation . . . . . 1
1.2 State of the Art . . . . . 2
1.3 Problem Statement . . . . . 4
1.4 Objectives and Limitations . . . . . 5
1.5 Structure of the Thesis . . . . . 5
1.6 List of Own Publications . . . . . 7
1.6.1 Journal Articles . . . . . 7
1.6.2 Conference Contributions . . . . . 8
1.6.3 Publications in Preparation . . . . . 8

**2 Theoretical Background** . . . . . **9**
2.1 Fundamentals of Adhesive Bonding . . . . . 9
2.1.1 Definitions and Polymer Structure . . . . . 9
2.1.1.1 Structure of Polymer Networks . . . . . 9
2.1.1.2 Engineering Classification of Adhesive Systems . . . . . 11
2.1.1.3 Silicone Elastomers . . . . . 12
2.1.2 Bonding Forces in Adhesive Joints . . . . . 13
2.1.3 Fundamental Mechanical Behavior of Polymers . . . . . 14
2.1.3.1 Aggregate States . . . . . 14
2.1.3.2 Entropic Elasticity . . . . . 15
2.1.3.3 Mullins Effect . . . . . 16
2.1.3.4 Payne Effect . . . . . 17
2.1.3.5 Incompressibility . . . . . 18
2.1.3.6 Time-Dependent Mechanical Behavior . . . . . 18
2.1.3.7 Dynamic Cyclic Viscoelastic Behavior . . . . . 19
2.1.3.8 Time-Temperature Superposition . . . . . 19
2.2 Mechanical and Dynamic Fundamentals . . . . . 20
2.2.1 Basic Mechanical Concepts . . . . . 20
2.2.2 Modeling of Mechanical Material Behavior . . . . . 22
2.2.2.1 Purely Elastic Material Behavior . . . . . 22
2.2.2.2 Hyperelastic Material Models . . . . . 23
2.2.2.3 Viscoelastic Models . . . . . 23
2.2.3 Fundamentals of Structural Dynamics . . . . . 26
2.2.3.1 Single-Degree-of-Freedom Systems . . . . . 28
2.2.3.2 Multi-Degree-of-Freedom Systems . . . . . 31
2.2.3.3 Numerical Evaluation of Dynamic Response . . . . . 32
2.3 Fatigue and Low-Cycle Fatigue of Materials . . . . . 33
2.3.1 Fundamentals of Fatigue and Cyclic Loading . . . . . 33
2.3.2 Fatigue Behavior of Adhesive and Polymeric Materials . . . . . 36
2.3.3 Low-Cycle Fatigue . . . . . 38

2.3.4 Definition and Interpretation of Cyclic Parameters . . . 39
2.3.4.1 Deviation of the Load Range . . . 39
2.3.4.2 Dynamic Stiffness . . . 39
2.3.4.3 Dissipated Energy Density . . . 40
2.3.4.4 Damping . . . 41
2.3.5 Failure Criteria Under Cyclic Loading . . . 42
2.4 Fundamentals of Seismology and Ground Motion . . . 43
2.4.1 Earthquake Generation and Classification . . . 43
2.4.2 Seismic Hazard and Regional Relevance . . . 44
2.4.3 Seismic Magnitude and Intensity Measures . . . 45
2.4.4 Ground Motion Parameters for Structural Analysis . . . 46
2.4.5 Response Spectra . . . 48
2.4.6 Seismic Loading in Structural Design . . . 49
2.4.6.1 Lateral Force Method of Analysis . . . 50
2.4.6.2 Modal Response Spectrum Analysis . . . 52
2.4.6.3 Nonlinear Analyses . . . 52
2.4.7 Determination of the Number of Equivalent Cycles . . . 52

**3 Glass and Facade Structures Under Seismic Loading . . . 55**
3.1 Adhesive Joints in Glass and Facade Construction . . . 55
3.1.1 Application of Structural Glazing . . . 55
3.1.2 Load-Bearing and Failure Behavior of SG Joints . . . 56
3.1.3 Influencing Factors . . . 57
3.2 Design of SG Joints Under Conventional Loading . . . 59
3.2.1 Normative Framework . . . 59
3.2.2 Determination of Mechanical Adhesive Properties . . . 60
3.2.3 Simplified Analytical Design Approaches . . . 63
3.2.3.1 ETAG 002-1 Approach . . . 63
3.2.3.2 Structural Spring Method . . . 64
3.2.4 Extended Numerical Modeling Approaches . . . 65
3.3 Seismic Behavior of Glass and Facade Structures . . . 67
3.3.1 Overview of Conventional Facade Systems . . . 67
3.3.2 Experimental Studies on SG-Facade Systems . . . 68
3.3.3 Analytical and Numerical Studies on SG-Facade Systems . . . 70
3.3.4 Existing Seismic Design Concepts . . . 71
3.4 Fatigue and Cyclic Loading of SG joints . . . 71
3.4.1 High-Cycle Fatigue of SG Adhesives . . . 72
3.4.2 Low-Cycle Fatigue of SG Joints . . . 72
3.4.3 Definition and Comparison of Low-Cycle Fatigue Load Patterns . . . 73
3.4.4 Influence of Low-Cycle Fatigue on Failure Strength . . . 75
3.5 Summary and Identified Research Gaps . . . 76

**4 Stress Assessment . . . 77**
4.1 General . . . 77
4.2 Structural System and Type of Load Application . . . 77
4.3 Seismic Load Characteristics . . . 78
4.3.1 Numerical Estimation of Stresses in SG Joints . . . 78
4.3.2 Resulting Stress Characteristics . . . 79
4.4 Relevant Test Frequency Range . . . 80
4.5 Relevant Joint Geometries . . . 81

4.6 Mean Stress Effect . . . 82
4.7 Summary . . . 82

**5 Specimen Manufacturing . . . 85**
5.1 Objective and Approach . . . 85
5.2 Specimen Design and Manufacturing . . . 85
5.2.1 Specimen Concept and Material Selection . . . 85
5.2.2 Bonding Procedure . . . 86
5.3 Influence of Curing and Manufacturing . . . 86
5.4 Summary . . . 88

**6 Quasi-Static Reference Performance . . . 89**
6.1 Objective and Approach . . . 89
6.2 Experimental Program . . . 89
6.3 General Load-Bearing Behavior . . . 89
6.4 Statistical Evaluation . . . 91
6.5 Summary . . . 93

**7 Low-Cycle Fatigue Performance . . . 95**
7.1 Objective and Approach . . . 95
7.2 Experimental Program and Testing Procedure . . . 96
7.2.1 Test Setup . . . 96
7.2.2 Test Matrix . . . 96
7.2.3 Experimental Procedure and Signal Processing . . . 98
7.2.4 Evaluation of the Load Levels . . . 99
7.3 Load-Bearing Behavior Under Low-Cycle Fatigue Loading . . . 101
7.3.1 Fundamental Low-Cycle Fatigue Behavior . . . 101
7.3.2 Cyclic Stress–Strain Curves . . . 102
7.3.2.1 Type of Load Application . . . 102
7.3.2.2 Load Level . . . 103
7.3.2.3 Test Frequency . . . 105
7.3.2.4 Joint Geometry . . . 105
7.4 Cyclic Parameters in SG Joints . . . 106
7.4.1 Deviation of the Feedback Signal . . . 107
7.4.2 Dynamic Stiffness . . . 109
7.4.3 Dissipated Energy Density . . . 111
7.4.4 Damping . . . 113
7.5 Discussion of Failure Criteria . . . 114
7.5.1 Concept for the Defining of Failure Criteria . . . 115
7.5.1.1 General Concept . . . 115
7.5.1.2 Preprocessing and Basis of Fitting Models . . . 116
7.5.2 Modified Fitting Models for Defining Failure . . . 117
7.5.2.1 Modified Dynamic Stiffness Criteria . . . 117
7.5.2.2 Modified Dissipated Energy Density Criteria . . . 121
7.5.3 Failure Criteria Comparison . . . 125
7.5.4 Qualitative Crack Progression . . . 129
7.5.5 Proposal for Failure Criteria in Low-Cycle Fatigue Testing . . . 130
7.6 Assessment of Low-Cycle Fatigue Strength . . . 131
7.6.1 Load Level and Test Control . . . 131

7.6.2 Test Frequency . . . 132
7.6.2.1 Analysis of Experimental S-N Curves . . . 132
7.6.2.2 Extension of the Basquin Model to Frequency-Dependent Fatigue 134
7.6.3 Joint Geometry . . . 137
7.6.3.1 Analysis of Experimental S-N Curves . . . 137
7.6.3.2 Applicability of the Extended Basquin Model . . . 139
7.6.4 Statistical Evaluation of the S-N Curves . . . 141
7.6.5 Comparison of Low Cycle Fatigue With Quasi-Static Performance . . . 142
7.7 Summary of Low-Cycle Fatigue Performance . . . 145

**8 Analysis of the Seismic Ground Motion Loading . . . 147**
8.1 Objective and Approach . . . 147
8.2 Development of an Engineering Simulation Method . . . 149
8.2.1 Single-Degree-of-Freedom Model . . . 149
8.2.2 Evaluation of General Calculation Parameters . . . 150
8.3 Definition of a Ground Motion Database . . . 152
8.3.1 Criteria for Defining Damage-Relevant Ground Motion . . . 152
8.3.1.1 Criteria for Good Quality and Reliable Database . . . 152
8.3.1.2 Assumption of Characteristic Limit Values for Relevant Earthquakes 153
8.3.1.3 Procedure for Minimizing the Number of Data Selections . . . 153
8.3.2 Analysis of the Selected Database . . . 154
8.3.3 Analysis of Seismic Peak Loading . . . 156
8.4 Determination of the Number of Equivalent Cycles . . . 156
8.4.1 Determination of the Master Curves . . . 157
8.4.1.1 Experimental Basis . . . 157
8.4.1.2 Mathematical Derivation of the Master Curves . . . 157
8.4.1.3 Influencing Parameters for Determining the Master Curves . . . 158
8.4.2 Parametric Determination of the Number of Equivalent Cycles . . . 161
8.4.3 Discussion of Parameters Influencing the Number of Equivalent Cycles . . . 163
8.4.3.1 Test Control Mode and Response Motion Type . . . 164
8.4.3.2 Natural Period of the SDOF-System . . . 165
8.4.3.3 Magnitude of the Ground Motion . . . 166
8.4.3.4 Joint Geometry . . . 167
8.4.4 Parametric Study on the Influence of the Slope of the Master Curve . . . 168
8.4.5 Influence of the Reference Load Level on the Number of Equivalent Cycles 170
8.5 Derivation of Frequency Dependent Design Parameters . . . 171
8.5.1 Statistical Analysis of the Number of Equivalent Cycles . . . 171
8.5.2 Derivation of Fatigue Damage . . . 174
8.5.2.1 General Calculation . . . 174
8.5.2.2 Master Curve . . . 174
8.5.2.3 Statistical Evaluation of the Master Curve . . . 175
8.5.2.4 Test Frequency . . . 175
8.5.2.5 Joint Geometry . . . 176
8.5.3 Derivation of Failure Load Levels . . . 177
8.5.4 Derivation of Failure Stress Levels . . . 179
8.5.5 Derivation of a Seismic Reserve Factor . . . 180
8.6 Summary of the Seismic Ground Motion Loading . . . 182

**9 Design Recommendations . . . 185**
9.1 Objective and Approach . . . 185

9.2 Discussion on the Safety Level in the Seismic Design of SG Joints . . . . . 185
9.2.1 Discussion on the Statistical Evaluation Interval of the Design Parameters . 185
9.2.1.1 Eurocode 0 – General Safety Level for Actions . . . . . 186
9.2.1.2 Eurocode 8 – Fundamental Requirements . . . . . 186
9.2.1.3 Eurocode 8 – Time-History Analysis . . . . . 186
9.2.1.4 Eurocode 0 – General Safety Level for Material and Product Properties . . . . . 187
9.2.1.5 Evaluation and Recommendation . . . . . 187
9.2.2 Code Based Reverse Engineering of Safety Coefficients for Seismic Design of SG Joints . . . . . 188
9.3 Methods for the Design of SG Joints Under Seismic Loading . . . . . 192
9.3.1 General . . . . . 192
9.3.2 Method 1: Verification as a Variable Action . . . . . 193
9.3.3 Method 2: Application of the Seismic Safety Level . . . . . 194
9.3.4 Method 3: Application of a Global Seismic Material Overstrength . . . . . 194
9.3.5 Method 4: Application of a Frequency-Dependent Seismic Material Overstrength . . . . . 196
9.4 Limitations . . . . . 197
9.5 Summary of Design Recommendations . . . . . 198

**10 Conclusion and Outlook . . . . . 201**
10.1 Conclusion . . . . . 201
10.2 Outlook . . . . . 202

**Declaration on the Use of Artificial Intelligence . . . . . 205**

**References . . . . . 207**

**Standards . . . . . 225**

**Appendix . . . . . 229**

**A Additional Data and Plots of Literature Data on Low-Cycle Fatigue of SG Joints 230**

**B Results of the Statistical Evaluation of the Number of Equivalent Cycles . . . . 232**
B.1 Master Curves and Response Motion Types . . . . . 232
B.2 Natural Period of the SDOF System . . . . . 232
B.3 Ground Motion Magnitude . . . . . 233
B.4 Joint Geometry . . . . . 233
B.5 Parametric Study on the Influence of the Master Curve Slope . . . . . 234

# Glossaries

## Abbreviations

| | |
|---|---|
| **CSSC** | cyclic stress strain curve |
| **DRSA** | Dynamic Response Spectrum Analysis |
| **EAD** | European Assessment Document |
| **ECDF** | empirical cumulative distribution function |
| **EOTA** | European Organisation for Technical Assessment |
| **ETA** | European Technical Assessment |
| **ETAG** | European Technical Approval Guideline |
| **FE** | finite element |
| **HCF** | high cycle fatigue |
| **LCF** | low cycle fatigue |
| **LIDA** | Linear Implicit Dynamic Analysis |
| **MDOF** | multi–degree–of–freedom |
| **PGA** | peak ground acceleration |
| **PGD** | peak ground displacement |
| **PGV** | peak ground velocity |
| **RMSE** | root mean square error |
| **RTV-1** | one-component room-temperature vulcanizing systems |
| **RTV-2** | two-component room-temperature vulcanizing systems |
| **SD** | standard deviation |
| **SDOF** | single–degree–of–freedom |
| **SG** | structural glazing |
| **TTS** | time–temperature superposition |

# Symbols

## Geometry and joint properties

| | | |
|---|---|---|
| $A$ | adhesive area of the SG joint assigned to a spring element | $mm^2$ |
| $A_0$ | initial cross-sectional area | $mm^2$ |
| $a_P$ | shorter side length of the glass pane | mm |
| $b$ | width of the SG joint | mm |
| $\Delta L$ | change in length | mm |
| $\Delta l$ | maximum relative thermal movement in the longitudinal direction of an SG joint | mm |
| $e$ | thickness of the SG joint | mm |
| $L$ | current length | mm |
| $L_0$ | initial length | mm |

## Material properties and mechanical quantities

| | | |
|---|---|---|
| $\alpha_T$ | shift factor of the time–temperature superposition principle | – |
| $c_{T,dyn}$ | dynamic torsional stiffness | Nm/rad |
| $E$ | Young's modulus | MPa |
| $E_{joint}$ | effective tensile modulus of an SG joint | MPa |
| $F$ | force | N |
| $G$ | shear modulus | MPa |
| $G_{joint}$ | effective shear modulus of an SG joint | MPa |
| $k_N$ | normal spring stiffness of an SG joint element | N/mm |
| $k_V$ | shear spring stiffness of an SG joint element | N/mm |
| $\nu$ | Poisson's ratio | – |
| $T_G$ | glass transition temperature | °C |
| $T_Z$ | decomposition temperature | °C |

## Stress and strain measures

| | | |
|---|---|---|
| $\alpha$ | shear angle | rad |
| $\delta_{\gamma(\mathrm{F})}$ | normalized absolute deviation of maximum shear strain | – |
| $\delta_{\tau(\mathrm{U})}$ | normalized absolute deviation of maximum shear stress | – |
| $\varepsilon$ | normal strain | mm/mm |
| $\varepsilon_{\mathrm{des}}$ | design normal strain | mm/mm |
| $\varepsilon_{\mathrm{w}}$ | true strain (Hencky strain) | mm/mm |
| $\gamma$ | shear strain | mm/mm |
| $\gamma_{\mathrm{des}}$ | design shear strain | mm/mm |
| $\gamma_{\mathrm{E}}$ | real acting strain level | mm/mm |
| $\gamma_{\mathrm{fail}}$ | cyclic shear strain for $D_t = 1.0$ | mm/mm |
| $\gamma_{\mathrm{Max}}$ | maximum shear strain per cycle | mm/mm |
| $\gamma_{\tau_0}$ | shear strain at initial shear stress | mm/mm |
| $\gamma_{\tau_{\mathrm{des}}}$ | shear strain at design shear stress | mm/mm |
| $\gamma_{\mathrm{ult}}$ | shear strain at failure | mm/mm |
| $\gamma_{\mathrm{ult,mean}}$ | arithmetic mean shear strain at failure | mm/mm |
| $\lambda$ | stretch ratio | – |
| $\sigma$ | normal stress | MPa |
| $\sigma_{\mathrm{des}}$ | design normal stress | MPa |
| $\sigma_{\mathrm{w}}$ | true stress | MPa |
| $\tau$ | shear stress | MPa |
| $\tau_0$ | lower reference shear stress | MPa |
| $\tau_{\mathrm{des}}$ | design shear stress | MPa |
| $\tau_{\mathrm{E}}$ | real acting stress level | MPa |
| $\tau_{\mathrm{fail}}$ | cyclic shear stress for $D_t = 1.0$ | MPa |
| $\tau_{\gamma_{\mathrm{Max}}}$ | shear stress at maximum strain | MPa |
| $\tau_{\mathrm{k}}$ | characteristic shear stress | MPa |
| $\tau_{\mathrm{k,ETA}}$ | characteristic shear stress according to the manufacturer's ETA approval | MPa |
| $\tau_{\mathrm{ult}}$ | shear stress at failure | MPa |
| $\tau_{\mathrm{ult,mean}}$ | arithmetic mean shear stress at failure | MPa |

## Energy-based quantities

| | | |
|---|---|---|
| $w_{\text{cum}}$ | cumulative dissipated energy density | MPa |
| $w_{\text{cum,fail}}$ | cumulative dissipated energy density at failure | MPa |
| $w_{\text{cum,fail,theo}}$ | theoretical cumulative dissipated energy density at failure obtained by linear extrapolation of $w_{\text{cum}}$ over the normalized cycle count and evaluated at $n^* = 1$ | MPa |
| $W_{\text{diss}}$ | dissipated energy | J |
| $w_{\text{diss}}$ | dissipated energy density | MPa |
| $w_{\text{el}}$ | elastic strain energy density | MPa |

## Dynamic and seismic response

| | | |
|---|---|---|
| $a_{\text{g}}(t)$ | ground acceleration time history | $\text{m/s}^2$ |
| $a_{\text{gR}}$ | reference peak ground acceleration on type A ground | $\text{m/s}^2$ |
| $C$ | damping matrix | Ns/m |
| $c$ | damping coefficient | Ns/m |
| $d_e$ | elastic displacement | m |
| $\delta_{\text{R}}$ | story drift | m |
| $d_s$ | seismic displacement | m |
| $\eta$ | loss factor | – |
| $\eta_{\text{c}}$ | damping correction factor (EC8) | – |
| $F_{\text{b}}$ | base shear force | kN |
| $\gamma_{\text{I}}$ | importance factor | – |
| $H$ | story height | m |
| IDR | interstory drift ratio | – |
| $K$ | stiffness matrix | N/m |
| $k$ | stiffness | N/m |
| $\lambda_{\text{c}}$ | correction factor for base shear (EC8) | – |
| $M$ | mass matrix | kg |
| $m_{\text{s}}$ | effective mass of the structural system | kg |
| $M_{\text{w}}$ | moment magnitude | – |
| $\Omega$ | excitation frequency | rad/s |
| $\omega$ | circular frequency | rad/s |

| | | |
|---|---|---|
| $\omega_\mathrm{d}$ | damped circular frequency | rad/s |
| $\omega_\mathrm{n}$ | natural circular frequency | rad/s |
| $\widehat{p}$ | load amplitude | N |
| $\varphi_0$ | initial phase angle | rad |
| $\psi$ | specific damping capacity | – |
| $p(t)$ | external load | N |
| $q$ | behavior factor (EC8) | – |
| $S_\mathrm{a}$ | pseudo-acceleration response spectrum | $\mathrm{m/s^2}$ |
| $S_\mathrm{d}$ | design acceleration response spectrum | $\mathrm{m/s^2}$ |
| $S$ | soil factor (EC8) | – |
| $S_\mathrm{u}$ | displacement response spectrum | m |
| $S_\mathrm{v}$ | pseudo-velocity response spectrum | m/s |
| $T$ | natural period of vibration | s |
| $t$ | time | s |
| $T_\mathrm{B}$ | lower limit of the constant spectral acceleration branch | s |
| $T_\mathrm{C}$ | upper limit of the constant spectral acceleration branch | s |
| $u$ | displacement | m |
| $u_0$ | initial displacement | m |
| $\ddot{u}$ | acceleration response | $\mathrm{m/s^2}$ |
| $\dot{u}$ | velocity | m/s |
| $u_\mathrm{g}(t)$ | ground displacement time history | m |
| $\widehat{u}$ | displacement amplitude | m |
| $\varphi$ | phase angle | rad |
| $v_\mathrm{g}(t)$ | ground velocity time history | m/s |
| $\zeta$ | damping ratio | – |

## Fatigue and cyclic loading

| | | |
|---|---|---|
| CSR | cyclic stress ratio | % |
| $CSR_{N=50}$ | cyclic stress ratio corresponding to failure after 50 load cycles | % |
| $CSR_{fail}$ | failure cyclic stress ratio for $D_t = 1.0$ | % |
| $CSR_{\gamma}$ | cyclic stress ratio based on shear strain normalization | % |
| $CSR_{Ref}$ | reference cyclic stress ratio for equivalent cycle evaluation | % |
| $CSR_{\tau}$ | cyclic stress ratio based on shear stress normalization | % |
| $D$ | damage parameter | – |
| $\Delta\sigma$ | stress range | MPa |
| $\delta_{\tau,test}$ | termination criterion based on the normalized reduction of the maximum shear stress | – |
| $D_t$ | target damage | – |
| $f$ | frequency | Hz |
| $G_{Max,i}$ | dynamic shear stiffness (secant modulus at maximum strain) | MPa |
| $G_{Max,Fail}$ | dynamic shear stiffness at failure | MPa |
| $n_{eq}$ | equivalent number of cycles | – |
| $N_f$ | number of cycles to failure at a given load level | – |
| $N_{fail}$ | number of cycles determined to failure | – |
| $N_i$ | cycle number | – |
| $n_i$ | number of applied cycles at a given load level | – |
| $N_{max}$ | maximum number of cycles | – |
| $N_{Ref}$ | reference number of cycles | – |
| $n^*$ | normalized number of cycles | – |
| $R$ | stress ratio | – |
| $\sigma_a$ | stress amplitude | MPa |
| $\sigma_m$ | mean stress | MPa |
| $\sigma_o$ | maximum stress | MPa |
| $\sigma_u$ | minimum stress | MPa |
| $t_f$ | time to failure | s |

## Design and safety

| | | |
|---|---|---|
| $A_{Ed}$ | design value of the seismic action | – |
| $E_d$ | design value of the effect of actions | – |
| $E_k$ | characteristic value of the effect of actions | – |
| $\gamma_M$ | material partial safety factor | – |
| $\gamma_{meth,ETAG}$ | method factor according to ETAG 002-1 | – |
| $\gamma_{meth,FKG}$ | reduced method factor according to FKG (with manufacturer approval) | – |
| $\gamma_{meth,s}$ | global seismic method factor in the ETAG format | – |
| $\gamma_{Q,1}$ | combined partial safety factor for leading variable action | – |
| $k_{mod}$ | modification factor for load duration and moisture content | – |
| $k_{sr}$ | seismic reserve factor | – |
| $k_{sr,ETA}$ | seismic reserve factor based on characteristic values from ETA | – |
| $k_{sr,k}$ | seismic reserve factor based on characteristic values of the reference series | – |
| $P$ | prestressing action | – |
| $\psi_{2,i}$ | combination factor for quasi-permanent actions | – |
| $Q_k$ | characteristic value of variable action | – |
| $R_d$ | design structural resistance | – |
| $R_k$ | characteristic structural resistance | – |

## Statistical and regression parameters

| | | |
|---|---|---|
| $a$ | scaling parameter of the S–N curve (Basquin model) | – |
| $a_{\mathrm{k}}$ | characteristic scaling parameter of the S–N curve (Basquin model) | – |
| $\alpha$ | parameter defining the confidence level $1-\alpha$ | – |
| $a_{\mathrm{Real}}$ | scaling parameter of the S–N curve in real stress space (Basquin model) | – |
| $a_w$ | regression parameter of the power-law model for cumulative dissipated energy density as a function of $n^*$ and CSR | – |
| $a_w^{\mathrm{F}}$ | regression parameter of the power-law model for cumulative dissipated energy density at failure as a function of CSR | – |
| $b_w$ | exponent of the power-law model for cumulative dissipated energy density | – |
| $b_w^{\mathrm{F}}$ | exponent of the power-law model for cumulative dissipated energy density at failure | – |
| $k_3$ | fractile factor | – |
| $m$ | slope parameter of the S–N curve | – |
| $n$ | sample size | – |
| $p$ | quantile level defining the lower fractile (here $p = 0.05$) | – |
| $R^2$ | coefficient of determination | – |
| $s$ | sample standard deviation | – |
| $s_{\mathrm{reg}}$ | residual standard deviation of the S-N regression in $\log N$ | – |
| $t_{1-\alpha,n-1}$ | quantile of Student's t-distribution for confidence level $1-\alpha$ and $n-1$ degrees of freedom | – |
| $w$ | weighting factor for regression | – |

# 1 Introduction

## 1.1 Motivation

Glass is increasingly used in modern construction as both a structural and an architectural element. The architectural demand for maximum transparency has led to the realization of large-area glass facades with highly slender support systems. In addition to mechanical fixings, structural glazing (SG) has become an established solution, in which glass elements are bonded to the supporting structure by load-bearing adhesive joints.

For the verification of such bonded facade systems, current guidelines such as (ETAG 002-1) and (DIN EN 13830) provide design and construction principles primarily for quasi-static actions, including wind and temperature loads. Numerous studies have investigated the load-bearing and deformation behavior of SG joints at ultimate limit state conditions and confirmed the general reliability of this connection technology under quasi-static loading. At the same time, geophysical natural hazards, particularly earthquakes, represent one of the most severe types of natural disasters worldwide. Approximately 56 % of fatalities caused by natural hazards are attributed to geophysical events. A comparison of the 2010 earthquakes in Haiti and New Zealand, which had similar magnitudes, highlights the decisive importance of building regulations and structural design. While no fatalities were recorded among approximately 300,000 affected people in New Zealand, about 220,000 people lost their lives in Haiti. Furthermore, global evaluations of seismic events without tsunami between January 2000 and June 2021 indicate an average of more than 22,000 fatalities and economic losses of approximately 14 billion US$ per year, underlining the persistent societal and economic relevance of seismic actions (Allen 2007; Wallemacq et al. 2018; CRED 2021).

These observations demonstrate that earthquakes, despite their relatively low probability of occurrence, involve a considerable damage potential. During an earthquake, the foundations and supports of structures are subjected to seismic ground motion, resulting in inertia-induced dynamic actions. These effects can significantly affect glass and facade constructions, particularly due to deformation demands imposed on facade systems.

When considering the performance of facades under seismic loading, two major consequences must be taken into account. These include hazards to people caused by falling glass fragments and substantial economic losses due to downtime and repair costs (Behr 2009). Damage to non-structural elements such as facade systems has been documented in numerous studies (Hosseini 2005; FEMA E-74; Baird et al. 2011; MacRae et al. 2012; Inca 2019; Perrone et al. 2019). Observed damage patterns, as illustrated in Figure 1.1, include failures

of glazing and facade components observed during the earthquakes in Chile in 2010 and Christchurch in 2011 (FEMA E-74; Baird et al. 2011).



(a) (b)

**Figure 1.1:** Damage patterns in facade systems: (a) glazing damage following the 2010 Chile earthquake (FEMA E-74); (b) facade damage in multi-story buildings following the 2011 Christchurch earthquake (Baird et al. 2011).

Despite the demonstrated relevance of seismic actions, current design standards do not explicitly address the verification of bonded glass facades under seismic loading. In practice, engineers often apply simplified approaches based on global structural analyses or provisions for non-structural components. This can lead to considerable uncertainties, particularly for large-scale glass elements, with potentially severe consequences in case of failure.

Therefore, there is a clear need to systematically investigate the load-bearing and failure behavior of SG joints under seismic loading. The present work contributes to this objective by providing a detailed analysis of the dynamic structural behavior and by establishing a basis for an engineering-oriented design of glass and facade constructions subjected to seismic actions.

## 1.2 State of the Art

The use of low-modulus silicone adhesives in SG systems to enable load transfer while accommodating deformations has been widely documented in the literature. General load-bearing characteristics and initial design approaches for SG joints have been established by (Hagl 2006; Hagl 2007). Numerous studies have investigated the performance of SG systems under environmental influences such as temperature, humidity, ultraviolet radiation, and cyclic movements (White et al. 2012; Van Lancker et al. 2016; Wallau 2023). Further experimental investigations have addressed the influence of joint geometry, temperature, ageing, and manufacturing processes on the mechanical properties of SG joints (Schuler et al. 2017; Bues et al. 2019; Bues 2021; Müller et al. 2023b). These studies provide a

comprehensive understanding of SG joints under quasi-static and environmental loading conditions and form the basis of current design practice.

In parallel, significant efforts have been devoted to the numerical modeling of SG adhesives using advanced hyperelastic material formulations (Dias et al. 2014; Richter 2018; Drass 2020; Rosendahl 2020; Van Lancker et al. 2020; Schaaf and Feldmann 2023; Schaaf 2024). In addition, various approaches have been proposed to predict failure behavior (Maniatis et al. 2015; Santarsiero 2015; Descamps et al. 2017; Staudt et al. 2018; Richter et al. 2021; Jordi Alcaine et al. 2024; Schaaf and Feldmann 2024). These methods typically rely on complex numerical models requiring extensive experimental calibration and are primarily developed for quasi-static loading conditions.

From a design perspective, several standards and guidelines provide simplified verification approaches for SG joints in facade systems, including (ETAG 002-1; ASTM C1401; DIN EN 13022-1; EAD 090010-00-0404; DIN EN 13830). These documents allow the dimensioning of SG joints within defined application limits, primarily for static loading scenarios. Application-oriented guidelines further extend these approaches to more complex configurations and provide guidance for combined wind and temperature loading (DVS 3303; FKG 01/2021). However, these design concepts are restricted to quasi-static actions and do not address seismic loading.

Seismic actions are characterized by inertia-induced forces resulting from ground motion and typically involve a small number of high-intensity load cycles. Established seismic design concepts are implemented in standards such as (EN 1998-1), which define analysis methods ranging from equivalent static approaches to nonlinear time-history analyses. In engineering practice, simplified methods are predominantly applied. While these concepts account for the global structural response, the behavior of facade systems and their connections is often considered in a simplified manner.

Extensive research has been conducted on the seismic performance of facade systems, including experimental investigations and numerical simulations of curtain wall structures (Huang et al. 2017a; Momeni and Bedon 2024). Most studies focus on glass failure and the global response of facade systems, often based on full-scale mock-up tests combined with analytical and numerical modeling. Further studies demonstrate that connection detailing plays a key role in accommodating deformations and preventing premature failure (Bedon and Amadio 2017; Bedon et al. 2019; Santarsiero et al. 2019). Nevertheless, the adhesive layer itself is frequently not the primary focus of investigation.

Despite the relevance of seismic actions, only a limited number of studies address the behavior of SG joints under cyclic loading representative of such conditions, namely under low-cycle fatigue (LCF). Early investigations reported no significant influence of prior cyclic loading on the ultimate strength (Zarghamee et al. 1996; Broker et al. 2012; Memari et al. 2012a). In contrast, other studies observed a reduction in strength following repeated deformation (Nardini and Doebbel 2016; Nardini and Doebbel 2020). Furthermore, cyclic

loading effects such as the Mullins effect have been characterized in SG adhesives (Palmieri et al. 2009; Schaaf et al. 2021).

In summary, existing research provides extensive knowledge on SG joints under quasi-static and environmental loading, as well as on numerical modeling and design approaches within current normative frameworks. Despite these findings, a consistent understanding of the load-bearing and failure behavior of SG joints under LCF and seismically relevant loading conditions is still lacking. This gap forms the basis of the present work.

## 1.3 Problem Statement

Based on the state of the art, clear knowledge gaps exist regarding the load-bearing and failure behavior of SG joints under seismic loading, the characterization of seismically induced loading demands, and engineering design recommendations for SG joints under seismic actions. The following research questions are addressed:

- What load-bearing and failure behavior do SG joints exhibit under LCF loading?
- Is it possible to predict the load-bearing performance of SG joints under LCF loading?
- Which loading conditions typically result from earthquake events, and how can they be characterized for the design of SG joints?
- Which recommendations can be derived for the engineering design of SG joints under seismic loading?

The following working hypotheses are formulated:

- Under LCF loading, SG joints exhibit different failure behavior compared to quasi-static loading, while the initial load-bearing response remains broadly comparable.
- The low-cycle fatigue performance of SG joints can be characterized through experimental investigations and described using an extended Basquin approach.
- Seismic loading on SG joints can be quantified to identify the governing parameters for engineering assessment and design.
- Based on the experimental and analytical findings, an engineering design concept for SG joints under seismic loading can be developed that is applicable within existing normative frameworks.

These working hypotheses are grounded in the current state of the art and the author's own prior work. Their verification or potential refinement through experimental and analytical findings forms the basis for the objectives defined in the following section.

## 1.4 Objectives and Limitations

The objective of the present work is to investigate the load-bearing and failure behavior of SG joints in glass and facade construction under realistic seismic loading conditions and to establish an engineering design concept based on these findings. The following specific objectives are pursued:

- Identification and delimitation of the governing parameters affecting the load-bearing behavior of SG joints under LCF loading.
- Experimental characterization of the load-bearing and failure behavior of SG joints, taking into account the relevant influencing factors.
- Analysis of seismic loading on glass and facade constructions and characterization of representative loading conditions.
- Development of an engineering methodology for the design of SG joints under seismic loading.

**Scope and limitations:** The focus of this work is on short-term cyclic loading resulting from seismic events. Long-term effects such as creep, ageing, or temperature dependence are not considered. The experimental and analytical investigations are limited to nominal joint geometries and result in phenomenological prediction models, without explicitly representing the actual failure mechanisms or the effective load-bearing cross-section of the SG joint. Furthermore, the derived recommendations are based on small-scale specimen tests and do not include the structural behavior of complete glass or facade systems.

## 1.5 Structure of the Thesis

The present work is structured into consecutive chapters covering theoretical foundations, experimental and analytical investigations, and the derivation of engineering design recommendations. The thesis considers both the action side and the resistance side of the interdisciplinary problem. The action side comprises the characterization of seismic loading demands on SG joints, whereas the resistance side comprises LCF performance of SG joints. Due to the dynamic nature of seismic actions, these aspects are closely coupled and cannot be considered independently. Therefore, the problem is addressed through their combined analysis within a coupled framework. The overall structure of the thesis is schematically illustrated in Figure 1.2.

Following the introduction in chapter 1, chapter 2 summarizes the theoretical background, including adhesive bonding, mechanical and dynamic fundamentals, fatigue, and seismic actions, and provides the basis for the subsequent investigations. Chapter 3 focuses on glass and facade systems and reviews the current state of research, with particular emphasis on SG facades under seismic loading, from which the relevant knowledge gaps are identified.

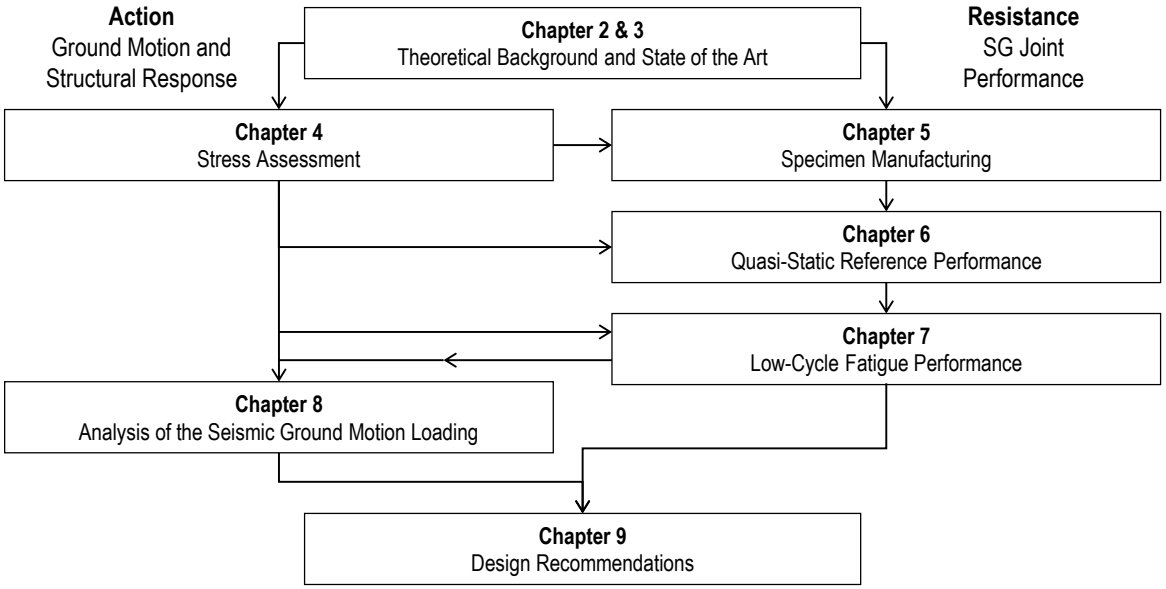


**Figure 1.2:** Schematic overview of the methodological framework of the present work, illustrating the interaction between loading, material behavior, experimental investigation, and engineering design.

Based on these findings, chapter 4 establishes the fundamental framework for the investigation by analyzing the stress conditions and defining the relevant loading characteristics, joint geometries, and influencing parameters. Chapter 5 addresses the specimen manufacturing and examines the influence of production and curing conditions on the material behavior, ensuring a consistent experimental basis. Chapter 6 defines the quasi-static reference behavior of the investigated SG joints, which serves as a baseline for the subsequent evaluation under cyclic loading.

Building on these results, chapter 7 investigates the load-bearing and failure behavior under LCF loading through experimental studies. The cyclic load-bearing behavior is analyzed using cyclic stress–strain curves, revealing a difference between force- and displacement-controlled tests. To further evaluate the cyclic performance, characteristic cyclic parameters are evaluated, which form the basis for defining suitable failure criteria for the displacement-controlled test. To describe the frequency-dependent load cycles to failure, typical fatigue models are applied and extended.

In chapter 8, the seismic loading is analyzed by means of an engineering-oriented simulation approach. Real ground motion records are evaluated and transformed into equivalent load cycles, using the frequency-dependent fatigue models from chapter 7. Combining the load-bearing behavior of the SG joint with real seismic load histories, the evaluation and derivation of frequency dependent design parameters is possible.

Based on the experimental and analytical results, chapter 9 derives multiple engineering design recommendations with varying degrees of complexity for SG joints under seismic loading. The thesis concludes with a summary of the main findings and an outlook on future research.

## 1.6 List of Own Publications

Parts of the results presented in this thesis have been previously published in peer-reviewed journals and conference proceedings. These publications form the basis for selected analyses and methodological developments presented in this work, which are extended and further developed within the framework of the present thesis.

The experimental investigations and parts of the analysis are based on results obtained within the *Industrielle Gemeinschaftsforschung* (IGF) research project *Dickschichtklebungen in Katastrophenszenarien (RISIKO)* (Müller et al. 2026b), which was conducted as a collaborative research project between Hochschule München, Universität der Bundeswehr München, and TU Braunschweig. The proposal and execution of the research project were carried out under the primary responsibility of the author of this thesis. The final project report will be prepared subsequently, in part based on the findings presented in this thesis. Several further publications are currently under review or in preparation at the time of submission of this thesis.

### 1.6.1 Journal Articles

- Müller, P., E. Stammen, T. Reisewitz, C. Schuler, G. Siebert, S. Koch, and K. Dilger (2026): Vom Versuch zur Bemessung: Dickschichtklebungen unter hoher zyklischer Beanspruchung sicher nachweisen.
  *Joining Plastics*. (Müller et al. 2026d)
- Müller, P., T. Reisewitz, D. Offereins, C. Schuler (2026): Kleben im konstruktiven Glasbau: Zum Tragverhalten unter Erdbebenbeanspruchung.
  *Stahlbau*. (Müller et al. 2026a)
- Müller, P., C. Schuler, and G. Siebert (2025): Analysis of the seismic ground motion loading on structural glazing connections in glass and facade constructions.
  *Bulletin of Earthquake Engineering*. (Müller et al. 2025b)
- Müller, P., C. Schuler, and G. Siebert (2025): Discussion of failure criteria and low-cycle fatigue performance of structural glazing connections under various seismic loading scenarios.
  *Construction and Building Materials*. (Müller et al. 2025c)
- Müller, P., C. Schuler, and G. Siebert (2025): Residual performance of structural glazing joints after seismic low-cycle fatigue loading.
  *Glass Structures & Engineering*. (Müller et al. 2025d)
- Müller, P., C. Schuler, and G. Siebert (2024): Experimental investigations on the cyclic load-bearing behavior of structural glazing joints under seismic load.
  *Glass Structures & Engineering*. (Müller et al. 2024)

- Müller, P., C. Schuler, and G. Siebert (2023): Investigations on the influence of manufacturing and curing effects on the properties of structural-glazing adhesives subjected to tensile stresses.
  *Glass Structures & Engineering*. (Müller et al. 2023a)

### 1.6.2 Conference Contributions

- Müller, P., C. Schuler, T. Reisewitz, G. Siebert, S. Koch, E. Stammen, and K. Dilger (2026): Bemessungsmodell für Dickschichtklebungen in Katastrophenszenarien.
  *26. Kolloquium Gemeinsame Forschung in der Klebtechnik*. (Müller et al. 2026c)
- Müller, P. (2025): Design of Structural-Glazing Joints under Seismic Loading
  *Young Engineers Colloquium 2025*. (Müller 2025)
- Müller, P., C. Schuler, and G. Siebert (2025): Seismic Performance of Structural Glazing Connections Under Low Cycle Fatigue Loading: A Study on Alternative Joint Geometries.
  *IABSE Symposium: Environmentally Friendly Technologies and Structures: Focusing on Sustainable Approaches*. (Müller et al. 2025e)
- Müller, P., C. Schuler, T. Reisewitz, G. Siebert, S. Koch, E. Stammen, and K. Dilger (2025): Bemessungsmodell für Dickschichtklebungen in Katastrophenszenarien.
  *25. Kolloquium Gemeinsame Forschung in der Klebtechnik*. (Müller et al. 2025a)
- Müller, P., C. Schuler, and G. Siebert (2025): Strukturelle Klebverbindungen im Glas- und Fassadenbau unter seismischer Beanspruchung.
  *Glas im konstruktiven Ingenieurbau 19 (GIKI19)*. (Müller et al. 2025f)
- Müller, P., C. Schuler, and G. Siebert (2023): Einfluss der Fertigung auf das Tragverhalten von SG-Klebungen.
  *Glas im konstruktiven Ingenieurbau 18 (GIKI18)*. (Müller et al. 2023b)

### 1.6.3 Publications in Preparation

- Müller, P., C. Schuler, and G. Siebert (2026): Modeling Frequency Effects in the Seismic Low-Cycle Fatigue Performance of Structural Glazing Joints Using a Modified S-N Approach.
  *Glass Structures & Engineering*. (In review)

# 2 Theoretical Background

This chapter introduces the theoretical background required for the experimental investigation of the LCF performance of SG joints, the analysis of seismic ground motion loading, and the subsequent determination of design recommendations, covering the fundamentals of adhesive bonding, mechanical and dynamic principles, fatigue and low-cycle fatigue, and seismology.

## 2.1 Fundamentals of Adhesive Bonding

This chapter introduces the fundamental principles of adhesive bonding. The focus is placed on structural glazing (SG) adhesives. For improved understanding, these materials are also discussed in comparison with other adhesive systems.

### 2.1.1 Definitions and Polymer Structure

According to (DIN EN 923), adhesives are defined as non-metallic materials that join substrates through adhesion and internal strength (cohesion). These materials are composed of macromolecular chains whose spatial arrangement governs their mechanical behavior.

Polymers exhibit complex mechanical behavior that depends on several factors. The most relevant parameters affecting the mechanical behavior of silicone adhesives include temperature, time, and the loading conditions, particularly the loading state, loading rate, and loading history.

#### 2.1.1.1 Structure of Polymer Networks

Polymer materials are commonly described as assemblies of macromolecules with different structures and chain lengths. These macromolecules may either form highly cross-linked networks or exist as uncross-linked chains in an amorphous coil structure. Consequently, the degree of cross-linking represents an important characteristic for classifying polymer materials, as it directly influences their mechanical properties. The fundamental structural forms of these polymer classes are schematically illustrated in Figure 2.1.

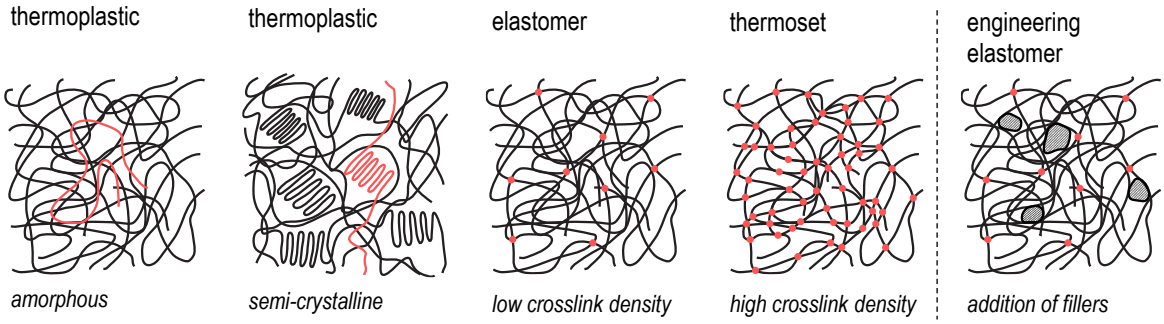


**Figure 2.1:** Schematic representation of different polymer material structures. Based on (Kuntsche 2015; Stommel et al. 2018).

According to (DIN 7724; Dominghaus et al. 2012), polymer materials can be divided into several main groups. These include thermosets (duroplastics), which are characterized by densely cross-linked networks, and thermoplastics, which occur in amorphous or semicrystalline forms without chemical cross-linking points.

The adhesive materials investigated in this work belong to the group of elastomers. Elastomers are characterized by an amorphous polymer network that contains only a limited number of chemical cross-links. In addition to the base polymer, the adhesive typically contains additives such as fillers that modify the technological properties depending on the required performance characteristics (Grambow 2003). Such materials are commonly referred to as technical polymer materials or engineering elastomers.

Alternatively, adhesives can be classified according to their curing mechanism. In this context, adhesives can be divided into chemically reacting adhesives, reactive hot-melt adhesives, and physically curing adhesives.

The silicone adhesives investigated in this work belong to the group of chemically reacting adhesives. Polymer chains are formed through polymerization, polyaddition, or polycondensation. The underlying monomers consist of specific combinations of chemical elements that enable the formation of chain molecules, as illustrated in Figure 2.2 (Habenicht 2009; Habenicht 2016; Feldmann et al. 2017).

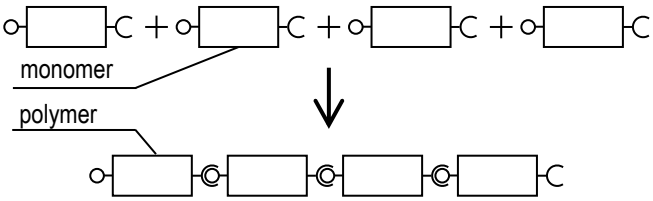


**Figure 2.2:** Schematic illustration of polymerization. Based on (Habenicht 2016).

The main difference between polymerization-, polyaddition-, and polycondensation-based adhesives lies in the underlying chemical reaction mechanism. Polymerization and polyaddition reactions proceed without the formation of low-molecular by-products, whereas polycondensation reactions are associated with the formation of such by-products. This

has direct consequences for the processing and curing behavior of the adhesive layer. Depending on the adhesive system, the polymer chains may be more densely or more loosely cross-linked, resulting in different network structures (Habenicht 2009; Rösler et al. 2019).

### 2.1.1.2 Engineering Classification of Adhesive Systems

As described in section 2.1.1.1 and illustrated in Figure 2.1, polymer materials differ in their network structure and degree of crosslinking, which directly influences their mechanical properties. Thermosets exhibit a highly crosslinked network and typically show elastoplastic material behavior with high stiffness. Elastomers consist of loosely crosslinked polymer networks and generally exhibit hyperelastic behavior, whereas thermoplastics do not possess a pronounced crosslinked network structure (Habenicht 2016; Feldmann et al. 2017).

Adhesive joints are commonly classified as structural or elastic bonding depending on the configuration and stiffness of the adhesive layer. Structural adhesive joints typically exhibit very small adhesive layer thicknesses and high stiffness. They are generally used to join similar materials. In contrast, elastic adhesive joints are typically characterized by hyperelastic material behavior and adhesive layer thicknesses of several millimeters, providing sufficient deformability to accommodate constraint-induced stresses (Habenicht 2016).

From a mechanical perspective, however, both types of adhesive joints exhibit elastic load-bearing behavior. For adhesive systems relevant to civil engineering applications, an alternative classification distinguishes between elastoplastic and hyperelastic systems (Feldmann et al. 2017; Richter 2018), as illustrated in Figure 2.3. In this context, the mechanical material behavior resulting from the polymer structure is the primary criterion. Depending on the application requirements, adhesive systems can therefore be selected either to accommodate large deformations within the adhesive layer or to provide high strength and stiffness. This distinction is of particular relevance for structural design and engineering assessment (Schaaf 2024).

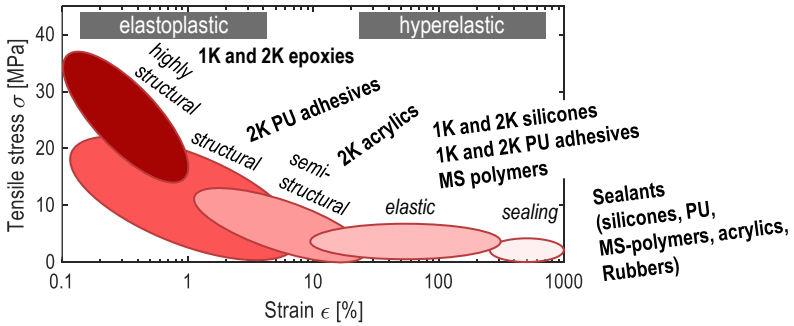


**Figure 2.3:** Classification of adhesives according to their mechanical properties. Based on (Feldmann et al. 2017; Abeln 2019).

#### 2.1.1.3 Silicone Elastomers

Silicones belong to the group of organosilicon compounds and are systematically referred to as polyorganosiloxanes (polysiloxanes) (Benedix 2020). In these materials, silicon atoms replace the carbon atoms typically found in the backbone of macromolecular compounds (Kaiser 2023). Polysiloxanes are characterized by siloxane chains (Si–O–Si), in which silicon atoms are linked by oxygen atoms. The remaining bonds of the silicon atoms are occupied by hydrocarbon groups (R), as illustrated schematically in Figure 2.4 (Benedix 2020).

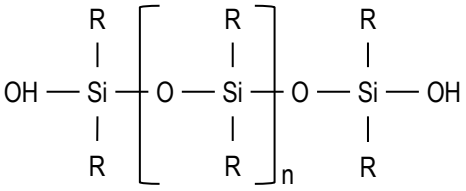


**Figure 2.4:** Schematic representation of the chemical structure of silicones. Based on (Habenicht 2009).

This structure forms an intermediate class between inorganic compounds, such as silicates, and organic polymers with carbon-based main chains (Habenicht 2016). Rotation around the Si–O bond enables high chain flexibility, allowing polysiloxane chains to adopt coiled configurations. This molecular mobility strongly influences the mechanical behavior of silicones under load (Benedix 2020).

According to (Habenicht 2009), curing can occur either as one-component room-temperature vulcanizing systems (RTV-1) or as two-component room-temperature vulcanizing systems (RTV-2). This process is irreversible.

In RTV-1 systems, curing proceeds through a polycondensation reaction initiated by atmospheric moisture. Crosslinking agents are used, which are typically hydrolysis-sensitive substances. These compounds prevent premature reactions by blocking hydroxyl groups while simultaneously increasing the number of reactive functional groups (Habenicht 2009). Because the vulcanization rate is governed by the diffusion of water molecules and increases with temperature, the curing process exhibits a clear temperature dependence. Adhesives that cure according to this mechanism are commonly referred to as one-component silicones.

Two-component silicones correspond to RTV-2 systems. These systems are primarily used when RTV-1 systems cannot cure completely or within acceptable time periods due to large adhesive layer thicknesses. The two components are mixed prior to application and cure through chemical crosslinking independent of atmospheric moisture. Consequently, these systems are particularly suitable for large adhesive layer thicknesses and bonding areas. Crosslinking occurs either through condensation curing with a catalyst, which produces a by-product, or through addition curing without the formation of by-products. In condensation curing, the reaction rate depends on temperature, pH value, catalyst concentration, and polymer structure. In contrast, addition curing is strongly temperature dependent and can be significantly accelerated at elevated temperatures (Habenicht 2009; Benedix 2020).

To obtain loosely crosslinked networks, silicones may contain functional additives such as vinyl or hydroxyl groups, resulting in silicone rubber with typical rubber-elastic material behavior. In addition, fillers can be incorporated to modify the mechanical and chemical properties of the polymer, as discussed in section 2.1.1.1. The resulting material exhibits the characteristic features of elastomers, with macromolecules forming randomly coiled chains within a loosely crosslinked network structure. Although covalent bonds limit the mobility of the polymer chains, chain segments remain sufficiently mobile to slide relative to each other, which governs the characteristic deformation behavior. The resulting mechanical response is dominated by entropic elasticity, as discussed in section 2.1.3.2 (Benedix 2020).

Silicones exhibit high thermal stability up to approximately +200 °C. Their elastic properties are retained at low temperatures down to approximately −70 °C, which corresponds to the glass transition temperature $T_G$, as discussed in section 2.1.3.1. Over this temperature range, silicones remain in the rubber-elastic state and thus maintain their characteristic deformability. They are resistant to weathering and show low susceptibility to radiation and chemical exposure. Silicones are particularly suitable for sealing applications because they are impermeable to liquid water while allowing water vapor diffusion (Habenicht 2016; Benedix 2020).

### 2.1.2 Bonding Forces in Adhesive Joints

The strength of an adhesive joint results from adhesion at the interface between adhesive and adherends and cohesion within the adhesive itself. These mechanisms are schematically illustrated in Figure 2.5 (Habenicht 2009; Geiß et al. 2012).

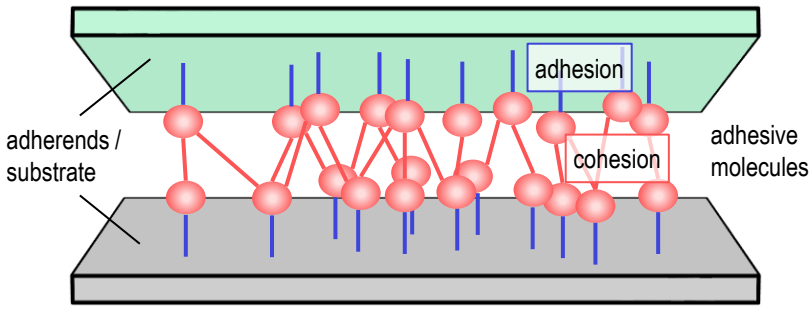


**Figure 2.5:** Schematic representation of adhesion and cohesion. Based on (Geiß et al. 2012).

Adhesion arises from interactions between adhesive molecules and the substrate surface. These include chemical bonds, such as covalent bonds, as well as intermolecular interactions, including hydrogen bonding and van der Waals forces. In addition, mechanical interlocking may occur when the adhesive penetrates surface irregularities of the adherend. Effective adhesion requires sufficient wetting of the substrate, as these interaction forces act only over very small molecular distances (Habenicht 2009; da Silva et al. 2018a; Wistuba 1980).

Cohesion describes the internal strength of the adhesive and is governed by intermolecular interactions and the molecular structure of the polymer network. In particular, chain

entanglement and crosslinking contribute to the load-bearing capacity and deformation behavior of the adhesive.

The strength of an adhesive joint depends on the interaction between adhesive and cohesive mechanisms and is strongly influenced by the surface condition of the adherends. In structural applications, particularly for SG applications, a reliable joint is typically characterized by cohesive failure within the adhesive layer rather than adhesive failure at the interface (Habenicht 2009; Rasche 2012; Albiez 2016).

### 2.1.3 Fundamental Mechanical Behavior of Polymers

Polymer materials exhibit mechanical behavior that is strongly governed by their molecular structure and the mobility of polymer chains. As a result, their response to mechanical loading is typically nonlinear and depends on temperature, loading rate, and time. The following sections summarize the fundamental mechanisms that govern the mechanical behavior of polymer materials.

#### 2.1.3.1 Aggregate States

The time- and temperature-dependent viscoelastic properties of polymer materials form the basis for their classification into elastomers, thermoplastic elastomers, thermoplastics, and thermosets (Grellmann and Seidler 2025). Depending on temperature, characteristic aggregate states of a polymer networks can be distinguished. These include the energy-elastic glassy state below the glass transition temperature $T_G$, the glass transition region, and the entropy-elastic rubbery state above $T_G$ (Schwarzl 1990; Habenicht 2016).

For elastomers, the rubber-elastic state extends continuously from $T_G$ to the decomposition temperature $T_Z$ without passing through a thermoplastic melt state. Consequently, elastomers are neither thermally formable nor weldable (Benedix 2020). The glass transition temperature of elastomers typically lies between approximately $-100$ °C and $-20$ °C. As a result, elastomers used in structural engineering applications operate at temperatures above $T_G$, where they exhibit entropy-elastic material behavior with significantly reduced stiffness (Benedix 2020; Kaiser 2023).

The characteristic temperature-dependent stiffness of elastomers, with a pronounced decrease in the glass transition region, is schematically illustrated in Figure 2.6. This representation shows that silicone adhesives used in construction generally operate within the rubber-elastic state (Schwarzl 1990; DIN 7724; Kuntsche 2015). The temperature-dependent transitions between these states and the associated reduction in mechanical properties can be experimentally determined using dynamic mechanical thermal analysis, which enables frequency- and temperature-dependent characterization of viscoelastic material behavior (Grellmann and Seidler 2025).

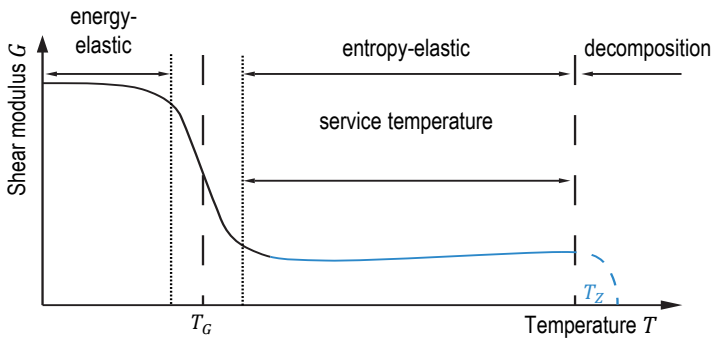


**Figure 2.6:** Schematic representation of stiffness as a function of temperature for elastomers. Based on (Schwarzl 1990; DIN 7724; Kuntsche 2015).

#### 2.1.3.2 Entropic Elasticity

The pronounced nonlinear stress–strain behavior of elastomers results from the highly coiled and statistically disordered polymer chains that exist above the glass transition temperature $T_G$ (Rösler et al. 2019; Grellmann and Seidler 2025). Under external mechanical loading, the macromolecules are stretched between their anchoring or crosslinking points. Complete sliding of the chains is not possible because their motion is strongly restricted by entanglements and crosslinks. The molecular mechanism of entropic elastic deformation, characterized by stretching of the polymer chains between anchoring points, is schematically illustrated in Figure 2.7 (Rösler et al. 2019).

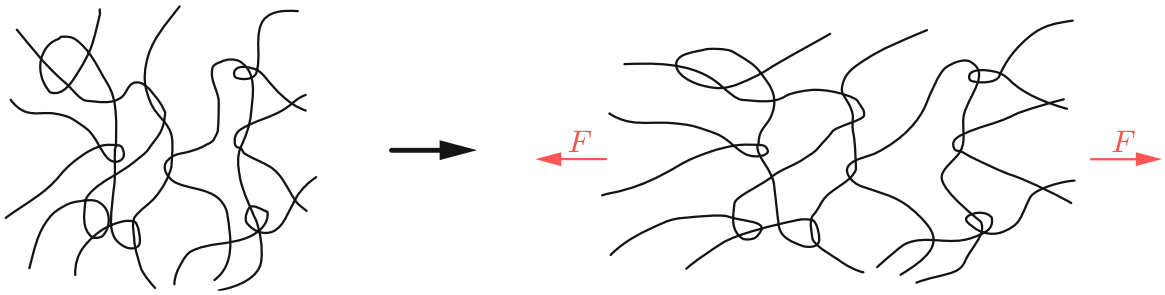


**Figure 2.7:** Molecular mechanism of entropic elastic deformation above the glass transition temperature, showing stretching of polymer chains. Based on (Rösler et al. 2019).

This alignment of the chains reduces the entropy of the system. After unloading, the polymer chains return to the statistically more probable coiled configuration due to the thermodynamic driving force toward entropy maximization according to the second law of thermodynamics. This process results in the reversible recovery of the deformation (Rösler et al. 2019; Grellmann and Seidler 2025). This restoring mechanism is referred to as entropic elasticity.

Entropic elastic behavior is characteristic of elastomers above the glass transition temperature $T_G$ because the covalent crosslinking of the polymer chains prevents plastic flow and allows large reversible strains of several hundred percent (Rösler et al. 2019). The resulting stress–strain relationship is strongly nonlinear. This material behavior is therefore described

as hyperelasticity and requires the application of large-deformation theories for mechanical modeling (Rösler et al. 2019; Grellmann and Seidler 2025).

In contrast, thermosets predominantly exhibit energy-elastic behavior due to their high crosslink density and the resulting strong restriction of chain mobility, even above the glass transition temperature (Rösler et al. 2019). In this case, elastic deformation mainly results from the displacement of atoms from their equilibrium positions, while entropic elastic effects play only a minor role. This leads to high stiffness combined with limited deformability (Rösler et al. 2019; Grellmann and Seidler 2025).

#### 2.1.3.3 Mullins Effect

The Mullins effect, named after its discoverer, describes the deformation-induced stress softening of filled and unfilled elastomeric materials under cyclic mechanical loading (Mullins 1969). This phenomenon is also observed in silicone-based structural adhesives. Phenomenologically, the Mullins effect appears as different loading and unloading paths in the stress–strain diagram, as illustrated in Figure 2.8. After initial loading, the unloading curve follows a path below the loading curve. Upon reloading to the same strain level, the loading curve lies significantly below the original virgin loading curve, approximately on the unloading path . With an increasing number of load cycles at constant maximum strain, the stress–strain response gradually stabilizes and approaches a steady-state condition (Kahraman 2015). If a higher strain level is subsequently reached, the stress–strain curve follows the original loading path above the previously attained strain level. In addition, a load-path-dependent residual strain at zero stress can occur. This residual strain is of viscoelastic origin and should not be interpreted as plastic deformation.

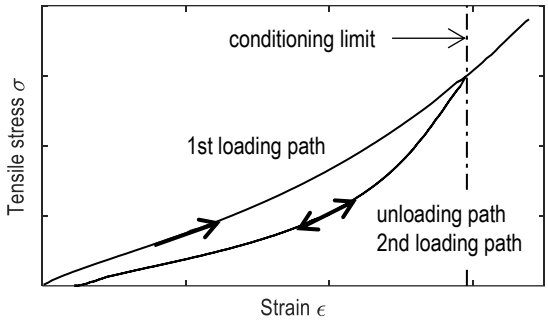


**Figure 2.8:** Schematic representation of the Mullins effect in a tensile test showing the first and second loading paths. Based on (Bues 2021; Schuler et al. 2023).

Furthermore, the Mullins effect may lead to anisotropic and inhomogeneous material behavior, although the elastomer is initially isotropic. Regions of a component that have previously experienced mechanical loading may respond either stiffer or softer than unloaded regions during subsequent or directionally changed loading, depending on their individual deformation history (Stommel et al. 2018). This load-path- and direction-dependent behavior is particularly relevant for elastomer components and adhesive joints subjected to complex stress states.

For structural design, a distinction must be made between the stiffness relevant for service conditions and the strength assessment in the ultimate limit state. The stiffness under operational loading should be described using a preconditioned stress–strain curve. In contrast, the load-bearing capacity is commonly evaluated based on the initial loading path, since the governing strains in ultimate limit states typically exceed those reached during service conditions, where the Mullins effect becomes less relevant (Bues 2021).

Several mechanisms have been proposed in the literature to explain the Mullins effect. In filled elastomers, the deformation-induced stress softening is mainly attributed to microstructural changes within the filler system, such as the cyclic rupture and partial reformation of filler–filler bonds and filler networks under mechanical loading (Bueche 1960; Bueche 1961; Heinrich and Klüppel 2000). In addition, sliding of polymer chains along filler surfaces and the rearrangement and reorientation of macromolecules are considered energy-dissipating mechanisms that contribute to the irreversible softening of the material (Heinrich and Klüppel 2000).

#### 2.1.3.4 Payne Effect

The Payne effect, first described by (Payne 1957), refers to the decrease in dynamic stiffness of filled elastomers with increasing strain amplitude under cyclic loading. Phenomenologically, this effect appears as a change in the shape and slope of the hysteresis loops, while the dynamic stiffness, defined as the slope of the line connecting the reversal points, decreases with increasing amplitude (Grambow 2003; Kaindl 2014; Stommel et al. 2018).

In addition to this amplitude dependence, the dynamic stiffness of elastomers also depends on the loading frequency. As illustrated in Figure 2.9a, the dynamic stiffness increases with increasing excitation frequency due to the viscoelastic material behavior. In contrast, Figure 2.9b illustrates the amplitude dependence, where the dynamic stiffness decreases with increasing strain amplitude. These amplitude-dependent changes in stiffness are commonly referred to as the Payne effect.

According to the model proposed by Payne, the stiffness of filled elastomers consists of the base stiffness of the unfilled polymer matrix and additional reinforcing contributions from the filler. The observed reduction in stiffness at larger amplitudes is attributed to the breakdown of the filler network, particularly the disruption of filler–filler interactions such as carbon black networks (Payne et al. 1972; Kaindl 2014). Further studies indicate that, in addition to the destruction of the filler network, changes in filler–polymer interactions and dissipative processes contribute to the pronounced hysteresis behavior (Heinrich and Klüppel 2000).

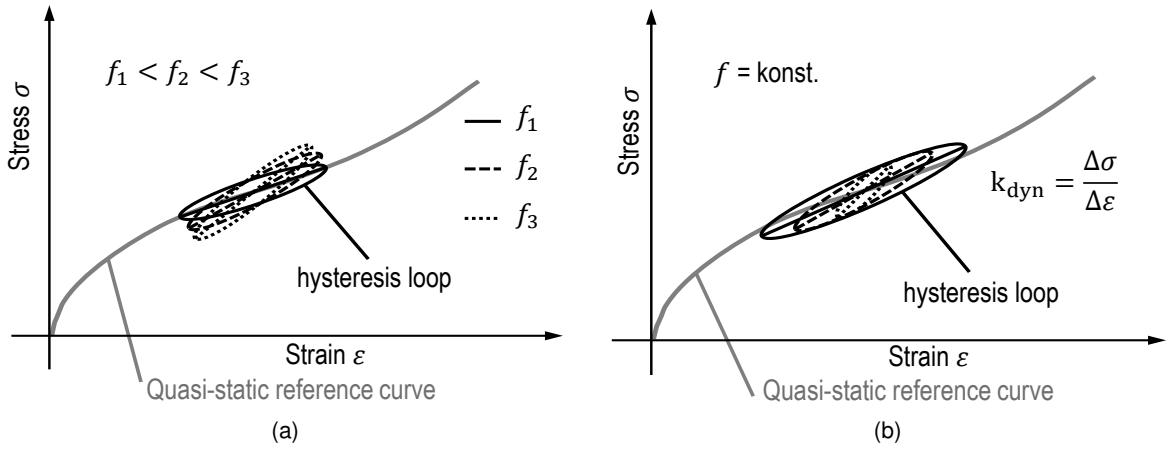


**Figure 2.9:** Schematic representation of the Payne effect: (a) frequency-dependent behavior, (b) amplitude-dependent behavior. Based on (Payne et al. 1972; Kaindl 2014).

#### 2.1.3.5 Incompressibility

Elastomeric materials are often described as exhibiting incompressible behavior. However, this designation does not imply strict volume constancy. Instead, it arises from the pronounced difference between the bulk modulus $K$ and the shear modulus $G$ in the rubber-elastic temperature range. While the bulk modulus remains nearly constant over a wide temperature range, the shear modulus decreases significantly above the glass transition temperature. For temperatures well above the glass transition temperature $T_G$, the relationship can therefore be approximated as $G \ll K$, which corresponds to a Poisson's ratio of $\nu \approx 0.5$, characteristic of nearly incompressible materials.

As a consequence of this relationship, shear deformations are several orders of magnitude larger than the associated volumetric strains under comparable stress levels. The resulting volume changes can therefore be neglected in the mechanical description. Under these conditions, elastomers can be treated as approximately incompressible materials, which is particularly relevant for the modeling and evaluation of adhesive joints with constrained lateral deformation (Schwarzl 1990).

#### 2.1.3.6 Time-Dependent Mechanical Behavior

The time-dependent mechanical behavior of elastomers is referred to as viscoelasticity and cannot be described by purely elastic or purely viscous constitutive laws. The fundamental relationships governing creep and stress relaxation were systematically formulated by (Schwarzl 1990). Under constant stress $\sigma$, the strain $\epsilon$ increases with time $t$, a behavior referred to as creep. The corresponding strain-time response is shown schematically in Figure 2.10a. In contrast, under constant strain $\epsilon$ the stress $\sigma$ decreases over time $t$, which is referred to as stress relaxation. The corresponding stress-time response is illustrated in Figure 2.10b (Flügge 1975; Schwarzl 1990; Schaaf 2024).

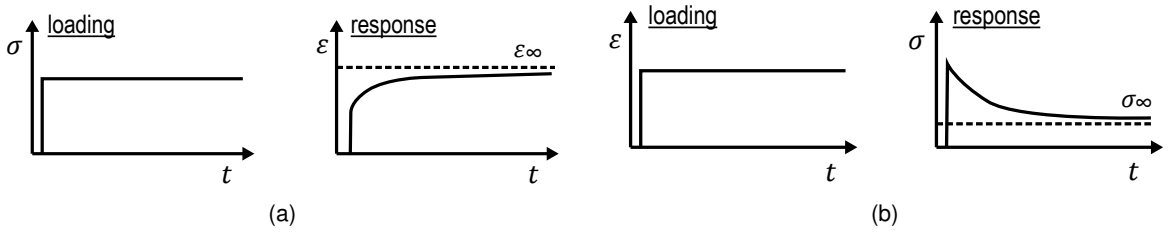


**Figure 2.10:** Schematic strain-time and stress-time response: (a) during creep, (b) during stress relaxation. Based on (Flügge 1975; Schaaf 2024).

Creep behavior is particularly relevant for elastomeric adhesive joints in which permanent loads, such as self-weight, are transmitted through the adhesive layer. Typically, primary, secondary, and tertiary creep stages can be distinguished. In structural engineering applications, however, only the primary and secondary stages are generally relevant (Stommel et al. 2018). These time-dependent deformation processes result from molecular rearrangements within the polymer structure and exhibit a strong dependence on temperature.

#### 2.1.3.7 Dynamic Cyclic Viscoelastic Behavior

Under cyclic loading, the viscoelastic behavior of polymers becomes particularly pronounced. A phase shift occurs between stress and strain, resulting in a hysteresis loop in the stress–strain diagram. The enclosed area represents the energy dissipated per load cycle and leads to self-heating of the material (Stommel et al. 2018).

Depending on the loading condition, a distinction is made between stress-controlled and strain-controlled cyclic loading. Under stress-controlled loading, the mean strain may increase over time due to viscoelastic effects. In contrast, under strain-controlled loading, the mean stress decreases. The dynamic material properties can be described using the storage modulus and the loss modulus, whose ratio characterizes the degree of viscoelasticity (Schwarzl 1990; Stommel et al. 2018).

#### 2.1.3.8 Time-Temperature Superposition

Viscoelastic polymer materials exhibit not only pronounced time dependence but also a strong temperature dependence of their mechanical behavior. This behavior results from thermally activated molecular motion and rearrangement processes that determine the relaxation and retardation spectrum. With increasing temperature, these processes occur at higher rates. As a result, characteristic viscoelastic material functions, such as the previously described creep or relaxation functions, shift toward shorter times along the logarithmic time axis, while their shape remains approximately unchanged (Schwarzl 1990; Grellmann and Seidler 2025).

This behavior is referred to as time–temperature equivalence and forms the basis of the time–temperature superposition (TTS) principle. The principle applies when changes in

temperature affect only the rate of molecular processes but not their type or number. Materials that satisfy this condition are described as thermorheologically simple (Schwarzl 1990; Bues 2021). By horizontally shifting viscoelastic material functions obtained at different temperatures along the logarithmic time axis, these curves can be combined into a continuous master curve at a reference temperature. The construction of such a master curve by TTS is illustrated schematically in Figure 2.11.

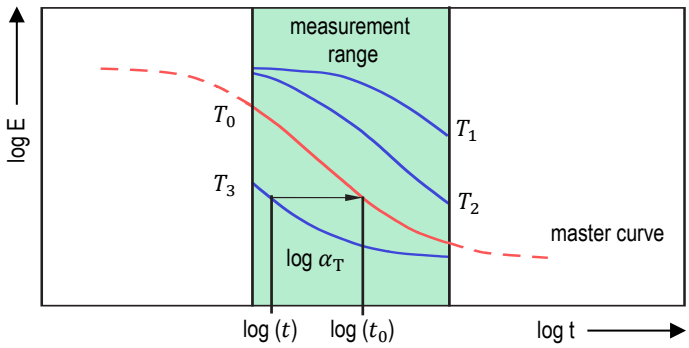


**Figure 2.11:** Schematic illustration of master curve construction using time–temperature superposition. Based on (Grellmann and Seidler 2025).

The required temperature-dependent shift factor $\alpha_T$ can often be described by an Arrhenius relationship depending on the temperature range considered, or by the Williams–Landel–Ferry equation in the region of the glass transition (Grellmann and Seidler 2025). The TTS principle is of considerable practical importance because it enables the prediction of long-term behavior of polymer materials at service temperatures based on short-term measurements conducted at elevated temperatures. For engineering applications, it therefore represents a key method for evaluating the time- and temperature-dependent mechanical behavior of viscoelastic materials (Schwarzl 1990; Bues 2021).

## 2.2 Mechanical and Dynamic Fundamentals

This section introduces the fundamental concepts required to describe the mechanical behavior of adhesive materials and their response under dynamic loading. It comprises basic mechanical principles, constitutive models for material behavior, and the fundamentals of structural dynamics.

### 2.2.1 Basic Mechanical Concepts

The description of the mechanical properties of construction products, particularly the adhesives investigated in this work, requires knowledge of fundamental concepts from polymer mechanics and continuum mechanics. The following section introduces the stress, strain, and stiffness measures used throughout this study.

Due to the interdisciplinary character of the work, the complex material behavior of the investigated polymers is intentionally represented by simplified models in several cases. This approach facilitates the formulation of relationships between the different disciplines involved. Definitions of the fundamental material parameters can be found in (Schwarzl 1990; Stommel et al. 2018; Grellmann and Seidler 2025).

Stress is defined as the force $F$ acting per unit area $A$ on a plane within a material. Depending on the direction of the applied force relative to the normal vector of the reference plane, two fundamental cases can be distinguished. If the force direction is parallel to the normal of the reference plane, the resulting stress is referred to as normal stress $\sigma$. For the simple case illustrated in Figure 2.12a, the normal stress $\sigma$ is defined as:

$$\sigma = \frac{F}{A_0} \tag{2.1}$$

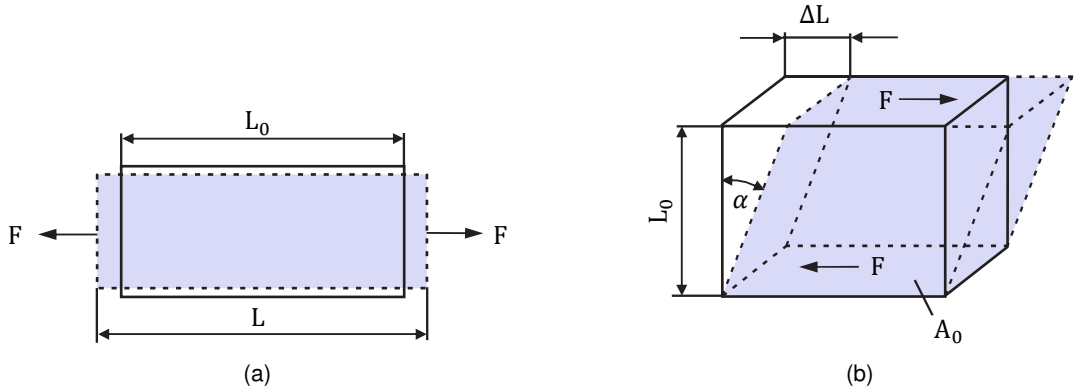


**Figure 2.12:** Schematic illustration of deformation: (a) under normal stress loading; (b) under shear stress loading. Based on (Grellmann and Seidler 2025).

When the cross-sectional area of the undeformed specimen $A_0$ is used as the reference area, the resulting quantity is referred to as nominal or engineering stress $\sigma$. If the force direction is perpendicular to the normal vector of the reference plane, as illustrated in Figure 2.12b, the resulting stress is termed shear stress $\tau$. In analogy to Eq. (2.1), the shear stress is defined as:

$$\tau = \frac{F}{A_0} \tag{2.2}$$

The applied loads induce relative deformations in the material body, which are described as normal strain or shear strain. For the tensile loading shown in Figure 2.12a, the nominal or engineering strain $\varepsilon$ is defined as the ratio between the change in length $\Delta L$ and the initial length of the undeformed specimen $L_0$:

$$\varepsilon = \frac{\Delta L}{L_0} = \frac{L - L_0}{L_0} \tag{2.3}$$

For simple shear loading, the nominal or engineering shear strain $\gamma$ is defined as:

$$\gamma = \frac{\Delta L}{L_0} = \tan \alpha \tag{2.4}$$

Alternatively, stress and strain measures can be defined with respect to the current configuration rather than the initial configuration. In this case, the true strain $\varepsilon_w$ (Hencky strain) can be determined using the stretch ratio $\lambda$:

$$\lambda = \frac{L}{L_0} = 1 + \varepsilon \tag{2.5}$$

$$\varepsilon_w = \int_{L_0}^{L} \frac{dL}{L} = \ln \frac{L}{L_0} = \ln \lambda = \ln(1 + \varepsilon) \tag{2.6}$$

Analogously, the true stress $\sigma_w$ is defined using the current cross-sectional area. Assuming incompressible material behavior ($\nu \approx 0.5$) and uniaxial tension, the true stress can be approximated without direct determination of the current cross-sectional area:

$$\sigma_w = \lambda \cdot \sigma = (1 + \varepsilon) \cdot \sigma \tag{2.7}$$

### 2.2.2 Modeling of Mechanical Material Behavior

The mechanical behavior of polymer-based adhesives cannot be described by linear elastic models. Appropriate constitutive models are therefore required to represent their nonlinear and viscoelastic response.

#### 2.2.2.1 Purely Elastic Material Behavior

For small deformations, purely elastic material behavior can be described by linear constitutive relations. A uniquely reversible relationship exists between the stress state and the deformation state, such that the mechanical work applied during deformation is stored entirely as potential energy and released upon unloading. A common conceptual representation of linear elastic material behavior is a spring with a linear force–displacement relationship, referred to as the Hooke model. For uniaxial tensile loading, normal stress $\sigma$ and strain $\varepsilon$ are related through Young's modulus $E$, a measure of material stiffness, as given in:

$$\sigma = E\,\varepsilon \tag{2.8}$$

Under shear loading, the relationship between shear stress $\tau$ and shear strain $\gamma$ is described by the shear modulus $G$:

$$\tau = G\,\gamma \tag{2.9}$$

In addition, tensile loading leads to lateral contraction, which is described by Poisson's ratio $\nu$. It is defined as the ratio of transverse strain ($\varepsilon_y, \varepsilon_z$) to longitudinal strain ($\varepsilon_x$). For uniaxial loading, this relationship is expressed as:

$$\nu = -\frac{\varepsilon_y}{\varepsilon_x} = -\frac{\varepsilon_z}{\varepsilon_x} \tag{2.10}$$

These relationships form the basis of linear elasticity theory and represent an idealized description of purely elastic material behavior that is valid primarily for small deformations. However, many polymeric materials exhibit large but reversible deformations that cannot be described adequately by linear elastic models.

#### 2.2.2.2 Hyperelastic Material Models

The mechanical entropic elastic behavior of elastomers under large, fully reversible deformations can be described in continuum mechanics using hyperelastic material models. This class of models assumes that the stress–strain relationship is nonlinear but purely elastic and can be derived from a strain energy density function that depends on the current deformation state. Classical hyperelastic models are mainly applied to quasi-static short-term loading conditions in which time-dependent effects such as creep, relaxation, or viscoelastic damping can be neglected (Stommel et al. 2018; Bues 2021).

The formulation is based on the theory of finite deformations. The material response is often expressed using invariants of the Cauchy–Green deformation tensor or principal stretches in order to satisfy objectivity requirements. Elastomers are typically assumed to exhibit nearly incompressible behavior, such that the strain energy can be decomposed into deviatoric and volumetric contributions. Representative models of this class include the Neo-Hookean, Mooney–Rivlin, Ogden, and Yeoh models, which differ in their mathematical formulations for describing the nonlinear stress–strain relationship (Stommel et al. 2018; Bues 2021). The continuum-mechanical foundations of hyperelastic material modeling and different approaches for describing nonlinear stress–strain behavior are presented in (Holzapfel 2010; Altenbach 2018; Stommel et al. 2018).

#### 2.2.2.3 Viscoelastic Models

**Spring and dashpot elements** The viscoelastic material behavior of elastomers described in section 2.1.3.6 can be represented at the engineering level using rheological models. These models consist of idealized mechanical elements that represent the fundamental elastic and viscous components of the material behavior. The theoretical foundations of this modeling approach are described in detail by (Schwarzl 1990) and are presented in classical form by (Flügge 1975), as well as in application-oriented descriptions, for example by (Schaaf 2024).

In this context, viscoelastic material behavior is represented by combinations of idealized spring elements and dashpot elements. The spring element represents time-independent elastic behavior, in which the stress depends directly on the applied strain. This relationship can be described, for example, by Hooke's law shown in Eq. (2.8).

In contrast, the dashpot element represents ideal viscous behavior, in which the stress is proportional to the time derivative of the strain, that is the strain rate $\dot{\varepsilon}$. Using the viscosity $\eta$ associated with the dashpot element, the following relationship is obtained:

$$\sigma = \eta\, \dot{\varepsilon}(t) \tag{2.11}$$

The loading and response behavior of the elastic spring element and the viscous dashpot element are illustrated in Figure 2.13.

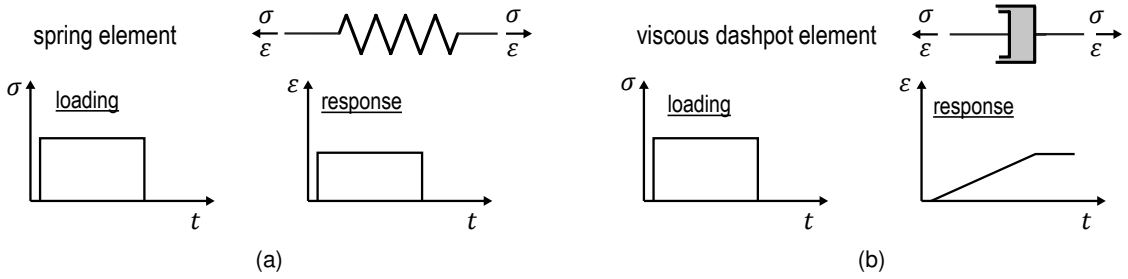


**Figure 2.13:** Idealized rheological elements with schematic loading and response diagrams: (a) elastic spring element; (b) viscous dashpot element. Based on (Flügge 1975; Schaaf 2024).

**Rheological base models** Simple rheological base models are used to describe linear viscoelastic material behavior. These models consist of combinations of spring and dashpot elements. They provide an intuitive interpretation of time-dependent material responses under idealized boundary conditions and form the basis for more advanced modeling approaches (Flügge 1975; Schwarzl 1990; Schaaf 2024).

The Kelvin–Voigt model is based on a parallel arrangement of a spring element and a dashpot element, as illustrated in Figure 2.14a. Both elements experience the same strain at all times, while the stresses are additive. Under constant stress, the strain develops with a time delay because the dashpot inhibits the immediate extension of the spring. In the final state, the spring carries the entire load. Due to the parallel configuration, no stress relaxation occurs under constant strain. The model therefore describes a fully reversible, delayed elastic behavior without permanent strain.

The Maxwell model consists of a series arrangement of a spring element and a dashpot element, as illustrated in Figure 2.14b. The same stress acts in both elements, while the strains are additive. Under loading, the spring responds first, followed by a time-dependent increase in strain of the dashpot. After unloading, a permanent strain remains. Under constant strain, the model predicts a time-dependent decrease in stress and thus represents stress relaxation.

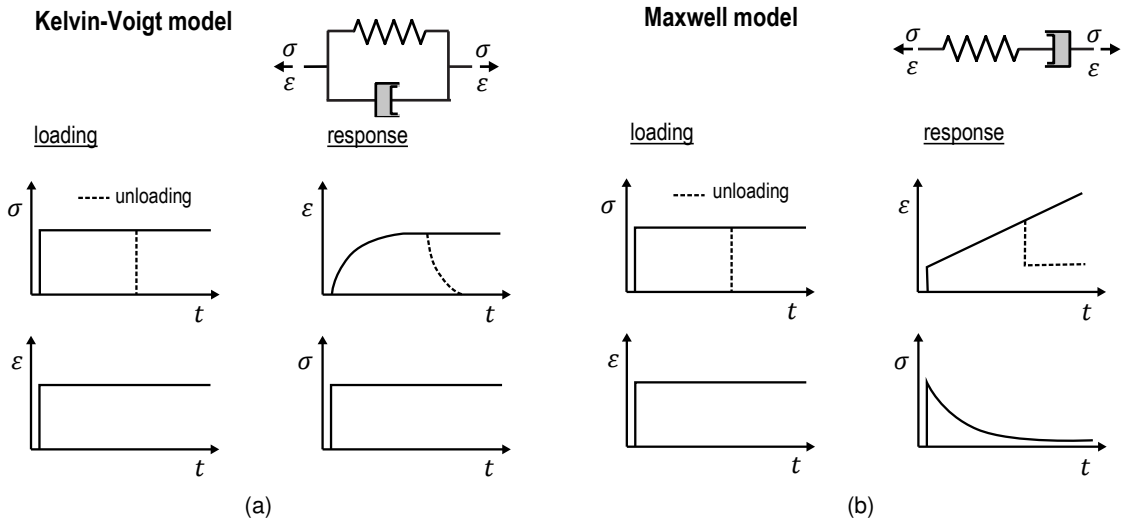


**Figure 2.14:** Comparison of basic rheological models with corresponding loading and response functions: (a) Kelvin–Voigt model; (b) Maxwell model. Based on (Flügge 1975; Schaaf 2024).

**Models for describing creep and relaxation** By extending the basic rheological models with an additional element, three-parameter viscoelastic models are obtained that allow both creep and relaxation processes to be described within a consistent framework (Flügge 1975; Schwarzl 1990; Schaaf 2024).

The three-parameter Kelvin model consists of a Kelvin–Voigt element connected in series with an additional spring, as illustrated in Figure 2.15a. When subjected to a constant stress, the total strain consists of an instantaneous elastic strain and a time-dependent strain caused by the dashpot element. The model therefore represents pronounced creep behavior with a finite asymptotic strain. If a constant strain is imposed instead, a time-dependent redistribution of stresses occurs between the elements connected in series, allowing stress relaxation to be described. The corresponding response functions approach finite asymptotic values.

The three-parameter Maxwell model is obtained by connecting an additional spring in parallel with the Maxwell element, as shown in Figure 2.15b. Under constant stress, the stresses are distributed between the parallel elements, while the strain is identical in both components. This results in limited creep behavior with a finite long-term strain. Under constant strain, the additional spring carries a time-independent stress component, whereas the Maxwell element produces a time-dependent decrease in stress. The model therefore describes stress relaxation with a finite long-term stress.

Both three-parameter models allow the description of creep and relaxation phenomena but emphasize different aspects of the material response. The Kelvin model is commonly used to represent creep loading, whereas the Maxwell model is typically applied to describe relaxation processes. However, both model types can also be applied to the respective other loading condition and therefore represent versatile rheological models (Flügge 1975).

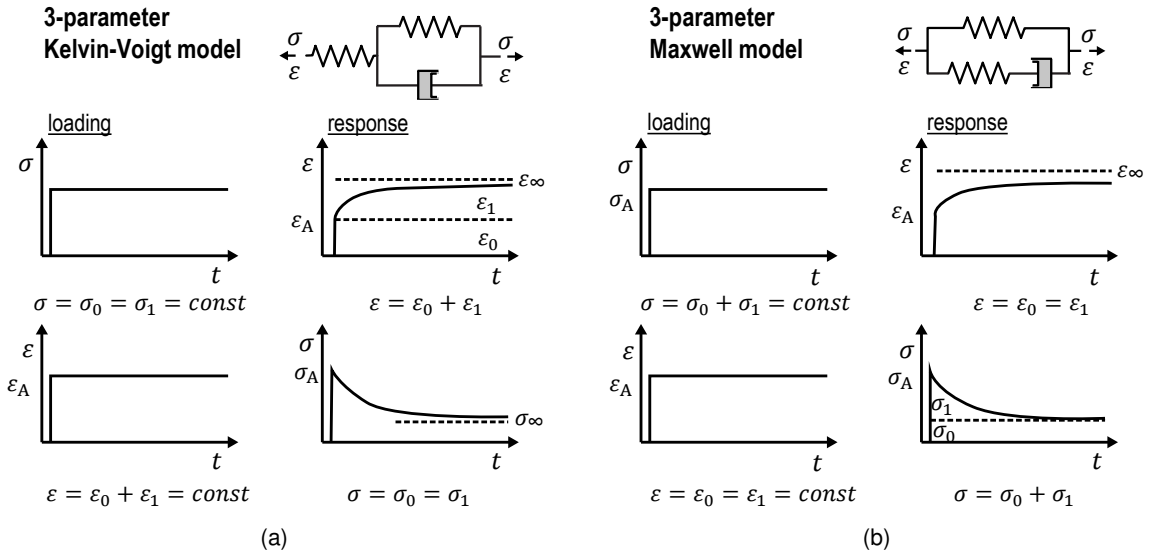


**Figure 2.15:** Comparison of three-parameter rheological models with corresponding loading and response functions: (a) three-parameter Kelvin–Voigt model; (b) three-parameter Maxwell model. Based on (Flügge 1975; Schaaf 2024).

By adding further spring–dashpot elements, generalized viscoelastic models can be formulated that allow the time-dependent material behavior to be represented more accurately over an extended time range. The associated creep and relaxation functions are obtained by combining elements with different elastic moduli and viscosities. The identification of the model parameters is considerably more demanding than for three-parameter models. For this reason, generalized models are not considered further in this work. A detailed discussion can be found in the relevant literature, for example in (Schwarzl 1990; Stommel et al. 2018; Abeln 2019; Rösler et al. 2019; Grellmann and Seidler 2025).

### 2.2.3 Fundamentals of Structural Dynamics

Dynamic actions such as wind, machinery vibrations or seismic loading induce time-dependent responses in structural systems. In contrast to static loading, the structural response depends not only on the applied forces but also on inertia and energy dissipation mechanisms within the system. The dynamic equilibrium of a structural system is therefore governed by the interaction of mass, damping and stiffness forces.

The fundamental principles of structural dynamics presented in this section are based on classical vibration theory and are widely documented in the literature. Comprehensive treatments of structural dynamics can be found in (Bachmann 1995; Chopra 2012; Petersen and Werkle 2017).

A simplified but widely used representation of structural dynamic behavior is the single-degree-of-freedom (SDOF) system. Despite its simplicity, this model captures the essential physical mechanisms governing the dynamic response of many structural systems and

provides fundamental insight into structural vibration phenomena. Consequently, the SDOF system forms the basis for understanding more complex structural models and plays a central role in earthquake engineering (Petersen and Werkle 2017). A schematic representation of an SDOF system is shown in Figure 2.16a.

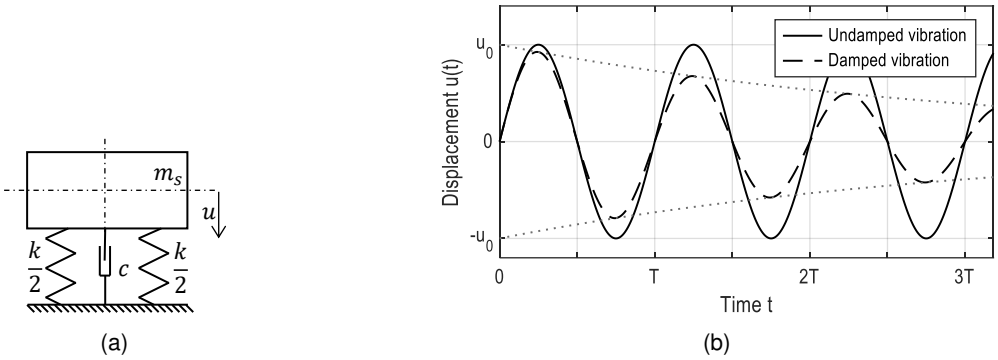


**Figure 2.16:** Fundamental vibration behavior of a SDOF system: (a) schematic representation of an SDOF system with mass $m_s$, stiffness $k$, and viscous damping $c$. Based on (Petersen and Werkle 2017)); (b) schematic displacement responses of undamped and damped free vibration.

For a linear SDOF system with mass $m_s$, viscous damping coefficient $c$, and stiffness $k$, the dynamic equilibrium can be expressed as:

$$m_s \ddot{u}(t) + c\dot{u}(t) + ku(t) = p(t) \tag{2.12}$$

Here, $u(t)$ denotes the displacement response of the system and $p(t)$ represents an external excitation force. The three terms correspond to inertia forces, damping forces and elastic restoring forces, respectively.

Two parameters are commonly used to describe the dynamic properties of the system. The natural circular frequency,

$$\omega_n = \sqrt{\frac{k}{m_s}} \tag{2.13}$$

characterizes the inherent oscillation frequency of the system, while the damping ratio,

$$\zeta = \frac{c}{2m_s\omega_n} \tag{2.14}$$

describes the relative magnitude of viscous damping compared to the critical damping of the system.

Dividing the equation of motion by the mass $m_s$ leads to the normalized form, which serves as the basis for describing various types of structural vibration:

$$\ddot{u}(t) + 2\zeta\omega_{\mathrm{n}}\dot{u}(t) + \omega_{\mathrm{n}}^2 u(t) = \frac{p(t)}{m_{\mathrm{s}}} \tag{2.15}$$

#### 2.2.3.1 Single-Degree-of-Freedom Systems

**Undamped free vibration** The simplest case of structural vibration occurs when no external excitation acts on the system and no energy dissipation mechanisms are present. Under these conditions the equation of motion reduces to:

$$\ddot{u}(t) + \omega_{\mathrm{n}}^2 u(t) = 0 \tag{2.16}$$

This situation is referred to as undamped free vibration. The system oscillates around its equilibrium position with constant amplitude and frequency determined solely by its mass and stiffness properties.

The solution of the differential equation can be expressed as:

$$u(t) = A\sin(\omega_{\mathrm{n}}t) + B\cos(\omega_{\mathrm{n}}t) \tag{2.17}$$

where the constants $A$ and $B$ depend on the initial displacement and velocity conditions.

Alternatively, the solution may be written in amplitude-phase form as:

$$u(t) = \widehat{u}\sin(\omega_{\mathrm{n}}t + \varphi_0) \tag{2.18}$$

where $\widehat{u}$ denotes the vibration amplitude and $\varphi_0$ the phase angle. This representation highlights the purely harmonic character of the motion. As illustrated in Figure 2.16b, the motion is purely harmonic and repeats periodically with constant amplitude and constant natural period:

$$T = \frac{2\pi}{\omega_{\mathrm{n}}} \tag{2.19}$$

Equivalently, the natural frequency is given by:

$$f = \frac{1}{T} = \frac{\omega_{\mathrm{n}}}{2\pi} \tag{2.20}$$

An increase in structural stiffness therefore leads to higher natural frequencies, while larger structural masses result in lower natural frequencies.

**Damped free vibration** In real structures, energy dissipation occurs through mechanisms such as material hysteresis, friction or interaction with surrounding media. A common idealization is viscous damping, where the damping force is assumed proportional to the velocity of the system.

Including viscous damping modifies the equation of motion to:

$$\ddot{u}(t) + 2\zeta\omega_{\mathrm{n}}\dot{u}(t) + \omega_{\mathrm{n}}^2 u(t) = 0 \tag{2.21}$$

The presence of damping causes the oscillation amplitude to decay with time as mechanical energy is dissipated. The resulting motion consists of an exponentially decreasing harmonic oscillation.

The solution of the equation of motion for an underdamped system represents a harmonic oscillation with an exponentially decaying amplitude. The displacement response can be written as

$$u(t) = \widehat{u}\, e^{-\zeta\omega_{\mathrm{n}}t} \sin(\omega_{\mathrm{d}}t + \varphi_0) \tag{2.22}$$

where $\widehat{u}$ and $\varphi_0$ are as defined in Eq. (2.18), and the exponential term describes the decay of vibration amplitude due to energy dissipation.

The oscillation occurs with the damped natural circular frequency:

$$\omega_{\mathrm{d}} = \omega_{\mathrm{n}}\sqrt{1-\zeta^2} \tag{2.23}$$

For most civil engineering structures the damping ratios are relatively small ($\zeta \ll 1$). Under these conditions the damped frequency is very close to the natural frequency of the undamped system:

$$\omega_{\mathrm{d}} \approx \omega_{\mathrm{n}} \tag{2.24}$$

Consequently, damping mainly influences the rate of amplitude decay rather than the oscillation frequency. In such lightly damped systems the displacement response may therefore be approximated by:

$$u(t) \approx \widehat{u}\, e^{-\zeta\omega_{\mathrm{n}}t} \sin(\omega_{\mathrm{n}}t) \tag{2.25}$$

which illustrates the exponentially decaying oscillation typically observed in structural systems, as shown schematically in Figure 2.16b.

**Damped forced vibration under harmonic excitation** When the system is subjected to an external time-dependent force, the vibration is referred to as forced vibration. A commonly studied case is harmonic excitation $p(t)$ of the form Eq. (2.26), where $\widehat{p}$ denotes the force amplitude and $\Omega$ the excitation frequency.

$$p(t) = \widehat{p}\sin(\Omega t) \tag{2.26}$$

The equation of motion then becomes:

$$\ddot{u}(t) + 2\zeta\omega_{\mathrm{n}}\dot{u}(t) + \omega_{\mathrm{n}}^2 u(t) = \frac{\widehat{p}}{m_{\mathrm{s}}}\sin(\Omega t) \tag{2.27}$$

In this case the system response consists of two components: a transient response governed by the homogeneous equation and a steady-state response determined by the excitation. After the transient effects decay, the system oscillates with the excitation frequency $\Omega$.

The amplitude of the steady-state response depends strongly on the ratio between the excitation frequency and the natural frequency. When the excitation frequency approaches the natural frequency of the system, resonance effects may occur, resulting in significantly amplified vibration amplitudes. The magnitude of this amplification is strongly influenced by the damping ratio of the system.

**Damped vibration under seismic excitation** In earthquake engineering, structural vibrations are not primarily caused by externally applied forces but by ground motion. During an earthquake the foundation of a structure moves together with the ground, imposing a base excitation on the structural system. A schematic representation of such a system subjected to ground acceleration is shown in Figure 2.17.

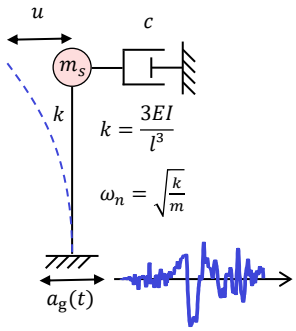


**Figure 2.17:** Schematic representation of an SDOF system subjected to base excitation due to ground acceleration. Based on (Chopra 2012).

The structural response is therefore commonly described in terms of the relative displacement between the structure and the moving ground. If $u_{\mathrm{g}}(t)$ denotes the ground displacement, $a_{\mathrm{g}}(t)$ the ground acceleration time history obtained from seismic recordings, and $u(t)$ the relative structural displacement, the equation of motion can be expressed as:

$$m_s\ddot{u}(t) + c\dot{u}(t) + ku(t) = -m_s a_g(t) \tag{2.28}$$

Dividing by the mass yields the normalized form:

$$\ddot{u}(t) + 2\zeta\omega_n\dot{u}(t) + \omega_n^2 u(t) = -a_g(t) \tag{2.29}$$

This equation forms the fundamental relationship describing the dynamic response of structures subjected to earthquake excitation. For a given ground acceleration input, the structural response depends solely on the natural frequency and the damping ratio of the system. Numerical integration methods can then be used to compute the resulting displacement, velocity and acceleration responses as functions of time, as discussed in section 2.2.3.3 (Chopra 2012; Petersen and Werkle 2017).

#### 2.2.3.2 Multi-Degree-of-Freedom Systems

While the SDOF system provides valuable insight into fundamental vibration mechanisms, real structures typically exhibit multiple independent deformation modes. Such systems are described as multi-degree-of-freedom (MDOF) systems, in which multiple degrees of freedom are required to represent the structural motion.

The dynamic equilibrium of an MDOF system can be expressed in matrix form as:

$$\mathbf{M}\ddot{\mathbf{u}}(t) + \mathbf{C}\dot{\mathbf{u}}(t) + \mathbf{K}\mathbf{u}(t) = \mathbf{p}(t) \tag{2.30}$$

where $\mathbf{M}$, $\mathbf{C}$, and $\mathbf{K}$ denote the mass, damping and stiffness matrices of the system, respectively. The vector $u(t)$ contains the generalized displacements associated with the individual degrees of freedom.

Under the assumptions of linear structural behaviour and small deformations, such systems can often be decomposed into independent vibration modes through modal analysis. Each mode can then be interpreted as an equivalent SDOF system characterized by a specific natural frequency and damping ratio.

Since the subsequent analyses in this work are primarily based on simplified SDOF representations, a detailed treatment of MDOF system dynamics is beyond the scope of this study.

#### 2.2.3.3 Numerical Evaluation of Dynamic Response

**Numerical time-stepping methods** Analytical solutions of the equation of motion are generally not available when general time-dependent excitations are present or when nonlinear structural behavior must be considered. In such cases, the dynamic response is determined using numerical time-stepping methods, in which the equation of motion is integrated stepwise in the time domain from given initial conditions. These methods utilize the kinematic relationships between acceleration, velocity, and displacement and are specifically formulated for equations of motion in structural dynamics. The accuracy, numerical stability, and computational effort depend primarily on the approximation adopted within a time step and on the formulation of the equilibrium conditions. Common classifications distinguish, among others, between explicit and implicit methods, single-step and multi-step methods, as well as direct and incremental solution approaches. Incremental approaches are particularly advantageous for physically nonlinear problems (Chopra 2012; Petersen and Werkle 2017).

**Newmark method** A widely used time-stepping method in engineering practice is the Newmark method, which is characterized by simple implementation, high computational efficiency, and favorable stability properties. The method introduces free parameters that control the assumed variation of acceleration within a time step, thereby governing the stability and accuracy of the numerical solution.

In the application of the Newmark method, two characteristic cases are typically distinguished based on the assumed temporal variation of acceleration within a time step: the case of constant average acceleration and the case of linearly varying acceleration. These assumptions lead to different parameter settings that are established in practice and represent the most commonly used variants of the method. For linear systems, the implicit formulation can be reformulated as an explicit recurrence scheme, avoiding the need for iterative solution (Chopra 2012; Petersen and Werkle 2017).

**Alternative numerical time-stepping methods** In addition to the Newmark method, several other numerical time-stepping schemes have been developed and systematically classified in the literature for solving the equation of motion. One extended approach is provided by the General Single Step Single Solve algorithms, introduced by (Zhou and Tamma 2004) as a unified framework for linear and nonlinear time-integration methods in structural dynamics. These algorithms are formulated to allow controlled numerical damping while remaining within the theoretical limits of linear multistep methods.

MATLAB implementations based on this framework are available, for example, in (Papazafeiropoulos 2015). The Linear Implicit Dynamic Analysis (`LIDA`) implementation enables a linearly implicit, direct time integration of the equation of motion for a linear-elastic SDOF oscillator. Due to its computational efficiency and straightforward implementation,

the method was used in the present work for the numerical evaluation of the dynamic response.

## 2.3 Fatigue and Low-Cycle Fatigue of Materials

Structural components in the construction industry are primarily designed for static or quasi-static actions such as dead load, wind, or snow. However, many structures are also subjected to time-varying loads that act repeatedly during their service life. These cyclic actions may arise, for example, from traffic, wind-induced vibrations, or machine operation. Repeated loading can lead to fatigue damage even when the stress levels remain below the static strength of the material. For this reason, the assessment of fatigue behavior represents an important aspect of structural reliability.

### 2.3.1 Fundamentals of Fatigue and Cyclic Loading

According to (Radaj and Vormwald 2007), material fatigue describes the damage or failure of a material or structural component subjected to time-varying, frequently repeated mechanical loading. Fatigue damage consists of crack initiation followed by crack propagation. Cracks typically initiate at stress concentrations such as defects, notches, or cross-sectional transitions after a certain number of load cycles. With increasing cycle numbers, these cracks propagate until final fracture occurs. Failure may therefore occur at stress levels significantly below the static strength of the material. In addition, increasing stress amplitude reduces fatigue life.

Cyclic loading refers to mechanical loading that varies with time and is applied repeatedly. The loading history may be deterministic (periodic or aperiodic) or stochastic. In fatigue testing, cyclic loading is often applied with constant amplitude, although variable-amplitude loading may also occur in practice. Cyclic loading may act about either a constant or a variable mean stress (Radaj and Vormwald 2007).

For a sinusoidal stress-time history between two fixed limits, the load cycle is characterized by the upper stress $\sigma_{\mathrm{o}}$, the lower stress $\sigma_{\mathrm{u}}$, the stress range $\Delta\sigma$, the stress amplitude $\sigma_{\mathrm{a}}$, the mean stress $\sigma_{\mathrm{m}}$, and the stress ratio $R$, as illustrated in Figure 2.18 (Radaj and Vormwald 2007).

Only two of these quantities are independent, the remaining parameters follow from their relationships. Frequently used definitions are:

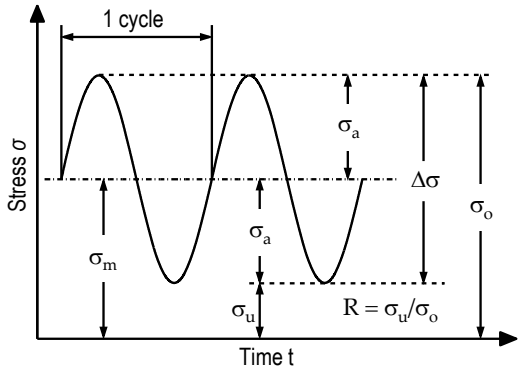


**Figure 2.18:** Characterization of constant-amplitude cyclic stress-time history. Based on (Radaj and Vormwald 2007).

$$\Delta\sigma = \sigma_o - \sigma_u \tag{2.31}$$

$$\sigma_a = \frac{\Delta\sigma}{2} \tag{2.32}$$

$$\sigma_m = \frac{\sigma_o + \sigma_u}{2} \tag{2.33}$$

$$R = \frac{\sigma_u}{\sigma_o} \tag{2.34}$$

These parameters allow a consistent description of periodic loading and can be extended analogously to the maximum values of load collectives in aperiodic or stochastic loading histories.

Depending on the combination of $\sigma_\mathrm{o}$ and $\sigma_\mathrm{u}$, different loading regimes are distinguished, as illustrated in Figure 2.19. Of particular relevance are fully reversed loading with $R = -1$ and $\sigma_\mathrm{m} = 0$, pulsating tension with $R = 0$ and $\sigma_\mathrm{u} = 0$, pulsating compression with $\sigma_\mathrm{o} = 0$, and static loading with $R = 1$ and $\sigma_\mathrm{o} = \sigma_\mathrm{u}$. This classification forms the basis for interpreting fatigue tests under constant-amplitude loading (Radaj and Vormwald 2007).

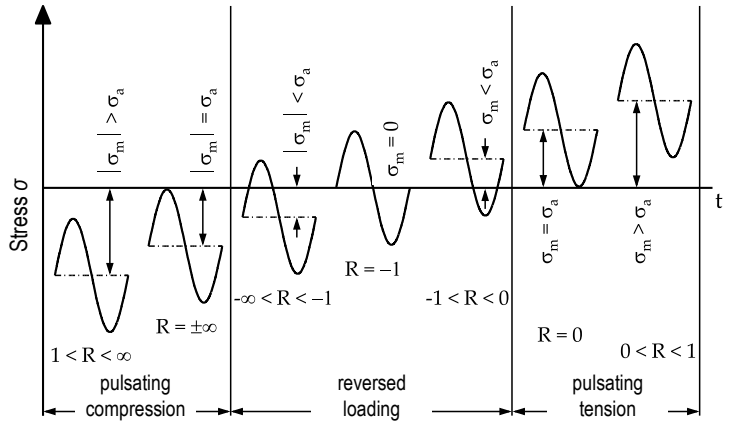


**Figure 2.19:** Classification of loading regimes under constant-amplitude cyclic loading. Based on (Radaj and Vormwald 2007).

For shear loading, the same definitions apply by replacing the normal stress $\sigma$ with the shear stress $\tau$. In this case, a distinction between tensile and compressive loading is not applicable. Instead, a sign change corresponds to a reversal of the shear direction.

The first systematic fatigue investigations were conducted by August Wöhler beginning in 1860 using railway axles (Wöhler 1860). These experiments demonstrated that the stress range, or equivalently the stress amplitude, governs fatigue behavior. In addition, the mean stress influences the magnitude of the tolerable stresses. The graphical representation of this relationship, now known as the Wöhler curve or S-N curve, and its mathematical description using a power-law formulation were introduced later by (Basquin 1910).

The experimental procedure of fatigue testing is described in detail in the literature (Haibach 2006; Manson and Halford 2006; Radaj and Vormwald 2007). In such tests, specimens or structural components are subjected to cyclic loading with constant amplitude, typically with a sinusoidal stress history. Either the mean load or the ratio between minimum and maximum load is kept constant (single-stage test). The test is terminated when a predefined failure criterion is reached, and the corresponding number of cycles to failure $N_\mathrm{f}$ is recorded. Determination of fatigue strength therefore requires multiple tests at different stress levels.

The experimental results are evaluated using a Wöhler diagram with a double-logarithmic scale. The applied stress ranges $\Delta\sigma$, or alternatively the stress amplitudes $\sigma_\mathrm{a}$, are plotted against the corresponding number of cycles to failure $N_\mathrm{f}$. A regression analysis of the experimental data yields the S-N curve, as illustrated in Figure 2.20.

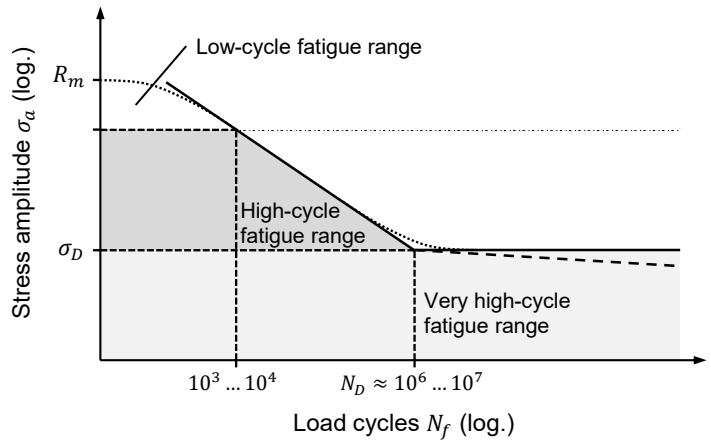


**Figure 2.20:** Classification of S-N curves for typical metallic materials or structural components. Based on (Götz and Eulitz 2022).

The S-N curve can be divided into several fatigue regimes (Manson and Halford 2006):

- Low-cycle fatigue (LCF) range (short-life region) from approximately 1 to $10^3 - 10^4$ load cycles.
- High-cycle fatigue (HCF) range up to approximately $1 \cdot 10^7$ load cycles.
- Very-high cycle fatigue range for load cycles above $N_D = 10^7$.

In the high-cycle fatigue range, the relationship between the number of cycles to failure $N_\mathrm{f}$ and the applied stress amplitude $\sigma_\mathrm{a}$ can be expressed by a power function proposed by (Basquin 1910):

$$N_f = a \cdot \sigma_a^{-m} \tag{2.35}$$

When plotted on logarithmic axes, this relationship appears as a straight line with slope $-m$, as expressed in Eq. (2.36) (Drebenstedt and Euler 2018):

$$\log N_f = \log a - m \cdot \log \sigma_a \tag{2.36}$$

In practical applications, loading usually consists of varying amplitudes and frequencies. Damage accumulation is therefore evaluated by classifying and counting stress cycles from stress-time histories. Various cycle-counting methods are available for evaluating random response histories. These methods decompose a random load history into individual, analyzable load cycles for subsequent classification. Common approaches include peak counting, level crossing, mean crossing, and rainflow counting, as described in (E1049-85). (DIN EN 1993-1-9) similarly identifies the rainflow method and the reservoir method as the primary cycle-counting procedures for determining stress-time histories. (Stelzer et al. 2020) identified a significant influence of the selected cycle-counting method on the resulting number of equivalent cycles.

One commonly used method for cumulative damage assessment is Miner's rule (Palmgren 1924; Miner 1945). The partial damage associated with each load level is defined by the ratio between the applied number of cycles $n_i$ and the tolerable number of cycles $N_{\mathrm{f},i}$. The total damage $D$ is obtained by summing the partial damage contributions (Haibach 2006; Radaj and Vormwald 2007; Götz and Eulitz 2022):

$$D = \sum_{i=1}^{m} \frac{n_i}{N_{\mathrm{f},i}} \tag{2.37}$$

Miner's rule assumes sequence-independent damage accumulation and does not account for load-order effects, which represents a known simplification. Several modifications of this rule for linear damage accumulation have been proposed in the literature, as summarized by (Götz and Eulitz 2022).

### 2.3.2 Fatigue Behavior of Adhesive and Polymeric Materials

Polymeric materials and structural adhesives are widely used in engineering applications and are frequently subjected to cyclic mechanical loading. Their fatigue behavior differs fundamentally from that of metallic materials because their mechanical response is governed by viscoelastic and temperature-dependent deformation mechanisms. Consequently, fatigue

processes in polymers involve coupled mechanical and thermal effects, which must be considered when evaluating their long-term structural performance.

The systematic investigation of fatigue in polymers began in the second half of the twentieth century, driven by the increasing use of plastics in structural and mechanical components (Bathias and Pineau 2013). Fundamental aspects of fatigue in polymers and elastomers are summarized in (Gent 2012; Bathias and Pineau 2013; Stommel et al. 2018; Rösler et al. 2019).

In contrast to many metallic materials, polymeric materials generally do not exhibit a distinct endurance limit in the HCF regime (Sauer and Richardson 1980; Rasche 2012). According to (Stommel et al. 2018), S-N curves for polymers are often determined up to $10^7$ load cycles without reaching a horizontal asymptote. This behavior reflects the time- and temperature-dependent deformation mechanisms inherent to polymers and structural adhesives.

As in metals, fatigue damage in polymers comprises crack initiation followed by crack propagation (Bathias and Pineau 2013). However, the underlying micromechanisms differ. Due to the viscoelastic and viscoplastic nature of polymers, cyclic loading may generate localized deformation zones in highly stressed regions of a bonded joint. Within these zones, chain scission, segmental sliding, cavitation, or craze formation may occur, depending on the polymer structure (Rösler et al. 2019). These processes create microdefects that act as initiation sites for crack growth. As the stress amplitude increases, the number of cycles to failure decreases, analogous to metallic materials. However, the fatigue life is additionally influenced by time-dependent material behavior.

A characteristic feature of fatigue in polymers is the distinction between mechanically and thermally dominated fatigue mechanisms. Mechanical fatigue occurs when the temperature rise during cyclic loading remains limited. In this case, failure is governed primarily by crack initiation and subsequent crack propagation. Although the macroscopic description resembles that of metallic fatigue, the crack-driving mechanisms are controlled by polymer-specific deformation processes such as chain rupture, shear band formation, or crazing. Fatigue life is mainly governed by stress amplitude, mean stress, and material structure.

Thermal fatigue, in contrast, results from the viscoelastic dissipation of mechanical energy. Cyclic loading produces hysteresis in the stress–strain response, and part of the mechanical work is converted into heat. Because polymers typically exhibit low thermal conductivity, the generated heat may accumulate within the material. If heat generation exceeds heat dissipation, the temperature increases progressively until temperature-dependent strength or stiffness limits are reached, which leads to failure. In thermoplastics, this process may cause plastic flow, whereas in elastomers and thermosets the temperature-dependent reduction in modulus promotes excessive deformation and subsequent fracture.

The transition between mechanical and thermal fatigue is not always clearly defined, since both mechanisms may contribute simultaneously depending on loading and boundary conditions. Consequently, the fatigue behavior of polymeric adhesives cannot be described

solely by stress amplitude and number of cycles, but must also be considered in relation to viscoelastic energy dissipation and temperature evolution (Rösler et al. 2019).

Loading frequency therefore represents an important parameter. Owing to the viscoelastic nature of polymers, the stress–strain response is strain-rate dependent (Gent 2012; Stommel et al. 2018). Increasing frequency generally results in higher apparent stiffness and modifies the hysteresis behavior. At the same time, cyclic deformation causes energy dissipation, which may lead to self-heating of the material. The interaction between mechanically and thermally dominated fatigue is illustrated in Figure 2.21, which presents S-N curves for polyoxymethylene at different loading frequencies. At low frequencies, failure is governed primarily by mechanical fatigue, whereas at higher frequencies thermally induced failure dominates. With decreasing stress amplitude, the curves associated with thermal fatigue converge toward the curve representing purely mechanical fatigue. Because stiffness and strength are temperature dependent, this thermo-mechanical coupling significantly influences fatigue life. Consequently, S-N data obtained at a given frequency are valid only for the corresponding loading rate and thermal boundary conditions (Rösler et al. 2019).

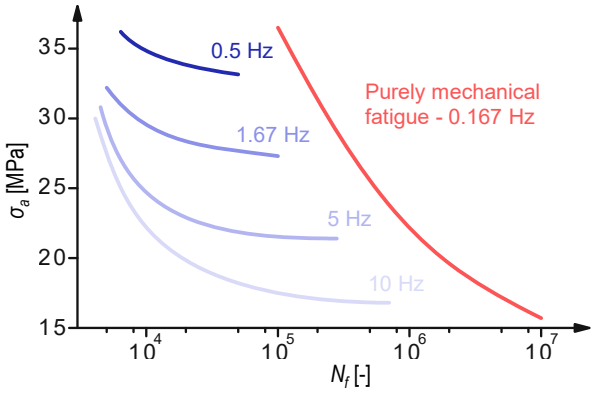


**Figure 2.21:** S-N curves for polyoxymethylene at different loading frequencies, illustrating the transition from mechanically dominated fatigue at low frequencies (red line) to thermally dominated fatigue at higher frequencies (blue lines). Based on (Rösler et al. 2019).

In addition to frequency, the loading control mode influences fatigue behavior. Under stress-controlled loading, stiffness reduction caused by damage evolution or temperature increase leads to increasing strain amplitudes during cycling, which may accelerate failure (Rösler et al. 2019). Under strain-controlled loading, a reduction in stiffness results in decreasing stress amplitudes and therefore modifies the evolution of cyclic damage (Bathias and Pineau 2013). Consequently, fatigue data obtained under one control mode cannot be directly transferred to another without considering the corresponding stress–strain evolution.

### 2.3.3 Low-Cycle Fatigue

LCF generally refers to fatigue failure occurring below approximately $10^4$ cycles, although no strict boundary between HCF and LCF is defined (Manson and Halford 2006; Rösler

et al. 2019). For cycle numbers below roughly $10^2$, the term very-low-cycle fatigue is sometimes used. In polymers, if the loading duration is shorter than the relevant relaxation times, the response may approach repeated quasi-static loading rather than classical fatigue behavior (Stommel et al. 2018).

In the LCF regime, failure occurs at comparatively high stress amplitudes, and the S-N curve typically exhibits a relatively shallow slope, so that small changes in stress amplitude result in large variations in the number of cycles to failure (Rösler et al. 2019).

In metallic materials, LCF behavior is commonly described using strain–life relationships in which the total strain amplitude is decomposed into elastic and plastic components. A widely used formulation is the Coffin–Manson relation (Coffin 1954; Manson 1965; Mander et al. 1994; Haibach 2006).

For polymeric materials, however, a generally accepted strain–life framework for LCF is not established. Due to viscoelastic and rate-dependent deformation mechanisms, a direct transfer of metallic strain-based concepts to polymers is not straightforward (Stommel et al. 2018). Consequently, stress-based S-N approaches are often applied even at comparatively low cycle numbers in component-oriented investigations.

### 2.3.4 Definition and Interpretation of Cyclic Parameters

The behavior of specimens under cyclic loading can be described using parameters analogous to those obtained from quasi-static tensile tests. These cyclic parameters characterize the stress–strain response during repeated loading and allow the evaluation of damage evolution and failure under cyclic conditions. The following subsections introduce the parameters used in this work.

#### 2.3.4.1 Deviation of the Load Range

In fatigue testing, particularly under LCF conditions, damage progression can be assessed using mechanical quantities obtained directly from the test setup. In displacement-controlled experiments, a common approach is to monitor the evolution of the load range during cyclic loading (Halford et al. 2000). A reduction in load range at constant displacement amplitude indicates stiffness degradation and therefore ongoing damage within the specimen.

#### 2.3.4.2 Dynamic Stiffness

As an alternative to evaluating the degradation of the load range, the stiffness or modulus of the specimen can be monitored throughout the cyclic test. Depending on the material system and the experimental configuration, different definitions of dynamic stiffness are used.

For LCF tests on steel plates designed for seismic energy dissipation, (Hou et al. 2019) define the reverse stiffness as the slope of the force–displacement curve immediately after a change in loading direction. This parameter characterizes the instantaneous response within each cycle and provides a measure of stiffness degradation that is largely independent of the absolute cycle amplitude, because it is evaluated within a near-linear elastic range of the response.

(Yu et al. 2024) quantify stiffness degradation during cyclic loading by introducing a softening index $\delta$, defined as the ratio of the dynamic shear modulus after $N$ cycles, $G_N$, to the initial dynamic shear modulus, $G_1$:

$$\delta = \frac{G_N}{G_1} \tag{2.38}$$

Dynamic stiffness is a relevant technical specification of elastomers. For linear behavior, it can be defined as the average stiffness curve of a hysteresis loop. However, elastomers typically exhibit nonlinear stiffness curves. Therefore, different linearization methods can be applied. A widely used approach due to its simple application is endpoint linearization, in which the dynamic stiffness is determined from the slope of the straight line connecting the two angular reversal points (Spitz 2012). As discussed in section 2.1.3.4, the dynamic stiffness can be defined as the slope of the line connecting the reversal points of the hysteresis loop under cyclic loading.

For torsion-loaded components, the dynamic stiffness $c_{\mathrm{T,dyn}}$ is obtained from the rotation angle–torque curve using the minimum rotation angle $\varphi_{\min}$ and maximum rotation angle $\varphi_{\max}$ , as well as the corresponding torques $T\left(\varphi_{\min}\right)$ and $T\left(\varphi_{\max}\right)$:

$$c_{\mathrm{T,dyn}} = \frac{\Delta T_{\mathrm{el}}}{\Delta \varphi} = \frac{T(\varphi_{\max}) - T(\varphi_{\min})}{\varphi_{\max} - \varphi_{\min}} \tag{2.39}$$

#### 2.3.4.3 Dissipated Energy Density

During cyclic loading, non-ideally elastic materials dissipate mechanical energy and exhibit hysteresis in the load–deformation diagram. For linear damping behavior, the hysteresis loop assumes an elliptical shape. For nonlinear damping, the loop deviates from this idealized form, as illustrated in Figure 2.22. The energy dissipated per load cycle, $W_{\mathrm{diss}}$, corresponds to the area enclosed by the hysteresis loop in the load–displacement diagram (Lazan 1968). The dissipated energy per cycle is given by:

$$W_{\mathrm{diss}} = \int F(U)\, dU \tag{2.40}$$

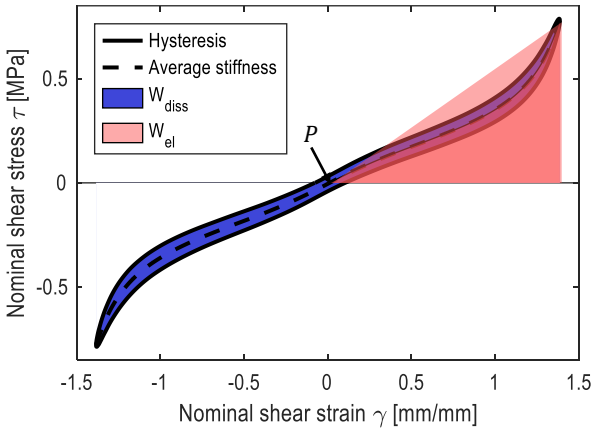


**Figure 2.22:** Evaluation of dissipated and elastic energy density from hysteresis data in the stress–strain diagram.

Alternatively, the dissipated energy can be determined using equivalent viscous damping models (Petersen and Werkle 2017). These approaches generally assume linear damping behavior and therefore idealized hysteresis characteristics.

For a normalized evaluation independent of specimen geometry, the dissipated energy can be calculated from the stress–strain diagram. In this case, the dissipated energy density $w_{\text{diss}}$ corresponds to the area enclosed by the hysteresis loop in the shear stress–shear strain representation, which is indicated schematically in blue in Figure 2.22, where $\tau(\gamma)$ denotes the shear stress and $\gamma$ the shear strain:

$$w_{\text{diss}} = \int \tau(\gamma)\, d\gamma \tag{2.41}$$

The dissipated energy and the dissipated energy density provide quantitative measures of internal damping and can be used to characterize cyclic material behavior and damage evolution. Energy-based interpretations have therefore been widely applied in fatigue investigations of adhesives and other viscoelastic materials. Studies have shown that dissipated energy measures capture the influence of load level, stiffness degradation, creep interaction, and damage accumulation during cyclic loading (Liu et al. 2021; Movahedi-Rad et al. 2021). In particular, power-law relationships between dissipated energy density and cyclic loading parameters have been reported, indicating that energy-based quantities represent robust cyclic parameters for viscoelastic materials.

#### 2.3.4.4 Damping

Damping represents an additional cyclic parameter for describing the behavior of structural materials under cyclic loading. In contrast to the dissipated energy density, damping parameters provide a normalized measure by relating dissipated to stored elastic energy.

Damping is also relevant for the design of structures subjected to seismic actions, as it governs the dissipation of vibrational energy.

For linear damping behavior, damping parameters can be derived directly from the reversal points of the hysteresis loop (Petersen and Werkle 2017). According to (da Silva et al. 2018b), the specific damping capacity $\psi$ is defined as the ratio of dissipated energy density $w_{\text{diss}}$ to elastic strain energy density $w_{\text{el}}$:

$$\psi = \frac{w_{\text{diss}}}{w_{\text{el}}} \tag{2.42}$$

The elastic strain energy density $w_{\text{el}}$ represents the recoverable energy stored in the system during loading. In the linear case, it corresponds to the triangular area under the mean stiffness line, as illustrated in Figure 2.22, and can be calculated as (Petersen and Werkle 2017):

$$w_{\text{el}} = \frac{1}{2}\tau_{\text{max}} \cdot \gamma_{\text{max}} \tag{2.43}$$

For nonlinear stiffness characteristics, determining the elastic strain energy becomes more complex. Linearization methods may be applied to approximate the mean stiffness (Spitz 2012). Alternatively, the elastic strain energy density can be obtained by numerical integration of the area under the mean stiffness curve.

Besides the specific damping capacity $\psi$, several additional parameters are used to characterize damping behavior. For small damping values, these parameters can be converted into one another. A commonly used alternative is the loss factor $\eta$, which is widely applied in dynamic mechanical analysis of adhesive materials and enables direct comparison of results in international research. The loss factor is directly related to the phase shift between stress and strain under harmonic loading and corresponds to the tangent of the phase angle $\varphi$. It is defined as (da Silva et al. 2018b; Damm 2023):

$$\eta = \frac{\psi}{2\pi} = \frac{w_{\text{diss}}}{2\pi\, w_{\text{el}}} = \tan(\varphi) \tag{2.44}$$

### 2.3.5 Failure Criteria Under Cyclic Loading

Within fatigue testing, appropriate failure criteria are required to define the number of cycles to failure and to construct S-N curves. In experimental investigations, complete fracture of the specimen is commonly adopted as the failure criterion (Radaj and Vormwald 2007). Alternatively, failure may be defined by the formation of a crack of a specified size or by a predefined reduction in stiffness.

When monitoring the degradation of the load range during fatigue tests, (Halford et al. 2000) reported that a reduction of approximately 5 % is often considered a reliable indicator

of the onset of significant damage. Depending on the application and material behavior, alternative threshold values such as 10 %, 20 %, or 50 % may also be used. Changes in the load ratio between minimum and maximum force can likewise serve as a failure indicator. These signal-based criteria rely exclusively on quantities recorded during standard testing and therefore provide a practical method for defining failure thresholds without additional instrumentation.

(Hou et al. 2019), referring to (Calado and Azevedo 1989; Castiglioni et al. 2007; Castiglioni and Pucinotti 2009), consider reductions in dissipated energy, stress, or stiffness as indicators of failure under cyclic loading. For the assessment of fatigue damage in steel components subjected to seismic loading, (Hou et al. 2019) proposed an energy-based damage criterion defined as the ratio of the dissipated energy in the $i$th cycle, $W_{\mathrm{diss},i}$, to the dissipated energy in the initial cycle, $W_{\mathrm{diss},0}$:

$$\frac{W_{\mathrm{diss},i}}{W_{\mathrm{diss},0}} \leq 0.5 \tag{2.45}$$

In addition, a reverse stiffness criterion is introduced, in which fatigue failure is defined as the point at which the average reverse stiffness decreases below 50 % of its initial value.

Investigations on steel pipe elbows subjected to seismic loading by (Kim et al. 2023) demonstrate that failure is governed by LCF combined with with ratcheting effects. The damage evolution can be described using cumulative damage models based on ductility and energy dissipation, which emphasizes the relevance of damage-based failure criteria for components subjected to seismic cyclic loading.

Further approaches for defining fatigue damage and failure criteria are based on cyclic stress–strain parameters. These concepts were originally developed for metallic materials and primarily address time-independent elastic–plastic behavior. The Smith–Watson–Topper approach relates fatigue damage to the product of the maximum stress and the strain amplitude within a load cycle, thereby incorporating mean stress effects in strain-controlled fatigue (Smith et al. 1970). A related but more general formulation was introduced by (Glinka et al. 1995), who proposed the maximum elastic strain energy density as a governing parameter for fatigue damage, particularly under multiaxial loading. Both approaches provide physically motivated scalar measures that can be used to define fatigue failure criteria.

## 2.4 Fundamentals of Seismology and Ground Motion

### 2.4.1 Earthquake Generation and Classification

Earthquakes relevant to structural engineering are predominantly of tectonic origin, resulting from the sudden release of stresses accumulated within the Earth's crust. Continuous

plate movements initially cause elastic and inelastic deformation, which leads to progressive stress concentrations along faults and plate boundaries. When the local shear or tensile strength of the rock mass is exceeded, brittle fracture and frictional slip occur, resulting in abrupt relative displacement and rapid stress redistribution. The released strain energy propagates through the surrounding medium primarily as compressional (P) waves and shear (S) waves, which constitute the fundamental source of seismic excitation acting on structures.

Other earthquake types, such as volcanic, collapse-related, reservoir-induced, or human-induced events, may occur regionally but are generally of secondary relevance for engineering-based seismic assessment and are therefore not considered further (Bachmann 1995; Petersen and Werkle 2017).

### 2.4.2 Seismic Hazard and Regional Relevance

Geophysical hazards, and earthquakes in particular, represent one of the most significant natural threats worldwide in terms of human casualties and economic losses. Based on global disaster loss assessments, geophysical events account for more than half of the fatalities caused by natural hazards over recent decades, highlighting the persistent relevance of seismic risk on a global scale (Wallemacq et al. 2018). However, the severity of earthquake consequences is not governed solely by seismic activity but is strongly influenced by regional exposure, structural vulnerability, and the level of seismic preparedness.

This dependency is illustrated by the 2010 Haiti and New Zealand earthquakes, which exhibited comparable seismic intensity but resulted in fundamentally different consequences. While the New Zealand event affected a large population without causing fatalities, the Haiti earthquake led to catastrophic loss of life. These differences are primarily attributed to variations in building quality, enforcement of seismic design provisions, and overall preparedness (Allen 2007; Wallemacq et al. 2018).

From an engineering perspective, seismic hazard is commonly described using probabilistic approaches that quantify the likelihood of exceeding specified ground motion levels at a given site. Regional seismic hazard assessments typically express this information in terms of horizontal peak ground acceleration (PGA), accounting for local soil conditions and characteristic return periods (Giardini et al. 1999; Shedlock and Tanner 1999). An exemplary probabilistic seismic hazard map for the Mediterranean region, corresponding to a 10 % probability of exceedance in 50 years, or equivalently a return period of 475 years, is shown in Figure 2.23 (Giardini et al. 2003). The map illustrates that significant seismic hazard exists not only in highly active regions but also in large parts of Southern and Central Europe, which is directly relevant for engineering applications in the European context.

Overall, global earthquake statistics confirm that seismic hazard remains a persistent design consideration. Despite advances in monitoring and early-warning capabilities, earthquakes

with damaging potential continue to occur, emphasizing the need for robust seismic design concepts and reliable assessment of structural performance under seismic loading.

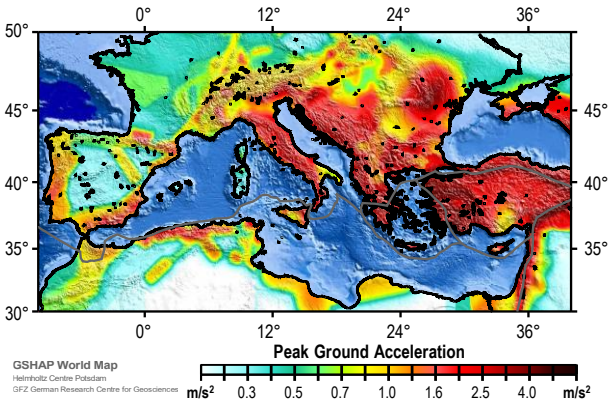


**Figure 2.23:** Seismic hazard map of horizontal peak ground acceleration for the Mediterranean region. Based on (Giardini et al. 2003).

### 2.4.3 Seismic Magnitude and Intensity Measures

The severity of an earthquake can be described using magnitude and intensity, which represent fundamentally different but complementary measures. Magnitude quantifies the size of an earthquake at its source and is independent of the observation location, whereas intensity characterizes the effects of ground shaking at a specific site and therefore depends on distance, local soil conditions, and structural vulnerability.

Early magnitude scales were developed based on instrumental recordings of ground motion amplitudes. The local magnitude scale $M_L$, introduced by (Richter 1935), relates the logarithm of measured ground displacement amplitudes to a reference event at a given epicentral distance. While $M_L$ provided a practical means of comparing moderate earthquakes, it is region dependent and subject to saturation for large events. For greater source-station distances, alternative formulations such as the body-wave magnitude $M_b$ were proposed by (Gutenberg and Richter 1956).

A physically more consistent description of earthquake size is provided by the moment magnitude $M_\mathrm{w}$, which is derived from the seismic moment and thus directly linked to fault geometry, slip, and material properties. The moment magnitude concept was introduced by (Kanamori 1977) and later formalized by (Hanks and Kanamori 1979). Unlike earlier scales, $M_\mathrm{w}$ does not exhibit saturation for large earthquakes and is therefore the preferred measure for seismic hazard analyses and earthquake catalog harmonization. For practical engineering applications, differences between magnitude scales are generally small for moderate events, while systematic deviations become relevant mainly for strong earthquakes (Bachmann 1995; Ristau 2009).

In contrast to magnitude, seismic intensity describes the observed effects of an earthquake at a specific location and is therefore inherently site-dependent. It represents a macroseismic

quantity derived from noninstrumental observations and reflects both the characteristics of local ground shaking and the response of the built environment. More specifically, the classification of intensity levels depends on the severity of the effects: at low intensity levels, it is primarily based on subjective human perception, while at intermediate levels the assessment of building damage becomes dominant. At very high intensity levels, additional effects such as ground failure or landscape-altering phenomena may be considered (Meskouris 2011).

Several macroseismic intensity scales are in use worldwide, all of which aim to classify the local impact of an earthquake based on human perception, structural damage, and observable environmental effects, rather than the energy released at the source. A widely used qualitative measure is the Modified Mercalli Intensity scale, originally developed by (Wood and Neumann 1931), which categorizes earthquake effects into twelve discrete levels (U.S. Geological Survey 1997). In Europe, the Medvedev–Sponheuer–Karnik scale was widely applied for decades and has largely been superseded by the European Macroseismic Scale, which incorporates modern building typologies and damage classifications (Grünthal 1998). In other regions, alternative formulations such as the Japanese Meteorological Agency scale are used. Despite regional differences, these scales share the common objective of describing the spatial variability of earthquake effects at the Earth's surface.

Such intensity measures are particularly valuable for the assessment of historical earthquakes and for regions lacking instrumental recordings. Moreover, because intensity inherently reflects local geological conditions and the characteristics of the building stock, it captures site effects that are not represented by source-based parameters such as magnitude or seismic moment (Meskouris 2011). However, due to their observational and noninstrumental nature, macroseismic intensity measures do not provide direct quantitative input for structural analysis.

### 2.4.4 Ground Motion Parameters for Structural Analysis

For engineering purposes, earthquake excitation is most effectively described by the time variation of ground acceleration, $a_g(t)$, because it directly enters the governing equations of motion for structural systems and thus defines the seismic input for dynamic analysis. Accordingly, strong-motion networks primarily aim to record three orthogonal components of ground shaking consisting of one vertical and two horizontal directions using strong-motion accelerographs, which are typically triggered by the onset of shaking and record the subsequent strong motion phase. An example of a recorded acceleration time history is shown in Figure 2.24 for the first horizontal component of the Northridge-01 earthquake (Bachmann 1995; Chopra 2012; Petersen and Werkle 2017).

In practice, two measurement concepts can be distinguished. From a seismological perspective, ground velocities are central for source characterization and wave-field interpretation, whereas structural engineering primarily relies on ground accelerations and their frequency content to interpret damage patterns and to derive design-relevant representations such as

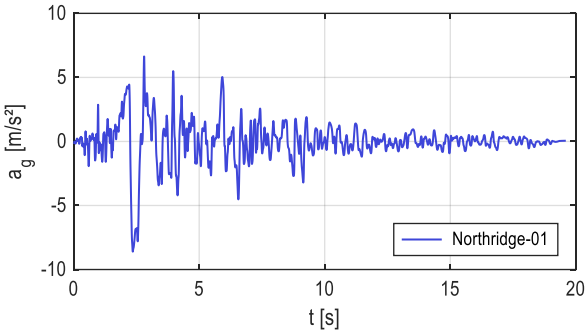


**Figure 2.24:** Ground acceleration of the Northridge-01 earthquake, first horizontal component (RSN 1063 from (Ancheta et al. 2013).

response spectra (Bachmann 1995). Modern accelerographs are designed for strong shaking and can record amplitudes on the order of 1 $g$ ($\approx 9.81$ m/s$^2$) and above. Digital devices commonly provide pre-event memory and automated triggering to ensure that the beginning of the record is captured, which is critical for subsequent processing (Bachmann 1995; Chopra 2012).

The fundamental record is the acceleration time history $a_g(t)$. The associated ground velocity $v_g(t)$ and ground displacement $u_g(t)$ time histories are obtained by numerical integration of $a_g(t)$.

$$v_g(t) = \int a_g(t)\, dt \tag{2.46}$$

$$u_g(t) = \int v_g(t)\, dt \tag{2.47}$$

These time histories are often used to interpret deformation-related demand. However, it is well established that the derived velocity and, in particular, displacement histories are highly sensitive to small recording errors and to long-period drift. Therefore, practical processing typically requires baseline correction and filtering procedures to suppress spurious low-frequency components; otherwise, unrealistically large displacements may result (Bachmann 1995; Chopra 2012; Petersen and Werkle 2017).

To characterize the severity of a recorded ground motion in a compact form, the peak values of these time histories are commonly used:

- Peak ground acceleration (PGA): $a_{g,\max}$
- Peak ground velocity (PGV): $v_{g,\max}$
- Peak ground displacement (PGD): $d_{g,\max}$

These parameters are site-specific and represent instrumental intensity measures of shaking. While PGA is widely used as a primary descriptor in engineering practice, PGV and PGD are particularly informative when deformation demand and longer-period response are of interest. Beyond peak values, two additional record characteristics are essential for structural response: the dominant frequency content (or equivalently the period range) and

the duration of strong shaking, both of which govern the accumulation of cyclic demand (Bachmann 1995; Chopra 2012; Petersen and Werkle 2017).

Because ground shaking varies markedly across a region, post-event mapping tools are used to represent its spatial distribution. ShakeMaps combine recorded ground-motion parameters (e.g., PGA and PGV) with site-amplification information to provide a spatially resolved depiction of shaking shortly after an earthquake. A key implication is that magnitude and epicentral location alone are insufficient to identify where the strongest shaking, and thus the highest structural demand, occurs (Wald et al. 2003).

In summary, acceleration time histories and their derived velocity and displacement records provide the quantitative basis for the engineering characterization of earthquake ground motion. These time-domain descriptions are the starting point for response spectra, which are introduced in the following section (Bachmann 1995; Chopra 2012).

### 2.4.5 Response Spectra

Response spectra represent a central tool in earthquake engineering. They are used both for the engineering interpretation of recorded earthquake motions and for the design of structures in the form of design response spectra. Response spectra therefore provide an important link between time-dependent earthquake excitation and practical structural design (Bachmann 1995).

The determination of a response spectrum for a recorded earthquake is based on a set of linear-elastic SDOF oscillators with identical damping ratios but different natural frequencies or natural periods $T$. As illustrated in Figure 2.25, each oscillator is subjected to the same ground acceleration time history. The dynamic response of each system is obtained by numerical integration of the equation of motion with base excitation given in Eq. (2.29). For each oscillator, the time-dependent response quantities are calculated, in particular the relative displacement between the mass and the base, the relative velocity, and the absolute acceleration of the mass. The maximum values of these response quantities are then extracted and plotted as a function of the natural frequency or natural period $T$. This procedure results in displacement, velocity, and acceleration response spectra for the specified damping ratio. In engineering practice, response spectra are commonly evaluated for several damping ratios $\zeta$, for example 0 %, 2 %, 5 %, and 10 % (Bachmann 1995; Chopra 2012).

Defined theoretical relationships exist between the displacement, velocity, and acceleration response spectra, which allow conversion between these quantities. The displacement response spectrum is defined by the maximum relative displacement of the oscillator:

$$S_u(\omega, \zeta) = \max|u(t)| \tag{2.48}$$

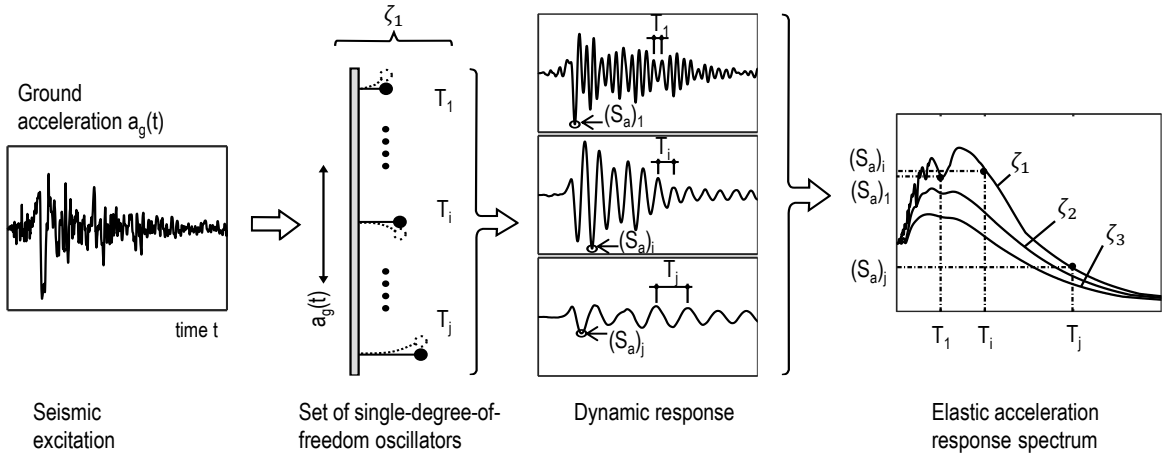


**Figure 2.25:** Schematic determination of elastic response spectra from ground motion records. Based on (Bachmann 1995).

For lightly damped systems, the pseudo-velocity spectrum can be expressed as:

$$S_v(\omega, \zeta) = \omega \cdot S_u(\omega, \zeta) \tag{2.49}$$

The corresponding pseudo-acceleration spectrum follows as:

$$S_a(\omega, \zeta) = \omega^2 \cdot S_u(\omega, \zeta) \tag{2.50}$$

The quantities $S_u$, $S_v$, and $S_a$ therefore denote the response spectra of relative displacement, pseudo-velocity, and pseudo-acceleration, respectively. These relationships allow consistent transformation between the different spectral representations (Bachmann 1995; Chopra 2012; Petersen and Werkle 2017).

### 2.4.6 Seismic Loading in Structural Design

This section presents a basic overview of the principles of structural design under seismic loads. Major variations between national standards exist because seismic risk varies significantly across regions. According to (Bachmann 1995), three basic properties are significant in seismic design:

- The stiffness
- The load-bearing resistance
- The ductility

Increasing stiffness against horizontal loads reduces displacements and interstory drifts. Consequently, damage to non-structural components such as partition walls or facades can be minimized, which is particularly important for relatively weak earthquakes. To minimize plastic deformations during an earthquake, the load-bearing resistance must be increased.

Ductility or plastic deformation capacity describes the amount of energy that a building can absorb or dissipate during an earthquake. A certain amount of ductility is required to prevent a structure from collapsing during a design earthquake. These properties are embedded in design principles of standards for earthquake-resistant structures and must be considered.

A comprehensive summary of worldwide regulations is provided in (Scavino 2014). In Europe, Eurocode 8 (EN 1998-1) defines the standard for earthquake-resistant design, with country-specific provisions given in the national annexes. Other important countries with high seismic activity are America (FEMA 450; ASCE/SEI 7-10), Australia (AS 1170.4), New Zealand (NZS 1170.5), China (GB 50011), India (IS 13935; IS 1893) or Japan (JASS 14).

For the design of structural components, the standards offer different calculation methods. On the basis of (EN 1998-1), the following calculation methods are available for the verification of seismic safety:

- Lateral force method of analysis
- Modal response spectrum analysis
- Non-linear static (pushover) analysis
- Non-linear time history (dynamic) analysis

These methods differ significantly in complexity. In practice, the first two methods are typically used for the design of new buildings. Both methods apply earthquake loads to structures using equivalent static forces. Thus, the calculation can be performed with tools similar to those used in static design, and fewer dynamic effects need to be considered. An introduction to the seismic design of steel structures is given in (Landolfo 2015).

#### 2.4.6.1 Lateral Force Method of Analysis

In the lateral force method, the seismic action is represented by the spectral acceleration derived from standardized elastic acceleration response spectra. The shape of the spectrum is illustrated by the solid line in Figure 2.26 and can be divided into three main regions. The elastic response spectrum $S_\mathrm{e}(T)$ depends on the natural period $T$ of the structure and corresponds to the pseudo-acceleration spectrum $S_\mathrm{a}(T)$ commonly used in structural dynamics. The reference ground acceleration on rock, $a_\mathrm{gR}$, is defined by seismic zoning maps, which account for regional seismicity. For design purposes, the design ground acceleration is given by $a_g = \gamma_\mathrm{I} \cdot a_\mathrm{gR}$, where $\gamma_\mathrm{I}$ is the importance factor. The influence of the soil conditions is considered by the soil factor $S$, while the damping correction factor is denoted by $\eta_\mathrm{c}$. All parameters are specified in the respective national annex.

In the constant spectral acceleration range, defined by the period limits $T_\mathrm{B} < T < T_\mathrm{C}$, the elastic response spectrum $S_\mathrm{e}(T)$ reaches its maximum value. According to (DIN EN 1998-1/NA), $T_\mathrm{B}$ typically ranges between 0.05 s and 0.1 s and $T_\mathrm{C}$ between 0.2 s and 0.5 s,

depending on the soil conditions. The maximum spectral acceleration is given by (EN 1998-1):

$$T_\mathrm{B} < T < T_\mathrm{C}: \quad S_\mathrm{e}(T) = a_g \cdot S \cdot \eta_\mathrm{c} \cdot 2.5 \tag{2.51}$$

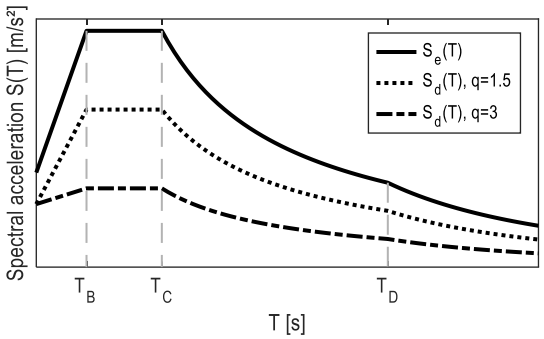


**Figure 2.26:** Shape of the elastic response spectrum $S_\mathrm{e}(T)$ and corresponding design response spectra $S_d(T)$ for different behavior factors $q$. Based on (EN 1998-1; Landolfo 2015).

The resulting spectrum describes only the elastic behavior of structures. As mentioned above, ductility plays an important role in the design of buildings for seismic loading. To take this behavior into account, (EN 1998-1) uses the so-called behavior factor $q$, which reduces the elastic acceleration response spectrum to a design spectrum. The maximum value $S_\mathrm{d}$ of these design spectra is calculated by:

$$T_\mathrm{B} < T < T_\mathrm{C}: \quad S_d(T) = a_\mathrm{g} \cdot S \cdot \frac{2.5}{q} \tag{2.52}$$

The capacity of structures to dissipate energy through plastic deformations is therefore taken into account, and the seismic design force is reduced relative to the linear elastic response. The actual structural analysis can be performed without non-linear analysis and well-established linear-elastic material properties can be used, which increases computational efficiency. The behavior coefficient $q$ depends strongly on the design concept and the construction type of the building and can assume values from 1 to 6. The effects of the behavior coefficient on the response spectrum and, therefore, on the seismic load are shown in Figure 2.26 for values of $q$ equal to 1.5 and 3.

The structural analysis with the lateral force method can only be performed for buildings that are regular in plan and elevation and for which higher-mode effects are negligible. In this case, the base shear force $F_\mathrm{b}$ can be determined as a function of the acceleration ordinate of the design spectrum $S_\mathrm{d}$ at the fundamental period $T_1$, $S_\mathrm{d}(T_1)$, the effective mass of the structural system $m_\mathrm{s}$, and a correction factor $\lambda_\mathrm{c}$:

$$F_\mathrm{b} = S_\mathrm{d}(T_1) \cdot m_\mathrm{s} \cdot \lambda_\mathrm{c} \tag{2.53}$$

The first fundamental period $T_1$ can be determined using methods of structural dynamics or by approximate empirical equations. The base shear force is applied in proportion to the shape of the first translational vibration mode.

#### 2.4.6.2 Modal Response Spectrum Analysis

For more complex or irregular buildings, where the lateral force method cannot be applied, the modal response spectrum analysis is typically used. In this method, all vibration modes that contribute significantly to the global response are considered. These modal contributions can be combined using the SRSS (square root of the sum of squares) or CQC (complete quadratic combination) rule.

#### 2.4.6.3 Nonlinear Analyses

In addition to the lateral force method and the modal response spectrum analysis, a non-linear pushover analysis or non-linear response-history analysis can be performed. Both methods have in common that the material and geometric behavior must be modeled using extended non-linear properties. This increases both computational effort and the demands on the engineer.

In addition to their use in structural design, these extended analysis methods or experimental investigations can be carried out to determine the behavior coefficient $q$ for a certain construction type. The results obtained from these approaches can then be related to the linear-elastic ultimate limit state, resulting in behavior coefficients. These investigations have been conducted for various construction types, as reported in (Bachmann et al. 1994; Dazio et al. 1995; Blaß and Schädle 2009; Blaß and Schädle 2011; Norda 2013), in order to determine the behavior of the respective type of construction with sufficient certainty.

### 2.4.7 Determination of the Number of Equivalent Cycles

The concept of converting random seismic loads into a number of equivalent cycles is a fundamental approach in structural engineering for analyzing damage due to seismic loading cycles. (Seed and Idriss 1970; Seed et al. 1975) adapted this concept to evaluate the cyclic liquefaction potential of soils, an inherently nonlinear material. The development of equivalent cycles for evaluating liquefaction potential has been further developed in subsequent studies, for example by (Green and Terri 2005).

Mathematically, these approaches are based on Miner's cumulative damage hypothesis, shown in Eq. (2.37), where the equivalent cycles are derived by equating the damage caused by variable peak loads to that induced by a uniform cyclic load. In essence, the component damage from irregular seismic loading is transformed into a comparable number of cycles at a reference stress level $\mathrm{CSR}_{\mathrm{Ref}}$, which induces failure in a reference number of cycles $N_{\mathrm{Ref}}$.

According to Green's formulation, $n_{\text{eq}}/N_{\text{Ref}}$ equals the sum of the partial damage ratios for each load cycle, where $n_i$ denotes the number of applied cycles at a given stress level and $N_{f,i}$ the corresponding number of cycles to failure, as shown in Eq. (2.54). This expression allows for the determination of the number of equivalent cycles $n_{\text{eq}}$, effectively simplifying complex seismic loads into manageable cyclic representations:

$$D = \frac{n_{\text{eq}}}{N_{\text{ref}}} = \sum_i \frac{n_i}{N_{f,i}} \Rightarrow n_{\text{eq}} = \sum_i n_{\text{eq},i} \cdot n_i = \sum_i \frac{N_{\text{ref}}}{N_{f,i}} \cdot n_i \tag{2.54}$$

To calculate the number of equivalent cycles $n_{\text{eq}}$, (Seed et al. 1975) proposed a procedure to normalize the cyclic stress ratio (CSR)-liquefaction curve and generate master curves. First, the cyclic stress ratio required to induce liquefaction in a single cycle ($\text{CSR}_1$) is determined. Subsequently, the ordinate values are normalized by dividing the cyclic stress ratio by $\text{CSR}_1$. Next, a safety factor is applied by dividing the CSR by the specified safety factor. Typically, the reference stress level is chosen as $0.65 \cdot \tau_{\text{max}}$, although other levels can be used, depending on the specifics of the seismic loading scenario. Based on this procedure, the reference number of cycles required to induce liquefaction, $N_{\text{Ref}}$, corresponding to a normalized peak amplitude of uniform cycles, is determined. Finally, the abscissa values are normalized as the ratio $N_{\text{Ref}}/\ N_{\text{Liq}}$.

Using this procedure, the equivalent number of load cycles $n_{\text{eq}}$ is determined based on empirical, nonlinear CSR-liquefaction curves, without the need for a mathematical description. By applying a search algorithm, the corresponding $n_{\text{eq}}$ values are obtained directly from the experimental master curve for each load cycle. For CSR-liquefaction relationships that are linear in log–log space, the influence of the safety factor and the selected reference amplitude on the computed $n_{\text{eq}}$ values is negligible, as noted by (Green and Terri 2005).

The concept of equivalent cycles forms the basis for the seismic loading assessment presented in chapter 8, where the CSR-liquefaction curve is replaced by experimentally determined S-N curves of the SG joint.

# 3 Glass and Facade Structures Under Seismic Loading

## 3.1 Adhesive Joints in Glass and Facade Construction

### 3.1.1 Application of Structural Glazing

Structural glazing (SG) systems describe facade constructions in which glass elements are bonded to a supporting substructure by means of continuous elastic adhesive joints, typically based on silicone adhesives. The load transfer between the glass and the supporting structure is achieved through the SG joint, allowing for a largely uninterrupted and transparent building envelope.

Figure 3.1 illustrates typical applications of elastic adhesive joints in structural glass construction. The schematic highlights different bonding concepts, including (a) the direct bonding of glass elements, (b) the connection of glass panes via factory-bonded carrier profiles, and (c) the adhesive attachment of insulating glass units. In all cases, the SG joint provides the primary load transfer path between the glass and the supporting structure.

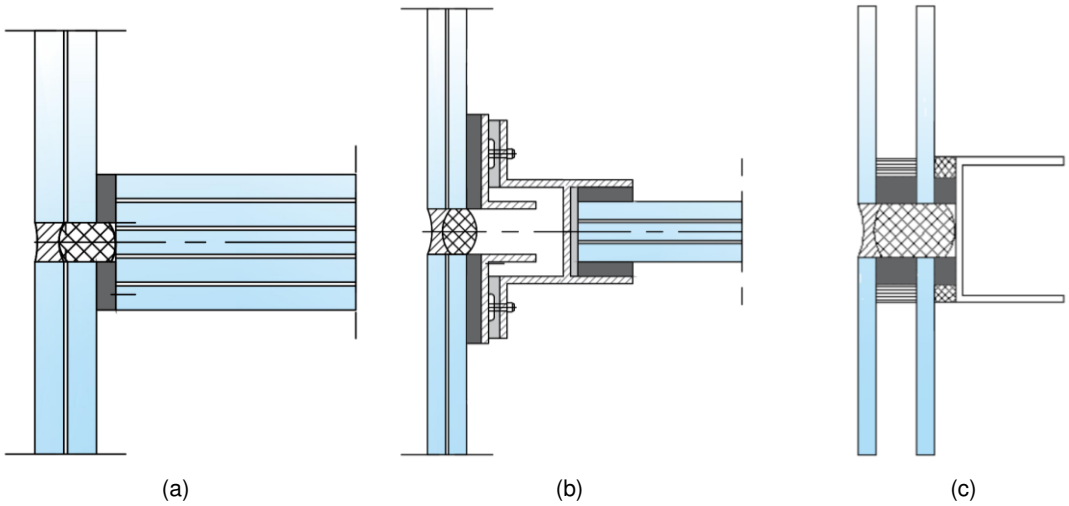


**Figure 3.1:** Examples of applications of elastic adhesive joints in structural glass construction according to (Bues 2021; Schuler et al. 2023): (a) direct bonding of glass elements; (b) connection of glass elements via factory-bonded carrier profiles; (c) adhesive attachment of insulating glass units.

In conventional curtain wall applications, insulating glass units are bonded along their edges to aluminum, steel, or timber frames. The continuous bond line enables a distributed introduction of loads, such as wind-induced pressures and suctions, into the supporting structure, in contrast to discrete mechanical fixings.

Beyond standard facade systems, adhesive bonding is also employed in architecturally demanding applications, including metallic facade claddings and highly transparent all-glass entrance structures. Exemplary applications are shown in Figure 3.2, illustrating both a SG facade and an adhesively bonded all-glass entrance structure. These examples demonstrate the structural relevance and versatility of SG joints in modern glass and facade construction.

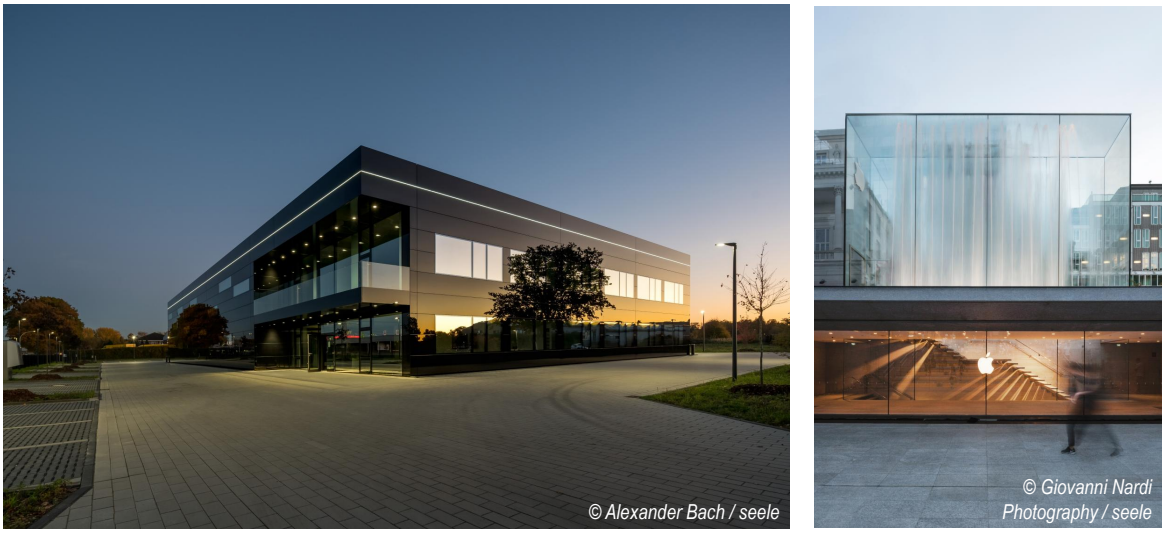


(a) (b)

**Figure 3.2:** Exemplary applications of SG: (a) SG facade with linear joints (© Alexander Bach / seele); (b) adhesively bonded all-glass entrance structure in Milan, Italy (© Giovanni Nardi Photography / seele).

### 3.1.2 Load-Bearing and Failure Behavior of SG Joints

In facade construction, SG joints are typically arranged as continuous joints. In-plane actions, such as temperature-induced expansions of the glass panels, are primarily accommodated by shear deformations within the SG joint. In contrast, actions acting orthogonally to the bonded interface, such as wind loads, induce tensile or compressive stresses in the joint.

SG joints are well suited to compensate differential deformations between the bonded components, particularly when materials with different coefficients of thermal expansion, such as glass and aluminum, are connected or exposed to non-uniform temperature fields. This behavior results from the low shear modulus and high deformation capacity of SG adhesives, in combination with the typically large joint thickness. Owing to the rubber-like nature of silicone elastomers (Treloar 1975), their mechanical response is characterized by

pronounced nonlinearities as well as a strong dependence on time and temperature (Martins et al. 2006; Meunier et al. 2008), as discussed in section 2.1.3.

The load-bearing behavior of SG joints is inherently anisotropic. Owing to the nearly incompressible material behavior of SG adhesives, the joint response under tensile or compressive loading is significantly stiffer than under shear loading. The magnitude of this stiffening effect depends on the degree of transverse strain restraint within the joint as well as on the elastic material properties, in particular the Poisson's ratio $\nu$. This behavior is illustrated in Figure 3.3, which shows exemplary stress–strain curves for SG specimens with dimensions of $12 \times 12 \times 100$ mm$^3$ (width × thickness × length). Tensile loading (solid lines) yields markedly higher stiffness than shear loading (dashed lines).

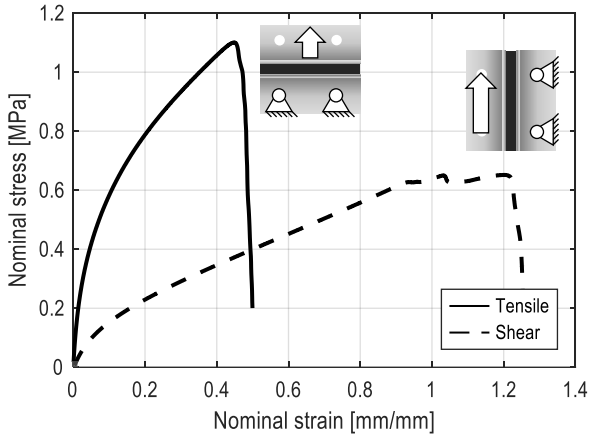


**Figure 3.3:** Stress–strain curve of linear bonded joints under tension and longitudinal shear load for a common SG adhesive system.

The tensile stress–strain curves exhibit a pronounced nonlinear response, with a high initial stiffness, followed by a gradual reduction in stiffness. In contrast, specimens subjected to shear loading exhibit an initially stiff response up to shear stresses of approximately 0.2 MPa, followed by a comparatively softer and nearly linear response over the remaining deformation range, while remaining markedly less stiff than under tensile loading throughout. In practical applications, the relevance of these stiffness differences is further amplified, as the governing deformation range under design conditions is typically limited to the initial portion of the stress–strain curves due to conservative safety concepts (Hagl 2006; Bues et al. 2019; Bues 2021; Schuler et al. 2023).

### 3.1.3 Influencing Factors

The load-bearing and failure behavior of SG joints is governed by several geometric, mechanical, and environmental factors. Early experimental investigations established fundamental load-bearing characteristics and provided initial design recommendations for SG joints (Hagl 2006; Hagl 2007). Building upon these studies, recent systematic experimental investigations have quantified the influence of key parameters on the mechanical behavior of SG

joints (Schuler et al. 2017; Bues et al. 2019; Bues 2021). Among these parameters, the joint geometry has a decisive effect, particularly under tensile loading conditions.

Figure 3.4 illustrates the influence of different joint geometries on the stress–strain response. The shear stress–strain curves, shown in Figure 3.4a, exhibit a comparable stiffness over a wide range of deformation, indicating that the shear stiffness is largely independent of the joint geometry. Instead, the shear stiffness is primarily governed by the deformability of the adhesive material, whereas variations in joint height or specimen geometry mainly affect the ultimate shear strength rather than the overall deformation behavior.

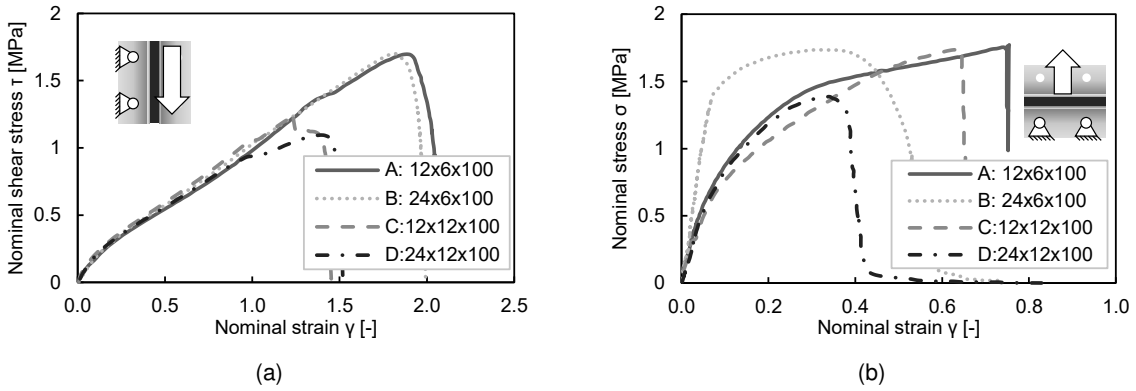


**Figure 3.4:** Influence of joint geometry on the load-bearing and failure behavior of SG joints: (a) stress–strain response under shear loading; (b) stress–strain response under tensile loading. Data from (Bues 2021).

In contrast, tensile loading exhibits a pronounced geometry-dependent response, as shown in Figure 3.4b. More compact joint geometries exhibit a significantly higher initial stiffness, followed by a characteristic plateau-like response prior to failure, while SG joints with less compact geometries show a softer initial response. This behavior is attributed to transverse strain restraint and the resulting hydrostatic stress state developing within the adhesive.

In addition to geometric parameters and loading conditions, the mechanical response of SG joints is significantly affected by loading rate and temperature. Figure 3.5a illustrates the influence of strain rate on the ultimate tensile stress. Increasing strain rates result in higher ultimate stresses, indicating a rate-dependent strengthening behavior of the SG joint. Figure 3.5b shows the effect of temperature on the ultimate shear stress. Elevated temperatures generally lead to a reduction in ultimate stress, whereas lower temperatures are associated with increased strength levels.

Environmental actions such as temperature variations, humidity, ultraviolet radiation, and long-term loading may further influence the durability and mechanical behavior of SG joints. Ageing processes, including artificial heat ageing, can lead to changes in material properties and thus affect both stiffness and strength characteristics (Schuler et al. 2017). These effects have been widely investigated in the literature, highlighting the sensitivity of SG systems to environmental exposure and long-term degradation (White et al. 2012; Van Lancker et al. 2016; Wallau et al. 2021; Wallau 2023).

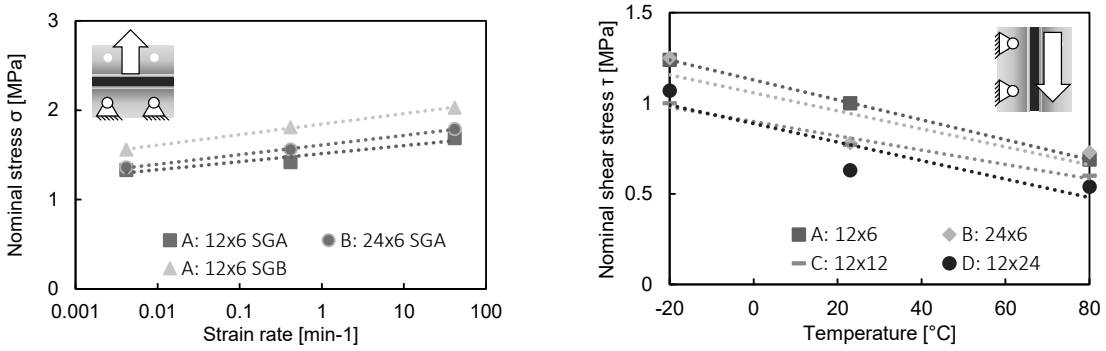


**Figure 3.5:** Influence of loading rate and temperature on the mechanical response of SG joints: (a) effect of strain rate on the ultimate tensile stress. Data from (Bues 2021); (b) effect of temperature on the ultimate shear stress. Data from (Schuler et al. 2017).

## 3.2 Design of SG Joints Under Conventional Loading

The design and verification of SG joints under conventional loading are based on a combination of normative frameworks, experimental evidence, and analytical as well as numerical modeling approaches. While normative frameworks establish fundamental design principles and safety concepts, experimental investigations provide essential insight into the actual load-bearing and deformation behavior of SG joints. These experimentally derived findings form the basis for simplified analytical design approaches.

### 3.2.1 Normative Framework

From a normative perspective, the design of SG joints is governed by a combination of European and international guideline documents that primarily address product qualification, quality assurance, and simplified design procedures. In Europe, the assessment of bonded glazing systems was traditionally based on the guideline (ETAG 002-1). In the course of the implementation of the Construction Products Regulation, the European Organisation for Technical Assessment (EOTA) initiated the transition from European Technical Approval Guidelines (ETAG) to European Assessment Documents (EAD), which now form the basis for issuing European Technical Assessments (ETA). Consequently, the EAD for Bonded Glazing Kits and Bonding Sealants (EAD 090010-00-0404) represents the successor document to (ETAG 002-1), as discussed in (Schaaf 2024).

In parallel to the European framework, international practice is supported by guidelines such as (ASTM C1401), which provides recommendations for the design and application of structural sealant glazing systems, particularly in North American contexts.

Although (ETAG 002-1) may still be used as an assessment basis, EOTA explicitly refers to the corresponding (EAD 090010-00-0404) as the current reference document. The requirements with respect to technical product properties remain unchanged. However, the former global

design concept or method of calculation included in (ETAG 002-1) is no longer part of the transferred EAD (Schaaf 2024).

In addition to the regulatory framework governing SG systems, the structural design and verification of glass components are addressed by separate, region-specific standards and guidelines, such as (DIN 18008; Feldmann et al. 2014; DIN EN 16612). These documents regulate the dimensioning and verification of glass elements independently of the bonded joint design and must therefore be considered in parallel when planning glass and facade structures.

Against this background, simplified analytical design approaches derived from (ETAG 002-1) remain relevant in engineering practice and are discussed in the following.

### 3.2.2 Determination of Mechanical Adhesive Properties

For the design of SG joints in glass and facade construction, representative mechanical adhesive properties are required to describe the load-bearing behavior of the adhesive joints. Within static design calculations and approval procedures, statistically validated strength and stiffness parameters are typically used. Owing to the complex and nonlinear stiffness behavior of SG adhesives, the mechanical response of SG joints is often approximated as linear-elastic in practical design applications, provided that predefined boundary conditions are satisfied.

For standard joint configurations within the scope of normative guidelines, relevant stiffness- and strength-related parameters are commonly provided by adhesive manufacturers, and characteristic strength values can often be obtained directly from the corresponding approvals of the adhesive systems. However, for joint geometries deviating from standardized configurations or within the context of project-specific approvals, these mechanical properties must be determined by means of experimental investigations.

**Strength-related parameters** According to (ETAG 002-1), the initial mechanical strength is represented by the arithmetic mean of the ultimate stresses $\tau_{\mathrm{ult,mean}}$ obtained from the ultimate shear stress $\tau_{\mathrm{ult}}$ of all specimens of the respective test series. An analogous evaluation can be performed for tensile loading using the ultimate failure tensile stress $\sigma_{ult}$. However, since the evaluation procedure is identical, the following explanations are limited to the shear case for clarity.

For a statistical interpretation, the characteristic ultimate stress $\tau_{\mathrm{k}}$, defined as the lower $p$-quantile with a confidence level of $1-\alpha$, can be calculated using Eq. (3.1), where $k_3(n, p, 1-\alpha)$ denotes the fractile factor and $s$ the sample standard deviation. According to (ETAG 002-1), the lower $p$-quantile is defined with $p = 0.05$ and a confidence level of $1-\alpha = 0.75$, which corresponds to a 5 % quantile, or equivalently a 95 % survival probability. The determination of the fractile factor $k_3$ requires the application of the non-central Student's

t-distribution with a non-centrality parameter $\delta$ (Beech and Owen 1962; Loch 2014). For practical use, values for the $k_3$ factors are given in (ETAG 002-1; ISO 16269-6). In this work, the calculation of the characteristic ultimate stress $\tau_k$ was performed according to (ETAG 002-1), ensuring comparability with the manufacturer's value $\tau_{k,ETA}$. Alternative statistical procedures for the determination of strength parameters are, for example, defined in (BAM 1979; Wesche et al. 1996).

$$\tau_k = \tau_{ult,mean} - k_3(n, p, 1-\alpha) \cdot s \tag{3.1}$$

**Stiffness-related parameters** For the design and assessment of SG joints, stiffness-related parameters are required to describe the deformation behavior of the SG joint under load. Owing to the hyperelastic and nearly incompressible material behavior of SG adhesives, stiffness cannot be regarded as a unique material constant but represents an effective parameter that depends on the deformation mode, strain level, joint geometry, and evaluation method.

Various standardized and guideline-based procedures for the experimental determination of stiffness parameters have been proposed in the literature. In (ETAG 002-1), the stiffness of SG joints is represented by a secant modulus determined at a strain level of 12.5 % on a standardized H-specimen. This initial stiffness is primarily used to assess the influence of artificial ageing on the stiffness properties of the adhesive system.

A direct approach for determining shear stiffness is described in (ISO 11003-2), where the shear modulus $G$ is defined as the ratio between shear stress $\tau$ and shear strain $\gamma$ at a point within the linear region of the stress–strain curve and can be calculated according to Eq. (2.9).

In structural engineering practice, the shear stiffness of the joint, denoted as $G_{joint}$, can be determined according to (FKG 01/2021). In this approach, a secant modulus through the origin is evaluated at the permissible shear stress $\tau_{des}$, where $\gamma_{\tau_{des}}$ denotes the corresponding shear strain:

$$G_{joint} = \frac{\tau_{des}}{\gamma_{\tau_{des}}} \tag{3.2}$$

The permissible stress $\tau_{des}$ is calculated using a method factor $\gamma_{meth} = 4$ or 6. In most cases, a method factor of $\gamma_{meth} = 4$ is applied for the experimental determination of stiffness parameters, as this value is typically adopted in conjunction with the structural spring model.

Since the evaluation of a secant modulus through the origin is sensitive to initial measurement inaccuracies, (ISO 527-1) proposes alternative evaluation procedures for determining stiffness. Both a strain-based secant method and a linear regression approach are applied

within a defined strain interval between 0.05 % and 0.25 %. However, this strain interval is intended for stiffer polymers and adhesives, and its direct application to the highly deformable SG adhesives used in this work was not appropriate.

Based on this concept, (Müller et al. 2023b) proposed a modified evaluation procedure for SG joints. In this approach, the secant modulus is determined between two defined stress levels, namely the design stress $\tau_{\text{des}}$ and a lower reference stress $\tau_0$. The corresponding shear strains are denoted as $\gamma_{\tau_{\text{des}}}$ and $\gamma_{\tau_1}$, respectively. The effective shear modulus, as illustrated in Figure 3.6, is then calculated as:

$$G_{\text{joint}} = \frac{\tau_{\text{des}} - \tau_0}{\gamma_{\tau_{\text{des}}} - \gamma_{\tau_0}} \tag{3.3}$$

In the present investigations, $\tau_0 = 0.02$ MPa was selected, providing a compromise between minimizing initial test artefacts and maintaining a meaningful evaluation range.

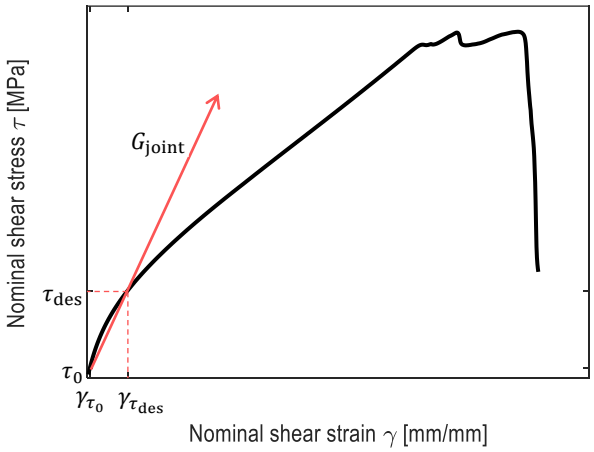


**Figure 3.6:** Determination of the effective shear stiffness of the joint $G_{\text{joint}}$.

In addition to these stress-based evaluation procedures, further approaches have been proposed for tensile-loaded joint-like specimens. In (Descamps et al. 2017; Descamps and Hayez 2018; Descamps et al. 2020), the effective joint modulus is derived from the Young's modulus of the adhesive material using a geometry-dependent stiffness factor $f_{\text{rigidity}}$, which accounts for the aspect ratio of the joint. This factor may significantly increase the apparent joint stiffness compared to the uniaxial material modulus and depends on both the joint geometry and the material properties (Feynman et al. 2010). These tensile- and model-based approaches were not further considered here, as the present work focuses exclusively on shear-dominated loading conditions.

### 3.2.3 Simplified Analytical Design Approaches

#### 3.2.3.1 ETAG 002-1 Approach

Within (ETAG 002-1), simplified analytical design rules are provided for four-sided bonded glass panes in curtain wall facades. The approach follows a global safety concept, where a single global method factor $\gamma_{\text{meth}}$ is introduced to convert characteristic strength values into design stresses, thereby implicitly covering uncertainties related to material behavior, environmental exposure, production variability and analytical simplifications. Design stresses are derived from characteristic strength values, and joint dimensions are determined using simplified closed-form expressions. The applicability of the method is restricted to predefined geometric validity limits.

The applicability of the simplified analytical design concept is restricted to joint geometries that satisfy specific dimensional constraints. In this context, $b$ denotes the joint width and $e$ the joint thickness. These geometric limits define the range within which the underlying assumptions of the analytical model remain valid:

$$e \leq b \leq 3 \tag{3.4}$$

$$e \geq 6\,\text{mm} \tag{3.5}$$

$$b \leq 20\,\text{mm} \tag{3.6}$$

Within the defined geometric validity range, the required joint dimensions are determined separately from tensile and shear actions. The required joint width $b$ is derived from tensile loading. In this context, $a_{\text{p}}$ denotes the shorter side length of the glass pane, $w$ the wind action expressed as stress, and $\sigma_{\text{des}}$ the design value of the tensile stress of the sealant. The minimum required joint width $b$ results from:

$$b \geq \left| \frac{a_{\text{p}} \cdot w}{2 \cdot \sigma_{\text{des}}} \right| \tag{3.7}$$

The required joint thickness $e$ is obtained from shear deformation compatibility. Here, $\Delta l$ represents the maximum relative thermal movement in the longitudinal direction of the joint, $G$ the shear modulus of the sealant, and $\tau_{\text{des}}$ the design value of the shear stress. The minimum required joint thickness $e$ is given by:

$$e \geq \left| \frac{G \cdot \Delta l}{\tau_{\text{des}}} \right| \tag{3.8}$$

The design stresses $\sigma_{\text{des}}$ and $\tau_{\text{des}}$ are determined from the corresponding characteristic strength values $\sigma_k$ and $\tau_{\text{k}}$ by applying the global method factor $\gamma_{\text{meth,ETAG}}$. For (ETAG 002-1), $\gamma_{\text{meth,ETAG}} = 6$. The design values are therefore defined as:

$$\sigma_{\mathrm{des}} = \frac{\sigma_{\mathrm{k}}}{\gamma_{\mathrm{meth,ETAG}}} \tag{3.9}$$

$$\tau_{\mathrm{des}} = \frac{\tau_{\mathrm{k}}}{\gamma_{\mathrm{meth,ETAG}}} \tag{3.10}$$

#### 3.2.3.2 Structural Spring Method

For more complex SG facade constructions, that fall outside the validity range of the simplified ETAG-based design approach, structural spring models are commonly applied in engineering practice (DVS 3303; FKG 01/2021; Schuler et al. 2019; Descamps et al. 2020; Schuler et al. 2023).

In this modeling approach, the SG joint is discretized into structural spring elements. Figure 3.7a shows a schematic representation of an SG joint between the supporting structure and the glass pane, including spring directions and geometric definitions. In the calculation model, the SG joint is idealized by discrete spring elements, each representing a joint segment of length $\Delta$. Figure 3.7b illustrates the definition and orientation of these spring elements in a sectional view of an exemplary calculation model. Each segment is represented by springs acting in the normal and shear directions. The stiffness values of the springs are derived from effective joint moduli obtained experimentally or provided by the adhesive manufacturer.

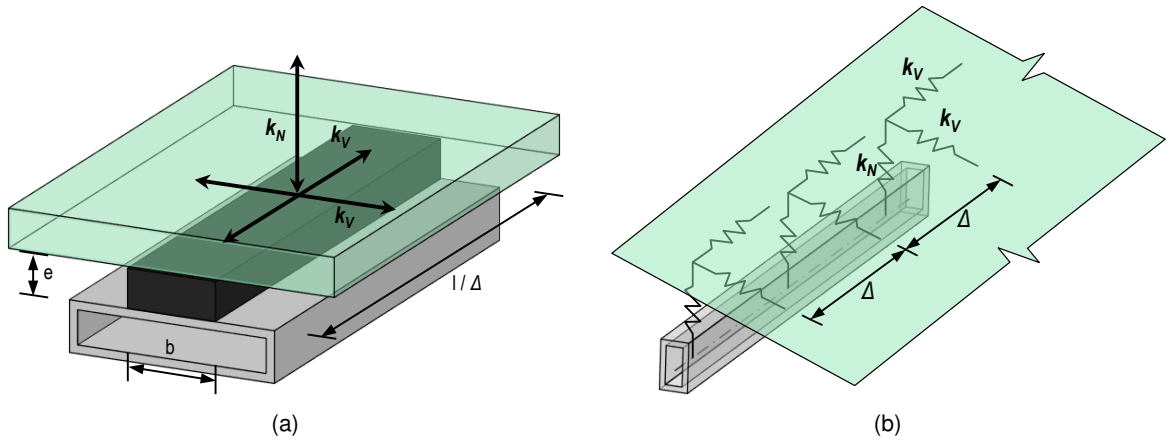


**Figure 3.7:** Idealization of an SG joint segment using structural spring elements: (a) schematic representation of an SG joint between the supporting structure and the glass pane, including spring element directions and geometric definitions; (b) spring elements and their orientations in a sectional view of a calculation model. Based on (FKG 01/2021).

Compared to full three-dimensional solid modeling of the adhesive layer, the spring-based approach significantly reduces computational effort. This is particularly relevant for large facade structures, where multiple geometric variants, joint configurations and load combinations according to (DIN EN 1990) must be considered. However, the limitations of this approach must be recognized. The simplified representation does not allow for the

evaluation of local stress states within the adhesive layer, and residual stresses or volumetric constraint effects cannot be resolved explicitly.

The decisive modeling parameter is the effective joint stiffness. According to (FKG 01/2021), stiffness values may be provided by the adhesive manufacturer if the joint geometry complies with the requirements of (ETAG 002-1). For joint geometries beyond these limits, project-specific stiffness values must be determined experimentally. Methods for the experimental determination of the effective tensile and shear joint stiffness are described in section 3.2.2. The corresponding stiffness parameters are subsequently implemented in the spring elements of the global structural model.

Using the design stresses $\sigma_{\text{des}}$ and $\tau_{\text{des}}$, the effective tensile joint modulus $E_{\text{joint}}$ and the effective shear joint modulus $G_{\text{joint}}$ are defined as:

$$E_{\text{joint}} = \frac{\sigma_{\text{des}}}{\epsilon_{\text{des}}} \tag{3.11}$$

$$G_{\text{joint}} = \frac{\tau_{\text{des}}}{\gamma_{\text{des}}} \tag{3.12}$$

Upon approval by the adhesive manufacturer, the method factor may be reduced to $\gamma_{\text{meth,FKG}} = 4$ (FKG 01/2021).

Based on these effective joint moduli, the spring stiffness values are obtained as:

$$k_{\text{N}} = \frac{E_{\text{joint}} \cdot A}{e} \tag{3.13}$$

$$k_{\text{V}} = \frac{G_{\text{joint}} \cdot A}{e} \tag{3.14}$$

where $A$ denotes the adhesive area of an SG joint assigned to the respective spring element and $e$ the thickness of the SG joint.

Representative material parameters for the widely used two-component SG adhesives DOWSIL 993 are summarized in Table 3.1. This adhesive was also used for manufacturing all specimens for the experimental investigations conducted within the scope of this thesis.

### 3.2.4 Extended Numerical Modeling Approaches

In addition to simplified analytical and spring-based modeling approaches, the mechanical behavior of SG joints can be investigated using three-dimensional finite element (FE) models. Such approaches become necessary when the geometric applicability limits of simplified models are exceeded or when a detailed assessment of local stress states and residual stresses within the adhesive layer is required (FKG 01/2021; Maniatis et al. 2015; Drass and Kraus 2020b).

**Table 3.1:** Material properties of DOWSIL 993.

| Property | Unit | Value | Source |
|---|---|---|---|
| $\sigma_{\mathrm{des},\gamma=6}$ | [MPa] | 0.14 | $\gamma = 6$ according to (ETA-01/0005) |
| $\sigma_{\mathrm{des},\gamma=4}$ | [MPa] | 0.21 | $\gamma = 4$ according to (FKG 01/2021), if approved by the manufacturer |
| $\sigma_{\mathrm{k,ETA}}$ | [MPa] | 0.84 | Derived from $\sigma_{\mathrm{des}}$ |
| $\tau_{\mathrm{des},\gamma=6}$ | [MPa] | 0.11 | $\gamma = 6$ according to (ETA-01/0005) |
| $\tau_{\mathrm{des},\gamma=4}$ | [MPa] | 0.165 | $\gamma = 4$ according to (FKG 01/2021), if approved by the manufacturer |
| $\tau_{\mathrm{k,ETA}}$ | [MPa] | 0.66 | Derived from $\tau_{\mathrm{des}}$ |
| $E_0$ | [MPa] | 1.4 | Tangent elastic modulus at the origin in tension (dogbone test) (ETA-01/0005) |
| $E_{\mathrm{Young}}$ | [MPa] | 1.95–2.3 | (Descamps and Hayez 2018) (Descamps et al. 2017) |
| $E_{\mathrm{joint}}$ | [MPa] | 4.1 | Effective joint modulus in thickness direction at the origin for $12 \times 12$ mm$^2$ SG joints (Descamps and Hayez 2018) |
| $G_0$ | [MPa] | 0.47 | Shear modulus tangent to the origin (ETA-01/0005) |
| $G_{\mathrm{joint}}$ | [MPa] | 0.67–0.7 | Effective joint modulus in transverse direction at the origin for $12 \times 12$ mm$^2$ SG joints (The Dow Chemical Company 2015; FKG 01/2021) |

Several studies have focused on the numerical representation of SG adhesives using advanced hyperelastic material models (Dias et al. 2014; Richter 2018; Drass 2020; Rosendahl 2020; Van Lancker et al. 2020; Schaaf and Feldmann 2023; Schaaf 2024). These investigations demonstrate that the nonlinear and nearly incompressible material behavior can be captured with high accuracy when appropriate advanced nonlinear material models and calibrated material parameters are employed.

In parallel, efforts have been undertaken to establish failure prediction criteria for bonded joints (Maniatis et al. 2015; Santarsiero 2015; Descamps et al. 2017; Staudt et al. 2018; Richter et al. 2021; Jordi Alcaine et al. 2024; Schaaf and Feldmann 2024). Furthermore, (Drass and Kraus 2020a; Kraus and Drass 2020a) propose a semi-probabilistic material safety concept based on experimental investigations under varying temperature conditions and artificial ageing. A Eurocode-compliant framework for the application of the FE method is presented in (Drass and Kraus 2020b).

A common characteristic of these extended numerical approaches is the necessity of developing and calibrating advanced nonlinear material models, often requiring extensive experimental input and significant computational effort. While such models provide detailed insight into local stress and failure mechanisms, their practical application within routine engineering design processes remains limited.

For this reason, the present work does not employ fully resolved three-dimensional FE models for design purposes but instead focuses on experimentally validated engineering-oriented modeling concepts. Nevertheless, the extended numerical approaches provide important background knowledge and serve as a reference framework for interpreting experimental findings.

## 3.3 Seismic Behavior of Glass and Facade Structures

### 3.3.1 Overview of Conventional Facade Systems

The seismic performance of facade systems has been investigated extensively over the past decades (Huang et al. 2017b; Momeni and Bedon 2024). In contrast to primary load-bearing structures, curtain wall facades are typically classified as non-structural components. Nevertheless, their behavior during seismic events is of significant importance due to potential hazards from glass breakage and fallout, as well as economic consequences related to repair and downtime (Behr 2009)

Seismic design provisions for non-structural components define the seismic demand on facade systems (EN 1998-1; ASCE/SEI 7-10). Under seismic excitation, these systems are governed by two principal demand mechanisms:

- Inertial forces resulting from the mass of the facade components
- Imposed interstory drift due to deformation of the primary structure

While inertial effects may govern local anchorage forces, interstory drift generally represents the critical action for glazing systems. The story drift $\delta_{\mathrm{R}}$ is defined according to (ASCE/SEI 7-10), and the corresponding interstory drift ratio (IDR) is given by:

$$\mathrm{IDR} = \frac{\delta_{\mathrm{R}}}{H} \tag{3.15}$$

The deformation capacity of conventional glazed systems is strongly influenced by geometric clearance, boundary conditions, and connection detailing. Early analytical approaches demonstrated that the in-plane drift capacity of glass panes in framed systems primarily depends on geometric parameters and frame clearance (Bouwkamp and Meehan 1960; Bouwkamp 1961). After contact between glass and frame, additional deformation may be accommodated through out-of-plane distortion mechanisms (Sucuoğlu and Vallabhan 1997).

Subsequent experimental investigations using full-scale mock-ups confirmed that curtain wall systems generally exhibit higher drift capacities than initially assumed (King and Lim 1991; King and Thurston 1992; Thurston and King 1992; Thurston and King 1993). Progressive damage evolution and post-breakage behavior of curtain wall systems were extensively investigated (Pantelides and Behr 1994; Behr et al. 1995; Behr 1998; Behr 2009).

These studies introduced dynamic racking protocols that later formed the basis of the so-called crescendo test (Behr and Belarbi 1996).

Full-scale racking tests on dry-glazed and curtain wall systems provided the experimental basis for the development of analytical and FE models aimed at describing deformation and failure mechanisms under seismic loading (Memari et al. 2003; Memari and Shirazi 2004; Memari et al. 2006b; Memari et al. 2006a; Memari et al. 2007; Broker et al. 2012; Memari et al. 2012a; Simmons and Memari 2013a; O'Brien et al. 2015; Caterino et al. 2017; Aiello et al. 2018a; Aiello et al. 2018b; Aiello et al. 2019). These models typically incorporate geometric nonlinearity, contact effects, and nonlinear link elements to reproduce system-level drift behavior observed in experiments.

Beyond conventional dry-glazed systems, more recent research has emphasized the importance of connection detailing and load redistribution mechanisms. Analytical and numerical studies demonstrated that appropriately designed mechanical connections, particularly steel components in seismic applications, can enhance deformation accommodation and introduce ductility through controlled plastic deformation, thereby delaying glass failure (Bedon and Amadio 2017; Bedon et al. 2019; Santarsiero et al. 2019; Oppe and Grün 2020; Oppe et al. 2021). The in-plane drift capacity of point-fixed facade systems was investigated in (Sivanerupan 2011; Sivanerupan et al. 2014). Additional studies examined the response of point-fixed canopies, railings, and facade elements to in-plane induced vibrations (Siebert and Haese 2009).

Overall, the seismic response of facade systems is governed by the interaction between glass stiffness, connection flexibility, boundary conditions, and imposed interstory drift. Experimental and numerical investigations have primarily focused on glass cracking, fallout resistance, and global drift capacity, forming the basis for current evaluation and testing procedures.

### 3.3.2 Experimental Studies on SG-Facade Systems

Experimental investigations on SG facade systems have primarily focused on their global drift capacity and the corresponding failure mechanisms under in-plane racking deformation. Early full-scale mock-up tests examined two- and four-sided SG configurations and provided first insights into deformation accommodation and load redistribution mechanisms within bonded facade assemblies (King and Lim 1991; King and Thurston 1992; Thurston and King 1992).

Subsequent studies investigated modified sub-frame concepts and connection details to improve drift accommodation, demonstrating that SG systems can sustain substantial interstory drift ratios without immediate glass fracture or adhesive failure (Zarghamee et al. 1996; Behr 1998). More comprehensive experimental programs addressed both serviceability and ultimate limit states for unitized and stick-built SG curtain walls (Memari et al. 2006b; Galli 2011; Broker et al. 2012; Memari et al. 2012a; Bianchi et al. 2022).

A consistent finding across these investigations is the enhanced drift capacity of SG systems compared to dry-glazed constructions. This applies both to the onset of glass cracking and to glass fallout resistance. Figure 3.8 summarizes comparative results reported in (Simmons 2011), indicating a significantly increased observed interstory drift for two-sided and four-sided SG facades relative to dry-glazed systems.

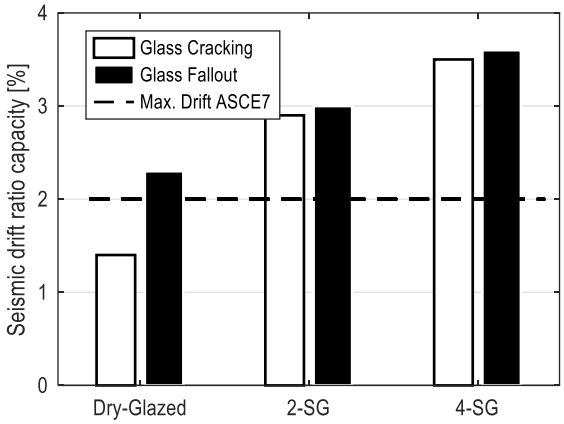


**Figure 3.8:** Glass cracking and glass fallout for different types of facades. Based on (Simmons 2011).

In addition to global drift capacity, boundary conditions and facade typology were identified as decisive parameters influencing the load transfer to the structural sealant (Broker et al. 2012). Experimental measurements, including video-based displacement tracking, enabled correlation between imposed story drift and local sealant deformation (Simmons and Memari 2013b; Nardini and Doebbel 2015; Nardini and Doebbel 2020)

Recent large-scale experimental programs have addressed the serviceability and ultimate seismic performance of unitized curtain walls, including investigations of facade detailing, damage mechanisms, and numerical model calibration (Bianchi et al. 2021; Bianchi et al. 2022; Nuñez Enriquez 2022; Hayez et al. 2023). Full-scale tests under quasi-static and dynamic loading enabled the evaluation of different facade configurations and highlighted the influence of key design parameters, such as joint geometry, frame detailing, and support conditions (Bianchi et al. 2022; Bianchi et al. 2024b; Bianchi et al. 2025). Recent studies further identified damage states and failure sequences in SG facades and derived fragility relationships, thereby linking global drift demand to local damage and post-earthquake functionality (Hayez et al. 2023; Bianchi et al. 2024a).

Overall, experimental research on SG facades has concentrated on system-level performance indicators such as drift capacity, glass cracking, and fallout resistance. The SG adhesive is primarily evaluated with respect to deformation accommodation within the facade assembly rather than as a cyclically degrading material.

### 3.3.3 Analytical and Numerical Studies on SG-Facade Systems

Analytical and numerical approaches have been developed to predict deformation and failure mechanisms in SG facade systems under seismic loading. For conventional curtain walls, early analytical models described glass failure primarily as a function of geometric clearance and boundary conditions (Bouwkamp and Meehan 1960; Sucuoğlu and Vallabhan 1997). These concepts were later extended to different facade configurations (Memari and Shirazi 2004; Memari 2013; O'Brien et al. 2015)

For two-sided SG systems, mathematical formulations were proposed to estimate sealant deformation under imposed drift (Memari et al. 2006a; Memari et al. 2012a). FE models of full-scale mock-ups were subsequently developed, typically representing the SG joint by plate elements with linear elastic material behavior (Broker et al. 2012; Memari et al. 2012b). These models allow reproduction of global deformation patterns and estimation of sealant stresses. However, nonlinear and load-step dependent effects are only captured in a simplified manner.

Material-oriented investigations examined bonded glass panes subjected to in-plane shear, focusing on stiffness characteristics and load–displacement behavior of different adhesive systems (Huveners et al. 2007; Huveners et al. 2008; Huveners et al. 2009). Based on these findings, numerical studies evaluated the influence of joint stiffness and thickness on global facade displacement capacity (Lago and Sullivan 2011). The results indicate a pronounced sensitivity of system behavior to joint properties.

Design-oriented approaches were proposed to support seismic verification of SG systems. (Khoraskani 2015) introduced a concept for glass panes under shear loading, primarily addressing plate buckling failure. (Nardini and Doebbel 2015; Nardini and Doebbel 2016; Nardini and Doebbel 2020) formulated a performance-based design concept for SG joints aligned with the performance levels defined in (JASS 14). For each level, allowable stress and strain limits for SG adhesive were specified. However, the underlying experimental data were obtained from Hockman cycle tests (ASTM C719), which involve significantly longer load durations and have been identified as not representative of seismic loading conditions (Zarghamee et al. 1996).

Existing analytical and numerical models therefore provide tools for estimating drift-induced stresses and deformations at system level. The SG joint is typically represented by simplified, predominantly linear material descriptions, and verification is performed using limit values associated with predefined performance levels. However, the experimental basis for these limits is generally not representative of seismic loading conditions, leaving a gap for seismically consistent design approaches.

### 3.3.4 Existing Seismic Design Concepts

Seismic verification of glass and facade systems is currently governed by national and international design standards. These provisions translate seismic actions into equivalent static forces, interstory drift limits, and allowable stress or strain criteria. A comparative overview of selected standards is given in Table 3.2.

**Table 3.2:** Comparison of the most important regulations for glass and facade structures under seismic loads in international standards. Based on (Müller et al. 2024).

| Country / Region | Applicable standards | Requirements | | Note |
|---|---|---|---|---|
| | | Force | Drift capacity | |
| Europe | (EN 1998-1) | X | (X) | No specific seismic displacement for non-structural parts |
| Italy | (CNR-DT 210) | X | (X) | No specific seismic displacement for non-structural parts |
| America | (ASCE/SEI 7-10) (FEMA 450) (AAMA 501.6) | X | X | Detailed calculation method for determining the seismic force and specific requirement for seismic displacement |
| Japan | (JASS 14) | X | X | Performance levels for drift performance |
| New Zealand | (NZS 1170.5) | X | (X) | Calculations based on performance levels with no specific displacement for non-structural parts |

For glass facades, the behavior factor is typically taken as $q = 1$ (Bedon et al. 2019). As a result, seismic actions are not reduced through ductility considerations, and verification is generally performed at essentially elastic demand levels.

Several standards introduce performance-based concepts to differentiate between serviceability, damage limitation, and life-safety requirements. (EN 1998-1) defines ultimate and damage limitation states, while (FEMA 356) specifies multiple performance levels for structural and non-structural components. A facade-specific framework is provided in (JASS 14), where distinct performance levels are associated with maximum allowable interstory drift values.

## 3.4 Fatigue and Cyclic Loading of SG joints

In contrast to the large-scale facade investigations discussed in section 3.3, this chapter focuses on small-scale tests of SG joints in order to characterize the material-level behavior of SG joints under and following cyclic loading. Studies on fatigue behavior in the context of SG joints are limited, as fatigue investigations in structural engineering have predominantly

focused on structural adhesive systems with higher strength and stiffness, which are not representative for SG adhesives.

### 3.4.1 High-Cycle Fatigue of SG Adhesives

Normative design documents, such as (ETAG 002-1), do not specify material parameters for SG joints under cyclic loading. (Carbary et al. 2007) investigated cyclic shear caused by daily thermal movements using 36 500 displacement-controlled cycles for two-part silicone adhesives. Partial degradation was observed, dependent on adhesive stiffness. Nevertheless, the number of cycles exceeds the typical seismic requirements, thereby precluding a direct transfer to this field of application without further investigation.

Further investigations of cyclic loading effects were carried out by (Tanaka and Koike 1995; Miyauchi and Tanaka 2000; Sugiyama 2000; Tanaka and Miyauchi 2000). Failures were observed within a few thousand cycles at 50 % strain or after up to 100 000 cycles at lower amplitudes, demonstrating amplitude-dependent degradation. (Dilger et al. 2022) performed cyclic Mullins tests on H-specimens according to (ETAG 002-1), focusing on the influence of mixing quality rather than fatigue behavior.

A general overview of factors influencing fatigue strength in high-strength adhesive systems for the construction sector is provided by (Ciupack et al. 2018). The study includes tensile and component-level tests using two-part polyurethane and acrylate adhesives. Such adhesive systems differ substantially from SG adhesives in stiffness and strength and are therefore not representative of SG applications. Additional studies on high-strength structural adhesives report similar findings (Hennemann et al. 2012; Baumgartner et al. 2016; Mayer et al. 2017; Schuler et al. 2022).

Overall, only limited data are available for SG adhesives under high-cycle fatigue. Existing studies either concern different adhesive systems or employ loading conditions unrelated to seismic scenarios. No systematic methodology for assessing fatigue resistance of SG adhesives under high-cycle loading has yet been established.

### 3.4.2 Low-Cycle Fatigue of SG Joints

First detailed investigations on SG joints were presented by (Zarghamee et al. 1996; Broker et al. 2012; Memari et al. 2012b). These studies applied cyclic preloading with multiple load cycles to simulate earthquake-induced movements, followed by destructive quasi-static tests to evaluate the resulting effects. (Nardini and Doebbel 2016; Nardini and Doebbel 2020) investigated the effect of repeated tensile loading on SG adhesives using cyclic extension tests at defined strain levels based on the Hockman test (ASTM C719). A distinct reduction in final strength was reported for specimens subjected to repeated loading at 25 % strain.

These investigations were conducted under tensile loading, while data on the LCF behavior of SG joints under shear-dominated loading, which governs in facade applications, are not available in the literature.

Several studies have also confirmed the characteristic Mullins effect (Mullins 1948) in SG adhesives, visible as a change in the load path after cyclic deformation (Palmieri et al. 2009; Schaaf et al. 2021). This behavior reflects internal microstructural rearrangements and stress softening but is not necessarily associated with strength loss.

### 3.4.3 Definition and Comparison of Low-Cycle Fatigue Load Patterns

For the evaluation of facade systems under seismic drift, the crescendo test has been established as the standard procedure (Behr and Belarbi 1996; AAMA 501.6). This test simulates interstory drift by applying gradually increasing cyclic displacements to full-scale facade elements, typically over a duration of several minutes. The resulting drift time history is shown in Figure 3.9. The procedure is well suited for component-level performance assessment but does not provide material-specific information on the adhesive behavior within the SG joint.

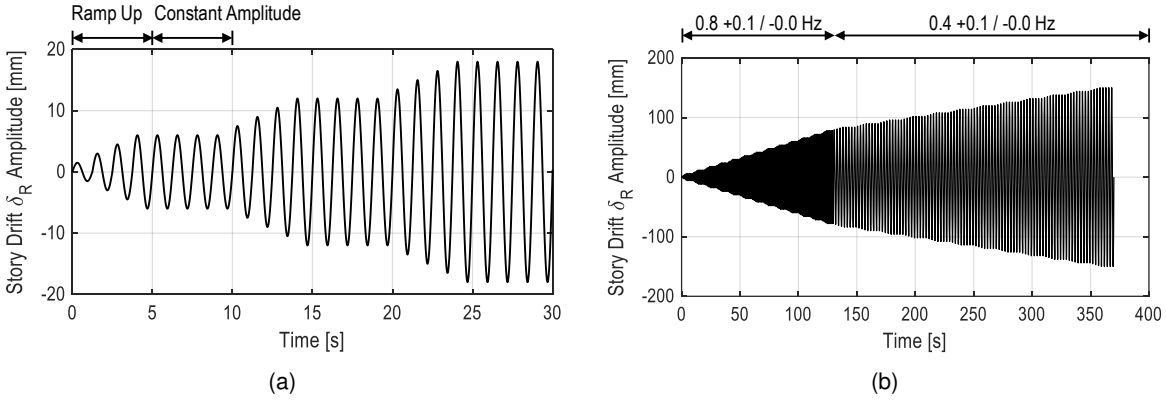


**Figure 3.9:** Drift time history of the crescendo-test: (a) first 30 seconds; (b) entire test. Based on (Behr and Belarbi 1996; AAMA 501.6).

To compare the different fatigue load protocols used in small-scale investigations on SG joints, four characteristic cycles can be distinguished and are summarized in Table 3.3. The main parameters defining these load patterns are the number of cycles, the maximum fatigue stress $\sigma_{\mathrm{Fat}}$ or strain level $\varepsilon_{\mathrm{Fat}}$, and the type of load control. The load histories of all four laboratory cycles are compared in Figure 3.10. In all cases, the cyclic loading was applied as a preconditioning sequence with multiple load cycles, followed by destructive quasi-static testing to evaluate its influence.

In (Zarghamee et al. 1996), medium- and high-modulus silicones were subjected to cyclic tensile loading between 0.069 MPa and 0.138 MPa for 50 cycles (Cycle A). (Broker et al. 2012; Memari et al. 2012b) applied a cyclic stress level of 0.345 MPa for four cycles to one- and two-component SG adhesives (Cycle B). (Nardini and Doebbel 2016; Nardini and

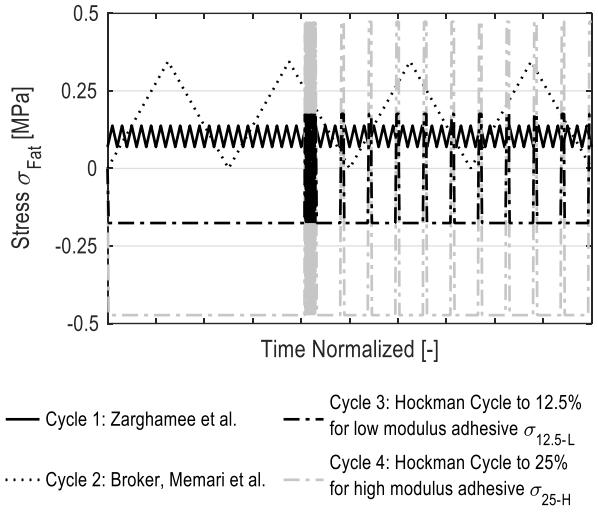


**Figure 3.10:** Comparison of fatigue load patterns (Cycles A–D) applied in small-scale SG joint tests.

**Table 3.3:** Comparison of the different fatigue cycles from literature.

| Source | Fatigue pattern | Cycle control | No. of cycles [-] | Load direction | Max stress $\sigma_{\text{Fat}}$ [MPa] | Max strain $\varepsilon_{\text{Fat}}$ [%] |
|---|---|---|---|---|---|---|
| (Zarghamee et al. 1996) | Cycle A | Stress | 50 | Tensile | **0.138** | - |
| (Broker et al. 2012; Memari et al. 2012b) | Cycle B | Stress | 4 | Tensile | **0.345** | - |
| (Nardini and Doebbel 2016) (Nardini and Doebbel 2020) | Cycle C | Strain | 20 | Tensile | (0.176–0.32) | **12.5** |
| | Cycle D | Strain | 20 | Tensile | (0.258–0.473) | **25.0** |

Doebbel 2020) conducted strain-controlled tests using the Hockman cycle (ASTM C719) with strain amplitudes of 12.5 % (Cycle C) and 25 % (Cycle D).

The maximum load in Cycles A and B was defined by stress control ($\sigma_{Fat}$), whereas in Cycles C and D the deformation was controlled through strain ($\varepsilon_{Fat}$). To enable comparison, the strain-controlled amplitudes were converted into equivalent stress levels using mean stress–strain data from (Nardini and Doebbel 2016; Nardini and Doebbel 2020). The resulting stress range extends from 0.176 MPa (at 12.5 % strain) to 0.473 MPa (at 25 % strain), depending on adhesive stiffness, and is shown in Table 3.3.

The Hockman cycles (Cycles C and D) are strain-controlled and characterized by extremely long test durations of about 400 hours at very low cyclic frequency. These conditions represent long-term thermal-movement fatigue rather than the short-duration, irregular loading typical of seismic excitation (Zarghamee et al. 1996).

Cycle D exhibits the highest load amplitudes and longest duration, implying the strongest material impact. Cycle B also shows elevated stress levels but only a few cycles, while

Cycle A involves lower stresses and a higher number of repetitions. Compared with actual seismic ground-motion records, discussed in section 2.4.4 and exemplarily shown in Figure 2.24, none of these small-scale fatigue protocols replicate the irregular, short, and random characteristics of seismic excitation. A detailed analysis of real ground motion records is provided in chapter 8.

All small-scale fatigue tests reported in literature were performed under tensile loading. However, in facade applications the SG joint primarily experiences shear deformation during interstory drift. Overall, the existing load patterns illustrate the large variation in experimental procedures used to evaluate SG joints. Differences in control type, number of cycles, and amplitude selection hinder direct comparison and prevent the derivation of design-relevant fatigue parameters.

### 3.4.4 Influence of Low-Cycle Fatigue on Failure Strength

To evaluate the influence of cyclic pre-loading on the failure strength of SG joints, results from the available literature were qualitatively compared. All studies were performed on tensile specimens and no data for shear loading were reported. To evaluate the influence of the various fatigue cycles, the normalized ultimate tensile strength deviation $\sigma_{\mathrm{Cycl,Norm}}$ was calculated from the reference ultimate strength $\sigma_{\mathrm{Ult}}$ and the ultimate strength following cyclic loading $\sigma_{\mathrm{Cycl}}$. The corresponding material parameters, test conditions, and normalized strength deviations are summarized in appendix A (Table A.1). The graphical evaluation of the normalized tensile strength deviations $\sigma_{\mathrm{Cycl,Norm}}$ is provided in Figure A.1 and Figure A.2.

The existing results reveal no consistent trend regarding the residual tensile strength after cyclic loading. In some cases, a slight increase in ultimate strength was observed for one-part silicones subjected to limited cyclic loading. In contrast, other investigations reported a reduction in ultimate stress, particularly for two-part silicones exposed to higher strain amplitudes. The reported deviations in normalized strength range from minor changes to reductions of up to approximately 40 %.

The observed scatter may be related to differences in curing and storage conditions rather than to fatigue degradation itself. Previous studies showed that curing history and specimen age can significantly influence the load-bearing capacity of SG adhesives, which may partly explain the inconsistent trends reported in literature (Müller et al. 2023a).

When comparing the results based on the applied load control, strain-controlled tests generally resulted in larger reductions of residual strength than stress-controlled tests. However, this tendency cannot be clearly separated from the influence of higher load levels and longer cycle durations characteristic of the strain-controlled protocols.

Overall, the available data indicate that cyclic loading can modify the mechanical response and residual strength of SG joints. However, due to the limited number of studies, differing

load histories, and exclusive use of tensile specimens, a quantitative assessment of fatigue-induced strength degradation is not possible. Furthermore, the absence of a standardized test method prevents a consistent evaluation of fatigue resistance under low-cycle loading.

## 3.5 Summary and Identified Research Gaps

The preceding sections demonstrate that the structural design of SG joints is primarily based on quasi-static strength and stiffness parameters. Current design concepts rely on characteristic stresses, global safety factors, and simplified linear-elastic stiffness representations derived from quasi-static tests. Cyclic degradation effects, fatigue phenomena, and frequency-dependent behavior are not explicitly incorporated into existing verification approaches.

Seismic assessment of glass and facade systems is performed predominantly at the system level. Verification procedures are based on interstory drift limits or allowable stress and strain criteria associated with predefined performance levels. The SG joint is typically represented by simplified material models, and the cyclic characteristics of seismic loading have not been systematically investigated at the material level and are therefore not addressed.

The available experimental investigations on cyclic loading of SG joints at small scale remain limited. Reported fatigue studies differ substantially in load protocol, control mode, amplitude definition, and number of cycles. Most investigations were conducted under tensile loading, although interstory drift in facade applications primarily induces shear deformation in the SG joint. Furthermore, the applied laboratory load histories do not reproduce the short-duration, irregular characteristics of seismic excitation. A consistent methodology for characterizing the residual strength and deformation behavior under seismically relevant cyclic loading conditions is not available.

Taken together, the current state of research reveals no consistent link between static design concepts, system-level seismic verification, and material-level cyclic behavior of SG joints. In particular, a systematic experimental characterization of SG joints under short-term, shear-dominated cyclic loading representative of seismic actions is missing. Consequently, no engineering-oriented design methodology for seismic loading has been established. The present work addresses these gaps by providing a systematic experimental characterization of SG joints under shear-dominated LCF loading and by developing an engineering-oriented design concept for seismic applications, with explicit characterization of seismic actions from real ground motion records.

# 4 Stress Assessment

## 4.1 General

The mechanical response of cyclically loaded SG joints is governed by multiple interacting parameters. Owing to the viscoelastic nature of SG adhesives, the load-bearing behavior depends not only on stress amplitude, but also on frequency, load history, and cycle number. Under seismic excitation, the loading is characterized by short-duration, irregular cycles with limited repetitions and comparatively high deformation amplitudes.

This chapter identifies and defines the stress parameters relevant for SG joints under seismic loading and derives representative boundary conditions for the subsequent experimental investigations. Parts of the analysis presented in this chapter are based on results obtained within the research project (Müller et al. 2026b) and build on work previously published in (Müller et al. 2024).

## 4.2 Structural System and Type of Load Application

SG has evolved from conventional facade applications to increasingly complex glass structures. Figure 4.1 illustrates two relevant structural concepts subjected to schematic seismic loading:

- a classical SG facade construction and
- a modern bonded all-glass construction.

In both systems, the adhesive connection is typically designed as a linear joint. However, the structural role of the bonded joint differs fundamentally.

In SG facade constructions, shown in Figure 4.1a, the glazing represents a secondary structural component. During an earthquake, the primary load-bearing structure is excited by ground motion. The resulting interstory drift induces relative displacements between floors, which are imposed onto the facade system. The bonded joint is therefore loaded predominantly by forced deformations. The load application is deformation-driven and can be simulated using displacement-controlled boundary conditions in cyclic tests.

In contrast, in bonded all-glass constructions, shown in Figure 4.1b, the glazing system itself forms part of the primary load-bearing structure. Under seismic excitation, the glass

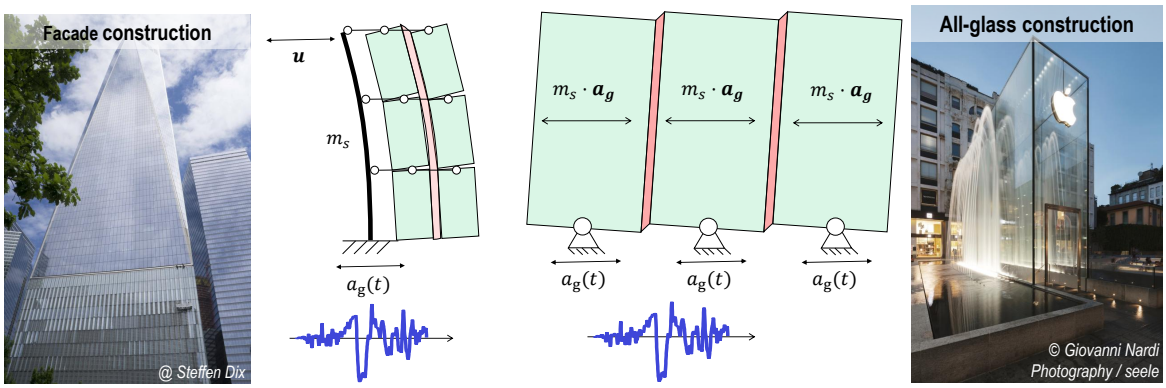


**Figure 4.1:** Relevant glass and facade structures under schematic seismic loading: (a) SG facade construction (secondary structure – displacement-controlled loading); (b) bonded all-glass construction (primary structure – force-controlled loading).

elements and the bonded joints are directly subjected to inertial effects associated with structural acceleration. In this case, the SG joint experiences load application that is primarily force-driven, which can be represented by force-controlled boundary conditions in cyclic tests.

To reflect these fundamentally different load application mechanisms, the subsequent experimental investigations distinguish between displacement-controlled loading for the secondary-structure behavior of SG facade constructions and force-controlled loading for the primary-structure behavior of bonded all-glass constructions.

## 4.3 Seismic Load Characteristics

### 4.3.1 Numerical Estimation of Stresses in SG Joints

To characterize the stress state in SG joints under seismic excitation, a numerical analysis previously published in (Müller et al. 2024) is summarized in the following. The aim is to estimate the order of magnitude, load direction, and temporal characteristics of stresses acting in SG joints during a seismic event.

A reinforced concrete frame structure was modeled in RFEM 5 as a beam–column system using rod elements (regular grid: 4 m; storey height: 3 m). The dead load of the structure was considered as mass in the dynamic analysis by applying a surface load of 4.0 kN/m$^2$ floor-by-floor. The resulting fundamental period was 1.057 s. This value lies within a realistic range for multi-storey buildings (Chopra 2012) and within the frequency range considered in the experimental investigations, as discussed in section 4.4.

For load assessment, a representative glazing unit with dimensions of 2.0 m (width) × 3.0 m (height) was introduced into one facade field. The SG joint was modeled in accordance with

the structural spring method from section 3.2.3.2 using line elements acting as structural springs between the glazing and the mullion (spacing: 100 mm; cross section: $12 \times 100$ mm$^2$; length: 12 mm), representing a nominal SG joint geometry of $12 \times 12$ mm$^2$. Linear elastic material behavior was assumed based on Table 3.1 ($E_{\text{joint}} = 4$ MPa; $G_{\text{joint}} = 0.67$ MPa). Stresses in the adhesive were evaluated at the center of the line element. An overview of the calculation model is shown in Figure 4.2a.

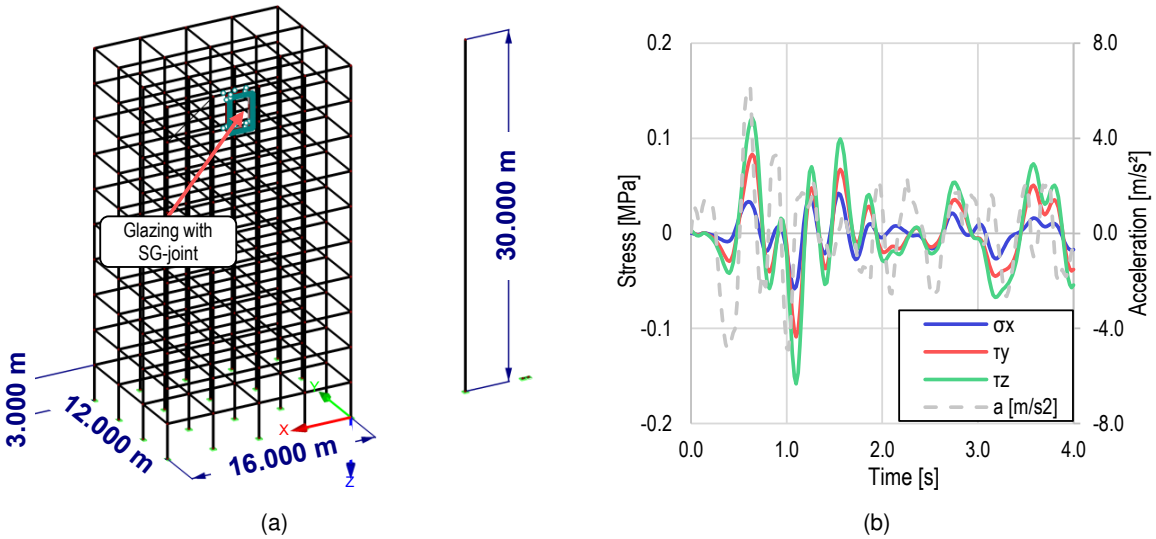


**Figure 4.2:** Numerical estimation of seismic stresses in SG joints: (a) finite element model of the bonded facade system; (b) excerpt of the stress time history in the SG joint and corresponding ground acceleration record ((Müller et al. 2024)).

The dynamic excitation was applied to the foundation of the complete structure using the recorded accelerogram of the 1989 Loma Prieta earthquake ("Corralitos—Eureka Canyon Road" station), as implemented in the software. The time history was evaluated for the SG joint located in the glazing corner region, which was identified as the most highly stressed location based on a preceding response spectrum envelope analysis.

### 4.3.2 Resulting Stress Characteristics

Figure 4.2b shows the time history of the stresses in the SG joint together with the applied ground acceleration. The response consists of a limited number of irregularly distributed load cycles acting in alternating directions, reflecting the short-duration and non-periodic nature of seismic excitation.

In the investigated example, the absolute maximum shear stress reached approximately 0.15 MPa, whereas the corresponding tensile stresses were significantly lower. The peak shear stresses exceeded the peak tensile stress by approximately 87 % in the y-direction and by more than 170 % in the z-direction.

Although the absolute stress level depends on the assumed joint properties and structural configuration, the relative magnitude of the stress components clearly indicates that, under

the investigated conditions, seismic loading induces predominantly shear loading parallel to the joint axis.

The identified stress history is characterized by comparatively high stress amplitudes combined with a limited number of irregular cycles. To enable an experimental investigation of such loading, methodological approaches from fatigue analysis in steel construction are adopted (Haibach 2006; Radaj and Vormwald 2007; Götz and Eulitz 2022). In these approaches, the structural behavior under random real loading is characterized by constant-amplitude fatigue tests at various defined stress levels (single-stage tests).

Accordingly, the subsequent investigations focus on shear-dominated cyclic loading at defined stress amplitudes. The seismic loading is characterized by comparatively high stress amplitudes combined with a limited number of cycles, which corresponds to the domain of LCF. This framework allows a systematic characterization of the load-bearing and failure behavior of SG joints under seismically induced cyclic action.

## 4.4 Relevant Test Frequency Range

The loading frequency acting on SG joints during seismic excitation is governed by the dynamic response of the supporting structure. In a first approximation, the relevant frequency range of the SG joint corresponds to the fundamental vibration frequency of the building.

Typical natural periods of representative building structures reported in (Chopra 2012) range between approximately 0.3 s and 3 s for multi-storey reinforced-concrete and steel buildings. This corresponds to a frequency range of roughly 0.3 Hz to 3.3 Hz. Structures with significantly longer periods, such as long-span bridges or special structures such as chimneys, exhibit substantially lower frequencies and are not representative for typical facade applications. Excluding such exceptional structures, the relevant frequency range for conventional glass and facade constructions can therefore be approximated as 0.3 Hz to 3.3 Hz.

For the experimental investigations in this work, a test frequency range of 0.5 Hz to 5 Hz was selected, which covers the predominant frequency domain of typical multistory buildings. This frequency range therefore includes a large section of the period domain in which the highest acceleration demands typically occur in seismic response spectra, as discussed in section 2.4.6.1. The section with frequencies above 5.0 Hz was not tested, as this exceeds the maximum test frequency achievable with the testing machine used in this work under the applied loading conditions. Furthermore, according to (Müller et al. 2025c), increased test frequencies lead to increased LCF performance, indicating that this range is less damage-relevant from a structural safety perspective.

This frequency dependence is investigated in detail within the present work in section 7.6.2. A comprehensive evaluation of response spectra and the associated seismic peak loading as a function of the natural period $T$ of the structures is presented later in section 8.3.3.

## 4.5 Relevant Joint Geometries

The mechanical characterization of SG joints within the European approval framework is based on the H-specimen defined in (ETAG 002-1) with a nominal joint cross-section of $12 \times 12$ mm$^2$ and a bonded length of 50 mm, shown on the left in Figure 4.3.

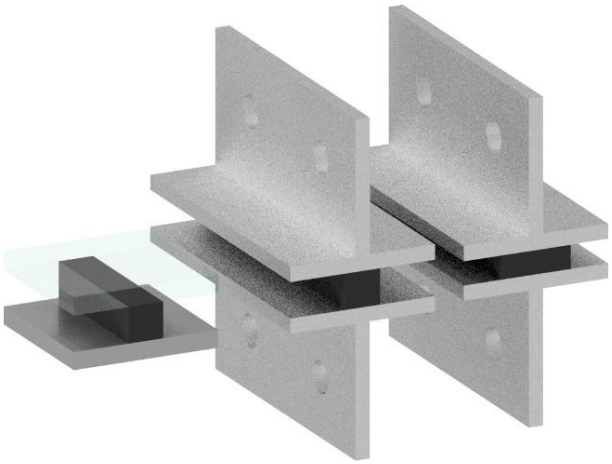

**Figure 4.3:** Standard H-specimen according to (ETAG 002-1) and modified H-specimens with $12 \times 12$ mm$^2$ and $8 \times 24$ mm$^2$ joint geometries (from left to right).

To investigate geometric influences beyond this reference configuration, a modified H-specimen was introduced in (Schuler et al. 2017; Bues et al. 2019; Bues 2021). In this modification, alternative joint geometries were systematically examined. In addition, the bonded length was increased to 100 mm in order to better represent the load-bearing behavior of a continuous joint segment and thus more realistically reproduce the joint-like structural function.

Following this approach, two joint geometries are considered in the present work: the reference geometry of $12 \times 12$ mm$^2$ and a compact geometry of $8 \times 24$ mm$^2$. Figure 4.3 illustrates the modified H-specimens with joint geometries of $12 \times 12$ mm$^2$ (center) and $8 \times 24$ mm$^2$ (right).

The compact $8 \times 24$ mm$^2$ joint geometry corresponds to the limiting ratio of joint width to joint thickness $b/e \leq 3$, ensuring that the findings of this work can be applied to the design methods according to (ETAG 002-1) and the spring model according to (FKG 01/2021). The investigated joint geometries are summarized in Table 4.1.

For the $8 \times 24$ mm$^2$ configuration, the joint width $b = 24$ mm slightly exceeds the limit of 20 mm specified in (ETAG 002-1). However, the governing geometric ratio $b/e \leq 3$ is satisfied, and the selected geometry therefore remains within the mechanically consistent application range of the established design concepts.

**Table 4.1:** Joint geometries of the investigated modified H-specimens.

| Geometry [mm$^2$] | Thickness $e$ [mm] | Width $b$ [mm] | Length $l$ [mm] |
|---|---|---|---|
| 12 x 12 | 12 | 12 | 100 |
| 8 x 24 | 8 | 24 | 100 |

## 4.6 Mean Stress Effect

The stress ratio $R$ is an influencing parameter in the analysis of polymers under cyclic loading, as it governs the interaction between maximum and minimum stress within each load cycle and thereby influences damage accumulation mechanisms.

An evaluation of 153 normalized ground motion records was performed in (Müller et al. 2024) using rainflow counting to determine the mean values of the individual stress cycles. The resulting distribution exhibits a pronounced peak at a mean value of zero, indicating that seismic loading is predominantly characterized by fully reversed loading cycles.

Accordingly, a stress ratio of $R = -1$ is considered representative for seismic excitation. To assess the relevance of the mean stress ratio for SG joints under cyclic loading, preliminary investigations were conducted and published in (Müller et al. 2025c). In these studies, both fully reversed loading ($R = -1$) and pulsating loading ($R = 0$) were examined under LCF conditions. The results showed a higher load-bearing capacity under pulsating loading compared to fully reversed loading, indicating that $R = -1$ represents the more critical loading condition.

Based on the seismic load evaluation and the findings of these preliminary investigations, the experimental program of the present work focuses on cyclic loading with a stress ratio of $R = -1$. Additional tests with $R = 0$ are not considered in the main experimental campaign.

## 4.7 Summary

The parameters influencing the cyclic load-bearing behavior of SG joints were identified and systematically evaluated. This identification is based on the combined assessment of the current state of research, engineering analysis, and preliminary investigations presented in (Müller et al. 2024; Müller et al. 2025c; Müller et al. 2026b), allowing the relevant variables to be reduced to those governing the structural response of SG joints under seismic loading.

Two fundamental types of load application were defined to represent the structural boundary conditions: displacement-controlled loading for SG facade constructions and force-controlled loading for bonded all-glass constructions. A numerical analysis further shows that seismic loading induces predominantly shear stresses in the joint, which were therefore selected as the governing loading direction for the experimental investigations.

The relevant frequency range was defined as 0.5 Hz to 5 Hz, reflecting the dynamic response of typical building structures under seismic excitation. With respect to joint geometry, the standard configuration of $12 \times 12$ mm$^2$ was complemented by a compact $8 \times 24$ mm$^2$ geometry to extend the application range toward the limits of current design provisions. The stress ratio was identified as $R = -1$, representing fully reversed loading as the critical case under seismic conditions.

Temperature effects and artificial aging are recognized as potential influencing parameters for SG adhesives but fall outside the scope of the present work. The experimental investigations are conducted under controlled laboratory conditions without additional environmental conditioning.

These parameters define the basis for the experimental matrix of the cyclic investigations, which is presented in chapter 7.

# 5 Specimen Manufacturing

## 5.1 Objective and Approach

Based on the literature review and the identified research gaps, and the boundary conditions derived in chapter 4, the present work aims to investigate the load-bearing and failure behavior of SG joints under LCF loading to simulate seismic loading. A reliable interpretation of cyclic test results requires stable and reproducible reference properties under quasi-static loading conditions.

However, the mechanical properties of SG joints are not solely governed by the material formulation. The manufacturing process, curing conditions, specimen age, and production-related influences may significantly affect strength and stiffness characteristics. Variations in these parameters may lead to systematic deviations in experimental results and therefore interfere with the evaluation of cyclic loading effects.

The objective of this chapter is therefore to define a consistent and experimentally validated manufacturing procedure for modified H-specimens. First, the specimen concept and bonding procedure are described. Subsequently, the influence of manufacturing and curing is summarized, and a standardized conditioning regime for all subsequent investigations is established.

## 5.2 Specimen Design and Manufacturing

### 5.2.1 Specimen Concept and Material Selection

The experimental investigations were carried out on modified H-specimens based on the geometry defined in (ETAG 002-1), as introduced in section 4.5. In addition to the standard joint geometry of $12 \times 12$ mm$^2$, a compact geometry of $8 \times 24$ mm$^2$ was investigated. To better represent the linear character of the SG joints, both geometries were manufactured with a bonded length of 100 mm and are summarized in Table 4.1.

Two T-profiles (T $50 \times 50 \times 5$ mm$^3$) were used as substrates to ensure a stiff load path between the testing machine and the adhesive joint. As substrate material, extruded aluminum EN AW 6060 T66 was selected to allow economical and reproducible specimen production while providing sufficient stiffness. The aluminum surfaces were cleaned with isopropanol and

treated with the manufacturer-recommended DOWSIL 1200 OS Primer prior to bonding. No additional mechanical surface treatment (e.g. abrasion) was applied.

Preliminary investigations showed no relevant influence of mechanical surface preparation on the load-bearing behavior (Müller et al. 2023a). Consequently, all specimens used for the curing analysis as well as for the subsequent experimental investigations in this work were manufactured using the untreated raw extruded aluminum surface.

As confirmed by the experimental results presented in chapters 6 and 7, 100 % cohesive failure was observed in all tested specimens throughout the entire experimental program. A relevant influence of the substrate surface on the mechanical results could therefore be excluded within the investigated scope.

### 5.2.2 Bonding Procedure

The specimens were manufactured under controlled conditions using the two-component SG adhesive DOWSIL 993, a product commonly applied in SG systems. Processing was performed with an industry-standard mixing and dispensing unit at the company sedak GmbH & Co. KG (Gersthofen, Germany).

Prior to bonding, the T-profiles were aligned parallel and fixed to mounting profiles. PTFE spacers were placed beneath the profiles to define the joint thickness, as shown in Figure 5.1a. The adhesive was applied from the top in a continuous motion. After filling, a second spacer was inserted to allow excess adhesive and entrapped air to escape laterally. The mounting profiles were clamped together to ensure dimensional stability during early curing. A fixed specimen with excess adhesive and two spacers is shown in Figure 5.1b.

After a minimum curing period of one day, the spacers were removed and excess adhesive was trimmed with a sharp blade. The finished specimens with both joint geometries are shown in Figure 5.1c and 5.1d. Prior to testing, the actual joint dimensions were measured using a digital caliper. All evaluations presented in this work are based on the measured real dimensions in order to avoid overestimation of load-bearing capacity.

## 5.3 Influence of Curing and Manufacturing

To evaluate the influence of specimen age and curing conditions, different conditioning regimes were investigated. In addition to curing at room temperature (RT), an accelerated curing approach based on tempering at 40 °C was examined (method “40 °C”). The method comprises a fixed pre-curing period of 7 days at RT, followed by tempering at 40 °C for a duration adjusted to achieve the target specimen age, and subsequent reconditioning at RT prior to testing for minimum 1 day. Specimens were tested at total ages of 14 and 21 days using this procedure. In addition, a longer post-curing period of 8 days at RT was

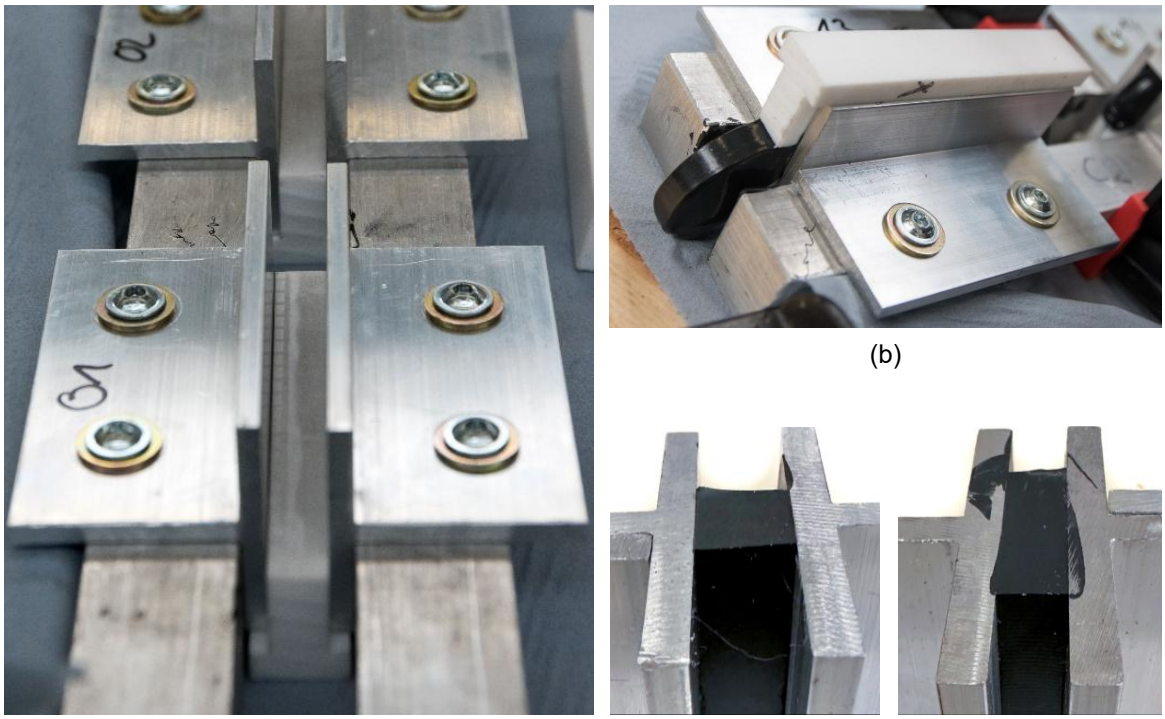

(a) (b) (c) (d)

**Figure 5.1:** Manufacturing of the modified H-specimens: (a) prepared T-profiles with lower spacer; (b) fixed specimen with excess adhesive and two spacers; (c) finished 12 × 12 mm$^2$ joint after trimming; (d) finished 8 × 24 mm$^2$ joint.

investigated ("40+"), showing no relevant influence on the mechanical response compared to the minimum reconditioning period.

A detailed analysis of the influence of curing on tensile-loaded specimens was published in (Müller et al. 2023a). Complementary investigations were conducted for shear-loaded specimens within the present work. For tensile-loaded specimens, a pronounced influence of specimen age and curing method was observed. With increasing curing degree, both ultimate tensile strength and initial stiffness increased significantly. For shear-loaded specimens, ultimate shear strength was only marginally affected by curing conditions, whereas shear stiffness increased noticeably with specimen age. Based on the conducted investigations, a minimum specimen age was defined beyond which stabilized adhesive properties can be assumed. The required minimum ages are summarized in Table 5.1.

In addition, an influence of the production batch was identified. Despite controlled manufacturing conditions, systematic differences in load-bearing behavior and ultimate strength were observed between different adhesive batches. This effect should be considered when interpreting experimental results.

Based on the results presented above, the curing method "40 °C" was selected for all subsequent experimental investigations. All specimens were conditioned for a minimum of 21 days and manufactured on two consecutive production days using the same adhesive batch to minimize intra-series variability.

**Table 5.1:** Required specimen age for stabilized adhesive properties depending on curing method and geometry. Based on (Müller et al. 2023a) and complementary shear tests conducted in this work.

| Geometry [$mm^2$] | Curing method | |
|---|---|---|
| | RT | 40 °C |
| $12 \times 12$ | 28 days | 21 days |
| $8 \times 24$ | 28 days | 21 days |

## 5.4 Summary

This chapter defined the specimen concept and manufacturing procedure for the modified H-specimens. The influence of curing conditions and production batch on mechanical properties was evaluated, and a minimum specimen age for stabilized adhesive behavior was established.

The detailed analysis of manufacturing and curing effects establishes the basis for producing high-quality specimens with reproducible properties. This forms the foundation for the cyclic investigations conducted in this work and enables a consistent and reliable experimental evaluation. All subsequent experimental investigations presented in this work are based on the standardized manufacturing and conditioning regime defined herein.

# 6 Quasi-Static Reference Performance

## 6.1 Objective and Approach

To determine the reference properties of the SG joints, quasi-static tests were conducted in the initial phase of the experimental program using modified H-specimens. The results of these tests were used to define the load levels for the subsequent LCF experiments.

In addition, the quasi-static reference parameters enable normalization of the applied cyclic loads relative to the quasi-static strength and facilitate interpretation of the results. They also allow direct comparison between different loading modes. Furthermore, these tests serve as basic quality control for the adhesive and manufacturing process and enable detection of relevant variations in adhesive properties across different production batches. As such, the reference tests ensure comparability with previous and subsequent test series.

## 6.2 Experimental Program

The quasi-static reference tests were performed under global shear loading, simulating a load acting parallel to the SG joint. A total of eight modified H-specimens per joint geometry, resulting in sixteen tests for reference characterization, were tested. All tests were conducted using a 100 kN universal testing machine (Instron 5982) equipped with a 10 kN load cell and operated in displacement control mode, as shown in Figure 6.1a. The specimens were bolted into a rigid steel fixture consisting of 10 mm thick plates to minimize boundary deformation. The test setup, as illustrated in Figure 6.1b, was designed to replicate the boundary conditions of the subsequent cyclic loading tests.

Displacement was measured via the crosshead travel of the machine. The displacement rates were selected according to (ETAG 002-1): 5.0 mm/min for specimens with a joint height of 12 mm and 3.3 mm/min for 8 mm joints, ensuring a consistent engineering strain rate, as summarized in Table 6.1.

## 6.3 General Load-Bearing Behavior

Figure 6.2 shows the stress–strain curves of the quasi-static specimens for both joint geometries. The diagram includes the eight individual curves in grey, differentiated by line

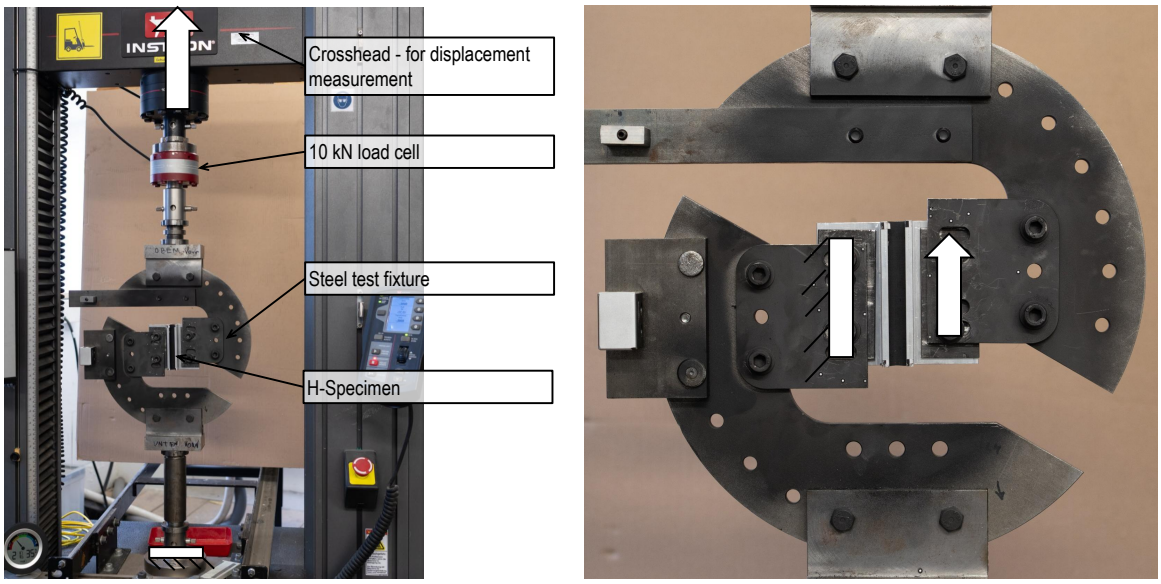


**Figure 6.1:** Test setup for the quasi-static tests: (a) overview of the testing machine; (b) detailed specimen with load application structure.

**Table 6.1:** Displacement and strain rates of the quasi-static tests.

| Geometry [mm$^2$] | Joint thickness [mm] | Displacement rate [mm/min] | Engineering strain rate [1/min] | No. of specimens [-] |
|---|---|---|---|---|
| 12 x 12 | 12 | 5.0 | 0.42 | 8 |
| 8 x 24 | 8 | 3.3 | 0.42 | 8 |

type. To facilitate interpretation, an average curve was computed from each joint geometry up to the failure point of the first specimen. These mean curves are colored according to joint geometry, blue for the $12 \times 12$ mm$^2$, red for the $8 \times 24$ mm$^2$ geometry. For both joint geometries, a similar load-bearing behavior is observed. Initially, up to a shear stress level of approximately 0.2 MPa, the curves exhibit a nonlinear reduction in stiffness. Beyond this point, a nearly linear relationship between stress and strain emerges. The onset of failure is marked by a minimum ultimate shear strain of $\gamma_{\text{ult}} = 106$ % and a minimum ultimate shear stress of $\tau_{\text{ult}} = 0.79$ MPa. The results show no obvious difference in failure shear stress between the two joint geometries, based on a qualitative assessment of the stress–strain curves. The compact $8 \times 24$ mm$^2$ geometry appears to exhibit slightly higher failure shear strain values. A detailed statistical evaluation of these parameters is provided in section 6.4.

According to (Schuler et al. 2017; Bues et al. 2019; Bues 2021; Schuler et al. 2023; Schaaf 2024), the load-bearing behavior of SG joints under shear loading is primarily governed by the deformation capacity of the adhesive, which can be characterized by the shear modulus $G$. The results of the reference tests confirmed that joint geometry has little influence on

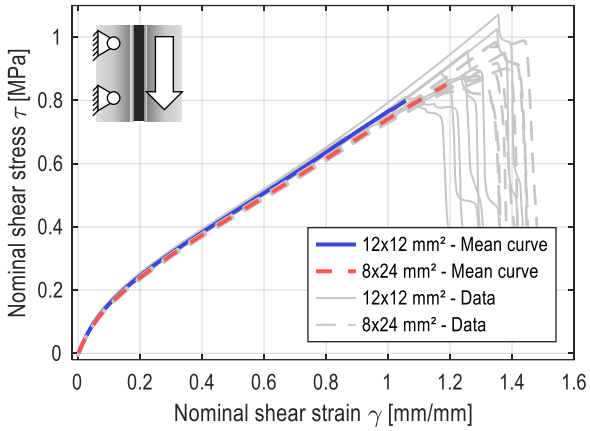


**Figure 6.2:** Stress–strain response of the quasi-static reference series with mean curves for each joint geometry.

deformation behavior, which is consistent with findings reported in literature. However, only a minor influence of joint thickness on ultimate strength was observed, which is not fully consistent with findings reported in literature.

## 6.4 Statistical Evaluation

To define stress and strain parameters for selecting and evaluating the load levels of the LCF tests, fundamental strength and stiffness properties were derived from quasi-static tests and subjected to statistical evaluation.

According to section 3.2.2, the initial mechanical strength of each specimen is represented by the ultimate failure shear stress $\tau_{ult}$. For each joint geometry, both the arithmetic mean value $\tau_{ult,mean}$ and the characteristic value $\tau_k$, according to Eq. (3.1), were determined. The strain at failure $\gamma_{ult}$ is defined at the point of maximum shear stress $\tau_{ult}$. Based on the strain data, the arithmetic mean strain at failure $\gamma_{ult,mean}$ and the characteristic strain at failure $\gamma_k$ were evaluated accordingly for each joint geometry.

The average load-bearing behavior of the series can only be partially represented by the combination of characteristic stress $\tau_k$ and strain $\gamma_k$ values, as illustrated in Figure 6.3. This is due to the differing standard deviations associated with the determination of these characteristic values, which may lead to inconsistent representations when these parameters are combined. To address this, the parameter $\gamma@\tau_k$ was additionally introduced. It denotes the strain of the average stress–strain curve at the location of the characteristic ultimate stress $\tau_k$, and is also shown in Figure 6.3. The parameter $\gamma@\tau_k$ thus provides an alternative means of characterizing the average deformation capacity of the respective series.

Analyzing the failure shear stress $\tau_{ult}$, no relevant influence of the joint geometry on the mean value $\tau_{ult,mean}$ can be identified, as shown in Figure 6.4a. However, the characteristic value $\tau_k$ of the $12 \times 12\,mm^2$ joint series is 18 % lower than that of the $8 \times 24\,mm^2$ joint,

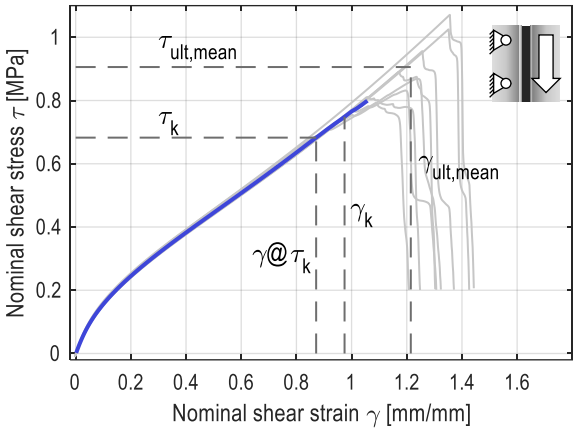


**Figure 6.3:** Definition of the statistical parameters.

which can be attributed to a higher standard deviation. For the mean strain at failure $\gamma_{ult,mean}$, the $12 \times 12\,mm^2$ series shows a 10 % lower value compared to the compact joint. The characteristic strain at failure $\gamma_k$ is 21 % lower for the standard $12 \times 12\,mm^2$ joint, as illustrated in Figure 6.4b. Consequently, due to the lower characteristic ultimate stress $\tau_k$ of the $12 \times 12\,mm^2$ joint, the derived value $\gamma@\tau_k$ is also 27 % lower compared to the compact joint.

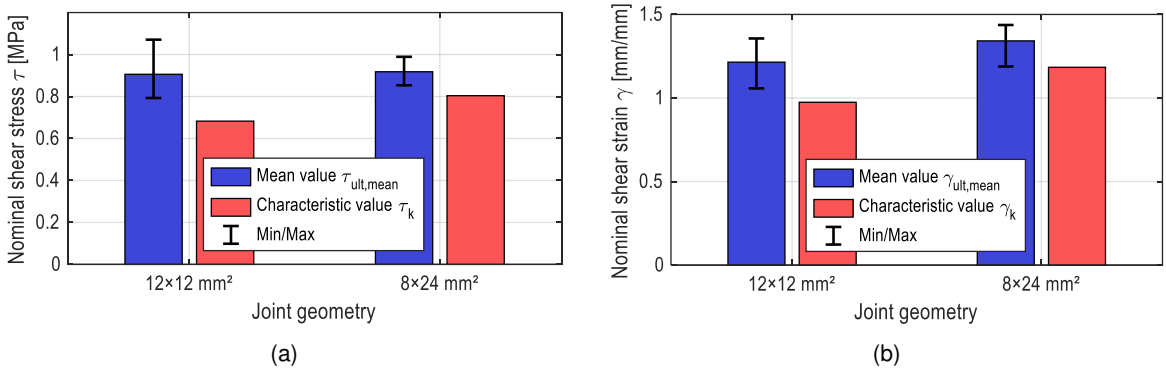


**Figure 6.4:** Statistical evaluation of the reference series: (a) ultimate stress; (b) strain capacity.

To characterize the design joint stiffness of the two joint geometries, the shear stiffness $G_{joint}$ was calculated according to Eq. (3.3). In addition to the calculation of $G_{joint,\gamma=4}$ at the design stress $\tau_{des}$, obtained using a method factor $\gamma_{meth} = 4$, a second stiffness value was determined. For this purpose, the characteristic shear stress $\tau_{k,ETA}$ from Table 3.1 was selected as the evaluation point, and the corresponding joint stiffness $G_{joint,\gamma=1}$ was calculated.

A summary of the statistical evaluation of ultimate stress $\tau_{ult}$ and strain capacity $\gamma_{ult}$ is provided in Table 6.2. The statistical evaluation of the design joint stiffness values is summarized in Table 6.3.

**Table 6.2:** Summarized statistical evaluation of ultimate stress $\tau_{ult}$ and strain capacity $\gamma_{ult}$.

| Parameter | Geometry [mm$^2$] | Min | Mean | Max | SD | Char. value $\tau_k \mid \gamma_k$ | $\gamma@\tau_k$ | Unit |
|---|---|---|---|---|---|---|---|---|
| $\tau_{ult}$ | 12 x 12 | 0.79 | 0.91 | 1.07 | 0.10 | 0.68 | – | MPa |
| $\tau_{ult}$ | 8 x 24 | 0.85 | 0.92 | 0.99 | 0.05 | 0.80 | – | MPa |
| $\gamma_{ult}$ | 12 x 12 | 1.06 | 1.21 | 1.36 | 0.11 | 0.97 | 0.87 | mm/mm |
| $\gamma_{ult}$ | 8 x 24 | 1.19 | 1.34 | 1.44 | 0.07 | 1.18 | 1.11 | mm/mm |

**Table 6.3:** Summarized statistical evaluation of design stiffness values.

| Parameter [-] | Geometry [mm$^2$] | Min [MPa] | Mean [MPa] | Max [MPa] | SD [MPa] |
|---|---|---|---|---|---|
| $G_{joint,\gamma=4}$ | 12 x 12 | 1.40 | 1.46 | 1.58 | 0.06 |
| $G_{joint,\gamma=4}$ | 8 x 24 | 1.34 | 1.41 | 1.46 | 0.04 |
| $G_{joint,\gamma=1}$ | 12 x 12 | 0.76 | 0.77 | 0.80 | 0.01 |
| $G_{joint,\gamma=1}$ | 8 x 24 | 0.73 | 0.74 | 0.76 | 0.01 |

## 6.5 Summary

Based on the quasi-static reference tests, characteristic parameters were derived for selecting appropriate load levels and for the normalized evaluation of the LCF experiments. The characteristic strength of both joint geometries exceeded the required design value $\tau_{k,ETA} = 0.66$ MPa specified in (ETA-01/0005) for the adhesive DOWSIL 993. However, it is noteworthy that the influence of joint geometry on the failure shear stress $\tau_{ult}$, which was previously reported in (Bues et al. 2019; Bues 2021) and (Müller et al. 2024; Müller et al. 2025e), could not be observed in the present test series. One possible explanation is variability between production batches, which may mask geometry-dependent effects on strength. In addition, the scatter of results is significantly higher compared to the reference tests reported in (Müller et al. 2024; Müller et al. 2025c; Müller et al. 2025e).

# 7 Low-Cycle Fatigue Performance

## 7.1 Objective and Approach

The objective of this chapter is to characterize the load-bearing and failure behavior of structural glazing (SG) joints under low-cycle fatigue (LCF) loading. As discussed in the stress assessment in chapter 4, seismic loading typically involves a limited number of load cycles that are intense and randomly distributed. In a simplified approach, this loading is experimentally approximated using constant-amplitude cyclic tests at high load levels, which fall within the LCF regime.

The methodological concept follows the classical fatigue verification procedure used in steel construction. In this approach, the structural resistance to a random load spectrum is characterized by cyclic constant-amplitude tests at various load levels. From these tests, S-N curves (Wöhler curves) are derived, enabling the prediction of fatigue life and the quantification of fatigue strength.

This concept was applied to SG joints in this work. The analysis focused on the load-bearing and failure behavior of the adhesive joint. A key influence parameter, particularly relevant for seismic loading of SG joints, was the type of load application, as described in section 4.2.

In conventional secondary SG facade constructions, interstory drift of the primary structure induces forced deformations in the SG joint. This deformation-driven load application was simulated using displacement-controlled cyclic tests. In contrast, in modern bonded all-glass structures, the glass elements, including the SG joints, are subjected directly to seismic loading due to ground acceleration and inertia forces. This force-driven load application was simulated using force-controlled cyclic tests. Additional influencing parameters, defined earlier in chapter 4, such as joint geometry and test frequency, were also investigated.

The experimental investigations and parts of the analysis presented in this chapter were based on results obtained within the research project (Müller et al. 2026b). The methodology for describing the load-bearing and failure behavior under LCF loading using cyclic stress–strain curves was previously published in (Müller et al. 2024). Furthermore, the methodology for defining failure criteria for displacement-controlled tests and for describing cycles to failure using S-N curves was presented in (Müller et al. 2025c). These approaches are significantly extended and consolidated within the present thesis based on a substantially expanded experimental database.

## 7.2 Experimental Program and Testing Procedure

### 7.2.1 Test Setup

Cyclic tests were conducted using a Schenck servo-hydraulic test frame equipped with a PL10K longitudinal cylinder and a 10 kN load cell (type 1720ACK, Interfaceforce). The system was operated using a EU3000 digital control unit with TestControl software (Inova). Tests were performed in either force-controlled or displacement-controlled mode, with peak value control activated.

Prior to the main test series, preliminary trials were conducted to determine appropriate PID controller settings for each test mode. These were optimized to balance test stability, accuracy of the target load level, and load consistency. For force-controlled tests, priority was given to maintaining a stable load level, even if minor deviations below the nominal target occurred. Specific PID controller parameters were defined separately for each of the two tested joint geometries to achieve optimal control performance. After testing, the actual load histories were evaluated to verify the accuracy of the control and to support precise interpretation of the results, as discussed in section 7.2.4.

The specimen was mounted in a rigid steel fixture using 10 mm thick plates and bolts to minimize deformation and mechanical play. The test setup was designed to replicate the setup from the quasi-static tests described in chapter 6 as closely as possible.

To enable detailed monitoring of the specimens during testing, an ARAMIS 5M digital image correlation system (GOM, Gesellschaft für Optische Messtechnik) was employed. This system enables non-contact, three-dimensional measurement of deformations and rigid body motions by tracking discrete surface points over time. This requires applying a stochastic speckle pattern to the specimen surface. However, preliminary tests showed that this pattern detached under repeated large deformations, which reduced the reliability of accurate crack tracking. Consequently, the system was used only to capture images during testing, which were later manually analyzed. A key advantage of this approach was the system's trigger function, which allowed synchronized image acquisition: the test system sent a record trigger signal shortly before each load maximum and minimum. This ensured that relevant deformation states were recorded and that the loading rate was sufficiently low for clear image acquisition.

An overview of the complete test setup, including the test frame and optical system, is shown in Figure 7.1a . The detailed load application structure with load direction is illustrated in Figure 7.1b.

### 7.2.2 Test Matrix

The experimental test program focused on the key parameters influencing the LCF behavior of the SG joints. Based on the fundamental stress assessment in chapter 4 and earlier work

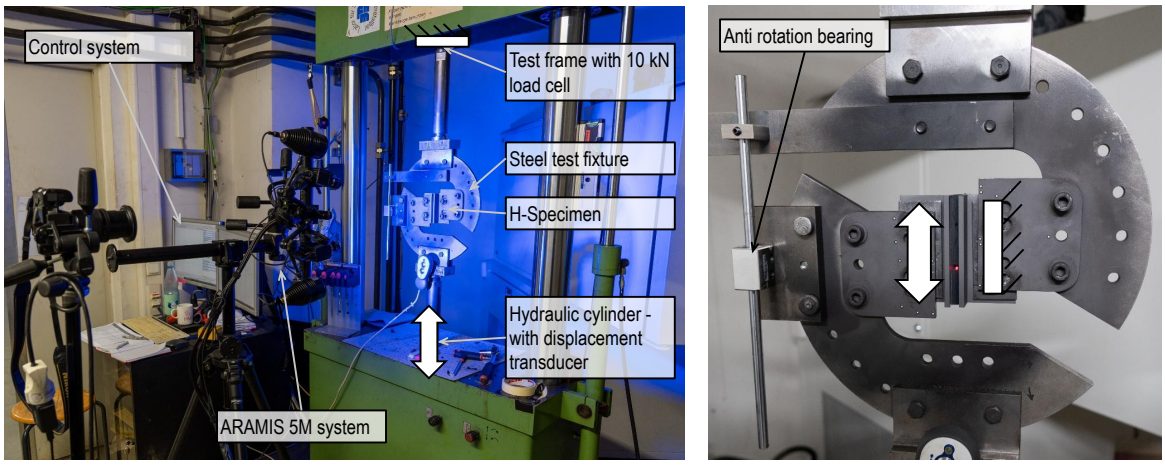


(a) (b)

**Figure 7.1:** Test setup for the cyclic tests with indicated load direction: (a) overview; (b) detail of the load application structure and test specimen.

(Müller et al. 2024; Müller et al. 2025c), some parameters were predefined or fixed to specific values for seismic loading scenarios in glass and facade structures and were therefore not investigated further in this study.

All tests were conducted at standard room temperature, ranging from 22 °C to 25 °C, with minor variations caused by heat generated by the hydraulic system during operation. Each specimen was subjected to fully reversed cyclic loading with a load ratio of $R = -1$, corresponding to fully reversed loading conditions. The load was applied in shear direction, acting parallel to the adhesive layer and along the length of the SG joint, thereby reproducing the global shear stress state relevant for SG joints under seismic loading, as analyzed in section 4.3.

With these fixed parameters, the key parameters were systematically varied within this test program. The applied load levels were defined relative to the mean fracture stress ($\tau_{ult,mean}$ and $\gamma_{ult,mean}$) obtained from quasi-static reference tests and tested in four discrete steps. To represent SG joints used in both primary and secondary load-bearing applications, two test control modes, force- and displacement-control, were employed, as discussed in section 4.2. Since the frequency showed a noticeable effect on cyclic performance, three test frequencies $f$ of 0.5 Hz, 1.0 Hz, and 5.0 Hz, were selected, as discussed in section 4.4. This range approximates the relevant frequency domain for dynamic effects in glass and facade construction.

In order to assess the influence of joint geometry and ensure the transferability of the results to applications within the limits of (ETAG 002-1), two different geometries were tested: a standard joint geometry of $12 \times 12$ mm$^2$ and a compact configuration of $8 \times 24$ mm$^2$, as discussed in section 4.5. For the $12 \times 12$ mm$^2$ joint geometry, tests at $f = 5.0$ Hz were conducted with two specimens per parameter combination. For a test frequency $f$ of 0.5 Hz and 1.0 Hz, three specimens were tested per combination to increase the statistical confidence and to better capture damage progression under more critical conditions. For

the 8 × 24 mm$^2$ geometry, two specimens were tested for each parameter combination. The resulting test matrix, including all parameter combinations and specimen counts, is presented in Table 7.1.

**Table 7.1:** Test matrix and specimen numbers for the low-cycle fatigue tests.

| Frequency $f$ [Hz] | Test control [-] | 12 × 12 mm$^2$ | | | | 8 × 24 mm$^2$ | | | |
|---|---|---|---|---|---|---|---|---|---|
| | | Load level | | | | Load level | | | |
| | | 1* | 2* | 3* | 4* | 1* | 2* | 3* | 4* |
| | | CSR ≈ 70 | CSR ≈ 80 | CSR ≈ 90 | CSR ≈ 100 | CSR ≈ 70 | CSR ≈ 80 | CSR ≈ 90 | CSR ≈ 100 |
| 0.5 | Force | 3 | 3 | 3 | 3 | 2 | 2 | 2 | 2 |
| | Displacement | 3 | 3 | 3 | 3 | 2 | 2 | 2 | 2 |
| 1.0 | Force | 3 | 3 | 3 | 3 | 2 | 2 | 2 | 2 |
| | Displacement | 3 | 3 | 3 | 3 | 2 | 2 | 2 | 2 |
| 5.0 | Force | 2 | 2 | 2 | 2 | 2 | 2 | 2 | 2 |
| | Displacement | 2 | 2 | 2 | 2 | 2 | 2 | 2 | 2 |

* The real load is evaluated and defined in section 7.2.4.

### 7.2.3 Experimental Procedure and Signal Processing

All tests were conducted as single-stage cyclic tests in either force-controlled or displacement-controlled loading mode, depending on the test series. In force-controlled tests, loading was applied until the specimen exhibited complete mechanical failure. In displacement-controlled tests, the test was automatically terminated when the peak shear stress of a load cycle dropped below 30 % of the maximum peak stress observed in the first cycle, indicating significant material degradation. This threshold was defined as the machine-specific termination criterion $\delta_{\tau\ \mathrm{test}}$.

All test data were processed in MATLAB following completion of the tests. The raw signals from the testing machine were recorded at a sampling frequency of 1000 Hz, corresponding to a time step of 0.001 s. The shear stress was calculated from the recorded force signal using the initial shear area $A_0$ of each specimen. The corresponding shear strain was derived from the machine deformation signal divided by the initial specimen height $e$.

Because the tests were conducted at different frequencies, the raw signals were interpolated in the time domain to create 1000 equally spaced data points per cycle. This standardization allowed for consistent comparison of the test data and enabled further processing without the need to explicitly account for the test frequency.

For further processing, the interpolated signals were smoothed using the `loess` method, which applies a quadratic regression within a moving window of 40 data points. The window width was determined through preliminary testing and represented a suitable compromise between preserving the essential features of the signal, particularly at the peaks of each cycle, and effectively reducing signal noise. An exemplary dataset from a test conducted under force control is presented in Figure 7.2, demonstrating that the smoothing procedure has no relevant influence on the shape or amplitude of the signal.

In two individual specimens, pronounced fluctuations occurred at the onset of failure. In these specific cases, the smoothing window was manually increased to 160 data points within the affected time range to improve data readability and support further post-processing.

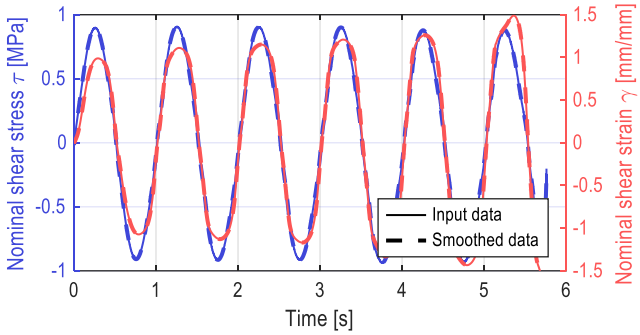


**Figure 7.2:** Input and smoothed signals for an exemplary cyclic test (load level = 4, $f$ = 1.0 Hz, force control).

### 7.2.4 Evaluation of the Load Levels

The load levels for the cyclic tests were defined based on the performance of the quasi-static reference series described in chapter 6. For test execution and control, the combination of high loading rates, large deformations, and nonlinear material behavior posed a considerable challenge. In the force-controlled tests, the PID controller settings could only be optimized to maintain a stable test sequence and approximately constant load amplitude. As a result, the actual load level slightly deviated from the nominal target.

To determine the real acting stress level $\tau_E$ in the force-controlled tests, the maximum force of each load cycle was extracted from the test data during evaluation. The corresponding shear stress was then calculated and averaged across all cycles. For displacement-controlled tests, the real acting strain $\gamma_E$ was determined analogously from the deformation signal. All evaluations in this thesis are based on these real acting stress $\tau_E$ and strain $\gamma_E$ values, rather than the nominal input parameters.

To allow a direct comparison between the test control modes and joint geometries, the cyclic stress ratio (CSR) was used as a normalization parameter. This also facilitates comparisons across different production series. The use of CSR for evaluating cyclic laboratory tests was

originally proposed by (Seed et al. 1975; Green and Terri 2005), particularly in the context of liquefaction analysis of soils under seismic loading.

In this thesis, the real applied stress $\tau_E$ in the force-controlled tests was related to the mean ultimate shear strength $\tau_{ult,mean}$ of the reference tests. The determination of the CSR based on the mean ultimate shear strength $\tau_{ult,mean}$ offers a clear advantage compared to an evaluation based on the characteristic strength value $\tau_k$. The mean value is significantly less sensitive to the scatter in the results of the reference tests. Therefore, this approach was preferred over the method used in (Müller et al. 2025c). The corresponding stress ratio $CSR_\tau$ is defined as:

$$CSR_\tau = \frac{\tau_E}{\tau_{ult,mean}} \tag{7.1}$$

For displacement-controlled tests, the stress ratio $CSR_\gamma$ was defined analogously using $\gamma_E$ and the mean ultimate strain $\gamma_{ult,mean}$:

$$CSR_\gamma = \frac{\gamma_E}{\gamma_{ult,mean}} \tag{7.2}$$

Throughout this thesis, CSR is expressed as a percentage, such that CSR = 70 corresponds to 70 %. This percentage notation is applied consistently in all subsequent evaluations and fitting models.

A summary of the evaluated real load levels is presented in Table 7.2, categorized by joint geometry and test control method.

**Table 7.2:** Summary of evaluated load levels from the cyclic tests.

| | | Stress-based quantities | | | | Strain-based quantities | | | |
|---|---|---|---|---|---|---|---|---|---|
| Geo-metry | Load level | $CSR_\tau$ | $\tau_E$ | Load | $\tau_{ult,mean}$ | $CSR_\gamma$ | $\gamma_E$ | Displace-ment | $\gamma_{ult,mean}$ |
| [mm²] | [-] | [%] | [MPa] | [N] | [MPa] | [%] | [-] | [mm] | [-] |
| 12 x 12 | 1 | 67.3 | 0.61 | 732.0 | 0.91 | 70.3 | 0.85 | 10.2 | 1.21 |
| | 2 | 76.2 | 0.69 | 828.2 | 0.91 | 79.9 | 0.97 | 11.6 | 1.21 |
| | 3 | 84.9 | 0.77 | 923.1 | 0.91 | 90.5 | 1.10 | 13.2 | 1.21 |
| | 4 | 94.0 | 0.85 | 1022.0 | 0.91 | 100.2 | 1.22 | 14.6 | 1.21 |
| 8 x 24 | 1 | 67.9 | 0.62 | 1496.0 | 0.92 | 70.6 | 0.95 | 7.6 | 1.34 |
| | 2 | 78.2 | 0.72 | 1722.8 | 0.92 | 80.8 | 1.08 | 8.7 | 1.34 |
| | 3 | 87.7 | 0.80 | 1931.0 | 0.92 | 91.0 | 1.22 | 9.8 | 1.34 |
| | 4 | 95.8 | 0.88 | 2110.0 | 0.92 | 100.5 | 1.35 | 10.8 | 1.34 |

## 7.3 Load-Bearing Behavior Under Low-Cycle Fatigue Loading

### 7.3.1 Fundamental Low-Cycle Fatigue Behavior

To gain an initial understanding of the load-bearing behavior under LCF loading, the hysteresis response of two exemplary LCF tests, one force-controlled (Force) and one displacement-controlled (Disp), is shown in Figure 7.3. Both tests were conducted at load level 3 with a frequency of 1.0 Hz using the standard $12 \times 12$ mm$^2$ joint geometry. Figure 7.3a provides an overview of the entire stress and strain range, while Figure 7.3b focuses on the positive section of the hysteresis loop to facilitate comparison. For reference, a stress–strain curve from a quasi-static reference test is also included.

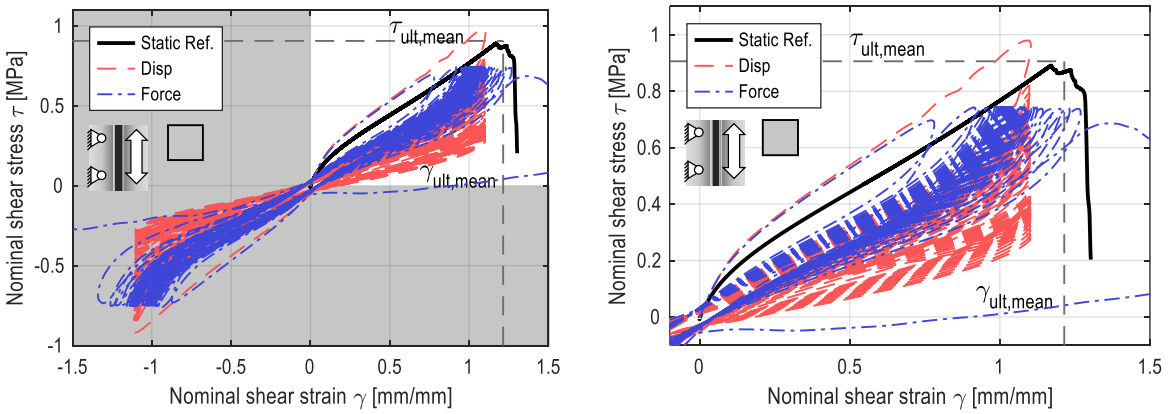


**Figure 7.3:** Basic LCF behavior shown in the stress–strain diagram (load level 3, $f$ = 1.0 Hz, $12 \times 12$ mm$^2$): (a) overview; (b) positive section of the hysteresis loop.

The initial loading path shows similar behavior for both control modes. Compared to the quasi-static reference curve, the cyclic tests exhibit a slightly stiffer response, which can be attributed to the significantly higher loading rate, as confirmed by (Schuler et al. 2017). In the displacement-controlled test, this increased stiffness resulted in a peak stress that exceeds the quasi-static ultimate stress $\tau_{ult,mean}$ in the first load cycle at load level 3. It could therefore be assumed that the specimen was already overloaded during the first cycle. This effect was not observed in the force-controlled test.

The first hysteresis loop in both cases has a significantly larger area than subsequent loops. This effect can be partially attributed to the Mullins effect (Mullins 1948). Another characteristic feature is the distinctly stiffer response in the first cycle, followed by a noticeable reduction in stiffness in subsequent cycles.

Over the course of the test, the specimen stiffness decreases steadily, corresponding to the onset of SG joint failure, with clear differences between the two control modes. In the displacement-controlled test, the absorbed stress decreases with continued loading, leading to stress relaxation. In contrast, in the force-controlled test, the applied stress maintains approximately constant, while the strain increases progressively, eventually forming a

plateau. This behavior is comparable to creep, as discussed in section 2.1.3.6 (Gent 2012; Schröder 2018). However, this apparent viscoelastic behavior results primarily from the progressive damage of the specimen during testing, leading to a continuous reduction of the effective bonded area.

Significant differences are also observed in the ultimate failure behavior. In the force-controlled test, the specimen can no longer bear the load in the final cycle, resulting in rapidly increasing deformation and ultimately sudden failure. This failure is visible in Figure 7.3 at a shear strain of approximately 1.25 mm/mm. In contrast, the displacement-controlled test shows a gradual reduction in the stress-bearing capacity, but no distinct or sudden failure occurs. Without a termination or failure criterion, the test would theoretically continue indefinitely.

For this reason, the pragmatic machine-specific termination criterion $\delta_{\tau\ \mathrm{test}}$ was defined. The test was stopped once the peak stress dropped by more than 30 % relative to the initial maximum stress, as explained in section 7.2.3. This method is commonly used in cyclic testing to terminate displacement-controlled tests or to define failure, as discussed in section 2.3.5. However, no consistent cutoff value could be derived from the literature. Therefore, the specific cutoff value applied in this thesis was deliberately chosen to ensure severe specimen damage before termination. To further evaluate performance, particularly in terms of the number of cycles to failure, alternative failure criteria are discussed in section 7.5. For the purpose of analyzing general load-bearing behavior under LCF conditions, the applied termination criterion was considered sufficient.

### 7.3.2 Cyclic Stress–Strain Curves

For a clearer representation and subsequent analysis of the load-bearing behavior under LCF loading, so-called cyclic stress–strain curves (CSSCs) were derived from the full test sequence shown in Figure 7.3. To generate these curves, only the maximum points of the controlled signal were extracted and plotted in the stress–strain diagram starting from the initial loading branch (Götz and Eulitz 2022). This resulted in the CSSCs shown in Figure 7.4, derived from the hysteresis loops in Figure 7.3b. In all subsequent illustrations of CSSCs, the colored curves including the maximum points represent a single exemplary specimen. The gray curves show the remaining specimens from the same series, plotted with the same line type to indicate variation.

#### 7.3.2.1 Type of Load Application

The different failure behavior resulting from the two types of test control, as well as the differences observed in the first load cycle, can also be identified in the CSSCs shown in Figure 7.4. However, in contrast to the full hysteresis representation, the energy dissipation, represented by the area enclosed by each hysteresis loop, is not captured in the CSSCs.

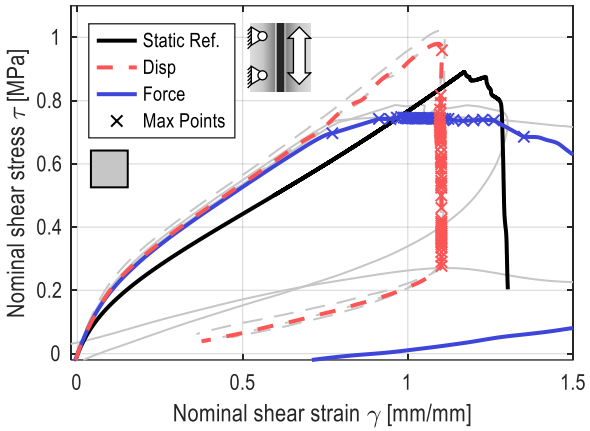


**Figure 7.4:** CSSCs for force- and displacement-controlled tests, derived from the hysteresis loops shown in Figure 7.3 (load level 3, $f$ = 1.0 Hz, 12 × 12 mm$^2$).

The difference in failure behavior between force-controlled and displacement-controlled tests is clearly reflected in the CSSC representation. In particular, the spacing between the maxima of each cycle becomes more distinct, allowing a clearer comparison of stiffness degradation. A similar spacing between the first and second peak can be observed, indicating a comparable initial stiffness reduction for the two test control modes. This behavior is further examined in section 7.5.4 by considering the development of crack propagation in the SG joint.

The response of the displacement-controlled test, which resembles a stress relaxation phenomenon, contrasts with the failure plateau observed in the force-controlled test. This plateau behavior resembles creep-like effects. Considering the scatter within each series, the CSSCs show very good agreement between the individual specimens. The low deviation among the three curves indicates high test quality and low variability. Because of its clearer representation and the ability to directly compare the load-bearing behavior, the CSSCs were preferred for analyzing the following parameters.

#### 7.3.2.2 Load Level

The influence of different load levels on the CSSCs is shown in Figure 7.5 for both test control modes. The exemplary tests shown were conducted at a frequency of 0.5 Hz using the standard 12 × 12 mm$^2$ joint geometry. One representative curve per load level, including the maximum points, is shown in color, while the remaining specimens of the same load level are plotted using the same line type.

In principle, the CSSCs of both control types exhibit similar stiffness characteristics. For the force-controlled tests shown in Figure 7.5a, the spacing between the four predefined load levels appears more irregular than in the displacement-controlled tests. This irregularity may be attributed to limitations of the control system. The combination of large deformations, high loading rates, nonlinear SG adhesive behavior, and the onset of failure

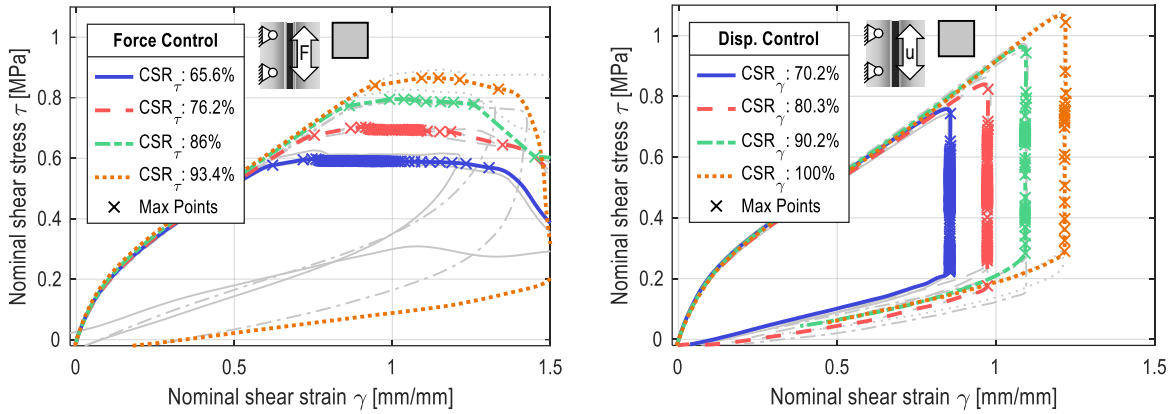


**Figure 7.5:** Effect of different load levels on the CSSCs for both control modes ($f$ = 0.5 Hz, 12 × 12 mm$^2$): (a) force control; (b) displacement control.

places considerable demands on the controller, despite preliminary measures to stabilize load application. To account for these effects, the actual stress values used for further evaluation were derived directly from the test data, as described in section 7.2.4. Consequently, deviations from the nominal load levels did not compromise the validity of the subsequent analyses.

For the displacement-controlled tests shown in Figure 7.5b, specimen failure occurs at each predefined strain amplitude. The largest drop in stiffness, reflected in the spacing between two adjacent maxima, occurs between the first and second cycles for all load levels. In addition to the previously discussed Mullins effect, this behavior can be attributed to pre-damage effects caused by the initial overload and the onset of failure. The underlying crack propagation is examined in detail in section 7.5.4. As the load level increases, the distance between successive maxima also increases, indicating a higher degree of damage per cycle. Consequently, the number of load cycles to failure decreased with increasing load level.

For the force-controlled tests, all specimens show a plateau region before complete failure, regardless of load level. In all cases, total specimen failure occurs at a strain level of approximately 1.2–1.3 mm/mm. This strain level corresponds to the quasi-static mean strain at failure $\gamma_{\text{ult,mean}}$ with a value of 1.21 mm/mm.

When comparing both control modes across all load levels, the spacing between maxima becomes more uniform after the first few cycles in both cases. However, in force-controlled tests, following a phase of uniform spacing, the spacing increases markedly toward the end of the test, resulting in more rapid and abrupt failure. In contrast, displacement-controlled tests show a largely uniform progression of peak values, interrupted by phases with larger spacing during the main part of the test. This pattern continues until the final cycles. These interruptions may be explained by more unstable failure behavior under displacement-controlled conditions and deviate from the results in (Müller et al. 2024), where uniform spacing was observed until the end of the test.

Overall, variations in load level have only a minor influence on the general load-bearing behavior under LCF loading. The stiffness behavior showes only small deviations for both control modes, whereas the major differences occur in the failure behavior due to the distinct control modes.

#### 7.3.2.3 Test Frequency

The effect of test speed, or test frequency $f$, is illustrated in Figure 7.6 using the standard $12 \times 12$ mm$^2$ joint geometry. All tests were conducted at load level 3, corresponding to a CSR of approximately 90 %. The real average load level for each series is indicated next to the legend. Tests were performed under force control (Figure 7.6a) and displacement control (Figure 7.6b).

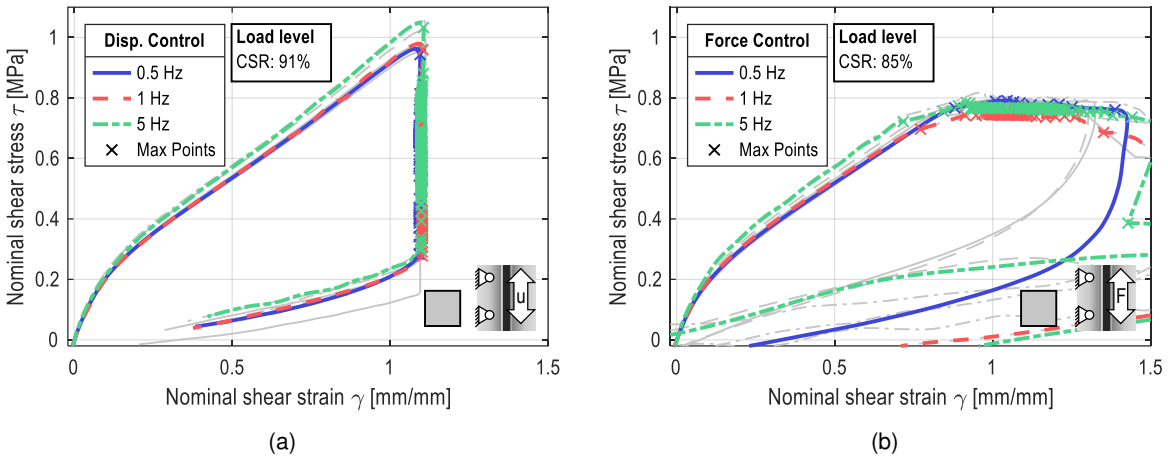


**Figure 7.6:** Effect of different test frequencies $f$ on the CSSCs for both control modes ($12 \times 12$ mm$^2$, load level 3): (a) force control; (b) displacement control.

The overall load-bearing behavior observed in both control modes is consistent with the results shown in Figure 7.4 and Figure 7.5. Only the initial stiffness shows a slight increase at higher test frequencies, which can be attributed to the increased loading rate. Apart from this minor difference, the frequency has little influence on the general load-bearing behavior under LCF loading. However, the spacing between successive maxima decreases with increasing frequency, resulting in a higher number of recorded load cycles. The results are similar for both control modes.

#### 7.3.2.4 Joint Geometry

Figure 7.7 presents exemplary CSSCs to evaluate the influence of joint geometry. The tests shown in Figure 7.7a were conducted at 0.5 Hz and load level 3 (CSR $\approx$ 90 %) for both joint configurations. Figure 7.7b shows results from tests at 5.0 Hz and load level 2 (CSR $\approx$ 80 %).

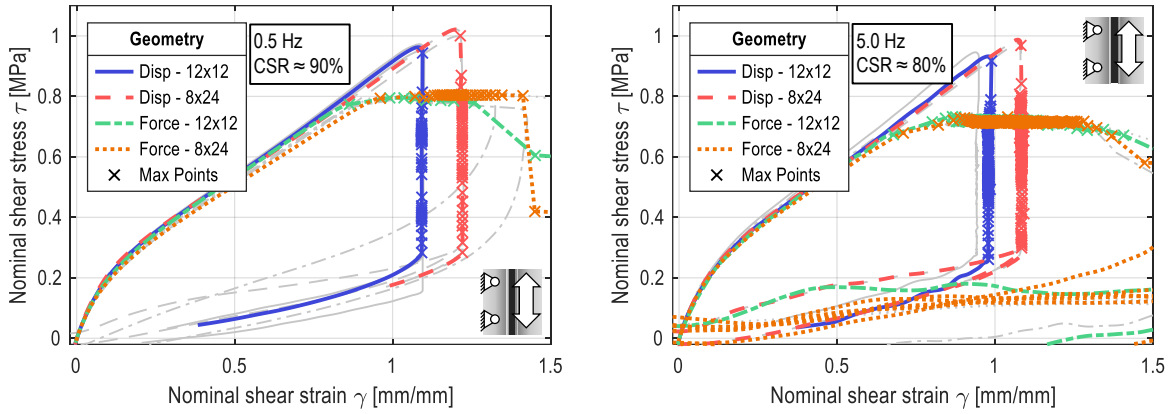


**Figure 7.7:** Effect of joint geometry on the CSSCs for both control modes: (a) 0.5 Hz and load level 3 test series; (b) 5.0 Hz and load level 2 test series.

Across all test conditions, control mode, load level, and frequency, both geometries exhibited comparable load-bearing behavior under LCF loading. The most apparent difference was the higher strain amplitude applied to the compact $8 \times 24$ mm$^2$ geometry in the displacement-controlled tests, which resulted from its higher characteristic strain at failure $\gamma_k$. These results suggest that the compact joint does not exhibit a fundamentally different structural response under LCF loading. The observed similarities indicate that transferring the findings to joint geometries within the limits of (ETAG 002-1), and consequently to full-scale applications, appears feasible.

In summary, SG joints under LCF loading exhibited load-bearing behavior broadly comparable to quasi-static loading during the initial cycles, while significant differences emerged in the failure behavior depending on the control mode. Force-controlled loading led to progressive increase in deformation followed by sudden failure, whereas displacement-controlled loading resulted in gradual stress reduction with remaining residual strength.

## 7.4 Cyclic Parameters in SG Joints

The determination and analysis of cyclic parameters is essential for evaluating the performance of SG joints under cyclic loading and serves specific purposes. Complementing the qualitative representation in section 7.3.2, these parameters enable a quantitative characterization of the joint response throughout the test. Firstly, these parameters enable the characterization of changes in key properties of the SG joint that occur throughout the cyclic test up to failure. In particular, stiffness and damping properties are important parameters in the design process and can be quantified using this approach. Moreover, selected cyclic parameters can be used to define failure criteria, especially for the displacement-controlled test series, thereby enhancing the comparability between the two control modes.

The cyclic parameters were computed automatically from the machine data using a MATLAB script. To this end, the entire test history was segmented into individual cycles, each of which was evaluated separately. This method enabled the continuous assessment of parameters from the undamaged state of the specimen through to failure. To facilitate comparisons between specimens with different total numbers of cycles, a normalized cycle count $n^*$ was introduced as the ratio of the current cycle number $N_i$ to the total number of cycles to failure $N_{\max}$:

$$n^* = \frac{N_i}{N_{\max}} \tag{7.3}$$

### 7.4.1 Deviation of the Feedback Signal

The deviation of the load range serves as a straightforward cyclic parameter for evaluating damage progression, as introduced in section 2.3.4.1. However, this parameter is applicable only to displacement-controlled tests and cannot be directly used to compare force- and displacement-controlled test series.

To enable such a comparison, the evaluation approach was modified by considering the absolute deviation of the feedback signal. In displacement-controlled tests, $\delta_{\tau(\mathrm{U}),i}$ corresponds to the reduction in maximum shear stress $\tau_{\mathrm{Max}}$, whereas in force-controlled tests $\delta_{\gamma(\mathrm{F}),i}$ corresponds to the increase in maximum shear strain $\gamma_{\mathrm{Max}}$. Figure 7.8 illustrates the definition and evaluation of these parameters. To account for the opposite trends, both quantities were expressed as normalized absolute deviations relative to the first cycle, where $\gamma_{\mathrm{Max},i}$ and $\tau_{\mathrm{Max},i}$ denote the maximum strain and stress in the $i$th cycle, and $\gamma_{\mathrm{Max},1}$ and $\tau_{\mathrm{Max},1}$ the corresponding values in the first cycle:

$$\delta_{\gamma(\mathrm{F}),i} = \left| \frac{\gamma_{\mathrm{Max},i} - \gamma_{\mathrm{Max},1}}{\gamma_{\mathrm{Max},1}} \right| \tag{7.4}$$

$$\delta_{\tau(\mathrm{U}),i} = \left| \frac{\tau_{\mathrm{Max},i} - \tau_{\mathrm{Max},1}}{\tau_{\mathrm{Max},1}} \right| \tag{7.5}$$

To avoid excessively long test durations in the displacement-controlled series, a termination criterion $\delta_{\tau\ \mathrm{test}}$ was introduced in the testing machine. All tests were automatically stopped when the maximum shear stress of the current cycle dropped below 30 % of the initial maximum shear stress. This corresponds to a normalized absolute deviation of the feedback signal of $\delta_{\tau\ \mathrm{test}} = 0.7$.

For a first analysis, only the test series with a frequency of 0.5 Hz and the $12 \times 12$ mm$^2$ joint geometry were considered, as only minor differences were observed between the remaining frequencies and joint geometries. The deviation of the feedback signal $\delta_{\gamma(\mathrm{F})}$ and $\delta_{\tau(\mathrm{U})}$ is shown in Figure 7.9a for the force-controlled tests and in Figure 7.9b for the displacement-controlled tests.

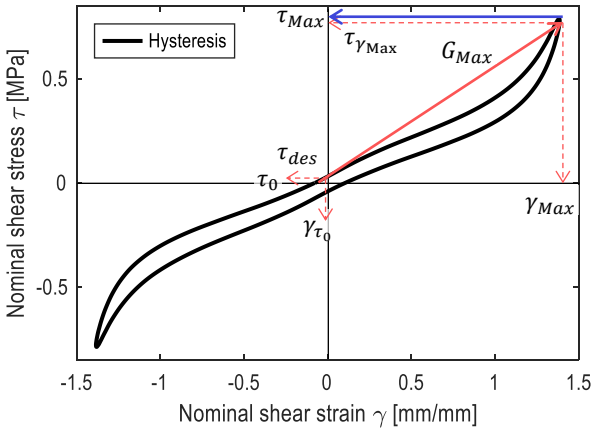


**Figure 7.8:** Evaluation points for determining the deviation of the feedback signal $\delta_{\gamma(\mathrm{F})}$, $\delta_{\tau(\mathrm{U})}$, and the dynamic stiffness $G_{\mathrm{Max}}$ from the hysteresis data.

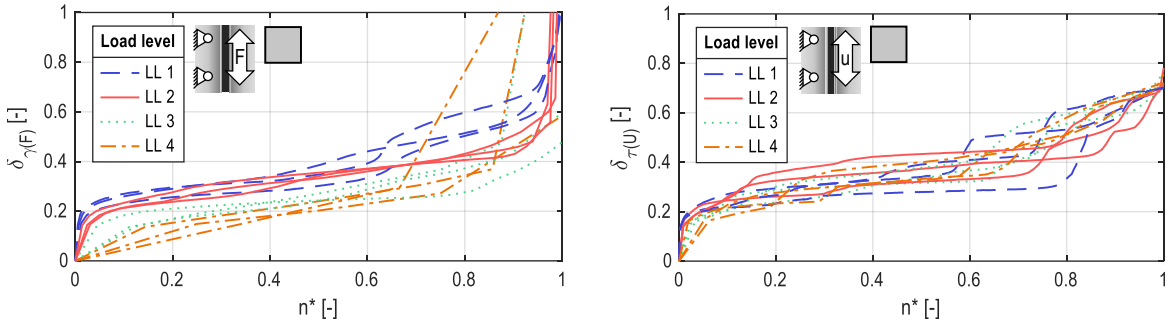


**Figure 7.9:** Progression of the deviation of the feedback signal ($f$ = 0.5 Hz, 12 × 12 mm$^2$): (a) force control, $\delta_{\gamma(\mathrm{F})}$; (b) displacement control, $\delta_{\tau(\mathrm{U})}$.

Regardless of the test control mode, the parameter behave similarly in both cases. The most pronounced increase in $\delta_{\gamma(\mathrm{F})}$ and $\delta_{\tau(\mathrm{U})}$ occurs at the beginning of the test, which can be attributed to the combined effect of the Mullins effect and the initiation of damage in the specimen. As the test progresses, ongoing damage leads to a gradual increase in both parameters.

In force-controlled tests, specimens subjected to higher load levels exhibit a slower increase in $\delta_{\gamma(\mathrm{F})}$. This apparent load dependence can be partially explained by the evaluation based on the normalized cycle count $n^*$, as well as by the more pronounced influence of the first and final cycles compared to the remaining test phase. Independent of the load level, $\delta_{\gamma(\mathrm{F})}$ shows a nearly linear evolution in force-controlled tests. Toward the end of the tests, a sudden increase in $\delta_{\gamma(\mathrm{F})}$ is observed. For the lowest load levels (1 and 2), this increase begins at values above $n^* = 0.9$, whereas for the highest load level (4), it begins at approximately $n^* = 0.75$. The earlier onset at higher load levels could be attributed to the smaller number of cycles in these tests in combination with the normalized cycle count $n^*$. As a result, the actual number of cycles at which a significant increase occurs was substantially higher at lower load levels.

In displacement-controlled tests, $\delta_{\tau(\mathrm{U})}$ exhibits a predominantly linear increase, interrupted by distinct and abrupt changes. This behavior appears randomly distributed throughout the test duration. It corresponds to the uneven spacing of peaks in the CSSCs observed in section 7.3.2 and could be attributed to more unstable failure behavior under displacement-controlled conditions. This trend was not observed in the cyclic parameters reported in (Müller et al. 2025c).

### 7.4.2 Dynamic Stiffness

As an alternative to evaluating the deviation of the feedback signals $\delta_{\gamma(\mathrm{F})}$ and $\delta_{\tau(\mathrm{U})}$, dynamic stiffness can be used to characterize the flexibility of SG joints, as described in section 2.3.4.2. The characterization of stiffness during cyclic tests serves multiple purposes: it enables the assessment of damage progression throughout the test and provides stiffness values for the design and numerical simulation of glass and facade structures. Based on these results, representative stiffness values can be defined for different failure states of SG joints.

However, existing approaches for determining dynamic stiffness reported in the literature were not directly applicable to SG joints due to differences in material behavior and test setup. To enable this characterization, the endpoint linearization proposed by (Spitz 2012) for determining the torsional dynamic stiffness $c_{\mathrm{T},dyn}$ in Eq. (2.39) was combined with standard methods for determining quasi-static material parameters in section 3.2.2. These methods were adapted for cyclic loading conditions.

In this thesis, the dynamic stiffness $G_{\mathrm{Max},i}$ was evaluated in each load cycle as the secant modulus between the point of maximum shear strain $\gamma_{\mathrm{Max},i}$ and a lower reference strain $\gamma_{\tau_0,i}$. The corresponding shear stresses are $\tau_{\gamma_{\mathrm{Max}},i}$ and $\tau_0$, as illustrated in Figure 7.8.

The value of $\tau_0 = 0.02$ MPa was selected in accordance with the evaluation of quasi-static parameters in section 3.2.2. The dynamic stiffness was calculated as follows:

$$G_{\mathrm{Max},i} = \frac{\tau_{\gamma_{\mathrm{Max}},i} - \tau_0}{\gamma_{\mathrm{Max},i} - \gamma_{\tau_0,i}} \tag{7.6}$$

Although the secant modulus only approximates the nonlinear stress–strain hysteresis, it effectively captures the stiffness degradation observed during the test. Moreover, this approach enables comparison between the two test control modes, as both exhibit a continuous reduction in stiffness over the course of the test.

The evolution of stiffness $G_{\mathrm{Max}}$ is shown in Figure 7.10 for both control types and joint geometries. Only the test series at 0.5 Hz are presented as representative examples. The other series at higher frequencies (1 Hz and 5 Hz) show slightly higher stiffness values but otherwise comparable behavior.

The increasing deviation of the feedback signal $\delta_{\gamma(\mathrm{F})}$ and $\delta_{\tau(\mathrm{U})}$ observed in all test series is accompanied by a continuous decrease in dynamic stiffness $G_{\mathrm{Max}}$. The initial change

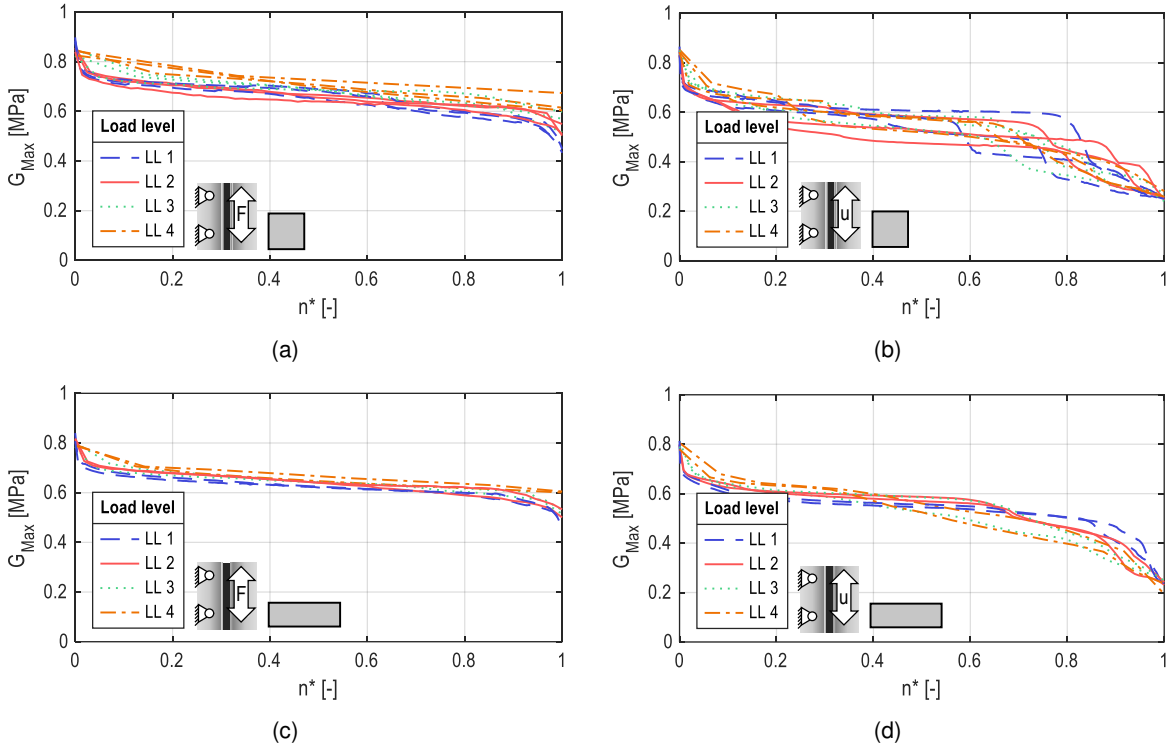


**Figure 7.10:** Progression of $G_{\mathrm{Max}}$ ($f$ = 0.5 Hz): (a) force control – 12 × 12 mm$^2$; (b) displacement control – 12 × 12 mm$^2$; (c) force control – 8 × 24 mm$^2$; (d) displacement control – 8 × 24 mm$^2$.

in $G_{\mathrm{Max}}$ at the beginning of the test is less pronounced but still noticeable compared to $\delta_{\gamma(\mathrm{F})}$ and $\delta_{\tau(\mathrm{U})}$, and can likewise be attributed to the Mullins effect and initial damage of the SG joint. In the force-controlled test series, illustrated in Figures 7.10a and 7.10c, this initial drop is followed by a continuous and approximately linear trend of $G_{\mathrm{Max}}$. In contrast, the displacement-controlled tests, illustrated in Figures 7.10b and 7.10d, show plateau-like phases of $G_{\mathrm{Max}}$ in the middle phase of the test, with distinct drops starting at around 0.6 of the normalized cycle count. This differs from the findings reported in (Müller et al. 2025c), where a continuous decrease in $G_{\mathrm{Max}}$ was observed throughout the entire test.

One possible explanation for this staircase-like parameter curve is that, particularly in the displacement-controlled tests and with the adhesive used, certain regions in the joint exhibit tougher material behavior. This could lead to slower crack propagation, until the crack breaks through such regions and propagation resumes at a slightly faster rate. However, this explanation cannot be confirmed conclusively based on the present investigations.

The sudden change in slope observed near the end of the force-controlled tests is less pronounced compared to $\delta_{\gamma(\mathrm{F})}$. No clear dependence on load level can be identified for either control mode. Overall, both cyclic parameters $\delta_{\gamma(\mathrm{F})}$ and $\delta_{\tau(\mathrm{U})}$ as well as $G_{\mathrm{Max}}$ show a continuous reduction in stiffness over the course of the test. For the simulation of SG joints in glass and facade structures under seismic loading, reduced stiffness values may be considered for highly stressed joints, provided that partial damage of the joint is acceptable in the event of an earthquake.

For all tests, a significantly higher stiffness was observed in the first load cycle, denoted as $G_{\text{Max,Initial}}$. This parameter was evaluated separately for all tests, and the results are presented in Figure 7.11. The initial stiffness $G_{\text{Max,Initial}}$ may be used in the design of glass and facade structures to model the stress in an SG joint during the first loading cycle of an earthquake. The bar colors distinguish between the two joint geometries, while the error bars represent the respective minimum and maximum values to illustrate the scatter. Figure 7.11a shows the force-controlled series, and Figure 7.11b the displacement-controlled series.

The results suggest that the initial stiffness $G_{\text{Max,Initial}}$, lies within a range of 0.8 to 1.0 MPa, regardless of the parameters considered. The compact joint geometry of $8 \times 24$ mm$^2$ exhibits slightly lower stiffness values for both control modes. In addition, a slight increase in stiffness is observed with increasing test frequency.

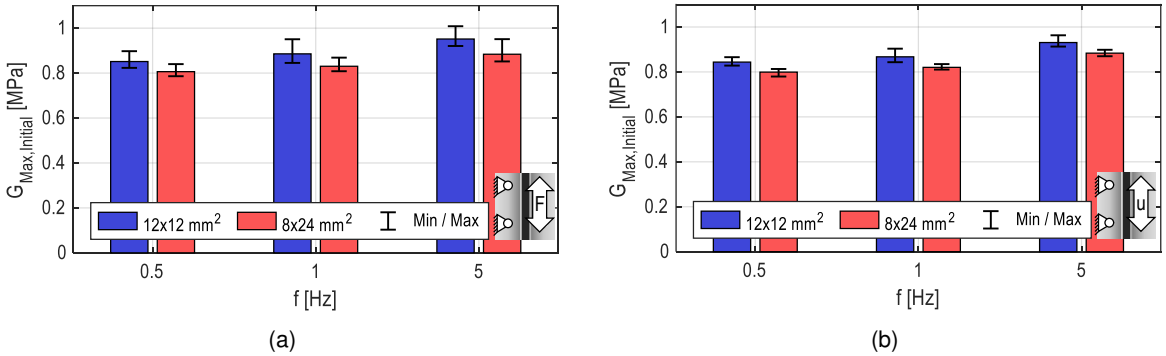


**Figure 7.11:** Analysis of the initial stiffness $G_{\text{Max,Initial}}$ as a function of the test frequency $f$: (a) force control; (b) displacement control.

### 7.4.3 Dissipated Energy Density

The dissipated energy is a key parameter for characterizing viscoelastic materials and describing their response under seismic loading.

In this work, the dissipated energy density $w_{\text{diss}}$ was determined from the area of the hysteresis loops, as described in section 2.3.4.3 and Eq. (2.41). This approach captures the nonlinear material behavior that occurs at higher strain levels. The dissipated energy density was evaluated from the hysteresis loops and reported in MPa, which is equivalent to MJ/m$^3$ and thus represents the energy dissipated per unit volume.

The evolution of the dissipated energy density $w_{\text{diss}}$ is shown in Figure 7.12 for the test series at a frequency of 0.5 Hz and the standard $12 \times 12$ mm$^2$ joint geometry. Figure 7.12a illustrates $w_{\text{diss}}$ for the force-controlled tests, Figure 7.12b for the displacement-controlled tests. Similar to other cyclic parameters, a distinct difference was observed between the first cycle and the subsequent course of the test. In the first cycle, all tests exhibited a higher dissipated energy density $w_{\text{diss}}$, while in the following cycles an almost constant trend is observed. In the force-controlled tests in Figure 7.12a, $w_{\text{diss}}$ increases slightly towards the

end of the test, whereas this effect is not apparent in the displacement-controlled tests in Figure 7.12b.

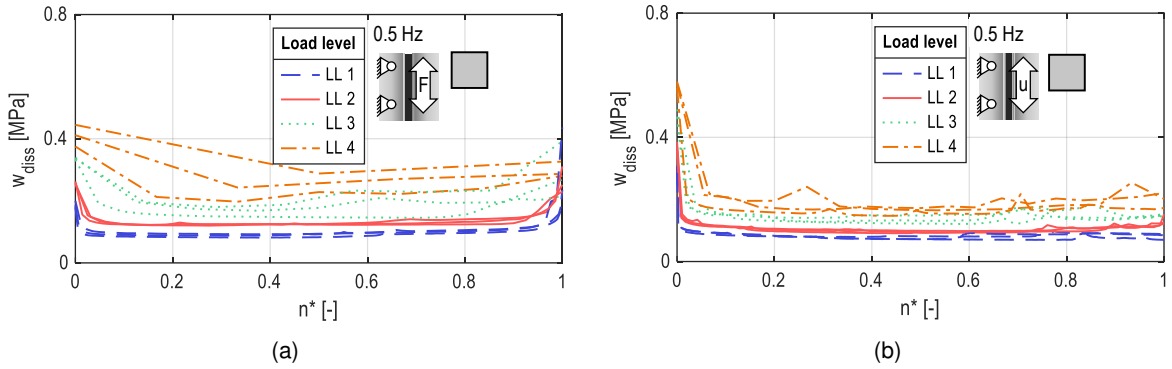


**Figure 7.12:** Progression of the dissipated energy density $w_{\text{diss}}$ ($f$ = 0.5 Hz, 12 × 12 mm$^2$): (a) force control; (b) displacement control.

In contrast to the previously discussed cyclic parameters, $w_{\text{diss}}$ shows a clear dependence on the load level, where higher load levels result in higher dissipated energy densities. The test series conducted at higher frequencies, particularly at 5.0 Hz, show a slightly reduced energy dissipation per cycle. No relevant influence was observed when comparing the standard joint geometry with the compact 8 × 24 mm$^2$ geometry.

Due to the almost constant progression, it is difficult to directly use $w_{\text{diss}}$ to define a failure criterion. Therefore, the dissipated energy density $w_{\text{diss}}$ per cycle was accumulated throughout the test, and the cumulative dissipated energy density $w_{\text{cum}}$ was calculated according to Eq. (7.7). This cumulative measure better reflects the total dissipated energy in the SG joint and can thus serve as a potential damage indicator.

$$w_{\text{cum}} = \sum_{i=1}^{n} w_{\text{diss},i} \tag{7.7}$$

Figure 7.13 shows the progression of $w_{\text{cum}}$ for the same test series as shown in Figure 7.12, at a frequency of 0.5 Hz and with the standard 12 × 12 mm$^2$ joint geometry. The parameter $w_{\text{cum}}$ exhibits a linear increase for all tests, with a clear dependence on the load level. While $w_{\text{diss}}$ in the respective cycles increases with the load level, the slope of the cumulative curve $w_{\text{cum}}$ becomes flatter at higher load levels.

Overall, a higher total dissipated energy density $w_{\text{cum}}$ up to failure is obtained for the tests at lower load levels. When comparing the control modes, the displacement-controlled tests Figure 7.13b show a higher cumulative dissipated energy density $w_{\text{cum}}$ at the end of the test compared to the force-controlled tests Figure 7.13a.

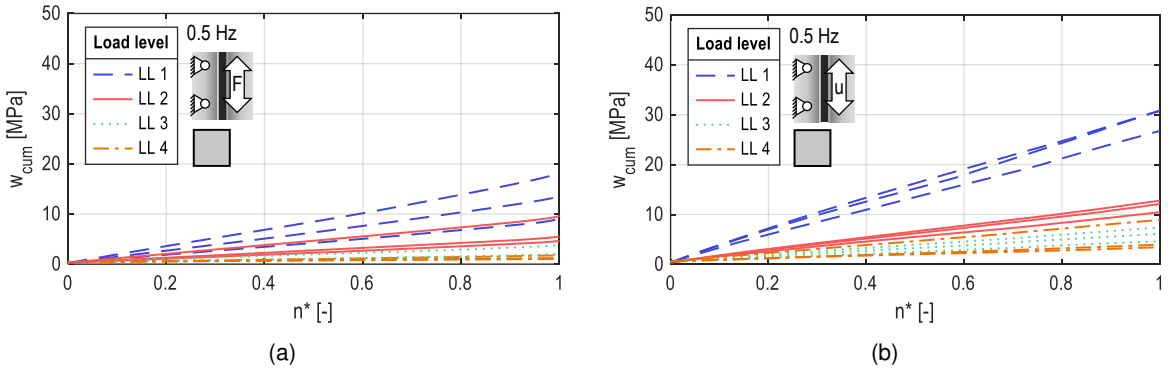


**Figure 7.13:** Progression of the cumulative dissipated energy density $w_{\mathrm{cum}}$ ($f$ = 0.5 Hz, 12 × 12 mm$^2$): (a) force control; (b) displacement control.

To analyze the influence of test frequency on the dissipated energy density $w_{\mathrm{cum}}$, Figure 7.14a shows the test series with a frequency of 5.0 Hz and the standard joint geometry under force control. Compared to the 0.5 Hz series in Figure 7.13a, the curves show a steeper increase, resulting in higher $w_{\mathrm{cum}}$ values. This indicates that at higher frequencies, more energy can be dissipated by the SG joint until failure.

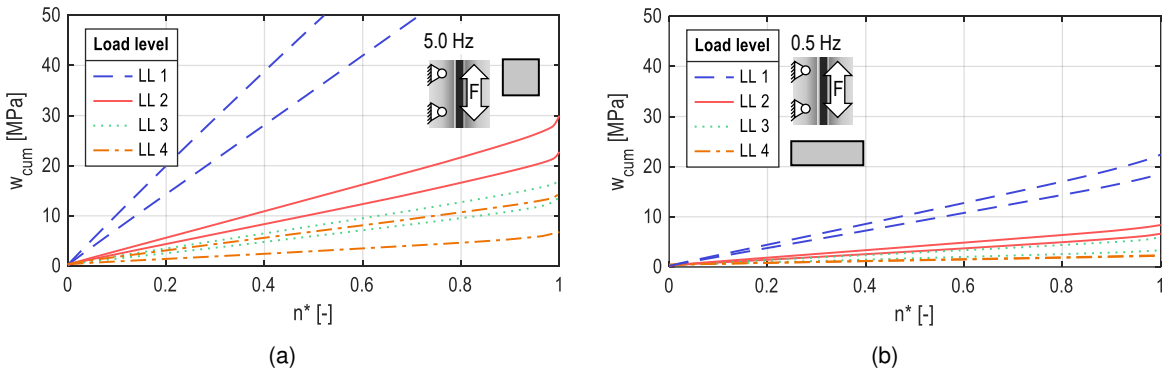


**Figure 7.14:** Progression of the cumulative dissipated energy density $w_{\mathrm{cum}}$ under force control: (a) 12 × 12 mm$^2$, $f$ = 5.0 Hz; (b) 8 × 24 mm$^2$, $f$ = 0.5 Hz.

To analyze the influence of joint geometry on $w_{\mathrm{diss}}$, Figure 7.14b presents the test series with a frequency of 0.5 Hz and the compact 8 × 24 mm$^2$ joint, in comparison with the standard geometry in Figure 7.13a. Only a slight increase in the slope and in $w_{\mathrm{cum}}$ is observed at the end of the test. The results indicate that the findings may be transferable to other joint geometries within the tested parameter range.

### 7.4.4 Damping

To characterize the damping properties of the SG joints, the specific damping capacity $\psi$ was calculated according to Eq. (2.42). The elastic strain energy $w_{\mathrm{el}}$ was calculated linearly to simplify the evaluation procedure. Preliminary tests showed only minor deviations between damping values calculated with linear and nonlinear stiffness assumptions. For the

assessment of damping under LCF loading, the specific damping capacity $\psi$ was converted to the loss factor $\eta$ based on Eq. (2.44).

The evolution of the loss factor $\eta$ is shown in Figure 7.15 for the test series conducted at 0.5 Hz with the standard $12 \times 12$ mm$^2$ joint geometry. Similar to the dissipated energy density $w_{\text{diss}}$, the highest value of $\eta$ is observed in the first cycle. Subsequently, differences between the two control modes become apparent. In the force-controlled tests shown in Figure 7.15a, $\eta$ exhibits a linear evolution until the end of the test, where a further increase occurs. In addition, higher load levels lead to higher damping values. In the displacement-controlled tests shown in Figure 7.15b, an increase in $\eta$ begins at a normalized cycle count of approximately $n^* = 0.6$. This increase may be explained by friction effects within the joint due to the high degree of partial failure. No clear dependence on the load level can be identified for the displacement-controlled tests.

Throughout most of the test duration, both cyclic parameters $w_{\text{diss}}$ and $\eta$ exhibit relatively continuous behavior.

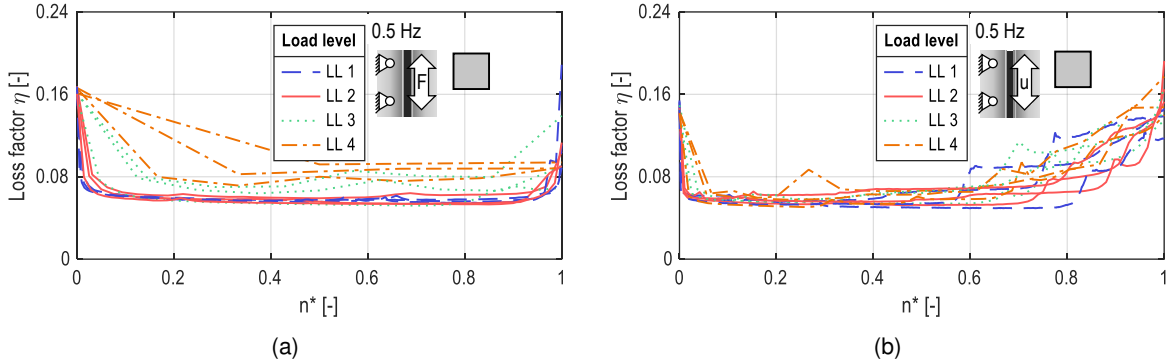


**Figure 7.15:** Progression of the loss factor $\eta$ ($f$ = 0.5 Hz, $12 \times 12$ mm$^2$): (a) force control; (b) displacement control.

To analyze the influence of the test frequency, Figure 7.16a shows the test series at 5.0 Hz with the standard $12 \times 12$ mm$^2$ joint geometry under force control. For comparison with the compact $8 \times 24$ mm$^2$ joint, Figure 7.16b presents the test series at 0.5 Hz under force control. Both test series in Figure 7.16 show a significantly lower dependence on the load level, despite being conducted under force control. Apart from this, both test series exhibit behavior similar to the force-controlled test series in Figure 7.15a at 0.5 Hz with the standard $12 \times 12$ mm$^2$ joint geometry.

## 7.5 Discussion of Failure Criteria

As described in section 7.3, termination criteria must be defined to end the cyclic tests, particularly under displacement control. Without such a definition, the test procedure would continue indefinitely, making it difficult to use the number of cycles as a performance measure, as commonly done in cyclic testing. As discussed in section 2.3.5, several approaches

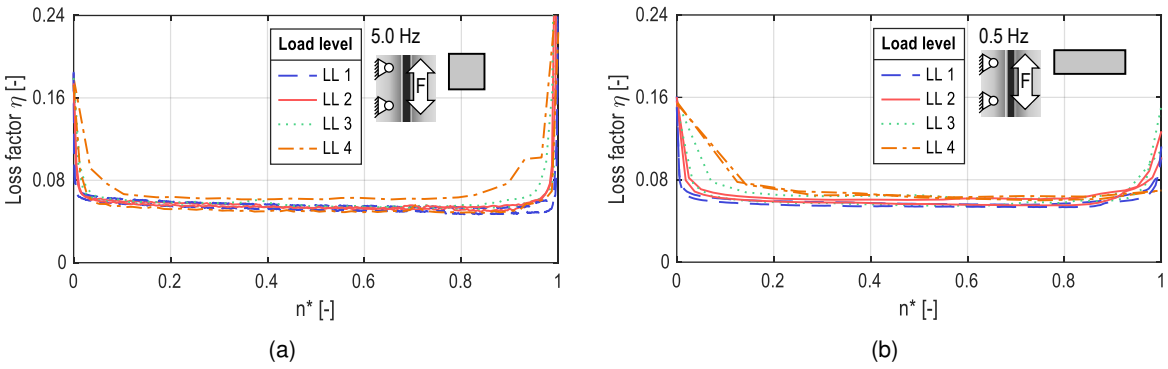


**Figure 7.16:** Progression of the loss factor $\eta$ (force control): (a) 12 × 12 mm$^2$ – $f$ = 5.0 Hz; (b) 8 × 24 mm$^2$ – $f$ = 0.5 Hz.

exist for defining termination criteria. However, most were developed for cyclic tests on steel or soil specimens and are therefore not directly applicable to SG joints.

Building on previous work by (Müller et al. 2025c), the four cyclic parameters introduced in section 7.4 were considered as potential failure criteria. Based on the results presented in (Müller et al. 2025c), which identified dynamic stiffness $G_{\mathrm{Max}}$ and cumulative energy density $w_{\mathrm{cum}}$ as the most robust and practically applicable parameters, this chapter, therefore, focuses on these parameters and evaluates their sensitivity to changes in test frequency and joint geometry. The loss factor $\eta$ and the deviation of the feedback signal $\delta_{\gamma(\mathrm{F})}$, $\delta_{\tau(\mathrm{U})}$ could, in principle, also be calibrated for the present dataset. While this would be feasible, it falls outside the scope of this thesis, as no clear benefit for the seismic design of SG joints can be expected from their application.

## 7.5.1 Concept for the Defining of Failure Criteria

### 7.5.1.1 General Concept

The fundamental behavior of all analyzed cyclic parameters showed notable similarities between force- and displacement-controlled tests. The progression of the parameters and the complete fracture of the specimen at the end of the force-controlled tests served as the basis for defining the failure of the SG joint. Building on these cyclic parameters, methods for defining failure criteria were proposed and compared.

The general procedure is illustrated in Figure 7.17 using the example of the dynamic stiffness $G_{\mathrm{Max}}$. To describe the parameter trend in the force-controlled tests, illustrated in Figure 7.17a, a polynomial function was fitted to the parameter curve. For the example of $G_{\mathrm{Max}}$, a first-degree polynomial was used. The value of the function at the time of failure $(n^* = 1)$, denoted as $G_{\mathrm{Max,Fail}}$, was then identified in the parameter history of the displacement-controlled tests (Figure 7.17b), and the corresponding number of cycles to failure $N_{\mathrm{f}}$ was determined from the associated $n^*$ value. Based on this approach, different failure criteria were defined, and their influence was subsequently examined and assessed.

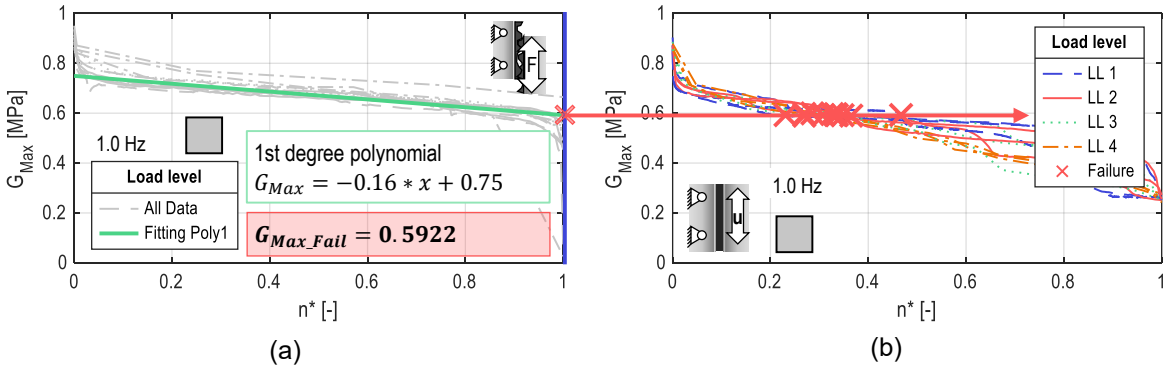


**Figure 7.17:** Scheme for determining the number of cycles to failure using the cyclic parameter $G_{\mathrm{Max}}$ as an example: (a) force-controlled test; (b) displacement-controlled test. Adapted from (Müller et al. 2025c).

#### 7.5.1.2 Preprocessing and Basis of Fitting Models

The fitting process for the different cyclic parameters was implemented in MATLAB. A continuous progression in the mid-range of the parameter curves was observed across all tests. A challenge lies in the unequal number of data points across different specimens, particularly between load levels. Tests conducted at lower load levels, which typically involve a higher number of cycles to failure, would disproportionately influence the fitting result. To compensate for this effect, a weighted least squares regression was used for all fittings. The weighting factor $w$ was defined based on the total number of data points per test, ensuring an overall normalized weight of 1 per test, as shown in:

$$w = \frac{1}{\text{Datapoints per experiment}} \tag{7.8}$$

The basis for the further analysis in this thesis is the set of fitting models used and published by (Müller et al. 2025c). Suitable polynomial functions were selected based on the shape of the characteristic parameter curves. The functions were chosen to accurately fit the stable region of the mean parameter curve. Due to the selected fitting algorithm and the use of low-order polynomial functions, the fitting results were only slightly affected by changes in the curve progression prior to specimen failure in the force-controlled tests. In all models, the normalized cycle count $n^*$, as defined in Eq. (7.3), was selected as one input. To define the failure values $G_{\mathrm{Max,Fail}}$ and $w_{\mathrm{cum,Fail}}$, the selected functions were evaluated at $n^* = 1$.

The failure criteria presented by (Müller et al. 2025c) were developed from experimental tests conducted at a loading frequency of 1.0 Hz using the standard $12 \times 12$ mm$^2$ joint geometry. In this thesis, the fitting models are further examined with respect to their dependence on frequency and joint geometry. Subsequently, it is analyzed to what extent a modification of the models has to be introduced to account for these effects. This analysis was performed with the two criteria recommended by (Müller et al. 2025c): the dynamic stiffness $G_{\mathrm{Max}}$ and the cumulative dissipated energy density $w_{\mathrm{cum}}$.

## 7.5.2 Modified Fitting Models for Defining Failure

### 7.5.2.1 Modified Dynamic Stiffness Criteria

Basis for the fitting model to represent the dynamic stiffness $G_{\mathrm{Max}}$ is a first-degree polynomial (Poly1) fit, as proposed in (Müller et al. 2025c). Due to the Mullins effect in the first cycle and the unstable complete failure at the end of the test, relevant deviations occur at the beginning and end of the curves. To ensure a reliable fit in the continuous region, without the need to manually exclude data points from the beginning and end, a robust least-squares regression using the bisquare weights method was selected. This method involves the adjustment of the weight of each data point according to its distance from the trend line, thereby minimizing the influence of outliers in the data set. As shown in section 7.4.2, and particularly when analyzing the parameter $G_{\mathrm{Max,Initial}}$ in Figure 7.11, an influence of the test frequency $f$ on the parameter course could be determined. This dependency on the test frequency was also analyzed in the main course of the parameter $G_{\mathrm{Max}}$ and therefore had to be described as a function of both the normalized cycle count $n^*$ and the test frequency $f$. To capture this influence in the fittings, different approaches were analyzed:

In a first approach, a separate first-degree polynomial fit was performed for each of the three tested frequencies, as proposed in the general concept shown in Figure 7.17. This resulted in one linear fitting per frequency, as shown in Table 7.3. The stiffness at failure $G_{\mathrm{Max,Fail}}$ was calculated in accordance with section 7.5.1.2 by solving the polynomial function at the moment of failure, corresponding to the normalized cycle count $n^* = 1$.

The second approach was the extension of the polynomial of first degree. In its initial form, the response $G_{\mathrm{Max}}$ was expressed as a linear function of a single variable, the normalized cycle count $n^*$. To account for the additional frequency dependency observed in the experiments, the model was extended to a two-variable first-order polynomial including an interaction term. The resulting formulation corresponds to a Poly11 fit, which is also given in Table 7.3. The stiffness at failure $G_{\mathrm{Max,Fail}}$ can then be calculated based on the test frequency $f$ by solving the Poly11 equation at the value $n^* = 1$. The surface of the Poly11 fit for the $12 \times 12$ mm$^2$ joint geometry is shown in Figure 7.18a with the data points and $G_{\mathrm{Max,Fail}}$ indicated as a red line.

To better adapt the Poly11 fitting approach to the behavior of polymeric materials, a further modification was introduced. To describe the behavior of polymeric materials under the influence of loading time or loading rate, for example in creep tests, an exponential function is a common approach (Schwarzl 1990). It was therefore possible to generate the two-variable first-order polynomial fit using the logarithm of the test frequency, resulting in the Poly1Log1 fit shown in Table 7.3.

To compare the three approaches, the resulting stiffness at failure $G_{\mathrm{Max,Fail}}$ is shown in Figure 7.19a in different colors. For the Poly1 approach, only the three reference points were calculated. Therefore, the connection between them is shown using a dashed line. For both two-variable first-order polynomial functions, the data points at the tested frequencies are

**Table 7.3:** Fitting functions for the modified dynamic stiffness criterion $G_{\mathrm{Max}}$ ($12 \times 12$ mm$^2$).

| Fitting model | Polynomial equation | Fitting result | $R^2$ | Failure value ($G_{\mathrm{Max,Fail}}$) | Unit |
|---|---|---|---|---|---|
| | | **$12 \times 12$ mm$^2$ joint geometry** | | | |
| Poly1 (0.5 Hz) | $p_1 \cdot n^* + p_2$ | $p_1 = -0.1801$<br>$p_2 = 0.7459$ | 0.96 | 0.5658 | [MPa] |
| Poly1 (1.0 Hz) | $p_1 \cdot n^* + p_2$ | $p_1 = -0.1573$<br>$p_2 = 0.7495$ | 0.97 | 0.5922 | [MPa] |
| Poly1 (5.0 Hz) | $p_1 \cdot n^* + p_2$ | $p_1 = -0.1505$<br>$p_2 = 0.7827$ | 0.98 | 0.6321 | [MPa] |
| Poly11 | $G_{\mathrm{Max}}(n^*, f) =$<br>$p_{00}+$<br>$p_{10} \cdot n^*+$<br>$p_{01} \cdot f+$<br>$p_{11} \cdot n^* \cdot f$ | $p_{00} = 0.7365$<br>$p_{01} = 0.009798$<br>$p_{10} = -0.1681$<br>$p_{11} = 0.002156$ | 0.98 | $0.5684+$<br>$0.0112 \cdot f$ | [MPa] |
| Poly1Log1 | $G_{\mathrm{Max}}(n^*, f) =$<br>$p_{00}+$<br>$p_{10} \cdot n^*+$<br>$p_{01} \cdot \log_{10}(f)+$<br>$p_{11} \cdot n^* \cdot \log_{10}(f)$ | $p_{00} = 0.7529$<br>$p_{01} = 0.04395$<br>$p_{10} = -0.1688$<br>$p_{11} = 0.02075$ | 0.98 | $0.5841+$<br>$0.0647 \cdot \log_{10}(f)$ | [MPa] |

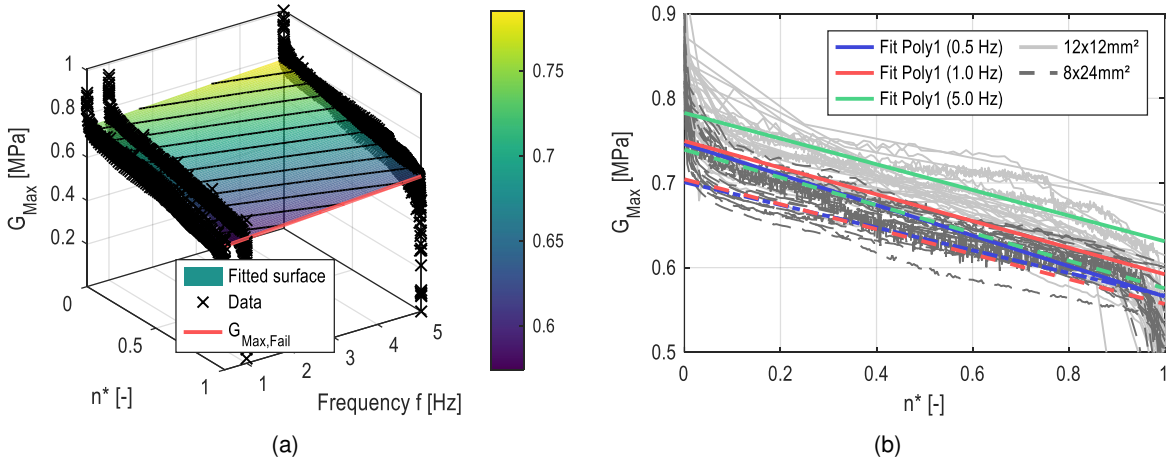


**Figure 7.18:** Modified fitting functions for the dynamic stiffness $G_{\mathrm{Max}}$ criteria: (a) Poly11 fit for the $12 \times 12$ mm$^2$ joint geometry under force control; (b) comparison of the Poly1 fitting for the two joint geometries.

also shown and connected with a solid line. In principle, all fitting models cover the trend of an increasing $G_{\mathrm{Max,Fail}}$ with an increasing test frequency $f$. It is notable, however, that the Poly1 and Poly1Log1 models show very good agreement, whereas the Poly11 model does not represent the pronounced increase of $G_{\mathrm{Max,Fail}}$ from 0.5 to 1.0 Hz as accurately.

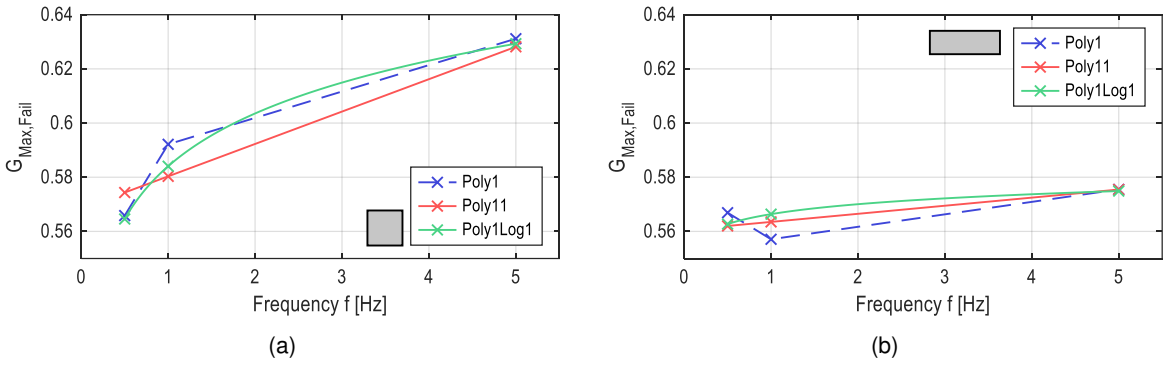


**Figure 7.19:** Resulting $G_{\mathrm{Max,Fail}}$ values for the three fitting models (force control): (a) $12 \times 12$ mm$^2$; (b) $8 \times 24$ mm$^2$.

As mentioned in section 7.4.2, the alternative, compact $8 \times 24$ mm$^2$ joint showed slightly lower stiffness in both control modes, with a minor dependency on the test frequency. To compare the two geometries in greater detail, Figure 7.18b shows the experimental data of the $G_{\mathrm{Max}}$-parameter, in light ($12 \times 12$ mm$^2$) and dark ($8 \times 24$ mm$^2$) gray, clearly illustrating the general stiffness deviation. The Poly1 fitting models of $G_{\mathrm{Max}}$ are also shown for the three test frequencies $f$, with the $12 \times 12$ mm$^2$ geometry represented by solid lines and the $8 \times 24$ mm$^2$ geometry represented by dashed lines.

Generally, the slightly decreased stiffness of the $8 \times 24$ mm$^2$ joint geometry was represented reasonably well by the locations of the Poly1 fittings. However, when analyzing the influence of test frequency on $G_{\mathrm{Max}}$, a slight difference between the joint geometries becomes apparent.

At the start of the test, the influence of the frequency is identical for both geometries, with the 5.0 Hz curve showing notably higher values, while the curves for 0.5 Hz and 1.0 Hz appear almost identical. This similarity at the start of the test changes as the test progresses, where the two geometries show diverging frequency-dependent behavior. For the $12 \times 12$ mm$^2$ joint geometry, three relatively parallel curves can be observed. In contrast, with the compact $8 \times 24$ mm$^2$ joint, the initial difference at the beginning of the test nearly disappears by the end, leaving only a minor difference.

To examine this effect in more detail, the stiffness values at failure $G_{\mathrm{Max,Fail}}$ are presented in Figure 7.19b for the compact joint geometry, compared to the standard joint geometry in Figure 7.19a, based on all three evaluated fitting models. Here, the increase in $G_{\mathrm{Max,Fail}}$ with test frequency observed for the standard $12 \times 12$ mm$^2$ geometry is barely visible for the alternative $8 \times 24$ mm$^2$ joint.

A noticeable aspect is the decrease in $G_{\mathrm{Max,Fail}}$ at a test frequency of 1.0 Hz when determined using the Poly1 model. Given the overall very minor frequency influence, this deviation may potentially be explained by typical scatter observed in experimental investigations. The two-parameter fitting models are unable to represent this deviation. An overview of all analyzed fitting models including the $G_{\mathrm{Max,Fail}}$ values for the compact $8 \times 24$ mm$^2$ geometry is provided in Table 7.4.

**Table 7.4:** Fitting functions for the modified dynamic stiffness criterion $G_{\mathrm{Max}}$ ($8 \times 24$ mm$^2$).

| Fitting model | Polynomial equation | Fitting result | $R^2$ | Failure value ($G_{\mathrm{Max,Fail}}$) | Unit |
|---|---|---|---|---|---|
| | | **$8 \times 24$ mm$^2$ joint geometry** | | | |
| Poly1 (0.5 Hz) | $p_1 \cdot n^* + p_2$ | $p_1 = -0.1340$<br>$p_2 = 0.7009$ | 0.95 | 0.5669 | [MPa] |
| Poly1 (1.0 Hz) | $p_1 \cdot n^* + p_2$ | $p_1 = -0.1473$<br>$p_2 = 0.7044$ | 0.94 | 0.5571 | [MPa] |
| Poly1 (5.0 Hz) | $p_1 \cdot n^* + p_2$ | $p_1 = -0.1638$<br>$p_2 = 0.7393$ | 0.99 | 0.5755 | [MPa] |
| Poly11 | $G_{\mathrm{Max}}(n^*, f) =$<br>$p_{00}+$<br>$p_{10} \cdot n^*+$<br>$p_{01} \cdot f+$<br>$p_{11} \cdot n^* \cdot f$ | $p_{00} = 0.6839$<br>$p_{01} = 0.01134$<br>$p_{10} = -0.1234$<br>$p_{11} = -0.008355$ | 0.98 | $0.5605+$<br>$0.0030 \cdot f$ | [MPa] |
| Poly1Log1 | $G_{\mathrm{Max}}(n^*, f) =$<br>$p_{00}+$<br>$p_{10} \cdot n^*+$<br>$p_{01} \cdot \log_{10}(f)+$<br>$p_{11} \cdot n^* \cdot \log_{10}(f)$ | $p_{00} = 0.6988$<br>$p_{01} = 0.05954$<br>$p_{10} = -0.1324$<br>$p_{11} = -0.04735$ | 0.98 | $0.5664+$<br>$0.0122 \cdot \log_{10}(f)$ | [MPa] |

Based on the current investigations, it was not possible to determine with certainty which of the examined models was the best option for defining the failure criteria. The advantage of the two-parameter fitting models is that $G_{\mathrm{Max}}$ values could be determined for intermediate frequencies not explicitly tested. Based on investigations into the $G_{\mathrm{Max,Fail}}$ values of the $12 \times 12$ mm$^2$ joint geometry, the Poly1Log1 model showed significantly better agreement with the Poly1 fitting compared to the Poly11 fitting.

However, the Poly1 model offered the best adaptability to the real test data at the respective test frequency, independent of the theoretical model approaches to frequency influence. Consequently, the load cycles to failure in this work were determined using the $G_{\mathrm{Max}}$ failure criterion based on Poly1 fittings. For the $12 \times 12$ mm$^2$ joint geometry, the $G_{\mathrm{Max,Fail}}$ values from Table 7.3 were used and for the 8 x 24 mm$^2$ joint geometries, the values from Table 7.4 were used.

In addition, the Poly1Log1 fitting model allows the determination of stiffness values for intermediate frequencies, enabling a continuous representation over the entire investigated

frequency range. This makes it possible to derive stiffness values as a function of both the failure state of the SG joint and the loading frequency, which may be relevant for the design of SG joints under seismic loading.

#### 7.5.2.2 Modified Dissipated Energy Density Criteria

The fitting model used to characterize cumulative dissipated energy density $w_{\text{cum}}$ was initially based on a two-variable polynomial model following the approach proposed by (Müller et al. 2025c). Due to the dependency of $w_{\text{cum}}$ on the load level CSR, a first-degree polynomial over the normalized cycle count $n^*$ was combined with a second-degree polynomial to capture the CSR dependency, resulting in a Poly12 model. As shown in section 7.4.3, an additional dependency on the test frequency $f$ was observed for $w_{\text{cum}}$. To account for this, separate fitting models were derived for each tested frequency series. Based on this framework, two different modeling approaches were analyzed to define failure criteria for $w_{\text{cum}}$:

For the first approach, the discrete failure values of the dissipated energy density $w_{\text{cum}}$ were fitted directly as a function of CSR. To define the failure values of $w_{\text{cum}}$, theoretical values of the dissipated energy density $w_{\text{cum,Fail,Theo}}$ were determined at the end of the test for each specimen. To this end, the parameter curves of $w_{\text{cum}}$ were fitted with a first-degree polynomial as a function of the normalized cycle count $n^*$ to exclude unstable signal behavior near test termination. The values of $w_{\text{cum,Fail,Theo}}$ were then evaluated at $n^* = 1$, as illustrated in Figure 7.20. Adopting the phenomenological approach proposed by (Müller et al. 2025c), a one-variable second-degree polynomial, referred to as Poly2($w_{\text{cum,Fail,Theo}}$), was used to model the dependency of $w_{\text{cum,Fail,Theo}}$ on CSR.

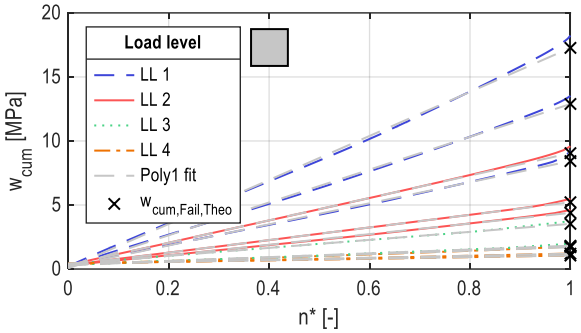


**Figure 7.20:** Schematic representation for determining the theoretical failure values of the dissipated energy density $w_{\text{cum,Fail,Theo}}$ ($f$ = 0.5 Hz, 12 × 12 mm$^2$).

For the second modeling approach, a combined surface fitting over both $n^*$ and CSR was used to represent the full parameter history. The same Poly12 model introduced above was applied as a surface fit, which yielded a good representation of the overall $w_{\text{cum}}$ behavior with respect to $n^*$ and CSR in (Müller et al. 2025c). The corresponding failure value $w_{\text{cum,Fail}}$, referred to as Poly12 @ $n^* = 1$, was analogously obtained by evaluating the surface fit of $w_{\text{cum}}$ at $n^* = 1$.

However, as shown in blue in Figure 7.21 for the 5.0 Hz test series as an example, both modeling approaches showed limitations when applied to the present dataset. In the direct regression of $w_{\mathrm{cum,Fail,Theo}}$, the quadratic polynomial Poly2($w_{\mathrm{cum,Fail,Theo}}$) produced a minimum at CSR = 90 %, while the two-variable Poly12 @ $n^* = 1$ fit resulted in negative values of $w_{\mathrm{cum,Fail}}$ at high load levels. Since both effects contradicted the expected material behavior, a monotonically decreasing function approaching zero at high CSR values, such as a power-law formulation, was found to better represent the load-level dependency.

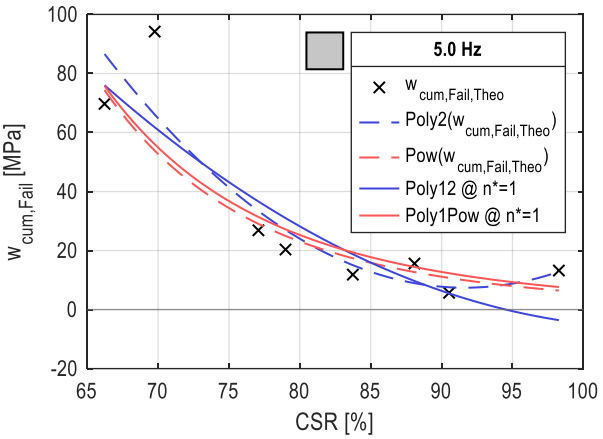


**Figure 7.21:** Comparison of fitting models for the dissipated energy density at failure $w_{\mathrm{cum,Fail}}$ ($f$ = 5.0 Hz, 12 × 12 mm$^2$).

This choice is supported by literature, where power-law functions have been used to describe the load-level dependence of dissipated energy in cyclic fatigue tests on adhesives and other viscoelastic polymeric materials (Liu et al. 2021; Movahedi-Rad et al. 2021). To address the modification of the phenomenological fitting model from (Müller et al. 2025c), both fitting models were re-evaluated based on a power-law formulation. For the first approach, a one-dimensional power-law fit, referred to as Pow($w_{\mathrm{cum,Fail,Theo}}$), was applied to the discrete values of $w_{\mathrm{cum,Fail,Theo}}$:

$$w_{\mathrm{cum,Fail,Theo}} = a_w^{\mathrm{F}} \cdot \mathrm{CSR}^{-b_w^{\mathrm{F}}} \tag{7.9}$$

Here, $a_w^{\mathrm{F}}$ and $b_w^{\mathrm{F}}$ denote the fitting parameters of the power-law model describing the dependence of $w_{\mathrm{cum,Fail,Theo}}$ on CSR, which is expressed as a percentage as defined in section 7.2.4. This power-law function can be linearized through a logarithmic transformation, allowing the fitting to be performed using standard linear regression analysis. The corresponding fitted curve is shown in Figure 7.21 for the 5.0 Hz series as a red dashed line.

For the second approach, a two-variable fitting model was implemented, using the full parameter history over the normalized cycles $n^*$ and CSR. To this end, the power-law from Eq. (7.9), which describes the dependency of $w_{\mathrm{cum}}$ on CSR, was combined with the linear increase of $w_{\mathrm{cum}}$ with the normalized cycles $n^*$. The two influences are represented in a product-type formulation referred to as the Poly1Pow model:

$$w_{\text{cum}} = a_w \cdot n^* \cdot \text{CSR}^{-b_w} \tag{7.10}$$

In this formulation, $a_w$ and $b_w$ denote model-specific fitting parameters for the Poly1Pow model. Since $w_{\text{cum}}$ is linear in $n^*$, the equation can still be fitted using linear regression despite representing a three-dimensional relationship. By expressing Eq. (7.10) in logarithmic form, the difference $\log_{10}(w_{\text{cum}}) - \log_{10}(n^*)$ can be treated as a single dependent variable, enabling a standard linear regression against $\log_{10}(\text{CSR})$:

$$\log_{10}(w_{\text{cum}}) - \log_{10}(n^*) = \log_{10}(a_w) - b_w \cdot \log_{10}(\text{CSR}) \tag{7.11}$$

This fitting approach corresponds to the established method for deriving S-N curves in fatigue analysis, as described by (Drebenstedt and Euler 2018). The logarithmic transformation allows for a more balanced treatment of residuals across the entire value range and avoids overweighting of high load levels, which would occur in a direct regression of Eq. (7.10) without transformation.

As described in section 7.4.3, the cyclic parameter $w_{\text{cum}}$ showed a rather continuous and stable progression throughout the tests without relevant deviations. Therefore, a weighted least-squares regression was used for all fits of $w_{\text{cum}}$, in contrast to the weighted robust least-squares regression applied for modeling the dynamic stiffness $G_{\text{Max}}$. The weighting factor $w$ was applied as shown in Eq. (7.8).

Figure 7.21 illustrates the fitting results for both approaches at an exemplary test frequency of 5.0 Hz. The two-variable Poly1Pow fit of Eq. (7.10), evaluated at $n^* = 1$ and referred to as Poly1Pow @ $n^* = 1$, is shown as a solid red line. The one-dimensional power-law fit of $w_{\text{cum,Fail,Theo}}$ from Eq. (7.9) as a function of CSR is shown as a dashed red line, together with the polynomial fits in blue.

Both fitting approaches based on the power function provided a consistent and physically plausible description of $w_{\text{cum,Fail}}$, avoiding unrealistic extrema or negative values. Consequently, the subsequent evaluation of $w_{\text{cum,Fail}}$ was based on these power-based fitting models.

To investigate the influence of the test frequency $f$ on the cumulative dissipated energy density $w_{\text{cum}}$, separate fitting models were created for each frequency series. The fitting results evaluated for $w_{\text{cum,Fail}}$ at $n^* = 1$ are presented in Figure 7.22a for the $12 \times 12$ mm$^2$ and in Figure 7.22b for the $8 \times 24$ mm$^2$ joint geometry, depending on CSR.

The trend of decreasing $w_{\text{cum,Fail}}$ with increasing CSR, previously observed in Figure 7.21, was confirmed for all test series. Regardless of the joint geometry, $w_{\text{cum,Fail}}$ increased significantly with increasing test frequency, indicating that the SG joint can sustain a higher number of load cycles before failure at elevated frequencies. The compact joint geometry,

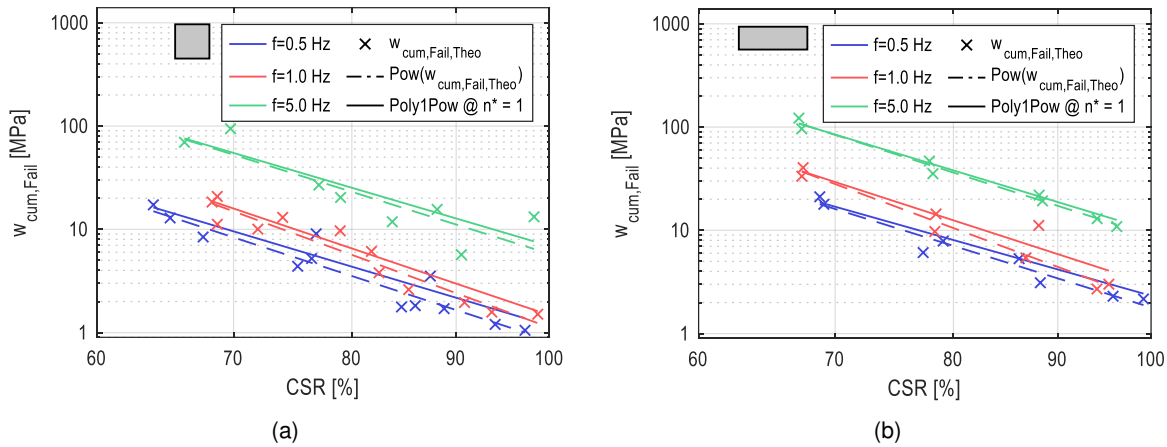


**Figure 7.22:** Fitting results for the cumulative dissipated energy density at failure $w_{\mathrm{cum,Fail}}$ as a function of the CSR for different test frequencies: (a) $12 \times 12$ mm$^2$; (b) $8 \times 24$ mm$^2$.

illustrated in Figure 7.22b, shows slightly higher values of $w_{\mathrm{cum,Fail}}$ across all test frequencies. However, the fundamental trends remained consistent with those of the standard geometry.

Comparing the two fitting approaches, the one-variable direct fitting Pow($w_{\mathrm{cum,Fail,Theo}}$) yielded slightly lower $w_{\mathrm{cum,Fail}}$ values in all cases than the Poly1Pow model. The Poly1Pow fitting tended to slightly overestimate $w_{\mathrm{cum,Fail,Theo}}$, especially at high load levels. However, since this approach considers the full parameter course of $w_{\mathrm{cum}}$ over the test duration, it benefits from a much larger number of input values available for the regression. As a result, this model is considerably less sensitive to potential outliers and generally more robust.

To analyze the influence of the test frequency $f$ on the cumulative dissipated energy density at failure $w_{\mathrm{cum,Fail}}$ in more detail, Figure 7.23 shows $w_{\mathrm{cum,Fail}}$ as a function of the test frequency $f$ for different load levels. Figure 7.23a presents the results for the standard $12 \times 12$ mm$^2$ joint geometry, while Figure 7.23b shows the values for the alternative $8 \times 24$ mm$^2$ geometry. The respective $w_{\mathrm{cum,Fail}}$ values were derived from the Poly1Pow fitting model by evaluating at representative CSR values. Due to the challenging test procedure, the experimental data for the different test frequencies could not be obtained at identical real load levels, making a direct comparison impossible.

To capture the frequency dependency, the different fitting approaches were evaluated. In addition to a first-degree polynomial (Poly1), a logarithmic function (Log10) and a power function (Pow) were used. It was found that both the Poly1 and power fittings yield good agreement for both joint geometries, while the Log10 fitting shows the most evident deviations. However, the limited range of tested frequencies makes it difficult to conclusively determine the most suitable fitting model. Based on these results, a linear increase of $w_{\mathrm{cum,Fail}}$ with frequency is assumed to be a reasonable approach within the investigated parameter range.

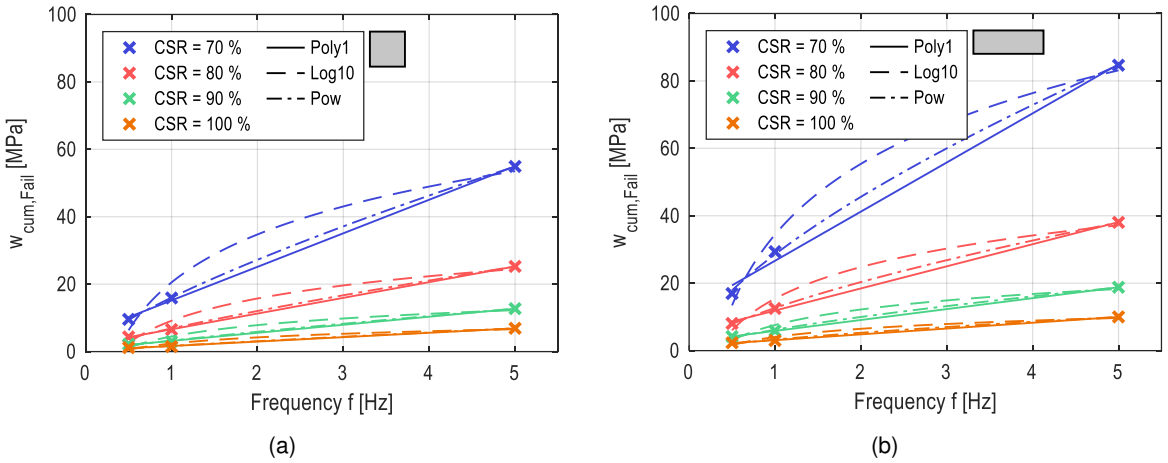


**Figure 7.23:** Fitting models for the cumulative dissipated energy density at failure $w_{\mathrm{cum,Fail}}$ as a function of the frequency for different load levels (CSR): (a) 12 × 12 mm$^2$; (b) 8 × 24 mm$^2$.

For the definition of the failure criteria in the scope of this work, a modification of the mathematical models to explicitly include frequency dependence was not necessary. As with the failure criterion based on the dynamic stiffness $G_{\mathrm{Max}}$, the failure criteria for $w_{\mathrm{cum}}$ were directly defined based on the experimental data for each tested frequency series. The progression of the cumulative dissipated energy density $w_{\mathrm{cum}}$ was described as a function of the normalized cycle count $n^*$ and the load level CSR. In contrast to earlier investigations in (Müller et al. 2025c), the Poly1Pow model was used here for the reasons discussed above. Table 7.5 summarizes the fitting parameters and the resulting failure values for the three tested frequencies and both joint geometries.

### 7.5.3 Failure Criteria Comparison

Based on the modified failure criteria from section 7.5.2, the number of cycles to failure $N_{\mathrm{f}}$ was determined for all displacement-controlled tests, according to the concept described in section 7.5.1. To this end, the cyclic parameter curves were compared with the theoretical failure values for each specimen and failure criterion, as determined by the previously defined fitting models. The cycle with the smallest deviation from the failure values $G_{\mathrm{Max,Fail}}$ and $w_{\mathrm{cum,Fail}}$ was identified and defined as the failure cycle.

To analyze the influence of the different failure criteria, the number of cycles to failure $N_{\mathrm{f}}$ for the force- and displacement-controlled test series are plotted against the load level CSR in Figure 7.24. For easier interpretation, the corresponding S-N curves were calculated and shown for each test series. In this initial approach, the S-N curves were obtained by fitting the data to the typical power law function shown in Eq. (2.35), with CSR used as the load parameter instead of $\sigma_a$. This function is commonly used to describe the failure behavior observed in HCF tests. The applicability of this approach to the investigations conducted at high load levels with few cycles to failure is discussed critically in the following.

**Table 7.5:** Fitting functions for the modified dissipated energy density criterion $w_{\mathrm{cum}}$.

| Fitting model | Polynomial equation | Fitting result | $R^2$ | Failure value ($w_{\mathrm{cum,Fail}}$) | Unit |
|---|---|---|---|---|---|
| **$12 \times 12$ mm$^2$ joint geometry** | | | | | |
| Poly1Pow (0.5 Hz) | $w_{\mathrm{cum}}(n^*, \mathrm{CSR}) = a \cdot n^* \cdot \mathrm{CSR}^{-b}$ | $a = 7.10 \cdot 10^{11}$<br>$b = 5.89$ | 0.828 | $7.10 \cdot 10^{11} \cdot \mathrm{CSR}^{-5.89}$ | [MPa] |
| Poly1Pow (1.0 Hz) | $w_{\mathrm{cum}}(n^*, \mathrm{CSR}) = a \cdot n^* \cdot \mathrm{CSR}^{-b}$ | $a = 3.14 \cdot 10^{13}$<br>$b = 6.66$ | 0.869 | $3.14 \cdot 10^{13} \cdot \mathrm{CSR}^{-6.66}$ | [MPa] |
| Poly1Pow (5.0 Hz) | $w_{\mathrm{cum}}(n^*, \mathrm{CSR}) = a \cdot n^* \cdot \mathrm{CSR}^{-b}$ | $a = 2.92 \cdot 10^{12}$<br>$b = 5.81$ | 0.723 | $2.92 \cdot 10^{12} \cdot \mathrm{CSR}^{-5.81}$ | [MPa] |
| **$8 \times 24$ mm$^2$ joint geometry** | | | | | |
| Poly1Pow (0.5 Hz) | $w_{\mathrm{cum}}(n^*, \mathrm{CSR}) = a \cdot n^* \cdot \mathrm{CSR}^{-b}$ | $a = 3.15 \cdot 10^{11}$<br>$b = 5.57$ | 0.866 | $3.15 \cdot 10^{11} \cdot \mathrm{CSR}^{-5.57}$ | [MPa] |
| Poly1Pow (1.0 Hz) | $w_{\mathrm{cum}}(n^*, \mathrm{CSR}) = a \cdot n^* \cdot \mathrm{CSR}^{-b}$ | $a = 1.86 \cdot 10^{13}$<br>$b = 6.40$ | 0.856 | $1.86 \cdot 10^{13} \cdot \mathrm{CSR}^{-6.40}$ | [MPa] |
| Poly1Pow (5.0 Hz) | $w_{\mathrm{cum}}(n^*, \mathrm{CSR}) = a \cdot n^* \cdot \mathrm{CSR}^{-b}$ | $a = 9.50 \cdot 10^{12}$<br>$b = 5.99$ | 0.958 | $9.50 \cdot 10^{12} \cdot \mathrm{CSR}^{-5.99}$ | [MPa] |

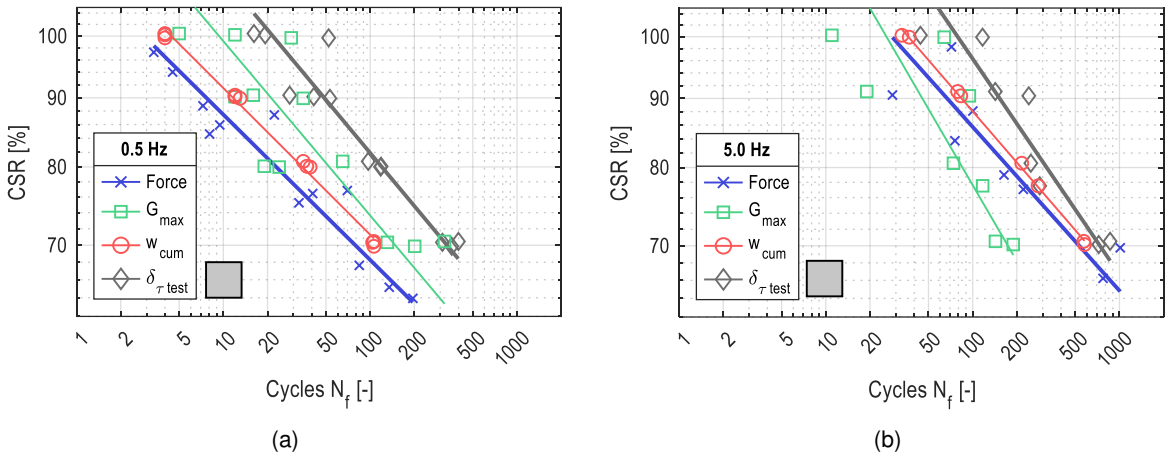


**Figure 7.24:** Resulting S-N curves for the different failure criteria analyzed: (a) $12 \times 12$ mm$^2$, 0.5 Hz; (b) $12 \times 12$ mm$^2$, 5.0 Hz.

The test results of the force-controlled series are shown in blue, while the results of the baseline displacement-controlled series with the machine-specific termination criterion $\delta_{\tau\ \text{test}}$ are shown in grey. The test results evaluated with the $G_{\text{Max}}$-criterion are shown in green, and the $w_{\text{cum}}$ criterion in red.

Figure 7.24a shows the series with a test frequency of 0.5 Hz, and Figure 7.24b shows the series with 5.0 Hz, both for the standard $12 \times 12$ mm$^2$ joint geometry. In both series, the force-controlled tests exhibited lower numbers of cycles to failure $N_{\text{f}}$ than the displacement-controlled series with $\delta_{\tau\ \text{test}}$ termination criterion.

Analyzing the results based on the dynamic stiffness parameter $G_{Max}$, a pronounced reduction in the number of cycles to failure $N_{\text{f}}$ is observed compared to the baseline $\delta_{\tau\ \text{test}}$ series. Notably, this $G_{Max}$-criterion shows high scatter, particularly at the two highest load levels. This scatter is greater than that observed for the other criteria. A possible explanation lies in the behavior of the cyclic parameter $G_{Max}$, as discussed in section 7.4.2. The reduction in stiffness during displacement-controlled tests was notably less consistent than in force-controlled tests and was characterized by extended plateau regions. If the failure stiffness $G_{Max,Fail}$ lay within such a region, it led to large variations in the number of cycles to failure $N_{\text{f}}$.

Another notable observation is the position of the $G_{Max}$ S-N curve for the two frequencies. At a test frequency of 0.5 Hz (Figure 7.24a), the curve lies between the force-controlled and the baseline $\delta_{\tau\ \text{test}}$ curves. At 5.0 Hz test frequency (Figure 7.24b), the curve is clearly shifted toward the force-controlled series, yielding significantly more conservative values. Since there was typically still considerable residual strength at the point when $G_{\text{Max,Fail}}$ was reached in the tests, as analyzed in (Müller et al. 2025d), the suitability of this highly conservative evaluation must be questioned.

The S-N curves based on the dissipated energy density $w_{\text{cum}}$ show significantly lower scatter within each parameter combination, regardless of load level or test frequency. Overall, they show much better agreement with the force-controlled series for all test frequencies, both in terms of position and slope of the curves. All S-N curves based on $w_{\text{cum}}$ lie slightly to the right of the force-controlled S-N curve, resulting in a slightly higher number of cycles to failure $N_{\text{f}}$.

To enable a more comprehensive analysis of the two failure criteria, considering all test frequencies and both joint geometries, two representative metrics were selected and calculated. Figure 7.25 shows the $R^2$ values of the power function fitting for each failure criteria as a measure of fit quality. The bar colors indicate the test frequency. Figure 7.25a presents the values for the standard $12 \times 12$ mm$^2$ joint geometry, and Figure 7.25b shows the values for the $8 \times 24$ mm$^2$ geometry.

Overall, the $R^2$ values for the $8 \times 24$ mm$^2$ joint geometry are consistently higher. For every parameter combination, values exceed 0.9. In contrast, for the $12 \times 12$ mm$^2$ geometry, both the failure criterion and, in some cases, the test frequency have a noticeable influence. In the force-controlled test series, the 5.0 Hz condition shows a slightly lower coefficient of

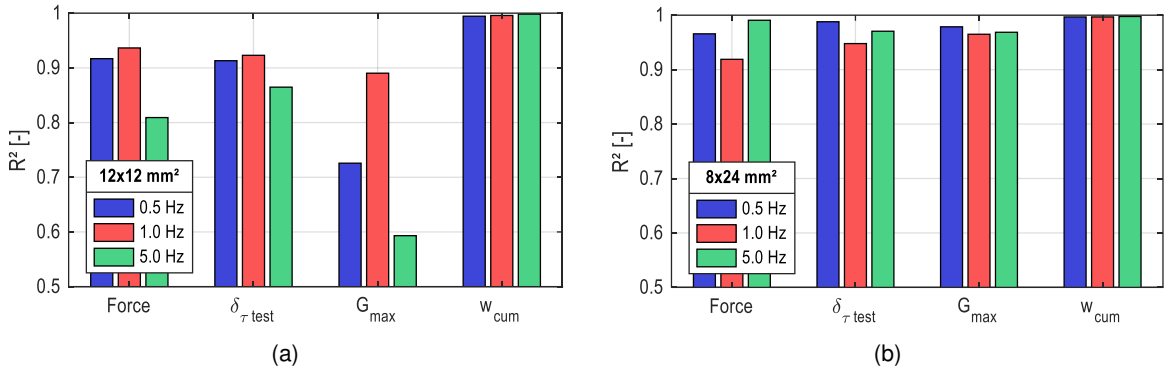


**Figure 7.25:** Analysis of the S-N curves: bar plot of the $R^2$ values of the S-N curve power function fits: (a) $12 \times 12$ mm$^2$; (b) $8 \times 24$ mm$^2$.

determination, which may be attributed to the more demanding test conditions under this parameter combination, specifically the high test speed at the operational limit of the testing machine for this joint geometry.

There are also substantial differences between the individual failure criteria for the displacement-controlled series. Notably, the low $R^2$ values for the $G_{\mathrm{Max}}$ criterion confirm the large scatter already observed in the previous section and visible in Figure 7.24. In contrast, the criterion based on the dissipated energy density $w_{\mathrm{cum}}$ yields the highest $R^2$ values across all frequencies.

To assess the agreement between the displacement-controlled and force-controlled test series, the root mean square error (RMSE) between the logarithmic number of load cycles to failure was calculated. For each data point of the displacement-controlled series, the theoretical number of load cycles to failure based on the force-controlled S-N curve was calculated to account for possible deviations in the load level. The results are shown in Figure 7.26a for the $12 \times 12$ mm$^2$ joint and in Figure 7.26b for the $8 \times 24$ mm$^2$ joint.

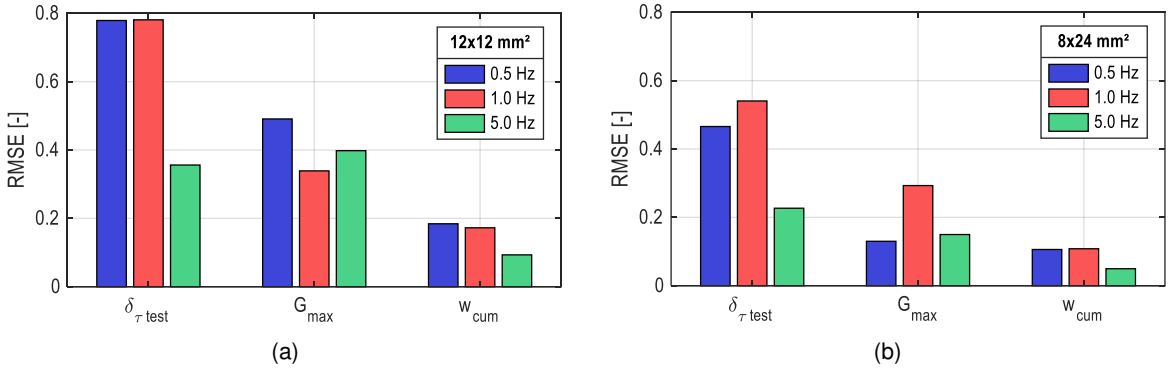


**Figure 7.26:** Analysis of the S-N curves: bar plot for the RMSE between the force- and displacement-controlled series: (a) $12 \times 12$ mm$^2$; (b) $8 \times 24$ mm$^2$.

For both joint geometries, the RMSE could be reduced by evaluating failure using the newly modified criteria based on $w_{\mathrm{cum}}$ and $G_{\mathrm{Max}}$, compared to the machine-based termination criterion $\delta_{\tau\ \mathrm{test}}$. Overall, the failure criterion based on the cumulative dissipated energy

density $w_{\mathrm{cum}}$ consistently showed the smallest deviation from the force-controlled series, regardless of the test frequency. The RMSE was also reduced using the $G_{\mathrm{Max}}$ evaluation for most parameter combinations.

### 7.5.4 Qualitative Crack Progression

The analyses presented in the preceding chapter for the definition of failure criteria of SG joints under LCF loading were based on evaluations of engineering stress and strain in the adhesive layer, determined with respect to the initial joint geometry prior to testing. The actual crack progression and the evolving joint geometry were not explicitly considered. To better contextualize the results, this section provides a qualitative analysis of crack propagation based on selected representative specimens.

For this purpose, two specimens tested at load level 3 under force- and displacement-controlled conditions were selected. Both tests were conducted at a loading frequency of 0.5 Hz. Image acquisition during the experiments was performed using the GOM ARAMIS system shown in Figure 7.1a. From the complete test sequences, representative images were selected to illustrate crack progression and are shown in Figure 7.27. For improved visibility, the crack paths were manually highlighted using colored curves.

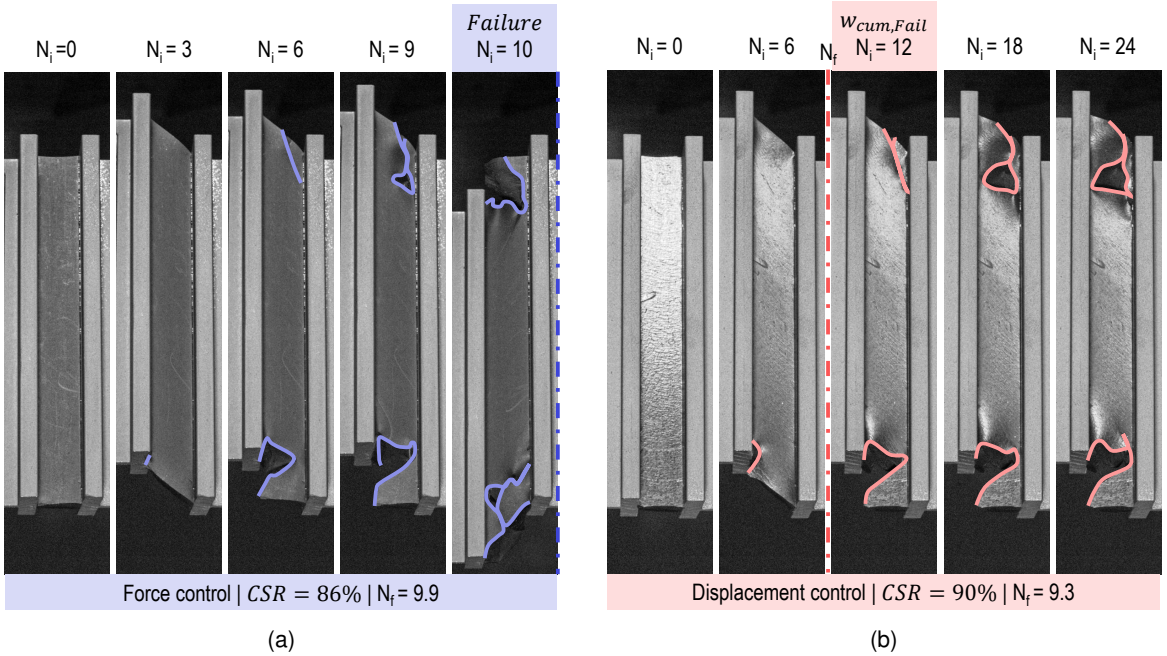


**Figure 7.27:** Crack progression in the SG joint during cyclic loading for the two control modes at $f$ = 0.5 Hz and load level 3: (a) force-controlled; (b) displacement-controlled.

Figure 7.27a shows the crack progression for the force-controlled specimen tested at a real load level of CSR = 86 %. The crack size increases continuously with the number of load cycles. Complete failure of the specimen occurs in the 10th cycle. The predicted number of cycles to failure, determined using the frequency-dependent extension of the Basquin model

introduced in section 7.6.2.2, is $N_f = 9.9$, which is in good agreement with the experimental observation for this exemplary specimen.

In contrast, Figure 7.27b shows the crack progression for the displacement-controlled specimen tested at CSR = 90 %. As this specimen was subjected to a significantly larger number of cycles, only every sixth cycle is shown for clarity. A distinct crack initiates within the first 12 cycles. However, further crack growth between 12 and 24 cycles remains limited. Even after 24 cycles, a substantial load-bearing cross-section of the joint is preserved. The specimen was subjected to more than 40 cycles until the termination criterion of the testing machine was reached. Based on the energy-based failure criterion $w_{\text{cum}}$ defined in this chapter, theoretical failure was identified at cycle $N_i = 12$ for this displacement-controlled specimen. At this stage, the crack length is comparable to that observed in the force-controlled specimen shortly before final failure ($N_i = 9$). The extended Basquin model predicts $N_f = 9.3$ cycles to failure.

These observations confirmed the fundamentally different failure behavior under the two loading conditions, as discussed in section 7.3.1 and section 7.3.2.1. The displacement-controlled specimen exhibited a significantly more gradual failure behavior, representing typical facade systems subjected to imposed deformations. At the point corresponding to the defined failure based on the $w_{\text{cum}}$ criterion, a substantial residual cross section remained, and crack propagation progressed only slowly with further cycling. The residual performance of SG joints after LCF loading was further analyzed in (Müller et al. 2025d). A strong correlation between residual load-bearing capacity and pre-damage levels was revealed, with significant residual performance at the theoretical failure of the displacement-controlled specimens.

In contrast, the force-controlled specimen, representing load-bearing SG joints in self-supporting glass constructions, showed critical behavior. A considerable load-bearing cross section remained until shortly before failure, followed by a complete loss of load-bearing capacity within the final cycle. These observations were consistent with the findings reported in (Müller et al. 2025d).

### 7.5.5 Proposal for Failure Criteria in Low-Cycle Fatigue Testing

In summary, a successful modification of the failure criteria defined by (Müller et al. 2025c) to accommodate different test frequencies and joint geometries was demonstrated. The cyclic parameter curves of the dynamic stiffness $G_{\text{Max}}$ and the cumulative dissipated energy density $w_{\text{cum}}$ were modeled mathematically. To model $w_{\text{cum}}$, a Poly1Pow model was used in contrast to (Müller et al. 2025c). Failure in the displacement-controlled tests could be defined accordingly. Based on the identified failure points, power law functions were fitted to generate the S-N curves.

Analogous to the analysis conducted by (Müller et al. 2025c), the S-N curve based on the $w_{\text{cum}}$ criterion showed the highest agreement with the force-controlled series. Additionally,

consistently high coefficients of determination were obtained for all parameter combinations, resulting in high quality fits with low scatter in the S-N curves. However, the determination of this cyclic parameter requires a complex calculation method. Due to the two-parameter fitting model required for each frequency, the parameter curve over test duration as well as the load dependence must be analyzed, increasing the evaluation effort.

The failure criterion based on $G_{\mathrm{Max}}$ can be used due to the simpler calibration and calculation procedure. In particular, the parameter can be determined directly within the testing machine. It should be noted, however, that with the experimental dataset tested for the thesis, noticeably larger scatter was observed compared to the results reported by (Müller et al. 2025c), which increased the uncertainty of the test results when using this criterion.

For the following evaluation in this thesis, the displacement-controlled test series and the corresponding S-N curves were evaluated based on the $w_{\mathrm{cum}}$ criterion, due to the clearly higher quality of the resulting S-N curves. Accordingly, "Disp" without further specification refers exclusively to the $w_{\mathrm{cum}}$-based evaluation throughout this thesis, for the sake of clarity.

## 7.6 Assessment of Low-Cycle Fatigue Strength

In this section, the LCF strength is analyzed based on the cycles to failure determined from experimental tests. Major factors influencing the performance of SG joints under LCF-loading, such as load level, type of test control, test frequency, and the joint geometry, are examined and evaluated.

### 7.6.1 Load Level and Test Control

As demonstrated in the discussion of failure criteria in section 7.5, there is a clear dependence of the number of cycles to failure $N_{\mathrm{f}}$ on the load level in SG joints for both types of test control. This relationship is shown in Figure 7.28a as a function of the real load level, for an exemplary test series using the standard $12 \times 12$ mm$^2$ joint geometry and a test frequency of 1.0 Hz. In addition to the curve of the force-controlled test series shown in blue, two curves from the displacement-controlled test series are shown in red. For this parameter combination, the two curves obtained from the $w_{\mathrm{cum}}$ and $G_{\mathrm{Max}}$ failure criteria show good agreement. However, their comparison highlights the dependence of displacement-controlled failure values on the selected failure criterion.

All curves show a decrease in the number of cycles to failure $N_{\mathrm{f}}$, as the load level increases. This relationship can be described by the typical power function given in Eq. (2.35). The strong agreement between the test data and the power fitting, particularly for the force-controlled tests and the displacement-controlled tests using the $w_{\mathrm{cum}}$ failure criterion, was already demonstrated by the high $R^2$ values shown in Figure 7.25 when comparing the

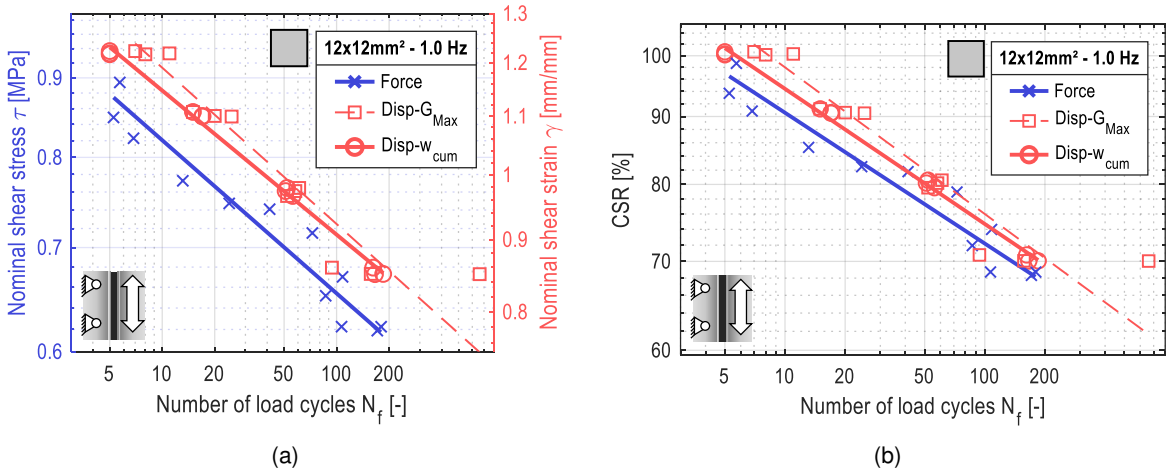


**Figure 7.28:** Effect of load level and test control on the number of load cycles based on: (a) real applied stress and strain values; (b) normalized CSR.

different failure criteria. Therefore, within the load range investigated, the number of cycles to failure $N_f$ can be predicted with high accuracy as a function of the load level. The larger deviations of the data points for the S-N curve with the $G_{Max}$ criterion are particularly evident at lower load levels.

To compare the two types of test control, the curves are plotted against the normalized (CSR) in Figure 7.28b. This clearly shows that the force-controlled test series yields the most conservative test results compared to the displacement-controlled tests with both failure criteria.

## 7.6.2 Test Frequency

### 7.6.2.1 Analysis of Experimental S-N Curves

To analyze the effect of the test frequency $f$ on the LCF performance of the SG specimens, three test series were conducted at frequencies of 0.5, 1.0, and 5.0 Hz for both types of test control. The influence of frequency is illustrated in Figure 7.29 for the standard $12 \times 12$ mm$^2$ joint geometry. Figure 7.29a presents the results for the force-controlled tests, while Figure 7.29b shows those for the displacement-controlled tests. An S-N curve was obtained for each frequency series by linear regression of the classical Basquin power law Eq. (2.35) to better visualize the data trend.

For both types of test control, a pronounced increase in $N_f$ with increasing test frequency $f$ is observed. A more detailed comparison reveals that the force-controlled data points in Figure 7.29a exhibit a distinctly more random distribution across the entire load range CSR. However, according to the test concept, they were tested at four specific load levels. This variability could be attributed to the more complex experimental control and the evaluation

based on actual load levels. In contrast, the displacement-controlled tests show much smaller variations in the real load level.

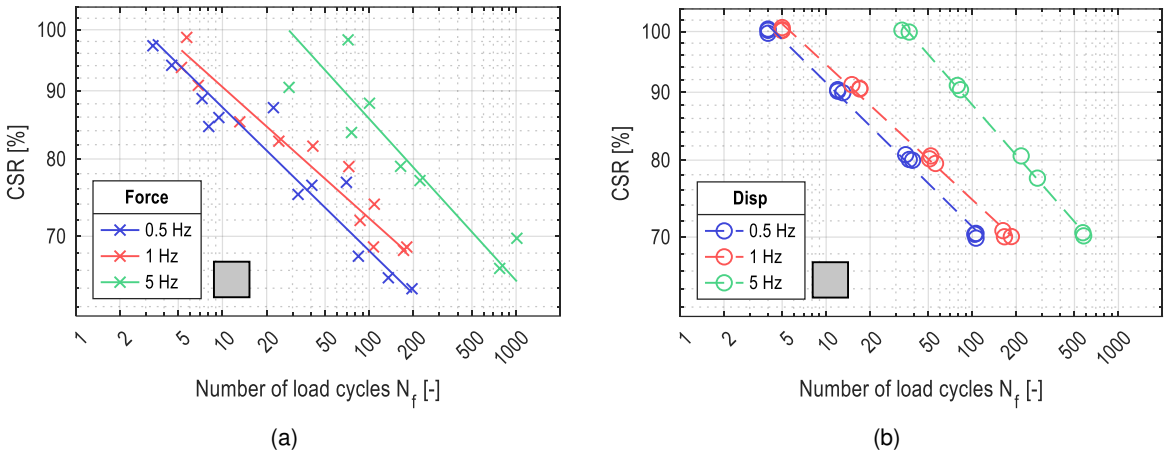


**Figure 7.29:** Effect of the test frequency $f$ on the number of load cycles to failure ($12 \times 12$ mm$^2$ joint geometry): (a) force-controlled test series; (b) displacement-controlled test series.

The scatter of the individual data points in the S-N curves for the force-controlled tests is comparable for the 0.5 Hz and 1.0 Hz series. The series at the highest frequency, 5.0 Hz, displays slightly larger deviations from the regression line, particularly at higher load levels, which may also result from the test setup. In the displacement-controlled tests, all data points align well with the regression lines, consistent with the discussion in section 7.5.3. However, it should again be noted that these results strongly depend on the chosen failure criterion.

All S-N curves determined for the different test frequencies show a comparable slope and a pronounced horizontal shift along the x-axis. To examine these relationships in greater detail, characteristic parameters of the regression lines were determined and evaluated. In general, S-N curves can be described by the slope $m$ and the parameter $a$. The parameter $a$ represents the number of cycles to failure at $\mathrm{CSR} = 10^0 = 1$, corresponding to the intersection of the regression line with $\log \mathrm{CSR} = 0$. Since this point lies outside the relevant range for describing the S-N curves, a theoretical value of the cyclic stress ratio $\mathrm{CSR}_{N=50}$ was additionally determined. The value $\mathrm{CSR}_{N=50}$ represents the load level at which failure is expected after 50 cycles. The choice of 50 cycles ensures that this value lies within the range of the experimental data for all curves.

To analyze the influence of test frequency on the LCF performance, the values of $\mathrm{CSR}_{N=50}$ and the slope $m$ are plotted in Figure 7.30 as a function of frequency $f$ for the different types of test control. For a more comprehensive interpretation, the data for the two failure criteria $G_{\mathrm{Max}}$ and $w_{\mathrm{cum}}$ are shown.

As shown for the parameter $\mathrm{CSR}_{N=50}$ in Figure 7.30a, all investigated configurations exhibit an increase in this parameter with increasing test frequency. This observation confirms the previous findings and indicates that a higher frequency allows a greater number of load cycles to be sustained before failure.

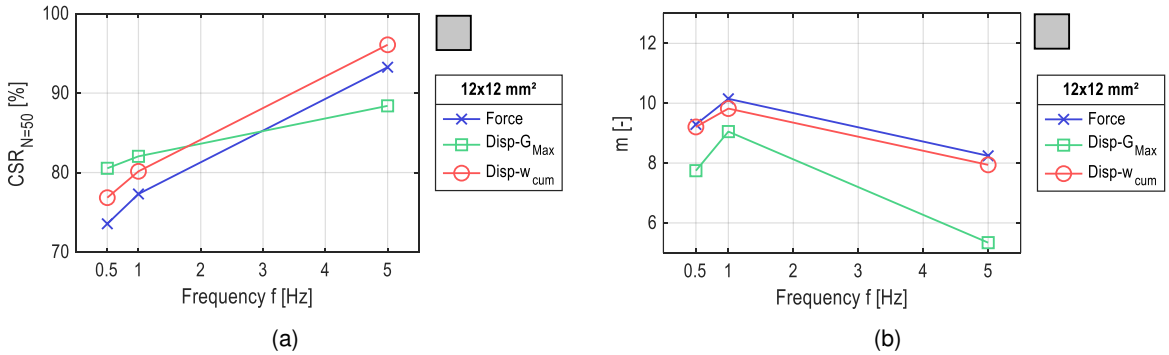


**Figure 7.30:** Analysis of frequency-dependent changes in S-N curve parameters for different failure criteria: (a) cyclic stress ratio at 50 load cycles to failure $\mathrm{CSR}_{N=50}$; (b) slope $m$.

For the slope $m$, shown in Figure 7.30b, no clear trend can be identified. An increase in test frequency from 1.0 to 5.0 Hz results in a decrease in the slope $m$ for all three configurations. However, this trend cannot be confirmed when the frequency is reduced from 1.0 to 0.5 Hz.

To describe the influence of frequency on the properties of polymers, the time–temperature superposition (TTS) principle can be used as an analogy. Although typically applied in the dynamic mechanical thermal analysis or creep experiments, it can, as shown by (Ciupack et al. 2018), also be adapted to fatigue tests. According to the TTS principle, a horizontal shift of the curves along the logarithmic time axis is possible, which would imply a negligible influence of the test frequency $f$ on the slope $m$. It should be noted, however, that the TTS principle was applied here as a qualitative analogy, as progressive damage and nonlinear material behavior may limit its strict validity in the present fatigue tests.

#### 7.6.2.2 Extension of the Basquin Model to Frequency-Dependent Fatigue

To enable the application of the TTS principle to the fatigue data obtained in this study, the X-axis showing number of cycles to failure $N_\mathrm{f}$ had to be converted into a time axis, following the approach proposed by (Ciupack et al. 2018). The corresponding failure time $t_\mathrm{f}$ can be calculated from the number of load cycles to failure $N_\mathrm{f}$ and the test frequency $f$ as follows:

$$t_\mathrm{f} = \frac{N_\mathrm{f}}{f} \tag{7.12}$$

Figure 7.31 presents the converted experimental data of the S-N curves from Figure 7.29 plotted against the failure time. For both types of test control, the data show very good agreement after conversion. The previously pronounced influence of the test frequency can be substantially reduced, or almost completely eliminated, by converting to the failure time $t_\mathrm{f}$. The relationship can still be described by a power law as a function of the load level CSR, expressed as a percentage as defined in section 7.2.4:

$$t_\mathrm{f} = a \cdot \mathrm{CSR}^{-m} \tag{7.13}$$

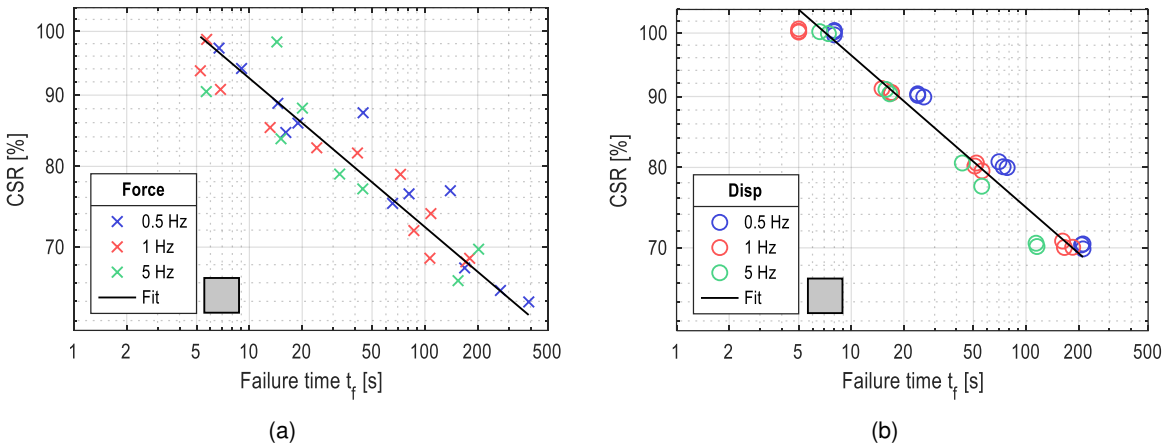


**Figure 7.31:** Failure time $t_f$ as a function of the load level CSR for all analyzed test frequencies ($12 \times 12$ mm$^2$): (a) force-controlled test series; (b) displacement-controlled test series.

Using Eq. (7.12), Eq. (7.13) can also be expressed in terms of the number of cycles to failure $N_f$ and the test frequency $f$ as follows:

$$\frac{N_f}{f} = a \cdot \mathrm{CSR}^{-m} \tag{7.14}$$

By rearranging this relationship, the extended frequency-dependent Basquin model for determining the number of cycles to failure $N_f$ can be defined. The value of $N_f$ can then be evaluated directly based on CSR and the test frequency $f$ using the two parameters $a$ and $m$, as follows:

$$N_f = a \cdot \mathrm{CSR}^{-m} \cdot f \tag{7.15}$$

On a decimal logarithmic scale, the experimental data can be approximated by a plane, indicating a linear relationship between the logarithm of the number of load cycles to failure $N_f$, the logarithm of the applied CSR, and the logarithm of the test frequency $f$:

$$\log_{10}(N_f) = \log_{10}(a) - m \cdot \log_{10}(\mathrm{CSR}) + \log_{10}(f) \tag{7.16}$$

The extended Basquin model introduces a frequency-dependent term $\log_{10} f$, accounting for the shift in fatigue life as a function of frequency without increasing the number of fitted parameters. As in the classic Basquin model, only the two parameters $m$ and $a$ must be determined. In logarithmic space, this formulation yields a planar relationship in three dimensions, extending the conventional two-dimensional S-N representation and capturing the observed trends in the experimental data.

The exemplary three-dimensional surface of the extended Basquin model used to determine the number of cycles to failure $N_f$, evaluated for the force-controlled test series with the standard $12 \times 12$ mm$^2$ joint geometry, is shown in Figure 7.32. In addition to the experimental

data used for the regression analysis, the S-N curves for the tested frequencies are shown in color for clarity. This representation shows very good agreement between the extended Basquin model and the experimental data. Table 7.6 summarizes the fitted parameters of the extended Basquin model for both types of test control.

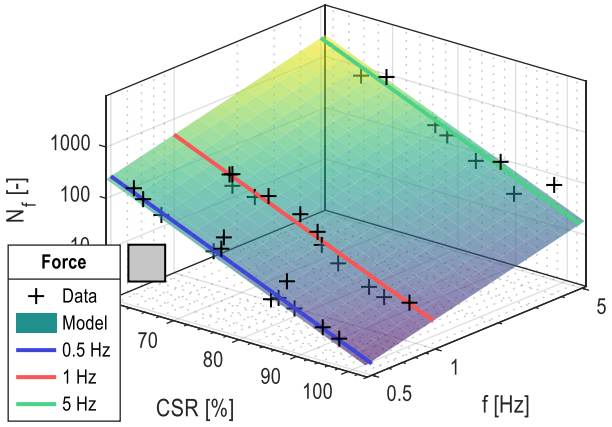


**Figure 7.32:** Extended frequency-dependent Basquin model for force-controlled tests with a 12 × 12 mm$^2$ joint geometry: three-dimensional surface of the number of cycles to failure $N_f$, including the experimental data and the resulting S-N curves for the investigated frequencies.

**Table 7.6:** Summary of the fitting parameters for the extended Basquin model in Eq. (7.15), with CSR expressed as a percentage and $f$ in Hz.

| Test control | Joint geometry | $m$ | Mean | | Prediction (95 % confidence) | | $R^2$ |
|---|---|---|---|---|---|---|---|
| | | | $\log_{10}(a)$ | $\mathrm{CSR}_{N=50}$ ($f$ = 1 Hz) | $\log_{10}(a)$ | $\mathrm{CSR}_{N=50}$ ($f$ = 1 Hz) | |
| Force | 12 × 12 mm$^2$ | 9.36 | 19.4 | 77.9% | 19.1 | 71.9% | 0.917 |
| | 8 × 24 mm$^2$ | 8.55 | 18.1 | 83.1% | 17.8 | 77.0% | 0.933 |
| Disp | 12 × 12 mm$^2$ | 9.12 | 19.1 | 80.8% | 18.9 | 77.4% | 0.977 |
| | 8 × 24 mm$^2$ | 8.61 | 18.3 | 84.9% | 18.1 | 79.5% | 0.947 |

To illustrate the difference between the S-N curves derived from the extended frequency-dependent Basquin model and those obtained from direct power-law fitting (see Eq. (2.35)), the curves from the extended Basquin model are shown as solid lines in Figure 7.33, whereas the direct power-law fits are represented by dashed lines. Figure 7.33a shows the force-controlled test series, and Figure 7.33b shows the displacement-controlled series. Overall, a good correlation between the two fitting approaches is observed for both control modes. Only a minor increase in the deviation between the S-N curves and the experimental data points is observed for the extended Basquin model. For the fitting process, this model offers the advantage that all three test frequencies can be combined within a single model, resulting in a larger data set and reducing the influence of outliers and experimental scatter.

The extended Basquin model incorporates the test frequency $f$ as a parameter and thus implicitly accounts for time-dependent effects. Although the model is formulated in terms

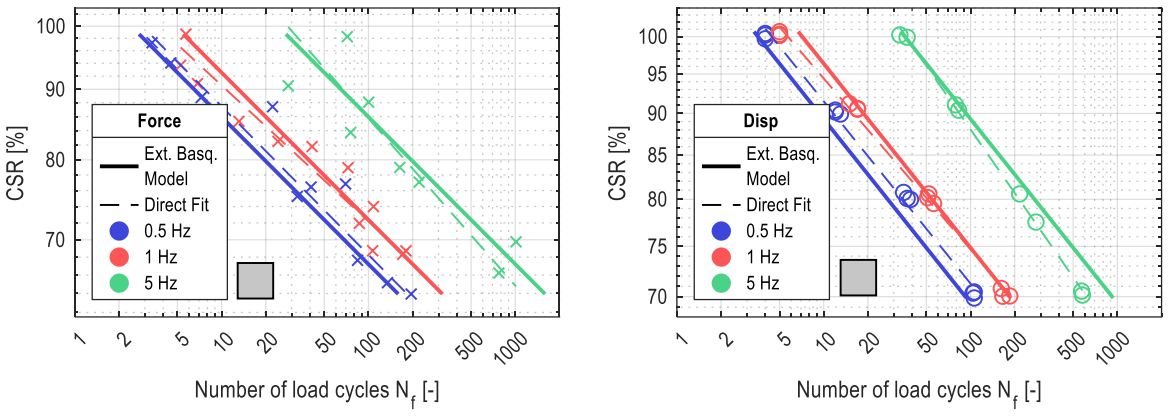


**Figure 7.33:** Difference between the S-N curves derived from the extended Basquin model and the direct fitting of the power function ($12 \times 12$ mm$^2$ joint geometry): (a) force-controlled test series; (b) displacement-controlled test series.

of the number of cycles to failure $N_f$, the frequency acts as a temporal scaling factor. Higher frequencies reduce the duration of each load cycle, particularly at peak load, thereby limiting damage progression per cycle. This results in an increased fatigue life with increasing frequency. Conversely, lower frequencies lead to longer load durations, which promote damage accumulation and accelerate failure.

Although the Basquin power law was originally developed for HCF, it represents a standard engineering approach for describing S-N relationships. In the present study, the model consistently yielded high coefficients of determination ($R^2 > 0.9$) for all parameter combinations, demonstrating that the power-law relationship accurately captured the observed behavior within the investigated load range. The Basquin approach was therefore retained. Extrapolation beyond the experimentally investigated range of load levels and cycle counts should be treated with caution.

## 7.6.3 Joint Geometry

### 7.6.3.1 Analysis of Experimental S-N Curves

This section examines the transferability of the findings on LCF performance obtained for the standard geometry to the compact joint geometry of $8 \times 24$ mm$^2$. The objective is to assess the applicability of the extended Basquin model within the intended application range defined by (ETAG 002-1; FKG 01/2021).

To illustrate the fundamental LCF strength, Figure 7.34 presents the number of cycles to failure $N_f$ for both tested joint geometries. Figure 7.34a shows the force-controlled tests, while Figure 7.34b depicts the displacement-controlled tests. For improved comparability between the different geometries, the data points of the $8 \times 24$ mm$^2$ joint are plotted with thicker markers than those of the standard geometry.

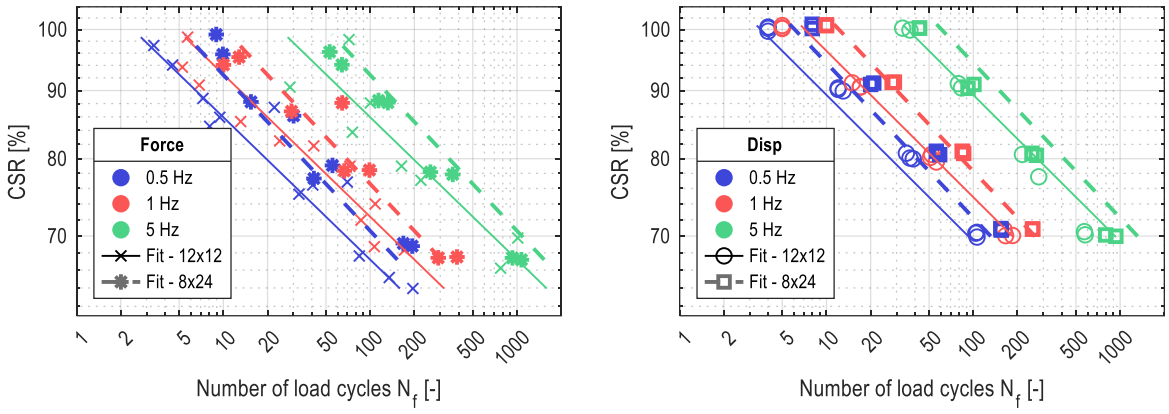


**Figure 7.34:** Effect of joint geometry on the number of load cycles to failure $N_f$ – comparison of experimental data and extended Basquin model fits: (a) force-controlled test series; (b) displacement-controlled test series.

In addition to the experimentally determined failure points, the regression lines corresponding to the individual test frequencies are shown to facilitate interpretation. In contrast to the representation in Figure 7.29, the previously developed extended Basquin model was directly applied to the datasets of both joint geometries. The applicability and transferability of this extended Basquin model to the compact joint configuration is examined in the following section.

For the compact joint geometry, the linear relationship between $N_f$ and CSR on a double-logarithmic scale, as previously identified for the standard joint geometry, is confirmed. In addition, $N_f$ increases with increasing test frequency $f$, consistent with the behavior observed for the standard joint geometry. Compared to the standard joint geometry, the compact joint geometry exhibited a slightly higher load-bearing capacity under LCF loading for all parameter combinations, despite normalization of the load level based on the quasi-static reference tests. Overall, the results showed fundamentally good agreement between the two joint geometries, with the compact joint geometry exhibiting slightly higher LCF performance.

Considering the regression lines of the extended Basquin model, the model reproduces the test series at 1.0 Hz with high accuracy for both test control modes. For the test series at 5.0 Hz, the regression line predicts slightly higher numbers of cycles to failure $N_f$ than observed experimentally. At 0.5 Hz, the regression line yields slightly lower $N_f$ than the experimental results. These deviations were more pronounced than those observed for the standard $12 \times 12$ mm$^2$ joint geometry. The phenomenon is examined in more detail in the following section.

### 7.6.3.2 Applicability of the Extended Basquin Model

As already shown for the standard $12 \times 12$ mm$^2$ joint geometry, the experimental data could also be represented as a function of the failure time $t_f$ according to Eq. (7.13). Figure 7.35a shows the converted experimental data for the $8 \times 24$ mm$^2$ joint geometry for both types of test control. The corresponding regression lines were determined based on Eq. (7.15).

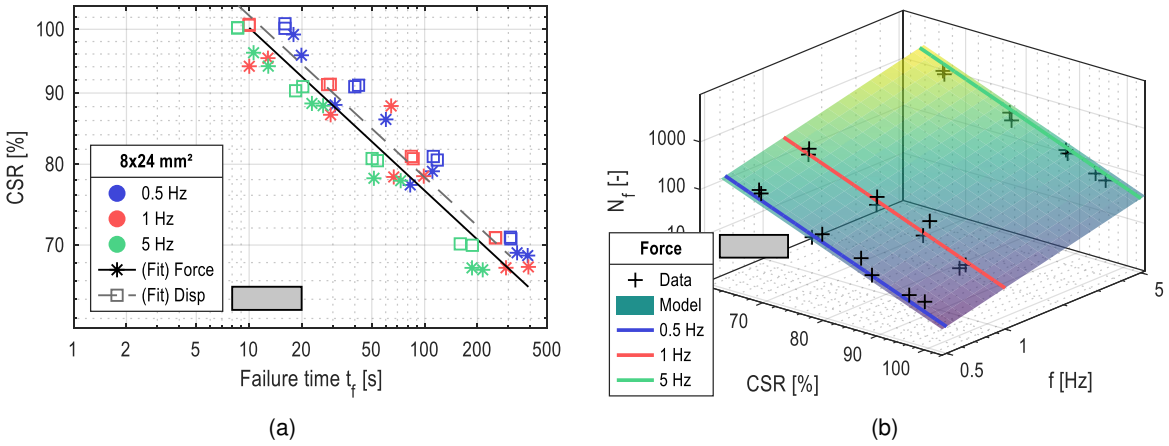


**Figure 7.35:** LCF strength for the compact $8 \times 24$ mm$^2$ joint geometry: (a) failure time $t_f$ as a function of the load level CSR for all analyzed test frequencies; (b) three-dimensional surface of the extended Basquin model with the experimental data used for fitting and the corresponding S-N curves for the tested frequencies (force-controlled tests).

This evaluation reveals overall good agreement between the two regression lines, with no noticeable difference in slope and a slight rightward shift of the displacement-controlled curve. However, analysis of the individual data points shows that they follow the regression line approximately in parallel but exhibit slight systematic shifts. The best agreement with the regression line is obtained for the data points recorded at 1.0 Hz. The data points of the test series conducted at 5.0 Hz show slightly lower failure time $t_f$ than predicted by the regression line, whereas the 0.5 Hz series tends to exhibit slightly higher $t_f$. This relationship is observed independently of the type of test control and contrasts with the behavior of the $12 \times 12$ mm$^2$ joint geometry, in which the data points are scattered around the regression line without any clear positional trend. This behavior also explains the small deviations between the S-N curves at 0.5 Hz and 5.0 Hz in Figure 7.34.

One possible explanation for this behavior is provided by the review of (Sousa et al. 2024), which identifies two opposing effects of loading frequency. On the one hand, an increasing loading rate leads to higher apparent strength, which is consistent with the results of this study. On the other hand, increasing frequency promotes self-heating within the adhesive layer, resulting in reduced strength and fatigue life (see section 2.3.2). The deviations observed for the compact joint geometry may therefore be attributed to increased heat accumulation within the adhesive layer, caused by the compact geometry and the associated more complex internal stress state.

Compared to the standard $12 \times 12$ mm$^2$ joint geometry, the extended Basquin model represented the frequency dependence of the $8 \times 24$ mm$^2$ joint with slightly lower accuracy. This limitation indicates that the assumed linear proportionality in logarithmic space captures the frequency effect less precisely for the $8 \times 24$ mm$^2$ joint. Nevertheless, Figure 7.35b illustrates that the model reproduces the fundamental behavior under LCF loading and the overall frequency dependence with good agreement. The corresponding fitting parameters obtained from the regression analysis for the compact joint are summarized in Table 7.6.

To evaluate the transferability of the findings obtained for the standard $12 \times 12$ mm$^2$ joint geometry to the alternative $8 \times 24$ mm$^2$ configuration, the coefficients of determination ($R^2$) from the regression analysis, summarized in Table 7.6, were first examined. The results showed that high $R^2$ values above 0.9 were obtained for both joint geometries and for both types of test control. Despite the previously observed minor deviation in representing the frequency dependence for the compact joint geometry, the $R^2$ values remained at a comparable level. This provides an initial indication that, within the frequency range considered, the load-bearing behavior under LCF loading can be accurately represented by the extended Basquin model for both joint geometries.

To examine the differences in LCF performance in more detail, the fitting parameters from Table 7.6 are compared in Figure 7.36, which presents the results as a bar plot. Figure 7.36a shows the value of $CSR_{N=50}$, which defines the load level at which failure is expected after 50 load cycles. For comparison between the models, this value was evaluated for the intermediate test frequency of 1.0 Hz. It is observed that both the displacement-controlled tests and the compact $8 \times 24$ mm$^2$ joint geometry exhibit slightly higher load-bearing capacities, compared with the force-controlled test series with the standard $12 \times 12$ mm$^2$ joint geometry. This increase in load-bearing capacity is also evident in the evaluated S-N curves shown in Figure 7.34.

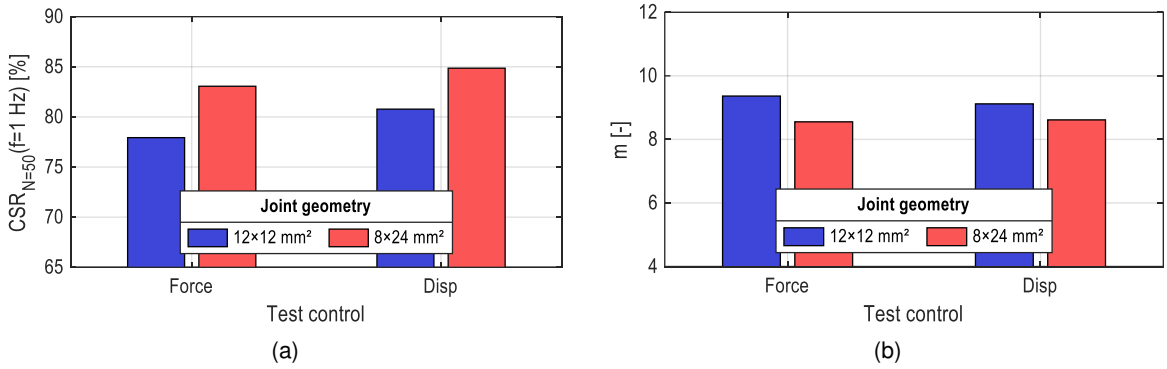


**Figure 7.36:** Comparison of the fitting parameters of the extended Basquin model: (a) $CSR_{N=50}$ value for a test frequency of $f$ = 1.0 Hz; (b) slope $m$.

When considering the slope $m$ of the curves shown in Figure 7.36b, the standard $12 \times 12$ mm$^2$ joint geometry shows a slightly higher value. The type of test control has almost no influence for either joint geometry. However, when examining the S-N curves in Figure 7.34, it becomes

evident that, within the investigated range of load levels, this difference has only a minor effect on the overall fatigue behavior.

Finally, it should be noted that, based on the findings presented here, the standard $12 \times 12$ mm$^2$ joint geometry produced slightly more conservative results. In contrast, the compact $8 \times 24$ mm$^2$ joint geometry consistently exhibited a slightly higher performance under LCF loading.

### 7.6.4 Statistical Evaluation of the S-N Curves

All previous evaluations and regression model parameters were determined using the classical least squares method. Consequently, the resulting S-N curves represent the mean behavior of the data. This means that, statistically, half of all subsequently tested specimens would be expected to fail above the calculated curve, corresponding to a survival probability of 50 %.

In structural engineering design, however, according to (ETAG 002-1; DIN EN 1990), characteristic material or component properties are typically defined such that at least 95 % of the population exceed the characteristic value. The same principle applies to the S-N curves derived in this study, which must therefore be converted into characteristic S-N curves. The statistical evaluation of fatigue test data was analyzed in (Drebenstedt and Euler 2018) for typical steel components according to (DIN EN 1993-1-9). It was shown that the approach proposed in (DIN EN 1990) for determining a single characteristic material property is equivalent to a lower prediction bound. Additionally, it was demonstrated that the lower prediction bound for a single future test with 95 % confidence and the lower 95 % tolerance bound with 75 % confidence are approximately equal (Drebenstedt and Euler 2018).

The characteristic intercept ($\log a_\mathrm{k}$) of the S-N curve for a single additional sample can be calculated using the following equation. The coefficient $t_{1-\alpha,n-1}$ of Student's t-distribution can be obtained from standard statistical tables or according to (Drebenstedt and Euler 2018). For the desired safety level, a confidence level of $1 - \alpha = 0.95$ is used. The number of degrees of freedom $(n - 1)$ is based on the number of samples $n$, and $s_\mathrm{reg}$ denotes the standard deviation of the scatter in $\log N$ obtained from the S-N regression:

$$\log(a_\mathrm{k}) = \log(a) - t_{1-\alpha,n-1} \cdot s_\mathrm{reg} \cdot \sqrt{1 + \frac{1}{n}} \tag{7.17}$$

Since the extended Basquin model represents the frequency influence without introducing additional fitting parameters, this approach can be directly applied to the data obtained in this study. The evaluation of the experimental data at the prediction level results in a parallel shift of the three-dimensional failure surface along the logarithmic axis of the number of cycles to failure $N_\mathrm{f}$, as illustrated in Figure 7.37a for the force-controlled test series of the $12 \times 12$ mm$^2$ joint geometry. The S-N curves determined for the three tested frequencies are additionally shown in Figure 7.37b for clarity. Here, the parallel shift of the curves within

the diagram is clearly visible. Overall, it was observed that the S-N curves evaluated at the prediction level consistently represented all experimentally obtained data points of all test configurations on the safe side.

The determined prediction intervals of the fitting parameter $a$ and the corresponding $CSR_{N=50}$ values are presented in Table 7.6, together with the mean values of these parameters for all parameter combinations. The evaluation of the models based on the prediction interval resulted in a reduction of the $CSR_{N=50}$ value of approximately 7 % for both force-controlled test series, about 4% for the displacement-controlled tests of the $12 \times 12$ mm$^2$ joint geometry, and approximately 6 % for the $8 \times 24$ mm$^2$ configuration.

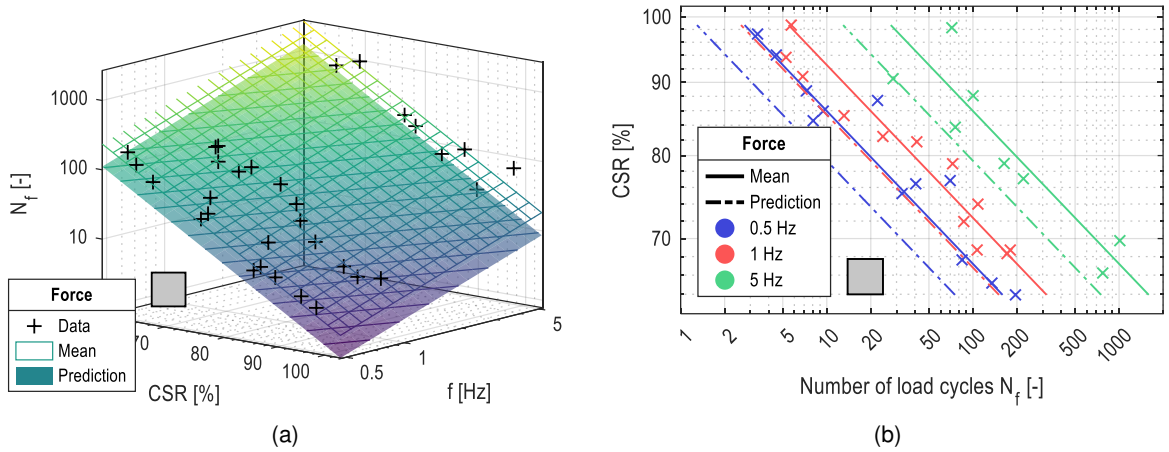


**Figure 7.37:** Statistical evaluation of the test results ($12 \times 12$ mm$^2$ – force-controlled): (a) three-dimensional failure surface of the extended Basquin model (mean surface shown as mesh, prediction surface shown with filled contours); (b) experimental data with S-N curves derived for the test frequencies.

### 7.6.5 Comparison of Low Cycle Fatigue With Quasi-Static Performance

Since the previous description and classification of the performance under LCF loading were based on the normalized load parameter CSR, this normalization is now converted back to the real load domain for a final comparison of the different test control modes and joint geometries.

To achieve this, the S-N curves had to be transformed from the normalized load level CSR to real stress values. The fitting parameters determined in Table 7.6 could not be used directly for this purpose. As the load level was calculated using Eqs. (7.1) and (7.2), the fitting parameters had to be converted accordingly.

The power-law relationship, exemplarily shown for the force-controlled tests according to Basquin, is given by:

$$N_\mathrm{f} = a \cdot \left( \frac{\tau_\mathrm{E}}{\tau_\mathrm{ult,mean}} \cdot 100 \right)^{-m} \tag{7.18}$$

The constant terms could be rearranged into a new fitting parameter $a_{\mathrm{Real}}$:

$$N_{\mathrm{f}} = a \cdot \left( \frac{100}{\tau_{\mathrm{ult,mean}}} \right)^{-m} \cdot \tau_{\mathrm{E}}^{-m} \tag{7.19}$$

$$a_{\mathrm{Real}} = a \cdot \left( \frac{\tau_{\mathrm{ult,mean}}}{100} \right)^{m} \tag{7.20}$$

This conversion enables the use of the model-derived fitting parameters with real stress and strain values. Consequently, the number of load cycles to failure can be determined directly without prior normalization. The corresponding converted fitting parameter $a_{\mathrm{Real}}$ is additionally listed in Table 7.7. The extended frequency-dependent Basquin model for determining the number of load cycles $N_{\mathrm{f}}$ based on the real stress $\tau_{\mathrm{E}}$ or strain $\gamma_{\mathrm{E}}$ values is given by:

$$N_{\mathrm{f}} = a_{\mathrm{Real}} \cdot \tau_{\mathrm{E}}^{-m} \cdot f \tag{7.21}$$

$$N_{\mathrm{f}} = a_{\mathrm{Real}} \cdot \gamma_{\mathrm{E}}^{-m} \cdot f \tag{7.22}$$

**Table 7.7:** Summary of the fitting parameters for the extended Basquin model based on the real stress and strain values for Eq. (7.21).

| Test control | Joint geometry [mm²] | $m$ | Mean | | Prediction (95 % confidence) | | $R^2$ |
|---|---|---|---|---|---|---|---|
| | | | $\log_{10}(a_{\mathrm{Real}})$ | Load at $N_f = 50$ ($f$ = 1 Hz) | $\log_{10}(a_{\mathrm{Real}})$ | Load at $N_f = 50$ ($f$ = 1 Hz) | |
| Force | 12 x 12 | 9.36 | 0.283 [MPa] | 0.706 [MPa] | -0.043 [MPa] | 0.652 [MPa] | 0.917 |
| | 8 x 24 | 8.55 | 0.691 [MPa] | 0.762 [MPa] | 0.411 [MPa] | 0.707 [MPa] | 0.933 |
| Disp | 12 x 12 | 9.12 | 1.62 [-] | 0.981 [-] | 1.45 [-] | 0.940 [-] | 0.977 |
| | 8 x 24 | 8.61 | 2.18 [-] | 1.14 [-] | 1.94 [-] | 1.07 [-] | 0.947 |

The resulting S-N curves are shown in Figure 7.38 for the $12 \times 12$ mm² joint geometry. In addition to the mean curves, the statistically verified S-N curves at prediction level determined in the previous section are included. These curves can be used to determine the corresponding characteristic component or material resistances for later design. For easier orientation and comparison, quasi-static reference strengths are represented as horizontal dotted lines in the diagrams. The mean quasi-static reference values, $\tau_{\mathrm{ult,mean}}$ and $\gamma_{\mathrm{ult,mean}}$, which define the baseline properties for the calculation of CSR, are also indicated for each test series. At this load level, CSR equals 100 %.

The results for the force-controlled test series are shown in Figure 7.38a. In addition to the characteristic quasi-static shear strength specified by the manufacturer ($\tau_{\mathrm{k,ETA}} = 0.66$ MPa), the characteristic strength of the quasi-static reference series ($\tau_{\mathrm{k}}$) determined in section 6.4, is also shown. For the displacement-controlled test series, the results for the energy-based

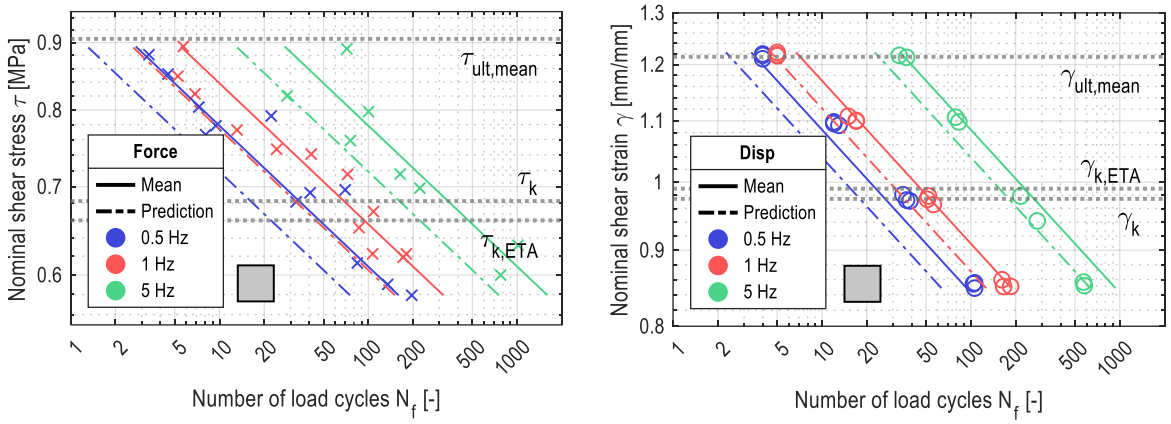


**Figure 7.38:** S-N curves for different test frequencies for real stress and strain values, based on the extended Basquin model ($12 \times 12$ mm$^2$): (a) force-controlled test series; (b) displacement-controlled test series.

failure criterion $w_{\text{cum}}$ are presented in Figure 7.38b. Since (ETA-01/0005) of the adhesive does not provide a value for the fracture strain ($\gamma_{k,ETA}$), it was determined using the following approach. Based on the linear-elastic Hooke's law from Eq. (2.9), the typical stiffness of an SG joint ($G_{\text{joint}} = 0.67$ MPa), and the characteristic shear strength ($\tau_{\text{k,ETA}}$) from Table 3.1, the characteristic fracture strain was calculated as $\gamma_{\text{k,ETA}} = 0.99$ mm/mm. In addition, the characteristic fracture strain obtained from the reference series $\gamma_{\text{k}}$ is shown.

For both test series, the experimentally determined characteristic material parameters were within a similar range as those derived from the adhesive's approval data. However, since the determination of characteristic material parameters strongly depends on the scatter of the quasi-static reference series, the following comparisons were based solely on the ETA parameters $\tau_{\text{k,ETA}}$ and $\gamma_{\text{k,ETA}}$.

For the force-controlled series, a test frequency of 0.5 Hz at a load level corresponding to $\tau_{\text{k,ETA}}$ resulted in 47.0 cycles to failure $N_{\text{f}}$, when evaluated using the mean S-N curve. This number decreased to $N_{\text{f}} = 22.2$, when evaluated at the prediction level. For the displacement-controlled tests evaluated with the $w_{\text{cum}}$ failure criterion, $N_{\text{f}} = 23.0$ cycles were obtained from the mean S-N curve at 0.5 Hz and a load level of $\gamma_{\text{k,ETA}}$, decreasing to $N_{\text{f}} = 15.6$ at the prediction level. These results indicate that, at the load level $\gamma_{\text{k,ETA}}$, the displacement-controlled tests with the $w_{\text{cum}}$ failure criterion yield slightly lower numbers of cycles to failure compared to the force-controlled tests.

A summary of the number of cycles to failure $N_{\text{f}}$ at quasi-static reference strength, evaluated for mean and prediction S-N curves, is provided in Table 7.8.

**Table 7.8:** Number of cycles to failure $N_f$, evaluated for mean and prediction S-N curves at quasi-static reference strength (12 × 12 mm$^2$ joint geometry).

| Frequency $f$ [Hz] | Force controlled | | | | Displacement controlled | | | |
|---|---|---|---|---|---|---|---|---|
| | Mean | | Prediction | | Mean | | Prediction | |
| | $\tau_k$ | $\tau_{k,\mathrm{ETA}}$ | $\tau_k$ | $\tau_{k,\mathrm{ETA}}$ | $\gamma_k$ | $\gamma_{k,\mathrm{ETA}}$ | $\gamma_k$ | $\gamma_{k,\mathrm{ETA}}$ |
| 0.5 | 34.2 | 47.0 | 16.2 | 22.2 | 26.6 | 23.0 | 18.0 | 15.6 |
| 1.0 | 68.5 | 93.9 | 32.3 | 44.3 | 53.1 | 46.0 | 35.9 | 31.1 |
| 5.0 | 342.5 | 469.5 | 161.7 | 221.7 | 265.6 | 230.1 | 179.7 | 155.7 |

## 7.7 Summary of Low-Cycle Fatigue Performance

The LCF performance was analyzed based on an extensive experimental test series. Overall, all experiments showed highly predictable behavior. Within the first few load cycles, all tested specimens exhibited load-bearing behavior comparable to the quasi-static reference tests. In contrast, the failure behavior under LCF loading differed fundamentally from quasi-static conditions and was primarily governed by the type of test control. For both control modes, cracks formed and increased in size with the number of cycles.

In the force-controlled tests, which simulate the load situation in primary all-glass constructions, the applied stress remained approximately constant while the strain increased. This behavior was comparable to creep. When the load could no longer be sustained, complete failure of the SG joint occurred in the final cycle.

In contrast, in the displacement-controlled tests, which simulate the load situation in typical secondary facade constructions, the stress decreased under constant strain, leading to stress relaxation. At the end of the test, a considerable residual cross-sectional area remained, especially when failure was defined using the energy-based failure criterion $w_{\mathrm{cum}}$. This remaining cross-sectional area resulted in a substantial residual load-bearing capacity of the joint, as demonstrated by (Müller et al. 2025d).

All other investigated parameters, such as test frequency and joint geometry, showed no significant influence on the load-bearing behavior. Cyclic parameters, including stiffness, dissipated energy density, and damping, were calculated and analyzed to characterize the evolution of the joint response throughout the test.

For the definition of the number of cycles to failure $N_\mathrm{f}$, appropriate failure criteria were established for the displacement-controlled tests. Among these, the energy-based criterion provided the most consistent results. Using this approach, comparable LCF performance was demonstrated for both types of test control.

To describe the number of cycles to failure $N_f$, typical S-N curves were derived from the test data. All test configurations revealed highly predictable performance based on the classical Basquin approach, with low scatter. To capture the influence of test frequency on the LCF performance, a description based on failure time $t_f$ was effective. The Basquin model was extended with an additional linear frequency term, which captures the effect of test frequency with a high degree of determination. This model provides the basis for evaluating seismic load histories in the following chapter.

The alternative compact $8 \times 24$ mm$^2$ joint geometry exhibited a slightly higher load-bearing capacity compared to the standard $12 \times 12$ mm$^2$ geometry. Consequently, it can be considered conservative for design purposes when evaluated in relation to the standard configuration.

# 8 Analysis of the Seismic Ground Motion Loading

## 8.1 Objective and Approach

Building upon the experimental analysis of the load-bearing and failure behavior of SG joints under LCF loading presented in chapter 7, this chapter focuses on the characterization of seismic ground motion and its transformation into cyclic stress and strain demands in SG joints. The methodological approach is based on the framework published in (Müller et al. 2025b), while the evaluation builds on the new experimental database and the extended Basquin model introduced in section 7.6.

To develop a safe and economical design concept for SG joints under seismic loading, the cyclic component of seismic loading, referred to as cyclic–seismic loading in the following, had to be quantified in addition to the experimentally determined LCF performance. Therefore, this chapter translates seismic ground motion into equivalent cyclic loading demands on SG joints. Based on this representation, the governing characteristics of cyclic–seismic loading are identified and expressed in terms of parameters suitable for engineering design of SG joints.

To this end, the following objectives are addressed:

- Define a suitable calculation method and establish a representative database of earthquake ground motions that enables the analysis of cyclic–seismic loading on SG joints in glass and facade structures.
- Characterize the cyclic–seismic loading of real earthquake events by determining an equivalent number of constant-amplitude cycles.
- Formulate recommendations for the design parameters of SG joints subjected to seismic loading.

The methodological framework applied in this chapter is summarized schematically in Figure 8.1 and consists of four main steps.

In the first step, a parametric SDOF simulation model was developed to systematically characterize the influence of cyclic–seismic loading. Several calculation approaches were verified to ensure numerical efficiency, and the key dynamic parameters were analyzed to

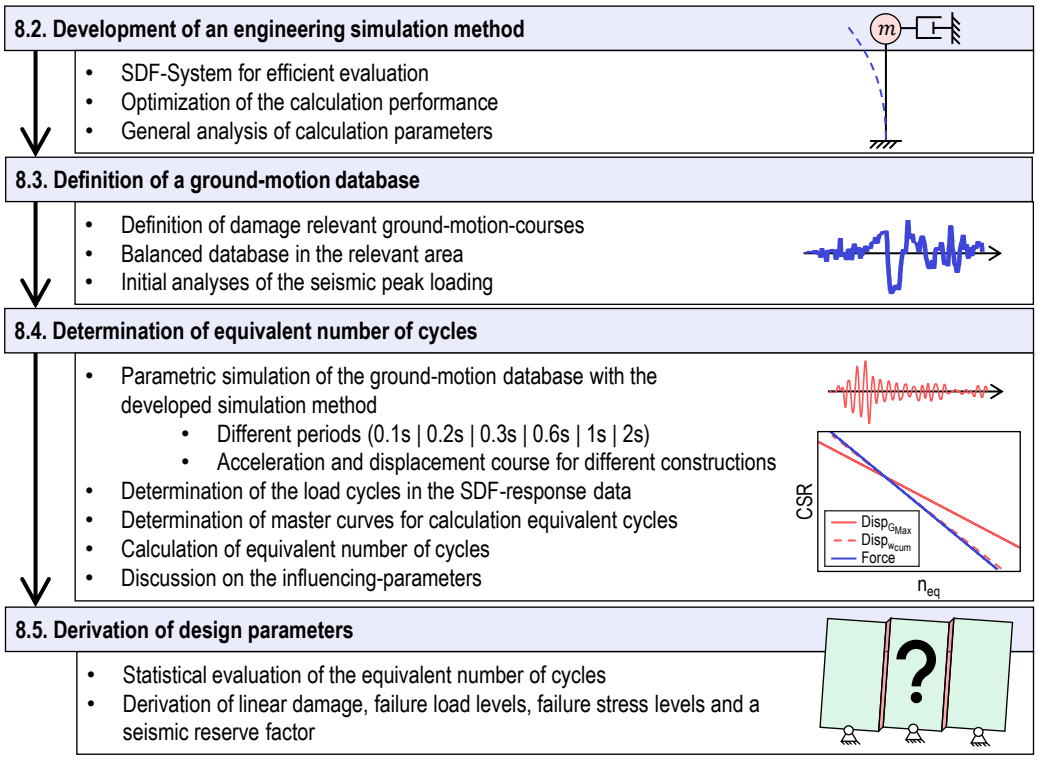


**Figure 8.1:** General concept for the analysis of seismic ground motion loading and derivation of design parameters. Adapted from (Müller et al. 2025b).

identify the most relevant relationships and to enhance the understanding of the underlying dynamic effects.

In the second step, a representative ground motion database was compiled based on (Ancheta et al. 2013). To obtain a balanced and computationally efficient dataset, ground motion records were systematically selected within the relevant loading range. The selected records were then analyzed to ensure that the final dataset adequately represents the characteristics of the original database. This includes an initial evaluation of the peak seismic loading on SG joints in glass and facade constructions.

In the third step, the cyclic component of the seismic loading was quantified by converting the random load histories into equivalent constant-amplitude cycles. This conversion was performed using parametric SDOF simulations with varying natural periods to represent constructions with different stiffness. The resulting acceleration and deformation responses were evaluated using cycle-counting methods to derive stress amplitude ranges, which were subsequently converted into equivalent cycles based on master curves obtained from the experimental results in chapter 7. The influence of various parameters on the cyclic seismic loading was then analyzed using the determined number of equivalent cycles.

In the final step, the equivalent number of cycles was statistically evaluated to quantify the cyclic–seismic loading demand and assess its damage potential. Based on this evaluation, statistically validated limit values for the seismic loading component acting on SG joints

were derived. Using these limit values and the frequency-dependent extended Basquin model from chapter 7, relevant design parameters for SG joints under seismic loading were derived.

## 8.2 Development of an Engineering Simulation Method

### 8.2.1 Single-Degree-of-Freedom Model

The effect of seismic events on structures depends on numerous influencing parameters. In addition to the overall structural design, local conditions such as soil properties and regional seismic activity play a decisive role. The stresses caused by random ground accelerations can generally be characterized as cyclic random loads within the LCF range. A typical ground acceleration record of the exemplary Northridge-01 earthquake (RSN 1063) obtained from (Ancheta et al. 2013) is illustrated in Figure 2.24.

Beyond the general principles of seismic design, the response of SG joints in glass and facade structures is affected by a large number of additional parameters. These are determined both by the specific detailing of the construction and by the complex viscoelastic material behavior, including the partial failure mechanisms of the SG adhesives used. The present study provided a first systematic analysis of the seismic loading acting on SG joints, taking into account the most relevant influencing parameters. The selected parameter ranges were derived from the stress assessment in chapter 4

To represent the structural response to ground acceleration, a single-mass oscillator corresponding to the SDOF system under seismic excitation, introduced in section 2.2.3.1 and illustrated in Figure 2.17, was used as the analytical framework. This approach provides a basis for understanding and interpreting the seismic response of more complex systems, such as facade structures, identifying the dominant parameters governing the dynamic behavior, and enabling seismic-resistant design (Bachmann 1995).

Different glass and facade constructions were represented by evaluating the deformation and acceleration responses of the SDOF system for varying stiffness ratios. Due to its computational efficiency, the SDOF approach allows for a broad parametric characterization of the seismic loading when combined with extensive ground-motion databases. The resulting response data provided the foundation for the subsequent evaluation of the number of equivalent cycles, forming the basis for the derivation of design parameters.

For the solution of the equation of motion, the Newmark integration scheme and the Linear Implicit Dynamic Analysis (LIDA) method, introduced in section 2.2.3.3, were investigated. The detailed comparison presented in (Müller et al. 2025b) showed that the LIDA method requires significantly less computation time and was therefore adopted for all subsequent analyses in this study.

### 8.2.2 Evaluation of General Calculation Parameters

To investigate the parameters influencing the dynamic time-history response and to gain a first understanding of the resulting load curves, this section examines the fundamental calculation results using an exemplary ground acceleration record.

The outcome of a dynamic analysis depends not only on the ground acceleration, but also on the damping ratio $\zeta$ and the natural period $T$ of the SDOF system. In general, increasing the damping reduces the vibration response (Chopra 2012). Since no experimental data on the damping characteristics of complete bonded glass or facade structures are currently available, all calculations in this study were carried out using a damping ratio $\zeta = 5\ \%$. This value was selected in accordance with (EN 1998-1). Based on experimental investigations of SG joints presented in section 7.4.4, which indicate loss factors in the range of $\eta \approx 6\ \%$, corresponding to $\zeta \approx 3\ \%$, the total damping of a complete facade system is expected to be in the range of $\zeta \approx 5\ \%$, as it includes contributions from the SG joint, the structural members, connections, and boundary conditions. The adopted damping ratio of $\zeta = 5\ \%$ is therefore considered a realistic assumption for typical facade constructions. The damping characteristics of large-scale facade components are further investigated within the research project RISIKO (Müller et al. 2026b).

The second key parameter in the dynamic analysis is the natural period $T$ of the SDOF system, which has a significant influence on the response of the system. However, to interpret the results properly, it is necessary to consider various design configurations of glass and facade systems, which result in different loading scenarios, as described in the stress assessment in chapter 4.

In all-glass structures, the glazing system itself forms the primary load-bearing structure and is directly subjected to seismic inertial effects. As a first approximation, the dynamic seismic load acting on the SG joint can therefore be described as a function of the acceleration response of the SDOF system. In contrast, the SG joints in facade constructions are subjected to loads induced by the imposed deformation of the primary structure, resulting in a load that depends on the deformation response of the SDOF system.

To investigate the influence of the natural period $T$, dynamic analyses of SDOF systems with varying $T$ were conducted. The exemplary Northridge-01 earthquake (RSN 1063 from (Ancheta et al. 2013)), shown in Figure 2.24, was chosen as the input ground acceleration as an illustrative example. The resulting acceleration and deformation responses are presented in Figure 8.2a and Figure 8.2b, respectively. Both responses show the characteristic irregular cyclic–seismic loading pattern with varying amplitudes. When evaluating the influence of the natural period on the results, a clear reduction in the maximum acceleration amplitude is observed for the highest natural period $T = 2\ s$ in Figure 8.2a. In contrast, the maximum deformation amplitude in Figure 8.2b clearly decreases for the vibration with $T = 0.5\ s$.

For a more detailed and accessible analysis of this correlation, the corresponding response spectra of the acceleration record were calculated and are presented in Figure 8.3. The abso-

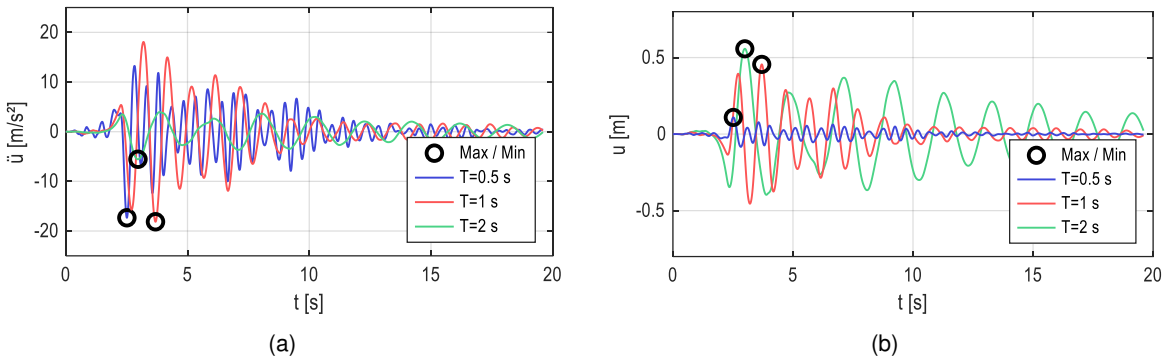


(a) (b)

**Figure 8.2:** Results of the dynamic calculation for different natural periods $T$: (a) acceleration response; (b) deformation response. Adapted from (Müller et al. 2025b).

lute maximum and minimum values of the curves shown in Figure 8.2 are also presented as examples. The acceleration spectrum in Figure 8.3a shows a decrease in acceleration from about 17–21 m/s$^2$ for the natural periods in the range of 0.25 s to 1 s to approximately 5.50 m/s$^2$ at a period $T = 2$ s. The acceleration further decreases with increasing natural period $T$. For the deformation spectrum in Figure 8.3b, the maximum deformation increases from 0.11 m at a period $T = 0.5$ s to 0.56 m at $T = 2$ s. As the natural period is further increased, no further increase is observed. Throughout this study, peak ground acceleration values from the database metadata are expressed as a percentage of the gravitational acceleration (%g), where 1 $g \approx 9.81$ m/s$^2$, while dynamic response quantities derived from time-history analyses are given in m/s$^2$.

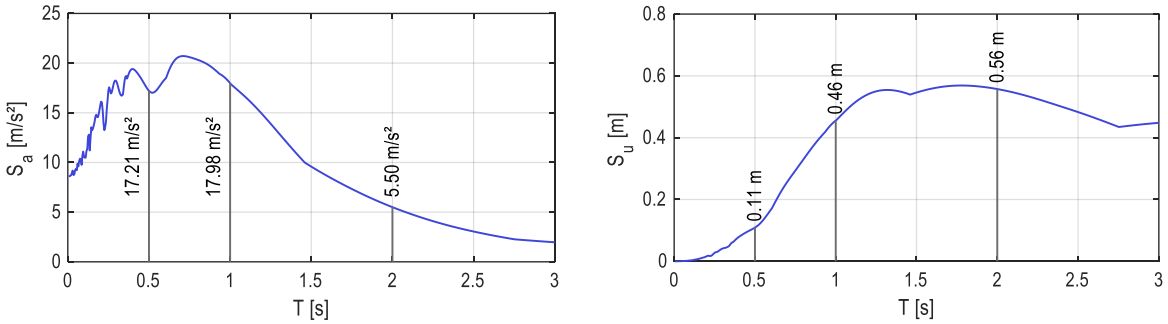


(a) (b)

**Figure 8.3:** Response spectra of the *Northridge-01* earthquake (RSN 1063 from (Ancheta et al. 2013)): (a) pseudo-acceleration response spectrum $S_a$; (b) displacement response spectrum $S_u$. Adapted from (Müller et al. 2025b).

The results shown here demonstrate the strong dependence of the response of the SDOF system on the natural period, but only provide specific results for an individual earthquake. For a more general analysis, a database of ground motion histories of past earthquakes is introduced in the following section and a more comprehensive analysis of the effects is conducted.

## 8.3 Definition of a Ground Motion Database

### 8.3.1 Criteria for Defining Damage-Relevant Ground Motion

A database of ground motion records was established to systematically analyze the seismic loading of SG joints in glass and facade structures. The objective was to provide a balanced and generally valid overview of the loads using a large number of different ground motion records. The defined database was subsequently applied to perform a parametric analysis of the time histories of structures with different natural periods, based on the engineering simulation method described in section 8.2. This enabled the derivation of generally applicable insights into the seismic loading behavior of SG joints in glass and facade systems. Alternative calculation methods, such as cloud analysis approaches (Jalayer et al. 2015; D'Ayala et al. 2015; Mattei et al. 2021), or selection procedures for suitable ground motion records (Iervolino et al. 2010), represent additional strategies for addressing this issue. However, they were not further considered within the scope of this thesis.

The earthquakes used in this study originate from the publicly available database of (Ancheta et al. 2013). The NGA West 2 ground motion database contains a very large set of ground motions from shallow crustal earthquakes in active tectonic regions worldwide. It contains 21 420 ground motion records from past earthquakes of varying magnitude and intensity that occurred worldwide. For a number of reasons, a smaller selection of records from the entire database was defined and subsequently used to perform the actual analysis of seismic effects on SG joints:

- Only high-quality ground motion records are selected.
- Only damage-relevant earthquakes are considered.
- Major earthquakes with numerous time histories should not be overrepresented.

To ensure both computational efficiency and a balanced representation of the damage-relevant intensity range, the number of records was limited to a manageable subset. The following sections describe the procedure used to define the ground motion database and to apply the previously defined selection criteria.

#### 8.3.1.1 Criteria for Good Quality and Reliable Database

The CB14 NGA-West2 horizontal ground-motion model developed by (Campbell and Bozorgnia 2014) was used for a preliminary selection of high-quality and reliable ground motions. The exclusion criteria defined by (Campbell and Bozorgnia 2008; Campbell and Bozorgnia 2013) were used to define reliable ground motions. The more than 20 000 records from the NGA-West2 database were reduced to a total of 15 521 records in the CB14 database. The database is divided into 7 208 near-source records with $R_{\mathrm{RUP}} \leq 80$ km and 8 313 far-source records with 80 km $< R_{\mathrm{RUP}} \leq 500$ km.

For the further evaluation of seismic loading on SG joints, the near-source database was used, as recordings at such distances are particularly relevant for seismic hazard assessment and engineering applications (Campbell and Bozorgnia 2014). To further reduce the number of ground motion records, all data lacking a specified peak ground acceleration (PGA) value in their metadata were excluded from the evaluation, as PGA is required for the subsequent damage-relevance assessment described in section 8.3.1.2. This reduces the dataset to 6 996 remaining records.

#### 8.3.1.2 Assumption of Characteristic Limit Values for Relevant Earthquakes

The parameters of magnitude and intensity are often used to assess the strength of an earthquake. When designing glass and facade structures in seismically active areas, damage must be expected, especially during stronger seismic events. According to (Petersen and Werkle 2017), earthquakes with a magnitude greater than $M > 5$ are defined as damaging earthquakes. According to (Michigan Technological University 2021), a magnitude of $M = 5.5 - 6.0$ can cause minor damage to buildings and non-structural components. (Meskouris 2011) also states that, at an intensity exceeding 5 or a maximum PGA $> 3$ % g , minor damage must be expected.

According to (Wald et al. 2003), earthquakes with moderate perceived shaking have a very low damage potential. Earthquakes with weak perceived shaking can be classified as having no damage potential. In order to consider only earthquake records with damage potential for the analyses in this study, datasets with a PGA $< 3.9$ % g and a peak ground velocity PGV $< 3.4$ cm/s were excluded from the ground motion database. This reduces the 6 996 good quality records to 964 damage-relevant records.

#### 8.3.1.3 Procedure for Minimizing the Number of Data Selections

To avoid overestimating the influence of earthquakes represented by numerous recordings, a systematic selection was performed for all earthquakes with more than 10 available records per event. The goal was to represent the full range of relevant intensities as comprehensively as possible. For this purpose, the logarithmic values of the PGA were used, as they show a much more uniform distribution. The range between minimum and maximum PGA was divided into even steps, and the records closest to the logarithmically spaced target values were selected for further evaluation. If an earthquake was selected more than once due to the distribution of the records, it was only included once in the final database.

The limit of 10 records per earthquake event was defined to provide a good representation of the earthquakes despite the limited number of records. For the exemplary earthquake *Christchurch, New Zealand,* the PGA values of all records, as well as those selected for further analysis, are shown in Figure 8.4.

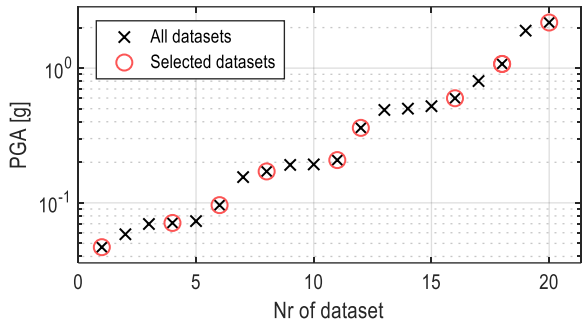


**Figure 8.4:** PGA of all records from the *Christchurch, New Zealand* earthquake, including those selected for further analysis. Reproduced from (Müller et al. 2025b).

Finally, the number of records was reduced from 964 to 332. After the download, a completeness check of the database revealed that 11 records could not be downloaded, leaving 321 records from 67 unique earthquake events available for evaluation.

### 8.3.2 Analysis of the Selected Database

For an initial descriptive analysis of the defined database, Figure 8.5 shows the earthquake magnitude $M_w$ and intensity in the form of the PGA of each ground motion record in the entire initial database as a black scatter plot. The ground motion records selected for further analysis in this study are additionally highlighted in red. When the full range of magnitudes and intensities is displayed, as in Figure 8.5a, it is evident that the selected damage-relevant earthquakes are located in a relatively narrow region of the entire database. For a more detailed analysis, only the damage-relevant records in this region are shown in Figure 8.5b. Despite the substantial reduction, the selected records are well distributed within the considered range.

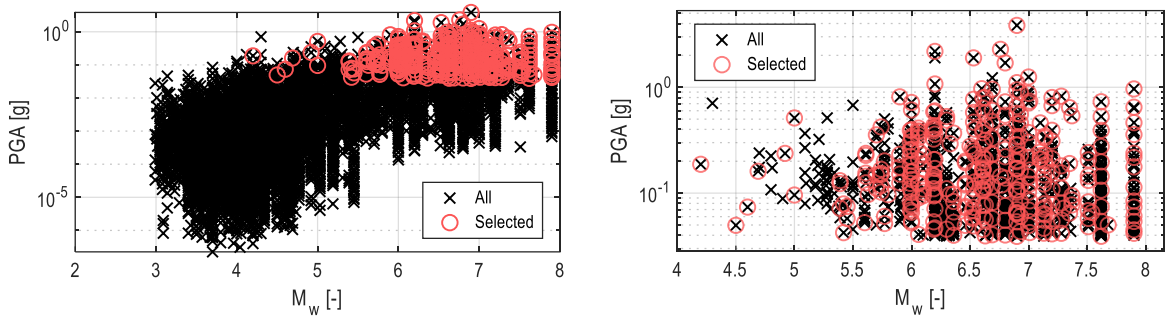


**Figure 8.5:** Representation of the full and selected database: (a) entire database; (b) damage-relevant records. Adapted from (Müller et al. 2025b).

To provide a more detailed view of the distribution of the damage-relevant ground motion records, these are shown in Figure 8.6 as a binned scatter plot. The data points are grouped according to their location in the magnitude–PGA space. The color of each bin corresponds to the number of data points within that bin. Figure 8.6a shows the damage-relevant records

of the entire database, corresponding to all data points shown in Figure 8.5b. The data show clusters with a high number of data points, especially in the low-intensity range. Only a few ground motion records are available in the high-intensity range. The final selected database is shown in Figure 8.6b. The bin coverage is very similar to that of the entire database. This indicates that the data reduction procedure successfully preserved the extreme ranges of the database while achieving a more uniform distribution of data points. The maximum number of data points in one group decreases from 91 to 18. In summary, this analysis shows that the procedure presented in the previous section provides a database that adequately represents the damage-relevant range and achieves a noticeably more uniform distribution of records over intensity compared to the original dataset.

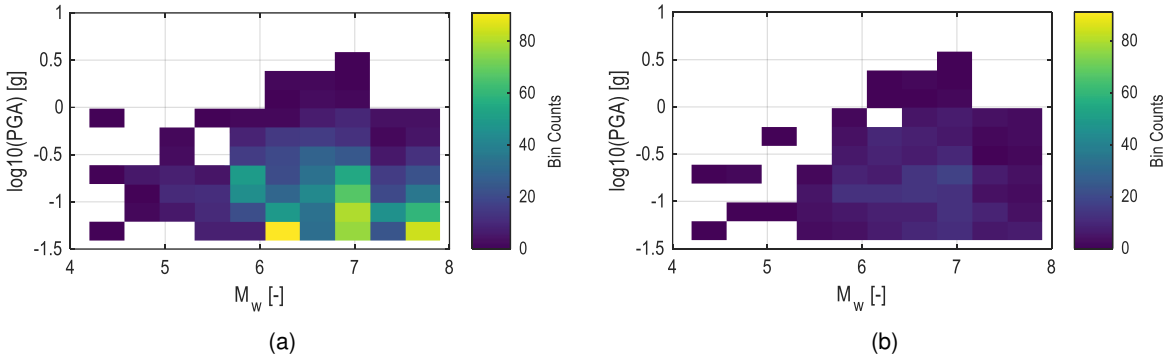


**Figure 8.6:** Binned scatter plot showing the distribution of data points of the damage-relevant ground motion records: (a) without selection; (b) final database after selection. Adapted from (Müller et al. 2025b).

The geographical distribution of earthquake events is shown in Figure 8.7, with the selected events indicated by red circles. This demonstrates that all regions with potential seismic activity from the NGA West 2 database are represented in the selection defined in this section.

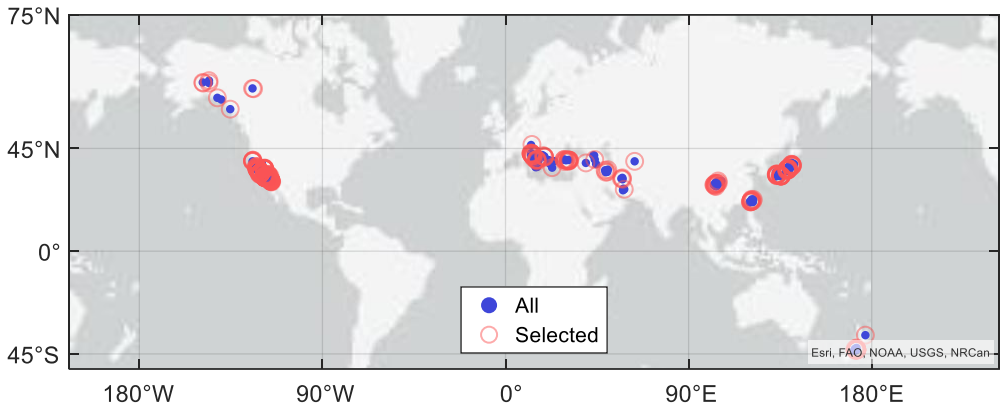


**Figure 8.7:** Geographical distribution of earthquake events, with selected events indicated by red circles. Reproduced from (Müller et al. 2025b).

### 8.3.3 Analysis of Seismic Peak Loading

For an initial analysis of the seismic peak loads on SG joints in glass and facade structures, the response spectra of the first horizontal component of all ground motion records were calculated and are shown in Figure 8.8. The spectra of the individual acceleration records are plotted in grey. To improve the readability of the figures, the mean curve of all spectra is also shown. To represent the variability of the spectra, the standard deviation, the 95 % and 98 % quantile curves were evaluated and plotted.

The exemplary results from section 8.2.2 are confirmed here. When analyzing the acceleration spectrum in Figure 8.8a, which approximates the stress on SG joints in all-glass structures, the maximum values occur at natural periods $T$ between 0.2 s and 0.8 s. As the natural period increases, the acceleration decreases continuously. In contrast, the deformation spectrum in Figure 8.8b shows a continuous increase in deformation with increasing natural period $T$, which is attributed to the increasing stress on SG joints in facade constructions, where the glazing acts as a secondary structural component subjected to imposed deformations from the primary structure, as discussed in chapter 4.

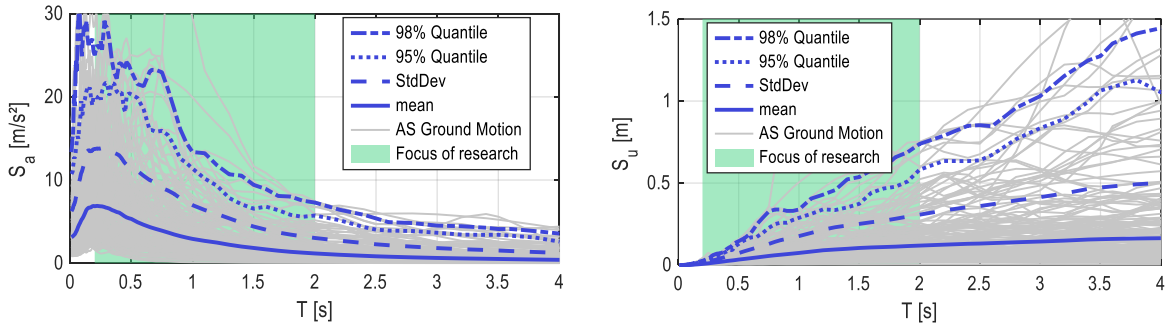


**Figure 8.8:** Response spectra calculated for the first horizontal component of all selected ground motion records from the final database: (a) pseudo-acceleration response spectrum $S_a$; (b) displacement response spectrum $S_u$. Adapted from (Müller et al. 2025b).

## 8.4 Determination of the Number of Equivalent Cycles

The evaluation of the response spectra showed that, in addition to the type of construction, the natural period of the structure has a major influence on the seismic loading of SG joints in glass and facade constructions. However, this assessment considers only the maximum load resulting from ground motion. In typical seismic design practice, a static equivalent load is often derived from this maximum value and used as the basis for design. Such an approach, however, neglects the cyclic stress component, which contributes to progressive fatigue damage in the SG joint during seismic loading.

To capture and quantify the cyclic stress component, an analytical method was developed and presented in this section. The method determines the number of equivalent cycles $n_{eq}$ from random seismic response histories.

## 8.4.1 Determination of the Master Curves

To weight the individual random cycles when calculating the number of equivalent cycles $n_{eq}$, master curves had to be determined. The following section describes the determination of these master curves from the experimental test data and analyzes the influencing parameters. The fundamentals of this concept are based on the studies by (Seed et al. 1975; Seed and Idriss 1970) and are presented in section 2.4.7.

### 8.4.1.1 Experimental Basis

The experimental basis for determining the master curves is provided in chapter 7. The number of cycles to failure $N_f$ is described by the extended Basquin model for frequency-dependent fatigue presented in section 7.6.2.2. Accordingly, $N_f$ can be directly evaluated as a function of the load level CSR and the test frequency $f$ using Eq. (7.15). The fitting parameters of the extended Basquin model are summarized in Table 7.6.

### 8.4.1.2 Mathematical Derivation of the Master Curves

In addition to the determination of master curves based on empirical and nonlinear CSR–liquefaction or S-N curves, a mathematical derivation of the master curves is possible if the relationship between CSR and the number of cycles to failure $N_f$ follows a power function. In this case, the number of equivalent cycles $n_{eq}$ can be calculated directly. Neither normalization by CSR nor the application of a safety factor affects the resulting $n_{eq}$ values (Green and Terri 2005).

The mathematical description of typical S-N curves can be derived from the basic equations for describing the fatigue strength, like Eqs. (2.35) and (2.36). According to (Seed et al. 1975; Green and Terri 2005), the number of equivalent cycles $n_{eq}$ can be determined based on the linear damage accumulation from Eq. (2.37) using the relationship in Eq. (2.54)

The typical S-N curve based on the power function is described by the fitting parameters $a$ and $m$. As already shown by (Müller et al. 2025c), the calculation of the reference load cycles $N_{Ref}$ and the load cycles to failure at the corresponding load level $N_{f,i}$ can also be done analytically using Eq. (2.35). The equivalent number of cycles for each load cycle $n_{eq,i}$ is determined from the reference load level $CSR_{Ref}$, the corresponding cycle load level $CSR_i$, and the slope of the master curve $m$, as:

$$n_{\mathrm{eq},i} = \frac{a \cdot \mathrm{CSR}_{\mathrm{Ref}}^{-m}}{a \cdot \mathrm{CSR}_i^{-m}} = \left( \frac{\mathrm{CSR}_{\mathrm{Ref}}}{\mathrm{CSR}_i} \right)^{-m} \tag{8.1}$$

With this mathematical description, it was shown that the number of equivalent cycles under seismic loading for the SG joints investigated in this study is independent of the intercept of the regression line or the parameter $a$ from the classic Basquin model in Eq. (2.35). This confirms the statement of (Green and Terri 2005) that neither the normalization by the CSR nor the safety factor has any influence on the number of equivalent cycles. Furthermore, it was shown that different statistical evaluation variants of the S-N curves, as shown in section 7.6.4, also have no influence on these results, as only the intercept of the S-N curves is modified. The mathematical implementation to determine the number of equivalent cycles $n_{\mathrm{eq}}$ also leads to a very efficient calculation compared to a determination from nonlinear master curves with a search algorithm.

To represent the frequency dependence of the SG joints under LCF loading, an additional frequency-dependent term $f$ was introduced in section 7.6.2.2 to define the extended Basquin model in Eq. (7.15). With this direct implementation of the frequency dependence without an additional exponent, the frequency term cancels out in the ratio forming $n_{\mathrm{eq}}$, as follows:

$$n_{\mathrm{eq},i} = \frac{N_{\mathrm{Ref}}}{N_{f,i}} = \frac{a \cdot \mathrm{CSR}_{\mathrm{Ref}}^{-m} \cdot f}{a \cdot \mathrm{CSR}_i^{-m} \cdot f} = \left( \frac{\mathrm{CSR}_{\mathrm{Ref}}}{\mathrm{CSR}_i} \right)^{-m} \tag{8.2}$$

It is noted that, although the loading frequency physically influences the fatigue life $N_{\mathrm{f}}$, it cancels out in $n_{\mathrm{eq}}$ since both $N_{\mathrm{Ref}}$ and $N_{\mathrm{f},i}$ are evaluated on the same frequency-dependent S-N curve.

The corresponding parameters for describing the extended Basquin model and therefore to calculate the $n_{\mathrm{eq}}$ are given in Table 7.6. The calculation of $n_{\mathrm{eq}}$ was based on the linear damage accumulation hypothesis according to Miner's rule. This approach represents a fundamental and widely adopted assumption in fatigue analysis and forms the basis of the equivalent cycle concept introduced by (Seed et al. 1975). The applicability of Miner's rule for SG joints under seismic LCF loading has not been directly verified and should be addressed in future experimental investigations.

#### 8.4.1.3 Influencing Parameters for Determining the Master Curves

Based on the mathematical formulation of the number of equivalent cycles $n_{\mathrm{eq}}$, an implementation in a MATLAB script and the subsequent evaluation of ground motion histories was possible. To improve the fundamental understanding of the parameters influencing the definition of the master curves, these parameters are analyzed in the following section. The S-N curves derived from the extended Basquin model presented in section 7.6.2.2 and summarized in Table 7.6 were used to generate corresponding master curves for SG joints under seismic loading by applying the procedure described in section 8.4.1.2.

According to Eq. (8.2), the reference load cycles $N_{\mathrm{Ref}}$ at the reference load level $\mathrm{CSR}_{\mathrm{Ref}}$ had to be defined. In Figure 8.9a, the influence of different reference load levels $\mathrm{CSR}_{\mathrm{Ref}}$ on the number of reference cycles to failure $N_{\mathrm{Ref}}$ is illustrated for the force-controlled test series with a test frequency of 1.0 Hz as an illustrative example. $N_{\mathrm{Ref}}$ increases with decreasing $\mathrm{CSR}_{\mathrm{Ref}}$.

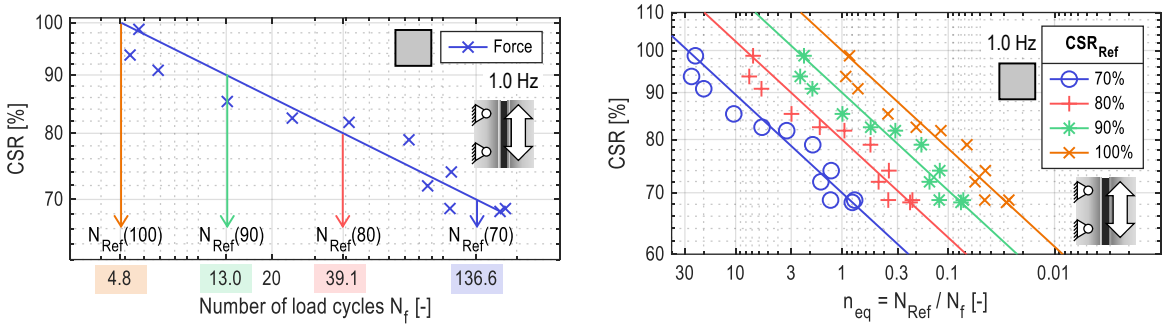


**Figure 8.9:** Determination of the master curves for different $\mathrm{CSR}_{\mathrm{Ref}}$ values based on the S-N curve from the extended Basquin model (force-controlled, $f$ = 1.0 Hz): (a) determination of $N_{\mathrm{Ref}}$; (b) normalized master curve.

To develop the final master curves, the number of equivalent cycles $n_{\mathrm{eq}}$ is plotted on the abscissa in Figure 8.9b. These were calculated as the ratio of the determined number of reference cycles $N_{\mathrm{Ref}}$ to the number of cycles to failure $N_{\mathrm{f}}$ of the corresponding S-N curve. This axis was rotated following (Seed et al. 1975). The different reference load levels $\mathrm{CSR}_{\mathrm{Ref}}$ result in parallel master curves, where higher numbers of equivalent cycles $n_{\mathrm{eq}}$ are determined at lower reference load levels $\mathrm{CSR}_{\mathrm{Ref}}$.

To account for the different load-bearing and failure behavior of SG joints in glass and facade structures under seismic loading, different test control modes were considered in this work, leading to different S-N curves, as shown in Figure 8.10a. Here, the number of reference cycles $N_{\mathrm{Ref}}$ was evaluated for the exemplary reference load level $\mathrm{CSR}_{\mathrm{Ref}} = 100$ %. For the force-controlled S-N curve, 4.8 reference cycles were determined, in contrast to 7.1 cycles for the displacement-controlled test series.

The resulting force and displacement master curves are shown in Figure 8.10. Due to the similar slope $m$ of the two S-N curves, the two master curves run almost parallel. As both master curves were determined at a reference load level $\mathrm{CSR}_{\mathrm{Ref}} = 100$ %, there is an intersection at this load level, corresponding to the number of equivalent load cycles $n_{\mathrm{eq}} = 1$.

A similar effect was observed when converting S-N curves from the different test frequencies to master curves, as illustrated in Figure 8.11. The S-N curves from different test frequencies resulted in clearly different numbers of reference cycles $N_{\mathrm{Ref}}$, as illustrated in Figure 8.11a. By normalizing the abscissa, one master curve independent of the test frequency was derived, as shown in Figure 8.11b. This confirms the findings from section 8.4.1.2, that the numbers of equivalent cycles $n_{\mathrm{eq}}$ can be calculated independently of the test frequency.

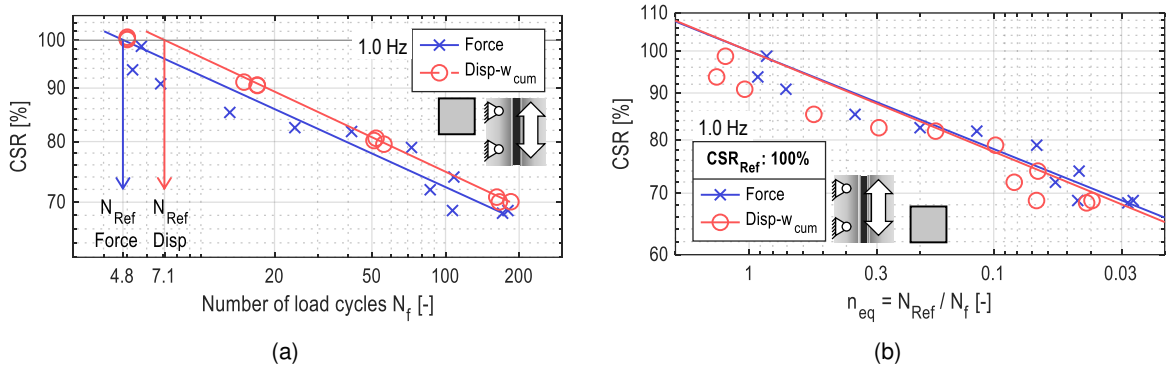


**Figure 8.10:** Determination of the master curves for the two test control modes ($f$ = 1.0 Hz): (a) determination of $N_{\mathrm{Ref}}$; (b) normalized master curve.

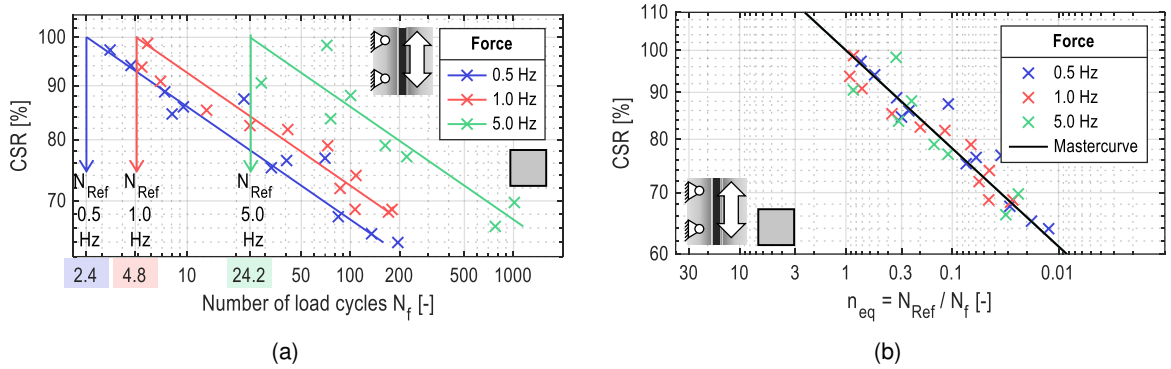


**Figure 8.11:** Determination of master curves for different test frequencies (force-controlled, 12 × 12 mm$^2$): (a) determination of $N_{\mathrm{Ref}}$; (b) normalized master curve.

To illustrate the influence of joint geometry on the master curves, the force-controlled S-N curves for the 12 × 12 mm$^2$ and 8 × 24 mm$^2$ geometries at 1.0 Hz, shown in Figure 7.34a, were used as an example. Figure 8.12a shows the determination of the number of reference cycles $N_{\mathrm{Ref}}$. A clear difference between the joint geometries was observed, with the compact 8 × 24 mm$^2$ joint leading to 10.2 reference cycles $N_{\mathrm{Ref}}$, compared to 4.8 cycles for the standard geometry. After normalizing the abscissa, the different joint geometries showed only a minor influence on the master curve, as illustrated in Figure 8.12b. This is consistent with the results obtained from the analysis of the influence of test frequency and test control mode.

In summary, only minor effects of the test control mode and joint geometry on the master curves were observed, due to the very similar slopes $m$ of the corresponding S-N curves. The mathematical derivation presented in section 8.4.1.2 was confirmed, showing no influence of the test frequency on the master curves. The extent to which these small deviations affect $n_{\mathrm{eq}}$ is analyzed in the following sections.

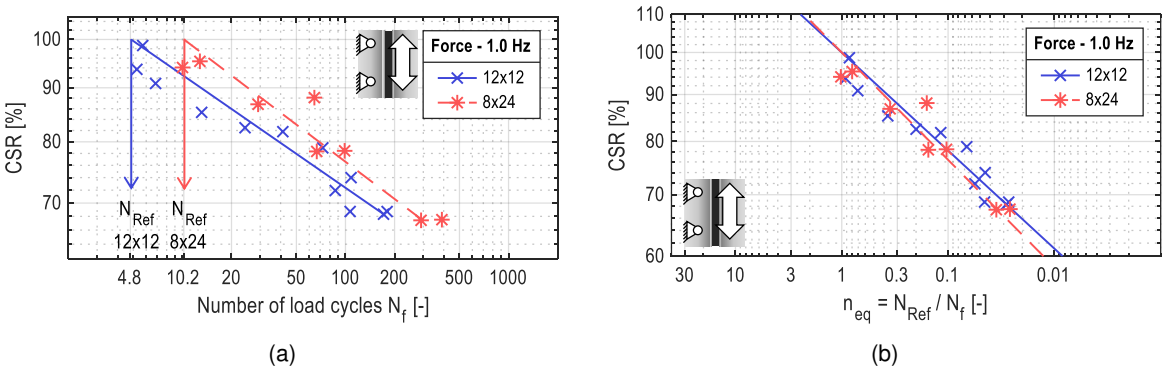


**Figure 8.12:** Determination of the master curves for different joint geometries (force-controlled): (a) determination of $N_{\mathrm{Ref}}$ at $\mathrm{CSR}_{\mathrm{Ref}} = 100$ %; (b) normalized master curve.

### 8.4.2 Parametric Determination of the Number of Equivalent Cycles

To systematically analyze the cyclic–seismic loading on SG joints and identify the relevant influencing parameters, a parametric study was carried out. Using the calculation model defined in section 8.2, simulations were performed for all ground motion records in the database described in section 8.3. The LIDA of the SDOF system was performed globally with a damping ratio of $\zeta = 5$ %, as discussed in section 8.2.2. All response vibrations were calculated using the first component of each ground motion record. To investigate the influence of stiffness variations resulting from different structural configurations, natural periods $T$ in the relevant range from 0.1 s to 2 s (0.1 s, 0.2 s, 0.3 s, 0.6 s, 1 s, and 2 s) were considered. The evaluation procedure is schematically illustrated in Figure 8.13.

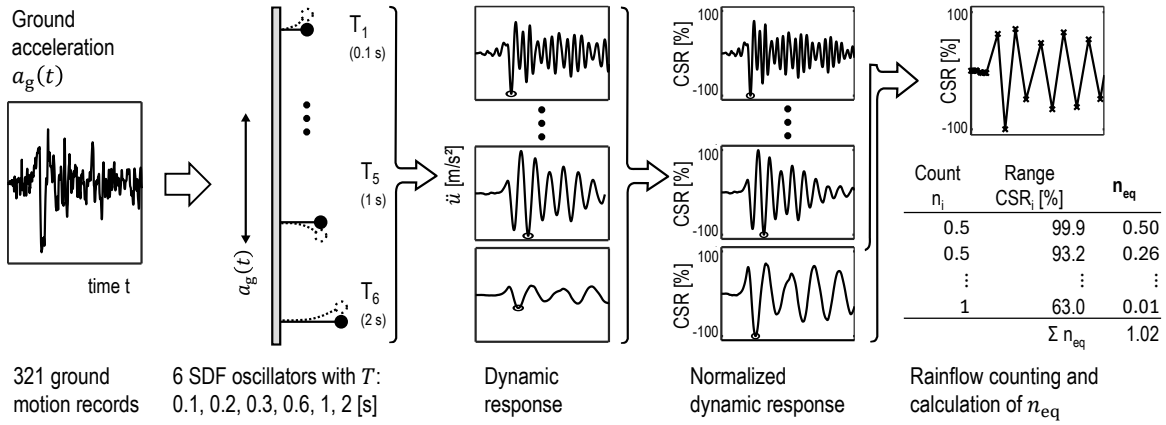


**Figure 8.13:** Schematic representation of the evaluation procedure for determining the number of equivalent cycles $n_{\mathrm{eq}}$ based on the dynamic response of SDOF systems with varying natural periods $T$.

In seismic design using response spectrum methods, seismic forces are determined as a function of the natural period $T$ of the specific structure and the design ground acceleration $a_g$, as shown in Eqs. (2.51) to (2.53). The strong dependence of the seismic demand on the natural period $T$ is illustrated by the response spectra in Figure 8.8, discussed in section 8.3.3. Accordingly, the resulting loading is inherently dependent on the structural properties and

the local seismic hazard. SG joints can be designed by adjusting their geometry such that the applied loads are sustained while achieving a high degree of utilization of the joint capacity. Consequently, for a given configuration, SG joints are designed to reach a degree of utilization of up to 100 % in the limiting case.

To define universally applicable design parameters, the stress histories obtained from the dynamic analyses were normalized to ensure a consistent load level across all investigated cases, corresponding to a uniform degree of utilization. By normalizing the stress histories after completion of the dynamic analysis and before determining the number of equivalent cycles, as illustrated in Figure 8.13, the influence of the natural period $T$ and the design ground acceleration $a_g$ on the response amplitude was removed. This normalization enabled the isolation of effects other than the period- and local seismic hazard-dependent variation in loading, allowing a focused analysis of the parameters governing SG joint behavior under cyclic–seismic loading. The resulting design parameters were therefore universally applicable, independent of the specific structural configuration and local seismic hazard.

To illustrate the strong dependence of cyclic–seismic loading on the natural period $T$, the number of equivalent cycles based on the unnormalized response vibrations $n_{\mathrm{eq,unnorm}}$ was calculated and is shown in Figure 8.14. Figure 8.14a presents $n_{\mathrm{eq,unnorm}}$ calculated based on the acceleration response, while Figure 8.14b shows $n_{\mathrm{eq,unnorm}}$ based on the displacement response. The distribution of $n_{\mathrm{eq,unnorm}}$ over $T$ follows the trend of the response spectra in Figure 8.8 for both cases, confirming that without normalization, the period-dependent variation in loading dominates the results and prevents a focused analysis of the general parameters affecting the cyclic–seismic loading.

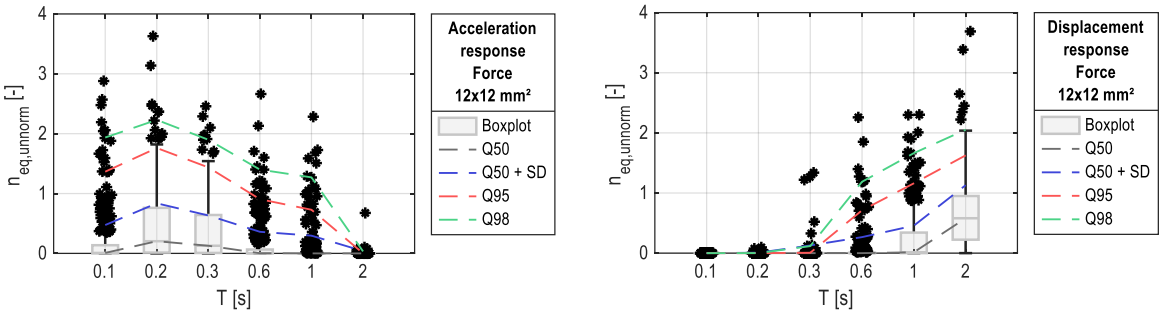


**Figure 8.14:** Box plots with statistical evaluation intervals as lines showing the influence of the natural period $T$ of the SDOF system on the unnormalized equivalent number of cycles $n_{\mathrm{eq,unnorm}}$ at $\mathrm{CSR_{Ref}} = 100$ %: (a) acceleration response; (b) displacement response.

Several normalization methods are available and are discussed, for instance, by (Liu et al. 2001). In the present study, each response history was normalized by its absolute maximum value, such that the maximum amplitude of every record equaled ±100 %, as illustrated in Figure 8.13. Nevertheless, when interpreting the results, the inherent dependence of the structural response on the natural period $T$ and the design ground acceleration $a_g$ must still be considered.

Various cycle-counting methods are available for evaluating random response histories, as discussed in section 2.3.1. When evaluating the influence of the counting method on $n_{eq}$ using the response histories from this database, the peak-counting method yielded values approximately 13 % to 22 % higher than those obtained with the rainflow method. This difference was less pronounced than the findings reported by (Stelzer et al. 2020), where peak-counting resulted in up to 35 % higher values relative to the rainflow method. According to (Köhler et al. 2012), the rainflow method produces the lowest scatter when comparing predicted and measured fatigue lifetimes. Furthermore, (DIN EN 1993-1-9) recommends the rainflow method over the peak-counting method. However, these results were obtained for HCF loading in steel structures. Whether this also applies to SG joints subjected to seismic LCF loading remains to be verified in future investigations.

In the subsequent analyses presented in this study, the rainflow counting method, which is implemented directly in MATLAB, was used for all evaluations. The evaluation was performed so that a vibration with a normalized amplitude of $\pm 100$ % corresponds to one counted cycle.

It should be noted that $n_{eq}$ is not an absolute quantity, as its magnitude depends on the selected reference load level $CSR_{Ref}$. A detailed discussion of this dependency is provided in section 8.4.5. Unless stated otherwise, all results in the following sections were evaluated at $CSR_{Ref} = 100$ %.

Following the cycle counting of the response histories, the identified cycles were converted into an equivalent number of cycles $n_{eq}$. Based on the master curves determined in section 8.4.1, the contribution of each cycle $n_{eq,i}$ was calculated and accumulated, as illustrated in Figure 8.13 on the right. This calculation was performed for each ground motion record, considering different natural periods $T$ and corresponding master curves. The implementation in a MATLAB script enables an efficient and flexible evaluation.

The calculation method for determining $n_{eq}$ was verified by comparison with the results of (Seed et al. 1975). Good agreement was found, with the present database generally covering the reference results, although some individual values exceeded them. A detailed description of this verification is provided in (Müller et al. 2025b).

### 8.4.3 Discussion of Parameters Influencing the Number of Equivalent Cycles

The following sections analyze the parameters influencing the number of equivalent cycles $n_{eq}$ in SG joints used in glass and facade structures. This analysis improves the understanding of seismic and cyclic effects on these joints and enables a systematic assessment of individual parameter effects. Ultimately, these investigations provide a basis for defining realistic load collectives for SG joints under seismic loading.

#### 8.4.3.1 Test Control Mode and Response Motion Type

The influence of different master curves and response vibration histories is shown in Figure 8.15 as a combination of violin and box plots. This representation combines statistical summary measures with density estimation. The box plot displays key descriptive statistics: the median (shown as a line within the box), the interquartile range (IQR), which spans the 25 % to 75 % quantile and is represented by the box height, and whiskers extending to the most extreme data points within 1.5 times the IQR. Outliers beyond this range are individually marked. The half-violin plot, attached to the right of the box, illustrates the probability density of the data, indicating where the data points are more concentrated. Wider sections of the violin correspond to a higher density of data points, revealing the shape and distribution characteristics of the data, such as skewness. This combined visualization provides a comprehensive qualitative representation of the dataset, highlighting both statistical measures and overall distribution.

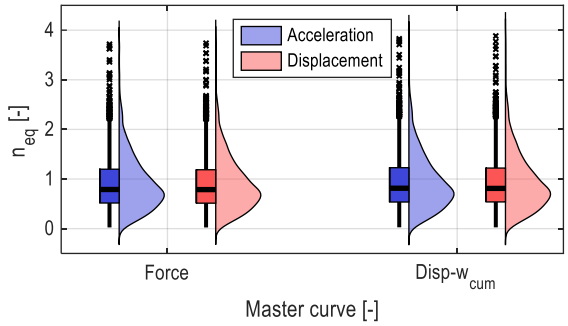


**Figure 8.15:** Half-violin box plot showing the influence of response motion type and master curve on the equivalent number of cycles $n_{\mathrm{eq}}$ at $\mathrm{CSR}_{\mathrm{Ref}} = 100$ %; data: all response histories, rainflow counting, 12 × 12 mm$^2$ joint geometry.

On the abscissa, the data were categorized according to the different master curves, with colors distinguishing between the two types of response motion: displacement and acceleration.

It is noteworthy that for both master curves, there was no relevant difference between the different types of response motion, displacement and acceleration, with respect to the number of equivalent cycles $n_{\mathrm{eq}}$. This result can be traced back to the kinematic relationship between displacement and acceleration. The acceleration response corresponds to the second time derivative of the displacement response. Since the system's equation of motion is described by a sinusoidal function, the second derivative results only in an amplitude scaling and a phase shift, both of which disappear during the normalization process.

The master curves of the deformation-controlled tests with the energy-based failure criterion $w_{\mathrm{cum}}$ and the force-controlled tests showed almost no difference in the number of equivalent cycles. This result was expected due to the very similar slope $m$ of the master curves.

A median of $n_{\mathrm{eq}} = 0.79$ cycles could be determined for the force master curve, compared to a value of $n_{\mathrm{eq}} = 0.81$ for the displacement master curve. With skewness values of 1.2 and a

coefficient of variation (CV) of 0.6 for both master curves, the similarity of the results was confirmed.

In summary, the number of equivalent cycles $n_{eq}$ was not affected by the different response motion types, displacement and acceleration. This makes it possible to evaluate the other influencing parameters based on only one response motion type. In this case, the displacement response vibration was selected for further evaluation unless otherwise specified. The different master curves also provide very similar numbers of equivalent cycles $n_{eq}$. Therefore, all further evaluations were based on the master curve determined from the force-controlled test series, as this test series provided the basis for calibrating the failure criteria of the displacement-controlled series and exhibited a clearly more critical failure behavior.

Comparing the results with those of (Müller et al. 2025b), the basic trends are confirmed, although the master curves in both studies are based on different experimental data sets. The most notable difference is the deviation in the quantitative magnitude of the number of equivalent cycles $n_{eq}$. The median value increased from $n_{eq} = 0.79$ for the force-controlled master curve to $n_{eq} = 1.4$ in (Müller et al. 2025b), while the 75 % quantile increased from $n_{eq} = 1.20$ to $n_{eq} = 2.07$. This deviation is most likely explained by the different slope values $m$ of the master curves. To investigate this effect in more detail, the influence of the slope $m$ is analyzed in a parametric study in section 8.4.4.

The detailed statistical values corresponding to the distributions shown in Figure 8.15 are summarized in Table B.1 in appendix B.

#### 8.4.3.2 Natural Period of the SDOF-System

To analyze the influence of the natural period $T$ of the SDOF system on the number of equivalent cycles $n_{eq}$, the calculated response vibration histories were categorized by $T$ and are illustrated in Figure 8.16. Important statistical parameters are presented as colored lines within the combined violin and box plots. Only the displacement vibrations from the force master curve are shown, due to the reasons discussed above.

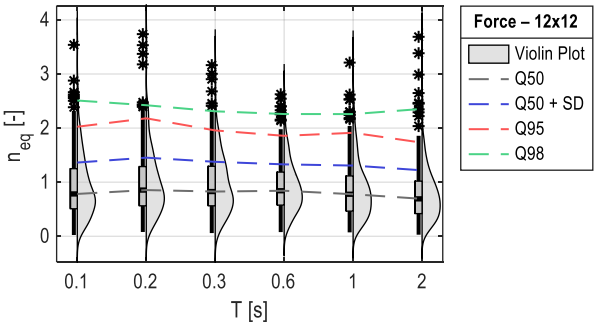


**Figure 8.16:** Half-violin box plots with statistical evaluation intervals as lines showing the influence of the natural period $T$ on the equivalent number of cycles $n_{eq}$ at $CSR_{Ref} = 100$ %; data: all displacement response histories, force master curve, 12 × 12 mm$^2$ joint geometry.

No clear trend was observed for the influence of the natural period $T$ on the number of equivalent cycles $n_{eq}$. Slightly higher values occurred for $T$ between 0.2 and 0.6 s, with decreasing values toward the limits of the investigated range. The dispersion and distribution characteristics remained similar across all periods. A detailed summary of the statistical parameters is provided in Table B.2 in appendix B. Compared to (Müller et al. 2025b), where a more consistent decrease in $n_{eq}$ with increasing $T$ was observed, the present results showed no clear trend.

Overall, the analysis of the natural period $T$ of the SDOF system shows no clear effect on the number of equivalent cycles $n_{eq}$, although small deviations between individual period groups are identified. The relevance of these deviations is addressed in the subsequent combined evaluation of all influencing parameters.

#### 8.4.3.3 Magnitude of the Ground Motion

To analyze the influence of the earthquake magnitude $M_w$ on the number of equivalent cycles $n_{eq}$, the values of $M_w$ were rounded to the nearest integer. The calculated response histories were then categorized accordingly and are illustrated in Figure 8.17a as combined violin and box plots.

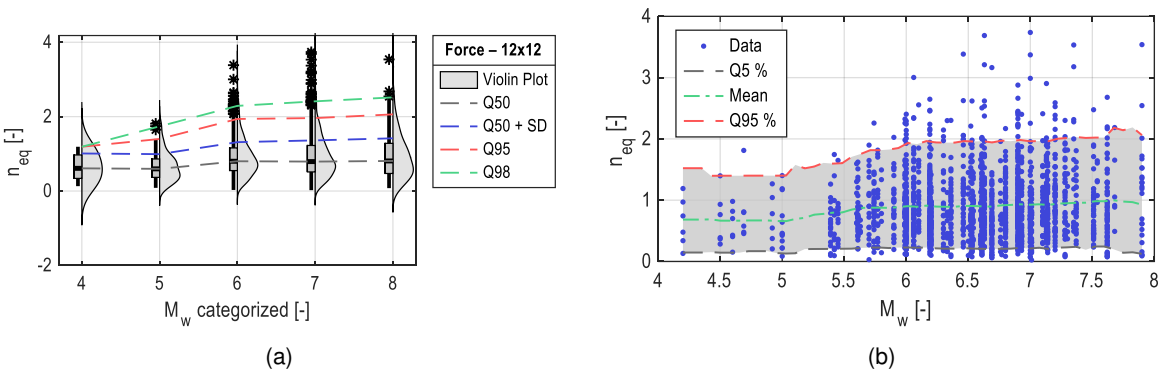


**Figure 8.17:** Influence of the earthquake magnitude $M_w$ on the equivalent number of cycles $n_{eq}$ at $CSR_{Ref} = 100$ %: (a) half-violin box plots with statistical evaluation intervals as lines; (b) scatter plot with 5 %, 95 %, and mean curves; data: all displacement response histories, force master curve, 12 × 12 mm² joint geometry.

For magnitudes $M_w = 4$–5, a median value of $n_{eq} = 0.6$ cycles was observed, while for magnitudes $M_w = 6$–8, the median increased to $n_{eq} = 0.8$ cycles, corresponding to an increase of approximately 30 %. Within the range $M_w = 6$–8, no further increase in the median values was observed. A similar pattern was observed for the 75 % and 95 % quantiles. A detailed statistical summary of $n_{eq}$ as a function of earthquake magnitude is provided in Table B.3 in appendix B.

Statistical analysis indicates that higher magnitude categories ($M_w = 6$–8) differ significantly from lower magnitudes with respect to the median number of equivalent cycles $n_{eq}$. However, load histories with magnitudes $M_w = 4$–5 accounted for only about 4 % of the

dataset. Therefore, despite the observed deviations in median values, the overall influence of earthquake magnitude on $n_{eq}$ is limited.

To examine the influence of magnitude on the number of equivalent cycles $n_{eq}$ in more detail, $n_{eq}$ is presented as a scatter plot in Figure 8.17b. To enable an initial statistical characterization of the distribution, the mean as well as the 5 % and 95 % quantiles were calculated and plotted as a moving average with a smoothing width of one order of magnitude. The results show that both the mean and the 95 % quantile of $n_{eq}$ increase from magnitudes $M_w = 5$ to $M_w = 6$, while no further increase is observed for higher magnitudes. The low density of data points for load histories with magnitudes $M_w = 4$–$5$ is also evident.

In summary, considering the densest range of the database, covering magnitudes $M_w \approx 6$–$7.5$, no significant influence of earthquake magnitude on the number of equivalent cycles $n_{eq}$ was observed, which contrasts with the findings of (Müller et al. 2025b). While the normalization removes the amplitude dependence of the response histories, it does not affect the duration-related cyclic content of the ground motion records, which may explain the continuous increase observed in (Müller et al. 2025b) and attributed to the longer duration of high-magnitude earthquakes (Bahrampouri et al. 2021; Mazzoni et al. 2023). As the present study and (Müller et al. 2025b) are based on the same ground motion database, the differing behavior is attributed to the slope $m$ of the underlying S-N curves. This effect is further investigated in the parametric study presented in section 8.4.4.

#### 8.4.3.4 Joint Geometry

To analyze the influence of joint geometry on the number of equivalent cycles $n_{eq}$, the calculated response vibration histories were categorized by the type of master curve and the joint geometry, as illustrated in Figure 8.18 by a combined violin and box plot.

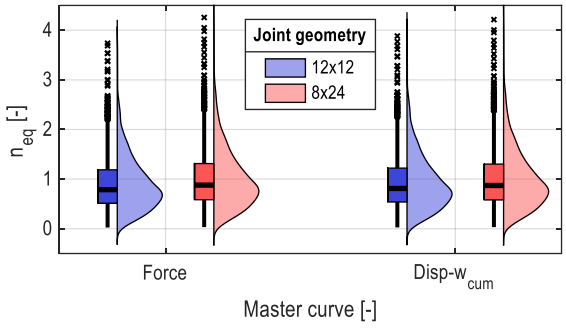


**Figure 8.18:** Influence of joint geometry and master curve on the equivalent number of cycles $n_{eq}$ at $CSR_{Ref} = 100$ %; data: all response histories, rainflow counting.

As already determined when analyzing the influencing parameters of the master curves in section 8.4.1.3, there are very similar results between the two joint geometries. For the force master curve, the median of the number of equivalent cycles increases from $n_{eq} = 0.79$ to $n_{eq} = 0.88$ for the compact $8 \times 24$ mm$^2$ joint geometry. When evaluated with the displacement master curve, the $n_{eq}$ values increase from $n_{eq} = 0.81$ for the $12 \times 12$ mm$^2$

joint to $n_{eq} = 0.87$ for the $8 \times 24$ mm$^2$ joint. A more detailed summary of the statistical evaluation is provided in Table B.4 in appendix B.

### 8.4.4 Parametric Study on the Influence of the Slope of the Master Curve

As demonstrated in the mathematical derivation of the master curves in section 8.4.1.2, the slope $m$ of the master curve defines the material-specific parameter used to determine the number of equivalent cycles $n_{eq}$. In addition to the earthquake-specific parameters investigated in section 8.4.3, such as earthquake magnitude $M_w$ and the natural period $T$ of the structure, the slope $m$ also influences the results. Since the slopes $m$ for the two test control modes in this study are very similar, the influence of $m$ on $n_{eq}$ became apparent only when comparing with the results of (Müller et al. 2025b), where different slope values were reported. Furthermore, the sensitivity of $n_{eq}$ to variations in $T$ and $M_w$ also depends on the slope $m$.

To examine the influence of the master curve slope in detail and to improve the general understanding of these relationships, the number of equivalent cycles $n_{eq}$ was calculated in a parametric study for slope values between 2 and 22. The lower limit of the investigated range was selected in accordance with (DIN EN 1993-1-9). For the upper limit, the maximum slopes reported by (Ciupack et al. 2018) were used. The slope was increased in increments of 2, resulting in 11 distinct levels.

To analyze the overall influence of the master curve slope $m$ on the number of equivalent cycles $n_{eq}$, the results are shown in Figure 8.19a as box plots. Each box plot represents one evaluated slope level. Since the visualization is strongly affected by outliers, Figure 8.19b shows the individual box plot metrics as line plots. Both representations clearly indicate a strong dependence of the number of equivalent cycles $n_{eq}$ on the slope $m$ of the master curve. The median decreased from $n_{eq} = 5.4$ at $m = 2$ to $n_{eq} = 0.3$ at the maximum investigated slope of $m = 22$. Similar trends were observed for the other statistical metrics.

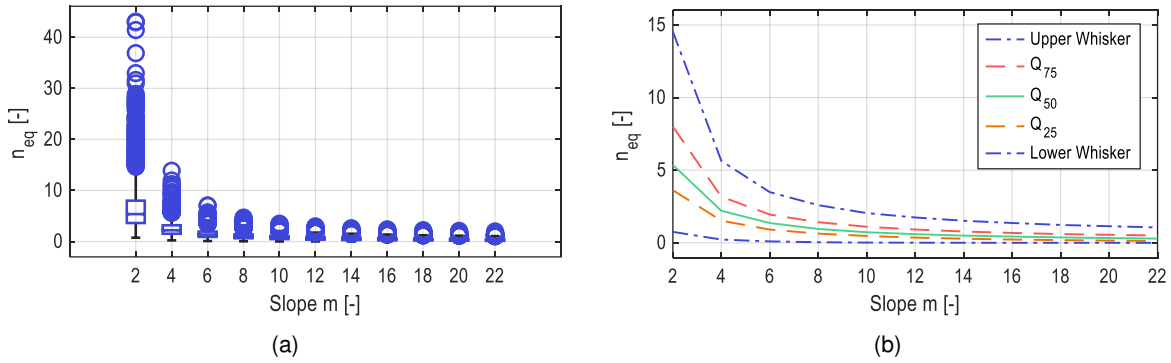


**Figure 8.19:** Influence of the slope $m$ of the master curve on the number of equivalent cycles $n_{eq}$ at $CSR_{Ref} = 100$ %: (a) box plot representation; (b) line plot of box plot metrics without outliers; data: all displacement-response histories.

To analyze the influence of the natural period $T$ on the number of equivalent cycles $n_{eq}$ as a function of the slope $m$, Figure 8.20 presents only the median values for each group of natural periods $T$. Moreover, only slopes in the range from 4 to 10 are shown, as slope values within this range have been reported in studies on the LCF behavior of SG joints (Müller et al. 2025c; Müller et al. 2025d). Figure 8.20a shows the median of $n_{eq}$ as a function of the natural period $T$. The results show that lower slope values $m$ yield higher overall levels of $n_{eq}$, as previously shown in Figure 8.19. At low slope values, $n_{eq}$ decreased markedly as the natural period $T$ increased.

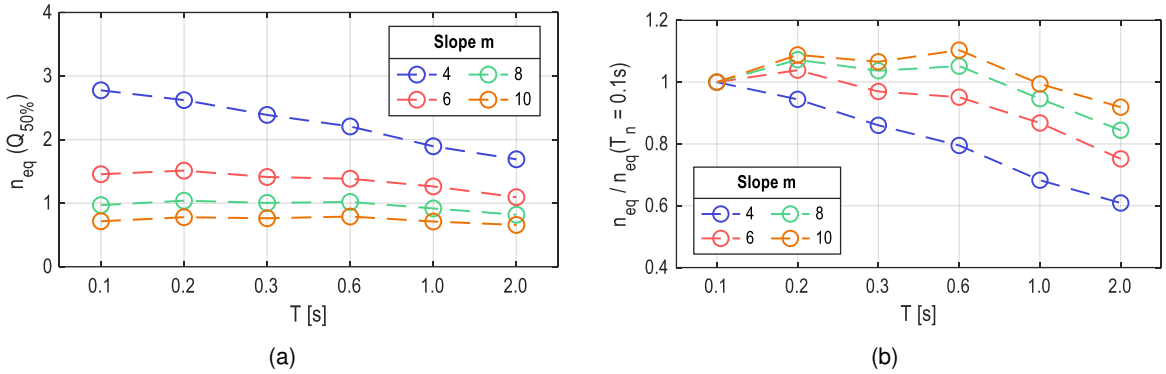


**Figure 8.20:** Influence of the natural period $T$ and the slope $m$ on $n_{eq}$ at $CSR_{Ref} = 100$ % with colors indicating different slope values: (a) line plot of the median of $n_{eq}$; (b) line plot of the normalized median of $n_{eq}$; data: all displacement-response histories.

To isolate the variation of $n_{eq}$ with $T$, independent of its absolute value, Figure 8.20b shows the normalized values of $n_{eq}$ relative to the value at $T = 0.1\ s$. For all slope values $m$, $n_{eq}$ was reduced at $T = 2.0\ s$ relative to $T = 0.1\ s$. However, as the slope $m$ decreases, the reduction in $n_{eq}$ becomes both more pronounced and more uniformly distributed across the investigated range of $T$.

A similar approach was used to analyze the influence of earthquake magnitude $M_w$ on the number of equivalent cycles $n_{eq}$. As before, the magnitude values were rounded to the nearest integer and grouped accordingly. Figure 8.21a presents the median $n_{eq}$ as a function of the categorized magnitude $M_w$, whereas Figure 8.21b presents the normalized median $n_{eq}$ relative to the group with $M_w = 5$, which represents the first group with a sufficient number of data points. The line colors indicate the slope values $m$.

In general, $n_{eq}$ increases as the slope $m$ decreases, as shown in Figure 8.19. Regarding the influence of earthquake magnitude, a clear increase in $n_{eq}$ was observed for $M_w = 5$–6, independent of the slope $m$. For the two lower slopes ($m = 4$–6), a further rise in $M_w$ also led to higher values of $n_{eq}$. At higher slopes ($m = 8$–10), $n_{eq}$ remained at a similar level for $M_w \geq 6$.

Overall, the slope $m$ strongly influences the number of equivalent cycles $n_{eq}$. For low slope values ($m \approx 4$–6), a dependence on both the natural period $T$ and the magnitude $M_w$ is also observed. This should be considered when applying the results of this work to alternative master curves derived from different adhesive systems or manufacturing batches. A detailed

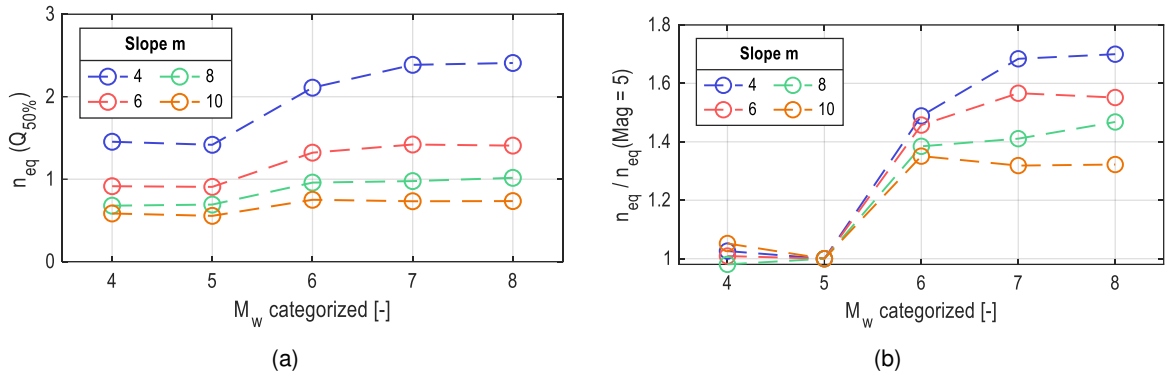


**Figure 8.21:** Influence of $M_\mathrm{w}$ and slope $m$ on $n_\mathrm{eq}$ at $\mathrm{CSR}_\mathrm{Ref} = 100\ \%$ with colors indicating different slope values: (a) line plot of the median of $n_\mathrm{eq}$ ; (b) line plot of the normalized median of $n_\mathrm{eq}$; data: all displacement response histories.

statistical summary of the equivalent number of cycles $n_\mathrm{eq}$ as a function of the slope $m$ is provided in Table B.5 in appendix B.

For the evaluation in this work, the experimentally determined master curves and their corresponding slopes were used to ensure that the results reflected the experimentally observed LCF behavior of the DOWSIL 993 adhesive as accurately as possible.

### 8.4.5 Influence of the Reference Load Level on the Number of Equivalent Cycles

To facilitate the interpretation of the overall magnitude of the equivalent number of cycles $n_\mathrm{eq}$, independent of individual parameter effects, the influence of the selected reference load level $\mathrm{CSR}_\mathrm{Ref}$ was examined.

The equivalent number of cycles $n_\mathrm{eq}$ depends explicitly on the selected reference load level $\mathrm{CSR}_\mathrm{Ref}$, as indicated by Eqs. (2.54), (8.1) and (8.2), and therefore does not represent an absolute quantity. For a given loading history, a change in the reference level from $CSR_{Ref,1}$ to $CSR_{Ref,2}$ results in a consistent rescaling of the equivalent number of cycles. Using the definition of $n_\mathrm{eq}$, the conversion between two reference load levels can be written as:

$$n_\mathrm{eq}(\mathrm{CSR}_\mathrm{Ref,2}) = \sum_i \left( \frac{\mathrm{CSR}_\mathrm{Ref,2}}{\mathrm{CSR}_i} \right)^{-m} = \sum_i \left( \frac{\mathrm{CSR}_\mathrm{Ref,2}}{\mathrm{CSR}_\mathrm{Ref,1}} \cdot \frac{\mathrm{CSR}_\mathrm{Ref,1}}{\mathrm{CSR}_i} \right)^{-m} \tag{8.3}$$

Factoring out the constant term and using the definition of $n_\mathrm{eq}(\mathrm{CSR}_\mathrm{Ref,1})$ gives:

$$n_\mathrm{eq}(\mathrm{CSR}_\mathrm{Ref,2}) = n_\mathrm{eq}(\mathrm{CSR}_\mathrm{Ref,1}) \cdot \left( \frac{\mathrm{CSR}_\mathrm{Ref,2}}{\mathrm{CSR}_\mathrm{Ref,1}} \right)^{-m} \tag{8.4}$$

This relation follows directly from the previously introduced formulation, since a change in the reference level leads to a uniform scaling of all cycle contributions, which can be factored out of the summation.

The concept of equivalent load cycles thus provides a consistent reduction of complex seismic loading histories to a scalar quantity suitable for evaluating the cyclic component of seismic loading and for the subsequent determination of design parameters. However, the absolute magnitude of the equivalent number of cycles does not allow a direct assessment of the actual damage induced by seismic loading, as it depends on the selected reference load level. Consequently, equivalent cycle values are not directly comparable to results from previous studies unless an identical reference level is applied. This explains the deviations in the magnitude of $n_{\mathrm{eq}}$ compared to the investigations of (Seed and Idriss 1970; Seed et al. 1975).

## 8.5 Derivation of Frequency Dependent Design Parameters

This section aims to translate the findings of the previous sections into parameters relevant to the structural design of SG joints under seismic loading. Based on the calculated number of equivalent cycles $n_{\mathrm{eq}}$, which quantifies the cyclic component of seismic loading, an initial statistical evaluation was performed. This provided the basis for estimating theoretical fatigue damage values $D$ using a linear damage accumulation approach. In a further step, failure load levels $\mathrm{CSR}_{\mathrm{fail}}$ were determined as potential design limits for different seismic scenarios.

For a better interpretation of these normalized values, the failure shear stress $\tau_{\mathrm{fail}}$ and the failure shear strain $\gamma_{\mathrm{fail}}$ were evaluated. Finally, the objective was to establish a relationship between the determined failure shear stress $\tau_{\mathrm{fail}}$ and failure shear strain $\gamma_{\mathrm{fail}}$ and the material properties commonly used in the design process of SG joints. To this end, a seismic reserve factor $k_{\mathrm{sr}}$ was introduced, which relates the seismic strength values to the quasi-static reference values. These values formed the basis for the design recommendations presented in chapter 9.

### 8.5.1 Statistical Analysis of the Number of Equivalent Cycles

To define limit values for the cyclic–seismic loading on SG joints, a statistical evaluation of the number of equivalent cycles $n_{\mathrm{eq}}$ is carried out based on the complete dataset. Selected statistical quantiles are evaluated and compared for both joint geometries and master curves. The results form the basis for the subsequent derivation of design-relevant parameters.

The following evaluation is based on the displacement response histories of the SDOF systems with different natural periods. In general, the master curve of the force-controlled test series is used in combination with the standard $12 \times 12$ mm$^2$ joint geometry. Figure 8.22a

shows the empirical cumulative distribution function (ECDF) of the complete dataset of calculated $n_{eq}$ values. For the statistical evaluation, selected empirical quantiles of the distribution are considered. In analogy to the characteristic values commonly used in structural engineering design (DIN EN 1990), the 95 % quantile (Q95) is included. In addition, the 98 % quantile (Q98) is considered, as characteristic wind actions according to (DIN EN 1991-1-4) are based on an annual exceedance probability of 2 %, corresponding to the 98 % non-exceedance quantile. The median (Q50) and the median plus one standard deviation (Q50 + SD) are evaluated for comparison.

With the force master curve, the median is $n_{eq} = 0.79$, increasing to $n_{eq} = 2.34$ at the 98 % quantile. The maximum value observed in the dataset is $n_{eq} = 3.74$.

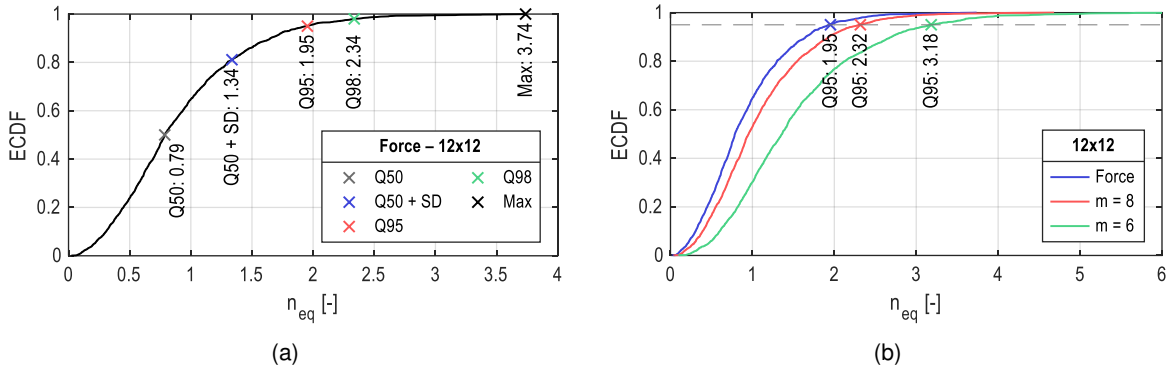


**Figure 8.22:** Statistical evaluation of $n_{eq}$ based on the complete dataset at $CSR_{Ref} = 100$ %: (a) different statistical evaluation intervals (force master curve – 12 × 12 mm$^2$ joint geometry); (b) 95 % quantile for different slope values $m$ of the master curves.

Figure 8.22b illustrates the influence of the slope $m$ of the selected master curve on the statistical evaluation of $n_{eq}$. For comparison, the 95 % quantile is used as a representative parameter. As very similar slope values and, therefore, similar $n_{eq}$ values were evaluated for the master curves in both test control modes, values from the parametric study in section 8.4.4 were taken as a comparison. With the force master curve, the 95 % quantile yielded $n_{eq} = 1.95$ for a slope $m = 9.36$. Reducing the slope to $m = 6$ leads to $n_{eq} = 3.18$.

For clarity, only two additional exemplary slope values are shown in Figure 8.22b. In order to enable a transfer of the methodological approach and evaluation in the following sections to different S-N curves, a detailed summary of the statistical evaluation of the number of equivalent cycles $n_{eq}$ for the slope values in the range of 2 to 22 is provided in Table B.5 in appendix B.

As discussed in section 8.4.3.3, the earthquake magnitude $M_w$ does not exert a relevant influence on the number of equivalent cycles $n_{eq}$. Similarly, as shown in section 8.4.3.2, the natural period $T$ of the SDOF system has no relevant effect on $n_{eq}$. Therefore, the following evaluation is performed on the complete dataset without explicitly accounting for these parameters. This simplification is justified by the high slope values of the master curves, as shown in section 8.4.4.

To summarize the number of equivalent cycles $n_{eq}$ for both joint geometries and the two investigated master curves, the statistical evaluation intervals from Figure 8.22a are shown in Figure 8.23 as a bar plot. For both joint geometries, the master curve has only a minor effect on the number of equivalent cycles $n_{eq}$. For the compact $8 \times 24$ mm$^2$ joint geometry, see Figure 8.23b, slightly higher $n_{eq}$ values are obtained than for the standard $12 \times 12$ mm$^2$ geometry shown in Figure 8.23a. A summary of the statistical evaluation of the number of equivalent cycles $n_{eq}$, for both joint geometries, based on the force and displacement master curves, can be found in Table 8.1.

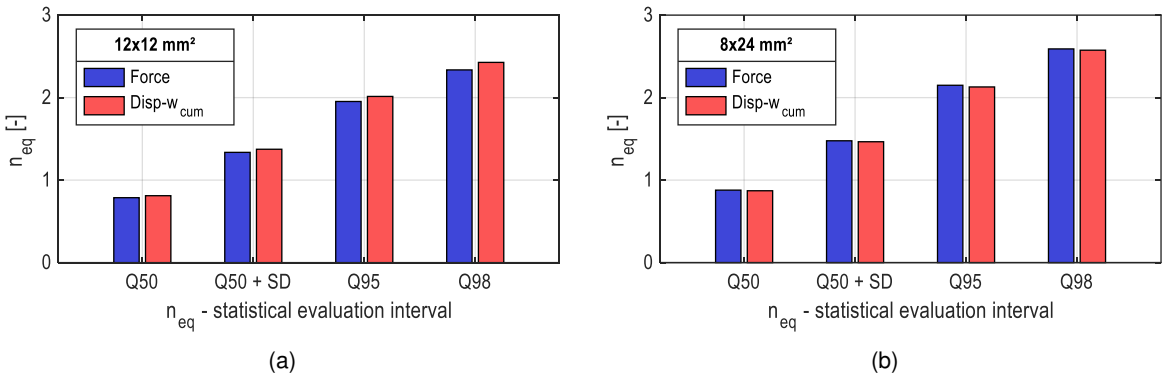


**Figure 8.23:** Bar plot of the number of equivalent cycles $n_{eq}$ at $CSR_{Ref} = 100$ % as a function of the statistical evaluation interval of $n_{eq}$ and the joint geometry: (a) $12 \times 12$ mm$^2$; (b) $8 \times 24$ mm$^2$; data: displacement response histories.

**Table 8.1:** Statistical evaluation of the number of equivalent cycles $n_{eq}$ at $CSR_{Ref} = 100$ % as a function of the statistical evaluation interval and the joint geometry for both master curves.

| Joint geometry [mm$^2$] | Master curve | Q50 [-] | Q50+SD [-] | Q95 [-] | Q98 [-] | Count [-] |
|---|---|---|---|---|---|---|
| $12 \times 12$ | Force | 0.787 | 1.336 | 1.953 | 2.336 | 1926 |
| | Disp-$w_{cum}$ | 0.811 | 1.374 | 2.014 | 2.427 | 1926 |
| $8 \times 24$ | Force | 0.878 | 1.477 | 2.150 | 2.590 | 1926 |
| | Disp-$w_{cum}$ | 0.871 | 1.465 | 2.129 | 2.575 | 1926 |

In summary, the choice of statistical evaluation interval is the primary factor, as it defines the basis for the subsequent derivation of design parameters. With the master curves determined in this study, no relevant influence of the master curve, the magnitude $M_w$, or the natural period $T$ on the number of equivalent cycles $n_{eq}$ is observed. Therefore, the subsequent evaluation is performed without categorizing the dataset based on the magnitude $M_w$ or the natural period $T$.

## 8.5.2 Derivation of Fatigue Damage

### 8.5.2.1 General Calculation

The previously evaluated values for the number of equivalent cycles $n_{\mathrm{eq}}$ are now used to calculate the fatigue damage $D$ of SG joints based on linear damage accumulation. The fatigue damage $D$ calculation is based on the general Miner's rule, as described in Eq. (2.37). This relationship leads to Green's formulation for the determination of $n_{\mathrm{eq}}$, as shown in Eq. (2.54). This relationship forms the theoretical foundation of the equivalent cycle concept and is therefore inherently embedded in the evaluation framework.

With the frequency-dependent extended Basquin model in Eq. (7.15), the fatigue damage $D$ can be determined using the fitting parameters $m$ and $a$, the test frequency $f$, and the selected reference load level $\mathrm{CSR}_{\mathrm{Ref}}$. As for the entire evaluation of the number of equivalent cycles $n_{\mathrm{eq}}$, a reference load level $\mathrm{CSR}_{\mathrm{Ref}} = 100$ was selected. This results in:

$$D = \frac{n_{\mathrm{eq}}}{N_{\mathrm{Ref}}} = \frac{n_{\mathrm{eq}}}{a \cdot \mathrm{CSR}_{\mathrm{Ref}}^{-m} \cdot f} = \frac{n_{\mathrm{eq}}}{a \cdot 100^{-m} \cdot f} \tag{8.5}$$

The corresponding fitting parameters for the master curves are provided in Table 7.6. Based on this mathematical formulation, it follows that unlike the determination of $n_{\mathrm{eq}}$, the fatigue damage $D$ additionally depends on the fitting parameter $a$ and the test frequency $f$. In the following, the relevant influence parameters are investigated in detail.

### 8.5.2.2 Master Curve

The fatigue damage $D_{mean}$, based on the mean interval of the master curve, is shown in Figure 8.24 as a function of the statistical evaluation interval of $n_{\mathrm{eq}}$ for the force- and displacement-controlled test series. As an example, only the results for the 0.5 Hz test frequency are shown.

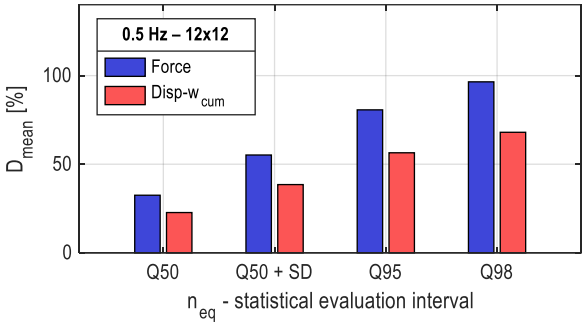


**Figure 8.24:** Bar plot of the fatigue damage $D_{\mathrm{mean}}$ as a function of the statistical evaluation interval of $n_{\mathrm{eq}}$ and the master curve; data: displacement response histories, $f$ = 0.5 Hz, 12 × 12 mm$^2$ joint geometry.

Despite nearly equal $n_{\mathrm{eq}}$ values for both master curves, the master curve based on the force-controlled tests results in higher fatigue damage $D_{mean}$, as it yields a lower number of reference cycles $N_{\mathrm{Ref}}$. The influence of the statistical evaluation interval on $D_{\mathrm{mean}}$ is consistent with the direct analysis of $n_{\mathrm{eq}}$. For the median interval, $D_{\mathrm{mean}}$ is reduced from 32.5 % to 22.7 %, for the 98 % quantile, from 96.5 % to 68.0 % when using the displacement master curve based on the $w_{\mathrm{cum}}$ failure criterion. This corresponds to a reduction of about 30 % compared to the force master curve.

#### 8.5.2.3 Statistical Evaluation of the Master Curve

Another parameter that influences the fatigue damage $D$, despite having no influence on the number of equivalent cycles $n_{\mathrm{eq}}$, is the statistical evaluation interval of the master curves. As shown in section 7.6.4 and Table 7.6, the prediction interval of the S-N curves was evaluated in addition to the mean curve. This interval defines the characteristic material properties for a target survival probability of 95 %.

The fatigue damage $D$ as a function of the statistical evaluation interval of the master curve is shown in Figure 8.25 for the two master curves. Only the damage values $D(n_{eq,Q98})$ corresponding to the 98 % quantile of $n_{\mathrm{eq}}$ are presented for a test frequency of 0.5 Hz and a $12 \times 12$ mm$^2$ joint geometry. For both master curves, the fatigue damage $D$ increases when using the prediction interval instead of the mean curve. Due to the higher scatter and corresponding higher standard deviation in the force-controlled test series, the prediction interval increases $D$ by 112 % for the force-controlled series and by 48 % for the displacement-controlled series, relative to the mean curve.

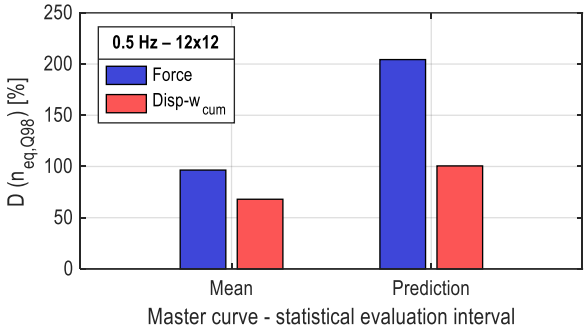


**Figure 8.25:** Bar plot of the fatigue damage $D(n_{\mathrm{eq,Q98}})$ based on the 98 % quantile of $n_{\mathrm{eq}}$ as a function of the statistical evaluation interval of the master curve; data: displacement response histories, $f$ = 0.5 Hz, $12 \times 12$ mm$^2$ joint geometry.

#### 8.5.2.4 Test Frequency

The test frequency $f$ was identified as the most relevant factor influencing the fatigue damage $D$. Similar to the influence of the statistical evaluation interval of the master curve, the test frequency has no influence on the calculation of $n_{\mathrm{eq}}$. Due to the definition of $N_{\mathrm{Ref}}$

on the basis of the extended Basquin model, a direct influence of $f$ on $D$ is evident from Eq. (8.5). When rearranging the equation for easier interpretation, the fatigue damage $D$ can be directly expressed as a function of the test frequency $f$, indicating that the accumulated damage is inversely proportional to the frequency. Consequently, doubling the frequency halves the fatigue damage $D$.

$$D(f) = \frac{n_{\mathrm{eq}}}{a \cdot \mathrm{CSR}_{\mathrm{Ref}}^{-m}} \cdot f^{-1} = \frac{n_{\mathrm{eq}}}{a \cdot 100^{-m}} \cdot f^{-1} \tag{8.6}$$

Figure 8.26 illustrates this relationship, with Figure 8.26a showing the conservative force-controlled master curve for the $12 \times 12$ mm$^2$ joint geometry and Figure 8.26b showing the displacement-controlled master curve with the $w_{\mathrm{cum}}$ failure criterion. The linear correlation in the log–log scale is evident, where an increase in test frequency leads to a decrease in $D$. Changing the statistical evaluation interval leads to a parallel shift of the curves. The evaluation interval of the master curve is indicated by the line type, with a solid line for the mean master curve and a dashed line for the prediction interval. The line colors indicate the different evaluation intervals of the number of equivalent cycles $n_{\mathrm{eq}}$.

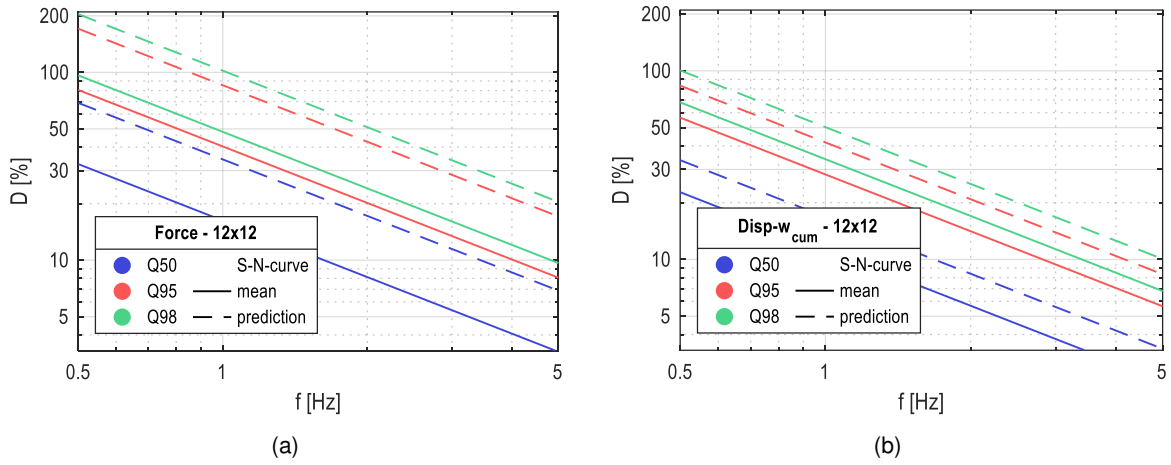


**Figure 8.26:** Plot of the fatigue damage $D$ as a function of the test frequency $f$ for different statistical evaluation intervals of the master curves and $n_{\mathrm{eq}}$: (a) force master curve; (b) Disp-$w_{\mathrm{cum}}$ master curve; data: displacement response histories, $12 \times 12$ mm$^2$ joint geometry.

For the force master curve at the 98 % quantile (shown in green), $D_{mean}$ decreases from 96.5 % for 0.5 Hz test frequency to 9.6 % at 5.0 Hz frequency. $D_{prediction}$ decreases from 204.3 % to 20.4 % when increasing the test frequency accordingly. This corresponds to a reduction of 90 % for both fatigue damage values. The results based on the displacement master curve show clearly lower damage values.

#### 8.5.2.5 Joint Geometry

As shown in section 7.6.3, the joint geometry has no relevant influence on $n_{\mathrm{eq}}$. To analyze the effect of the joint geometry on the fatigue damage $D$, Figure 8.27 shows the fatigue damage

$D(n_{eq,Q98})$ based on the 98 % quantile of $n_{\mathrm{eq}}$ as a function of the master curve and joint geometry. As the effect of the test frequency on the fatigue damage $D$ follows an inversely proportional relationship, only $f = 0.5$ Hz is shown as an example. Figure 8.27a shows the fatigue damage $D_{mean}\ (n_{eq,Q98})$ based on the mean master curves, whereas Figure 8.27b shows the fatigue damage $D_{prediction}\ (n_{eq,Q98})$ based on the prediction interval.

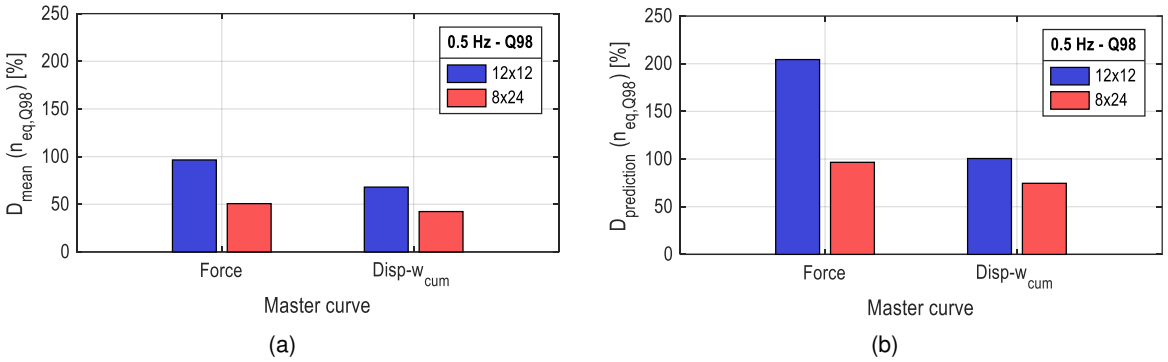


**Figure 8.27:** Bar plot of the fatigue damage $D$ based on the 98 % quantile of $n_{\mathrm{eq}}$ as a function of the master curve and joint geometry: (a) $D_{\mathrm{mean}}(n_{\mathrm{eq,Q98}})$; (b) $D_{\mathrm{prediction}}(n_{\mathrm{eq,Q98}})$; data: displacement response histories, $f$ = 0.5 Hz.

It is evident that, despite the minor influence of the joint geometry on the number of equivalent cycles $n_{\mathrm{eq}}$, a clear difference in fatigue damage between the two geometries is observed. For the fatigue damage $D_{mean}\ (n_{eq,Q98})$ and the force master curve, a reduction of 47 % is observed for the $8 \times 24$ mm$^2$ joint geometry. For $D_{prediction}\ (n_{eq,Q98})$, the reduction increases to 53 %.

The more conservative fatigue damage values are obtained for the standard $12 \times 12$ mm$^2$ joint geometry. Therefore, the following evaluation of design parameters will be performed with this joint geometry.

### 8.5.3 Derivation of Failure Load Levels

While the previous section focused on the fatigue damage $D$ expected for a statistically characterized seismic event normalized to $\pm 100$ %, the approach can also be reversed. Instead of evaluating the damage at a fixed load level, the failure load level $\mathrm{CSR}_{\mathrm{fail}}$ is introduced as the load level at which exactly one seismic event leads to complete failure of the SG joint, thereby providing a direct design limit for the seismic load capacity of SG joints. For this purpose, complete failure of the SG joint is selected as the target damage, $D_{\mathrm{t}} = 1.0$.

The selection of $D_{\mathrm{t}} = 1.0$ corresponds to complete failure of the SG joint, meaning the full 100 mm bonded length has ruptured in the force-controlled experiments, and represents a possible threshold value for the ultimate limit state verification of SG joints under seismic conditions. Even at lower damage values, partial damage of the SG joint is expected, as

shown in (Müller et al. 2025d). This target damage can be interpreted as satisfying the "no-collapse" requirement of (DIN EN 1998-1), which permits limited damage while retaining residual load-bearing capacity. For the "damage limitation" requirement, a lower target damage level may need to be considered. However, the appropriate value depends on the associated safety levels and seismic actions and requires further investigation.

The calculation of the failure load level $\mathrm{CSR}_{\mathrm{fail}}$ is based on the fundamental assumptions of linear damage accumulation in Eq. (2.37) and the extended Basquin-Model in Eq. (7.15). First, the number of cycles to failure $N_{\mathrm{fail}}$ is determined from the evaluated $n_{\mathrm{eq}}$ and the target damage level $D_{\mathrm{t}}$, using Eq. (8.7). This relation can then be substituted into the extended Basquin model to calculate the corresponding failure load level $\mathrm{CSR}_{\mathrm{fail}}$ using Eq. (8.8). This formulation highlights that $\mathrm{CSR}_{\mathrm{fail}}$ follows a power-law dependence on $f$, indicating a monotonic increase with increasing test frequency, with the exponent $1/m$ determined by the slope of the master curve.

$$N_{\mathrm{ref}} = N_{\mathrm{fail}} = \frac{n_{\mathrm{eq}}}{D_{\mathrm{t}}} \tag{8.7}$$

$$\mathrm{CSR}_{\mathrm{fail}}(f) = \left(\frac{N_{\mathrm{fail}}}{a \cdot f}\right)^{-\frac{1}{m}} = \left(\frac{n_{\mathrm{eq}}}{D_{\mathrm{t}} \cdot a \cdot f}\right)^{-\frac{1}{m}} = \left(\frac{n_{\mathrm{eq}}}{D_{\mathrm{t}} \cdot a}\right)^{-\frac{1}{m}} \cdot f^{\frac{1}{m}} \tag{8.8}$$

The direct dependence of the failure load levels $\mathrm{CSR}_{\mathrm{fail}}$ on the test frequency $f$ is shown in Figure 8.28, with Figure 8.28a showing results for the force master curve and Figure 8.28b for the displacement master curve. The different behavior compared to the fatigue damage $D$ is evident. While the failure load level $\mathrm{CSR}_{\mathrm{fail}}$ increases with increasing test frequency $f$, this increase follows a power-law relationship with a small exponent $1/m$. As a result, the frequency dependence is clearly less pronounced than for the fatigue damage $D$, although still relevant over the considered range.

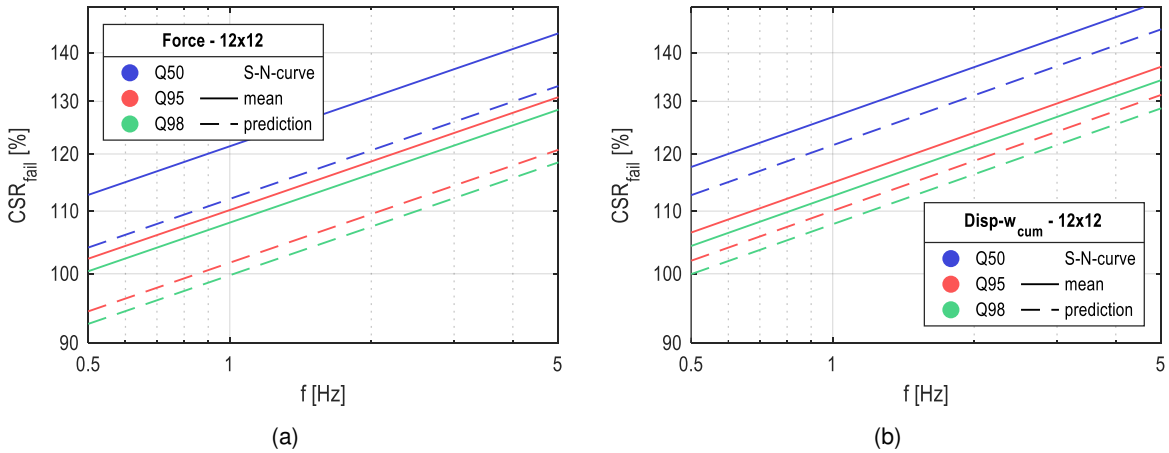


**Figure 8.28:** Plot of the failure load level $\mathrm{CSR}_{\mathrm{fail}}$ as a function of the test frequency $f$ for different statistical evaluation intervals of the master curve and of $n_{\mathrm{eq}}$: (a) force master curve; (b) Disp-$w_{\mathrm{cum}}$ master curve; data: displacement response histories, 12 × 12 mm$^2$ joint geometry.

For the most conservative case (98 % quantile of $n_{eq}$, prediction interval, force master curve), the failure load levels $CSR_{fail}$ range from 118.5 % for the 5.0 Hz test frequency to 92.7 % for the slowest 0.5 Hz frequency tested. This implies that under 0.5 Hz loading frequency, a loading of 92.7 % of the quasi-static reference stress $\tau_{ult,mean}$ can be applied, before failure within one seismic event is expected.

### 8.5.4 Derivation of Failure Stress Levels

All previous results were expressed in terms of the normalized cyclic stress ratio CSR to enable a universal characterization independent of specific material properties. To relate the results to material properties used in typical design practice, and to develop recommendations for the design of SG joints under seismic loading in the following chapter of this thesis, the results were converted back to real stress and strain values. According to Eqs. (7.1) and (7.2) from section 7.2.4, the real applied stress values $\tau_E$ and $\gamma_E$ were normalized by the corresponding mean ultimate strength from the quasi-static reference test. The quasi-static reference strength $\tau_{ult,mean}$ and $\gamma_{ult,mean}$ are given in Table 6.2.

With this relation, the failure load level $CSR_{fail}$ can be converted to the failure shear stress $\tau_{fail}$ and failure shear strain $\gamma_{fail}$:

$$CSR_{\tau,fail} = \frac{\tau_{fail}}{\tau_{ult,mean}} \quad \Rightarrow \quad \tau_{fail} = CSR_{\tau,fail} \cdot \tau_{ult,mean} \tag{8.9}$$

$$CSR_{\gamma,fail} = \frac{\gamma_{fail}}{\gamma_{ult,mean}} \quad \Rightarrow \quad \gamma_{fail} = CSR_{\gamma,fail} \cdot \gamma_{ult,mean} \tag{8.10}$$

The failure shear stress $\tau_{fail}$ is shown in Figure 8.29a, and the failure shear strain $\gamma_{fail}$ in Figure 8.29b, both as a function of the test frequency $f$. The two statistical evaluation intervals of the master curve are represented by solid and dashed lines, whereas the different statistical evaluation intervals of $n_{eq}$ are indicated by different colors, consistent with the previous figures.

For the prediction interval of the master curve and the 98 % quantile of $n_{eq}$, a minimum failure shear stress $\tau_{fail} = 0.84$ MPa at a test frequency $f = 0.5$ Hz was obtained for the force-controlled master curve. This value increases to $\tau_{fail} = 1.07$ MPa at a test frequency of 5.0 Hz. For the displacement-controlled master curve, the same statistical evaluation interval corresponds to a minimum failure shear strain $\gamma_{fail} = 1.21$ at 0.5 Hz, increasing to $\gamma_{fail} = 1.56$ at 5.0 Hz. All these values clearly exceed the characteristic quasi-static reference strength values given in Table 6.2 as well as the characteristic material properties from the manufacturer ETA in Table 3.1.

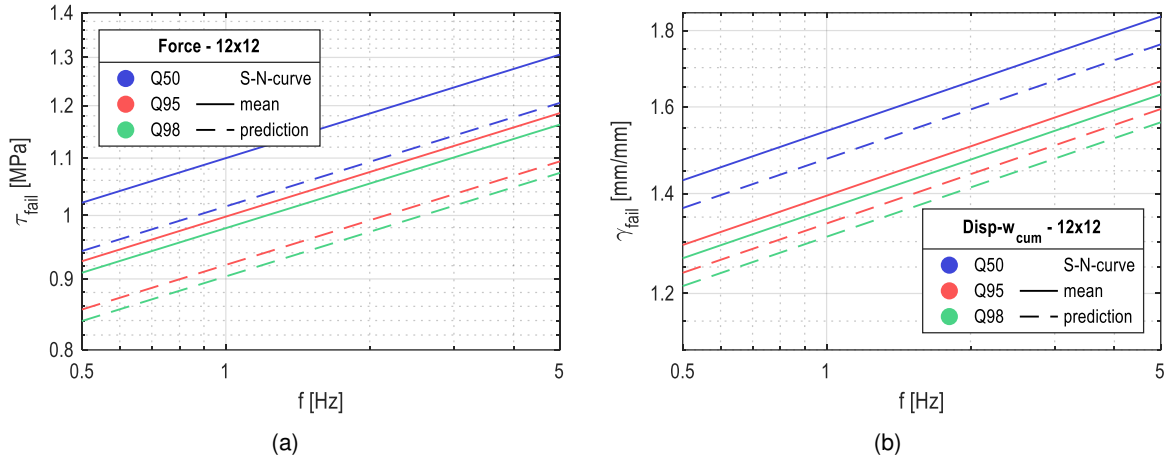


**Figure 8.29:** Plot of the failure shear stress $\tau_{\text{fail}}$ and strain $\gamma_{\text{fail}}$ values as a function of the test frequency $f$ for different statistical evaluation intervals of the master curve and of $n_{\text{eq}}$: (a) $\tau_{\text{fail}}$ for the force master curve; (b) $\gamma_{\text{fail}}$ for the Disp-$w_{\text{cum}}$ master curve; data: displacement response histories, 12 × 12 mm$^2$ joint geometry.

### 8.5.5 Derivation of a Seismic Reserve Factor

The objective is to establish a relation between the failure shear stress $\tau_{\text{fail}}$ and the failure shear strain $\gamma_{\text{fail}}$ and the typical material properties defined and used in the design process of SG joints.

Therefore, a seismic reserve factor $k_{\text{sr}}$ is introduced. This factor relates the seismic strength values to the quasi-static reference values. Two possibilities are considered. As the first variant, the seismic reserve factor $k_{\text{sr,k}}$ can be determined using the characteristic strength properties of the quasi-static reference series from chapter 6: $\tau_{\text{k}}$ and $\gamma_{\text{k}}$. These values are provided in Table 6.2 and were calculated using Eq. (3.1). The seismic reserve factor $k_{\text{sr,k}}$ is calculated as follows:

$$k_{\text{sr,k}} = \frac{\tau_{\text{fail}}}{\tau_{\text{k}}} = \frac{\gamma_{\text{fail}}}{\gamma_{\text{k}}} \tag{8.11}$$

Since the characteristic strength values depend on the statistical evaluation of the experimental dataset, including the standard deviation and number of specimens tested, an additional variant is considered. The seismic reserve factor $k_{\text{sr,ETA}}$ is defined based on the material properties provided in the manufacturer's approval documents, given in Table 3.1 in section 3.2.3.2, and is calculated as follows:

$$k_{\text{sr,ETA}} = \frac{\tau_{\text{fail}}}{\tau_{k,\text{ETA}}} = \frac{\gamma_{\text{fail}}}{\gamma_{k,\text{ETA}}} \tag{8.12}$$

The seismic reserve factor $k_{\text{sr}}$ is given in Figure 8.30 as a function of the test frequency $f$ for different statistical evaluation intervals of the master curve and of $n_{\text{eq}}$. Figures 8.30a

and 8.30b present $k_{sr,k}$ based on the characteristic strength values of the reference series, while Figures 8.30c and 8.30d present $k_{sr,ETA}$ based on the approval document properties.

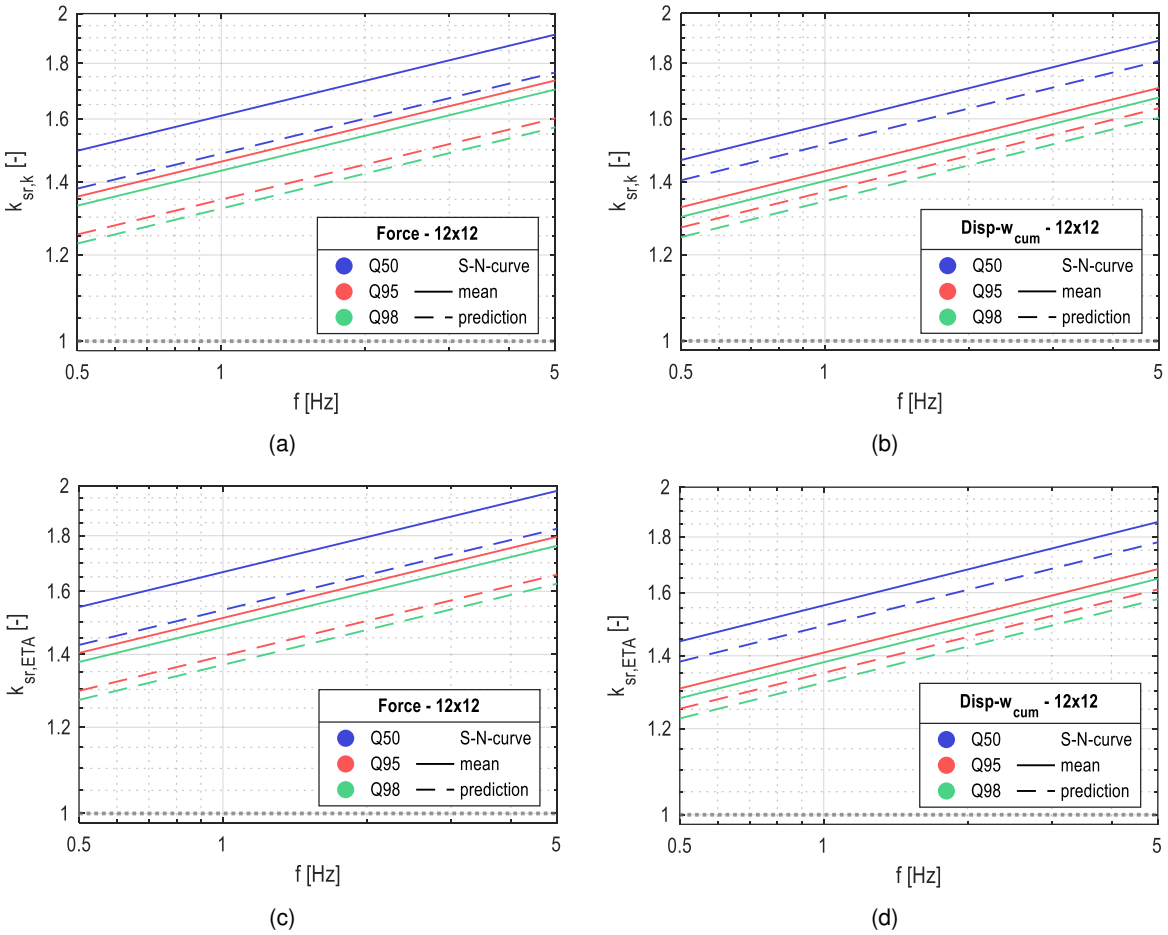


**Figure 8.30:** Plot of the seismic reserve factor $k_{sr}$ as a function of the test frequency $f$ for different statistical evaluation intervals of the master curve and of $n_{eq}$: (a) $k_{sr,k}$ for the force master curve; (b) $k_{sr,k}$ for the Disp-$w_{cum}$ master curve; (c) $k_{sr,ETA}$ for the force master curve; (d) $k_{sr,ETA}$ for the Disp-$w_{cum}$ master curve; data: displacement response histories, 12 × 12 mm$^2$ joint geometry.

For the force master curve, shown in Figures 8.30a and 8.30c, the seismic reserve factor $k_{sr,ETA} = 1.27$ is slightly larger compared to the seismic reserve factor $k_{sr,k} = 1.23$, evaluated at $f = 0.5$ Hz and the 98 % quantile of $n_{eq}$. With the conservative minimum value selected, this corresponds to a possible load reserve of 23 %.

For the displacement master curve, shown in Figures 8.30b and 8.30d, the seismic reserve factor $k_{sr,ETA} = 1.23$ is slightly smaller compared to the seismic reserve factor $k_{sr,k} = 1.25$. Again, both values are evaluated for the 0.5 Hz test frequency and the 98 % quantile. Similar to the force master curve, a possible load reserve of 23 % is identified as the conservative value.

Overall, both variants yield very similar seismic reserve factors. Since a conservative assessment requires verification against both the experimentally determined characteristic strength values and the approval-based material properties used in engineering practice,

both variants are considered and carried forward into the design recommendations in chapter 9.

## 8.6 Summary of the Seismic Ground Motion Loading

This section analyzed and quantified the cyclic–seismic load characteristics that SG joints in glass and facade constructions are subjected to during earthquake events.

As a first step, a parametric calculation model based on an SDOF system was developed. A ground motion database of recorded earthquake histories was then defined to serve as input for the cyclic–seismic loading analysis. Using the model, response histories were computed for structures with different natural periods. By evaluating both acceleration and deformation responses, the structural behavior of SG joints in various glass and facade configurations was approximated. The calculated response histories were then processed using cycle counting methods and converted into a number of equivalent cycles $n_{eq}$ with the aid of master curves. These master curves were derived from experimental LCF tests from chapter 7.

Response spectra were calculated using the ground motion database to describe the seismic peak load. It was shown that maximum acceleration responses occurred within a natural period range of 0.2 to 0.8 s, while maximum deformation responses increased with increasing period.

The cyclic component of the seismic load was characterized by the number of equivalent cycles $n_{eq}$, and the relevant influencing parameters were analyzed. Without normalization, $n_{eq}$ followed the course of the response spectra when evaluated over the natural period $T$. After normalization of the response histories, $n_{eq}$ obtained from acceleration- and deformation-based response histories showed no relevant difference. When analyzing the parameters influencing $n_{eq}$, no relevant influence of the natural period $T$ or the earthquake magnitude $M_w$ was detected for the master curves determined in this study. A parametric study on the influence of the slope $m$ of the master curve showed that, for lower slope values, the number of equivalent cycles $n_{eq}$ increases, and a stronger dependence on the natural period $T$ and the magnitude $M_w$ was observed.

Based on statistically verified values of the number of equivalent cycles $n_{eq}$, relevant parameters for the design of SG joints were evaluated. The fatigue damage $D$ in SG joints caused by a single seismic event was calculated based on linear damage accumulation. The applied master curve, the statistical evaluation interval, and the joint geometry all influenced $D$. The most pronounced influence was the test frequency $f$, with lower frequencies leading to higher fatigue damage $D$. Overall, the $12 \times 12$ mm$^2$ joint with the force-controlled master curve showed the most conservative results.

The failure load level $CSR_{fail}$ was introduced as the seismic load level at which failure is expected to occur within a single seismic event. To enable comparison with material

properties used in the typical design process, $CSR_{fail}$ was converted to the failure shear stress $\tau_{fail}$ and the failure shear strain $\gamma_{fail}$. To clearly express the relation between seismic and quasi-static material properties used in the design process of SG joints, the seismic reserve factor $k_{sr}$ was introduced as the final design parameter. All values showed a pronounced dependence on the test frequency and the selected master curve. For the most conservative case investigated, with the force-controlled master curve at a test frequency of 0.5 Hz, a seismic reserve factor of $k_{sr,k} = 1.23$ was determined, indicating a load reserve of 23 %.

These design parameters, combined with the results from the investigations on the LCF performance, formed the foundation for developing the design recommendations in the following chapter.

# 9 Design Recommendations

## 9.1 Objective and Approach

The objective of this chapter is to develop design recommendations for SG joints in glass and facade constructions subjected to seismic loading. Particular focus is placed on compatibility with existing design concepts and standards used in engineering practice.

In the first step, the safety levels defined in existing design standards are analyzed, and the corresponding approaches for statistical evaluation are discussed. Subsequently, the potential to derive a global method factor for the design of SG joints under seismic loading is examined based on current seismic design codes.

Building on these considerations, several verification methods for SG joints under seismic loading are introduced. These approaches differ primarily in their complexity, particularly regarding the representation of SG joint material behavior and the consideration of structure-specific loading conditions.

Finally, the assumptions and limitations of the proposed concepts are summarized to define the scope and applicability of the presented recommendations.

## 9.2 Discussion on the Safety Level in the Seismic Design of SG Joints

### 9.2.1 Discussion on the Statistical Evaluation Interval of the Design Parameters

As shown in section 8.5, the chosen statistical evaluation level has a significant influence on the magnitude of the derived design parameters. To develop final design recommendations, the appropriate statistical evaluation interval must be established. The relevant provisions from applicable design standards are summarized and evaluated in the following.

#### 9.2.1.1 Eurocode 0 – General Safety Level for Actions

For characteristic values of actions, (DIN EN 1990) defines that these may be specified as mean values, upper or lower values, or as nominal values. For variable actions, the characteristic value $Q_k$ is defined either as an upper value that is not exceeded within a specified reference period with a given probability, or as a lower value that is reached within this period with the same probability.

According to (DIN EN 1991-1-4), the characteristic action for wind loading is defined by an annual exceedance probability of 2 %, corresponding to a mean return period of 50 years. This exceedance probability corresponds to the 98 % quantile of the annual wind load.

#### 9.2.1.2 Eurocode 8 – Fundamental Requirements

(DIN EN 1998-1; E DIN EN 1998-1-1) define a design seismic action for the verification of structures under seismic loading. This reference seismic action is specified by a reference exceedance probability $P_{NCR}$ within 50 years or by a corresponding reference return period $T_{\mathrm{NCR}}$. The recommended values are $P_{NCR} = 10$ % and $T_{\mathrm{NCR}} = 475$ years.

According to (Aucun et al. 2012), the mean return period is defined as the inverse of the mean annual rate of occurrence of a seismic event exceeding a given threshold. Based on the reference return period of $T_{\mathrm{NCR}} = 475$ years, the mean annual rate of occurrence is $\lambda = 1/T_{\mathrm{NCR}}$, and the corresponding annual exceedance probability $P$ for at least one such event can be calculated assuming a Poisson process:

$$P(X \geq 1) = 1 - P(X = 0) = 1 - e^{-\lambda} = 1 - e^{-\frac{1}{475}} \approx 0.0021 \tag{9.1}$$

This corresponds to an annual non-exceedance probability of approximately 99.79 %, meaning that the reference seismic action defined by (DIN EN 1998-1) represents the 99.79 % quantile of the ground motion intensity distribution.

Such a high quantile represents a very conservative statistical evaluation interval for design parameters based on the number of equivalent cycles $n_{\mathrm{eq}}$. Selecting this interval would implicitly double-count the targeted safety level within the design process. First in the derivation of the design parameters, and again in the determination of the seismic acceleration values prescribed by the relevant Eurocodes.

#### 9.2.1.3 Eurocode 8 – Time-History Analysis

(DIN EN 1998-1) specifies that, for the nonlinear time-history analysis of building structures, at least seven acceleration records shall be used. In this case, the mean value of the response

quantities obtained from all analyses may be adopted as the design value of the corresponding action effect. The selected acceleration records shall be representative of the seismic characteristics of the site.

The updated version, (E DIN EN 1998-1-1), provides similar recommendations and includes additional guidance on the scaling of input ground motions. The acceleration records must be scaled such that their response spectra are consistent with the target spectrum corresponding to the seismic action under consideration.

By using the mean value of the response quantities, the seismic demand is represented as accurately as possible without additional conservatism on the response side. The desired safety level is achieved through the appropriate scaling of the acceleration amplitudes defined by the respective design spectra.

#### 9.2.1.4 Eurocode 0 – General Safety Level for Material and Product Properties

In addition to the provisions for actions, (DIN EN 1990) also defines rules for specifying the properties of construction materials and products. These properties shall likewise be expressed in terms of characteristic values. Unless otherwise specified in the relevant parts of the Eurocodes, the characteristic value is defined as the 5 % quantile for material or product properties leading to unfavorable effects, and as the 95 % quantile for properties leading to favorable effects.

#### 9.2.1.5 Evaluation and Recommendation

Although the characterization of the cyclic–seismic loading in chapter 8 addresses the action side of the verification, the derived design parameters in this chapter combine action and resistance quantities. Specifically, the evaluation aims to characterize the load-bearing and failure behavior of SG joints under seismic loading. The seismic reserve factor $k_{sr}$ relates the seismic failure load to the quasi-static material properties, thereby accounting for the component-specific overstrength of the SG joint, and can be interpreted as a material-related design parameter.

Against this background, it appears appropriate to adopt the characteristic values for material and product properties defined in section 9.2.1.4, corresponding to the 5 % and 95 % quantiles, for the statistical evaluation of the design parameters. This approach provides a consistent basis for quantifying the material-related uncertainty in the derived design parameters.

An evaluation based on the 475-year reference return period, on the other hand, is not considered appropriate in this context, as this safety level is already accounted for on the action side of the seismic design through the definition of the ground acceleration in design response spectra.

When applying the 95 % quantile, the question arises at which stages of the evaluation this safety level should be applied. On the one hand, it is used in the fatigue strength assessment when evaluating the master curve at the prediction level. On the other hand, it is also applied in the determination of the number of equivalent cycles $n_{\mathrm{eq}}$ and thus in the derivation of the design parameters. The extent to which a double consideration leads to an overall overly conservative assessment cannot be quantified precisely at this stage. However, given the pronounced statistical scatter in both datasets, the application of a safety margin at both levels appears justified. This conservative approach appears appropriate for a first application of the proposed concept. A fully probabilistic treatment of the seismic design of SG joints exceeds the scope of the present work and is identified as a subject for future research, as it would allow the combined conservatism of the proposed approach to be quantified and potentially reduced.

### 9.2.2 Code Based Reverse Engineering of Safety Coefficients for Seismic Design of SG Joints

In this section, a practical method is developed to define safety factors for the design and dimensioning of SG joints subjected to seismic loading. The primary objective is to base these factors on the currently applicable design codes, thereby ensuring that the resulting approach can be easily implemented in engineering practice. Alternative methods for the direct definition of Eurocode-compliant design values, particularly for quasi-static verification, are proposed, for example, by (Drass and Kraus 2020a; Kraus and Drass 2020b; Kraus and Drass 2020a; Schaaf and Feldmann 2024).

The normative basis for the following considerations is provided by (ETAG 002-1; FKG 01/2021) for the design of SG joints and by (DIN EN 1990) in combination with (DIN EN 1998-1) for seismic design. In current engineering practice, SG joints are typically designed using the simplified spring model according to (FKG 01/2021), as summarized in section 3.2.3.2, applying a method factor of $\gamma_{\mathrm{meth,ETAG}} = 6$ according to (ETAG 002-1), which may be reduced to $\gamma_{\mathrm{meth,FKG}} = 4$ upon agreement with the adhesive manufacturer and the relevant building authorities. For the following analysis, it is assumed that the design under seismic loading is not performed using the simplified formulas of (ETAG 002-1), and $\gamma_{\mathrm{meth,FKG}}$ is therefore adopted as the basis for the reverse engineering of the seismic safety factors. In principle, the same considerations can also be applied to $\gamma_{\mathrm{meth,ETAG}}$.

Based on this assumption, the design follows the verification scheme presented in section 3.2.3.2 in accordance with (ETAG 002-1; FKG 01/2021). The verification is based on a global safety concept and can be expressed independently of the considered stress components of the SG joint in terms of the characteristic action $E_{\mathrm{k}}$ and the characteristic resistance $R_{\mathrm{k}}$ as follows:

$$E_{\mathrm{k}} \leq \frac{R_{\mathrm{k}}}{\gamma_{\mathrm{meth,FKG}}} \tag{9.2}$$

The initial value representing the existing global safety level $\frac{R_k}{E_k}$ for the quasi-static verification can be determined as follows:

$$\frac{R_k}{E_k} \geq \gamma_{meth,FKG} \geq 4 \tag{9.3}$$

The global safety level $\frac{R_k}{E_k}$ is illustrated schematically in Figure 9.1, which shows the procedure for determining a global method factor $\gamma_{meth,s}$ for the seismic design of SG joints.

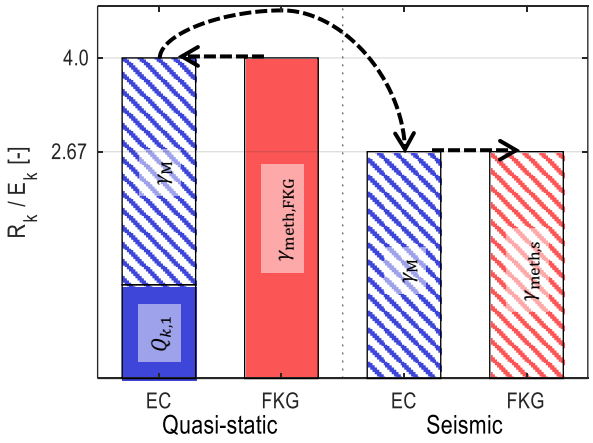


**Figure 9.1:** Schematic procedure for determining the global seismic method factor $\gamma_{meth,s}$, illustrating the global safety level $\frac{R_k}{E_k}$ between the Eurocode partial safety format and the ETAG global safety concept.

Within the semi-probabilistic safety concept of (DIN EN 1990), the fundamental verification of structural safety is performed by comparing the design values of the actions $E_d$ and the design resistance $R_d$:

$$E_d \leq R_d \tag{9.4}$$

The design value of the actions $E_d$ for persistent or transient design situations, also referred to as the fundamental combination, results from the combination of the relevant effects of actions. These include permanent loads, prestressing effects, and variable loads, which are combined using the corresponding partial safety factors and combination factors.

In typical glass and facade constructions, no permanent loads are introduced into the SG joint because the glass elements are mechanically supported. For the simplified case of a single variable action $Q_{k,1}$, which in glass and facade structures is typically the wind load, the design value of the action can be expressed as follows:

$$E_d = \gamma_{Q,1} \cdot Q_{k,1} \tag{9.5}$$

This combined partial safety factor for the leading variable action, taking model uncertainties and variations in action effects into account, can be defined as $\gamma_{Q,1} = 1.5$ according to (DIN

EN 1990). Since both $E_k$ from (ETAG 002-1) and $Q_{k,1}$ from (DIN EN 1990) represent the characteristic value of the action, they can be considered equivalent for the case of a single action, and the design value of the action $E_d$ is given by:

$$E_d = \gamma_{Q,1} \cdot Q_{k,1} = \gamma_{Q,1} \cdot E_k = 1.5 \cdot E_k \tag{9.6}$$

The design resistance $R_d$ can be determined from the characteristic resistance $R_k$ and a partial safety factor for material properties $\gamma_M$, which already accounts for model and dimensional uncertainties, as follows:

$$R_d = \frac{R_k}{\gamma_M} \tag{9.7}$$

Accordingly, for the quasi-static wind load verification, the following design relationship can be derived from Eq. (9.4) with Eqs. (9.6) and (9.7):

$$\gamma_{Q,1} \cdot E_k \leq \frac{R_k}{\gamma_M} \tag{9.8}$$

At present, no explicit values for $\gamma_M$ for SG joints are specified in current standards. As illustrated in Figure 9.1, one possibility to determine $\gamma_M$ could be to equate the global safety levels between the verification formats according to (ETAG 002-1) from Eq. (9.3) and (DIN EN 1990) from Eq. (9.8):

$$\frac{R_k}{E_k} \geq \gamma_{Q,1} \cdot \gamma_M = \gamma_{meth,FKG} \geq 4 \tag{9.9}$$

$$\gamma_M = \frac{\gamma_{meth,FKG}}{\gamma_{Q,1}} = \frac{4}{1.5} = 2.67 \tag{9.10}$$

Since (ETAG 002-1) does not specify explicit requirements for seismic design verification, the corresponding provisions of (DIN EN 1998-1; DIN EN 1990) are adopted to define a global safety level for seismic design. In principle, the verification format defined in Eq. (9.4) remains valid. For the simplified case with only one leading variable wind load, the design value of the seismic action can be determined as follows:

$$E_d = E\{A_{Ed}; \psi_{2,i} \cdot Q_{k,i}\} \tag{9.11}$$

In the present case, with one variable wind load and mechanically supported glass elements, the recommended values in (DIN EN 1990) define the combination factor for variable actions as $\psi_2 = 0$. Therefore, for the seismic load case, the design value of the action $E_d$ simplifies to the seismic action $A_{Ed}$ itself:

$$E_d = A_{Ed} \tag{9.12}$$

In engineering practice, the seismic action $A_{\mathrm{Ed}}$ is determined according to (DIN EN 1998-1) by linear-elastic analysis methods, such as the lateral force method or the multi-modal response spectrum analysis. The acting seismic force is derived from the ordinate of the design response spectrum $S_{\mathrm{d}}$ and the total mass of the structure, where the relevant safety levels are already included in $S_{\mathrm{d}}$. Alternatively, nonlinear analysis methods may also be applied.

The overall verification for the seismic design of SG joints according to Eq. (9.4) can therefore be written as follows:

$$A_{\mathrm{Ed}} \leq \frac{R_{\mathrm{k}}}{\gamma_{\mathrm{M}}} \tag{9.13}$$

Consequently, the global seismic safety level $\frac{R_{\mathrm{k}}}{A_{\mathrm{Ed}}}$ can be expressed as:

$$\frac{R_{\mathrm{k}}}{A_{\mathrm{Ed}}} = \gamma_{\mathrm{M}} = 2.67 \tag{9.14}$$

This safety level can be transferred back to the (ETAG 002-1) verification format, as illustrated in Figure 9.1, where it serves as the proposed target safety level. For this purpose, a verification format similar to Eqs. (9.7) and (9.13) is proposed. However, to distinguish between the approaches, a specific seismic safety or method factor $\gamma_{\mathrm{meth,s}}$ is introduced:

$$A_{\mathrm{Ed}} \leq \frac{R_{\mathrm{k}}}{\gamma_{\mathrm{meth,s}}} \tag{9.15}$$

Since the verification formats from Eq. (9.13), based on (DIN EN 1990), and the proposed approach from Eq. (9.15), based on (ETAG 002-1), differ only in the notation of the safety factor, $\gamma_{\mathrm{meth,s}}$ can be set equal to the material partial safety factor $\gamma_{\mathrm{M}}$:

$$\gamma_{\mathrm{meth,s}} = \gamma_{\mathrm{M}} = \frac{\gamma_{\mathrm{meth,FKG}}}{\gamma_{\mathrm{Q,1}}} = 2.67 \tag{9.16}$$

The seismic method factor $\gamma_{\mathrm{meth,s}}$ is derived from the fundamental safety level defined in (ETAG 002-1). By relating the safety levels of the ultimate limit state verification according to (DIN EN 1990) for fundamental and seismic design situations, the original method factor $\gamma_{\mathrm{meth,FKG}}$ is reduced accordingly.

The proposed scheme is based on the assumption of a single variable action, such as wind load, which simplifies the load combinations defined in (DIN EN 1990). The resulting value of $\gamma_{\mathrm{meth,s}}$ lies within the range recommended by (ASTM C1401), where a minimum design factor of 2.5 is proposed for SG systems under static tensile loading. Although no explicit design factor for seismic loading is defined in (ASTM C1401), this comparison served as a plausibility check for the derived seismic method factor. According to (DOW Silicones Deutschland GmbH 2020), a value of 2.5 was approved for dynamic shear loading on a project-specific basis.

## 9.3 Methods for the Design of SG Joints Under Seismic Loading

In this section, four methods for verifying SG joints under seismic loading are proposed. All methods are based on the established verification concepts for SG joints according to (FKG 01/2021), which are combined with the seismic design approaches of (DIN EN 1998-1; DIN EN 1990). The findings of this work, derived from both experimental and theoretical investigations, are used to integrate the material- and action-specific load-bearing behavior into the verification process, enabling lower safety factors and a more economical design.

### 9.3.1 General

The verification of conventional facade elements under seismic loading is typically performed in accordance with the guidelines for non-structural components. In general, international standards define two main requirements for the evaluation of such components:

- Transfer of a seismic-induced equivalent force due to the mass of the component, and
- Accommodation of deformations resulting from the seismic interstory drift of the main structure.

This verification concept has already been presented in section 3.3.4 and is therefore not repeated in detail here.

As discussed throughout this work, and particularly illustrated in Figure 4.1 in section 4.2, the structural configuration of the glass or facade construction must be taken into account when designing SG joints under seismic loading. For conventional facade constructions, verification according to the guidelines for non-structural components may be sufficient. However, in addition to the seismic action caused by inertial forces from the mass of the component, the loading is mainly governed by imposed deformations of the primary structure.

These imposed deformations were simulated experimentally in displacement-controlled tests conducted in this work. In these tests, the SG joints exhibited a load-bearing behavior comparable to the quasi-static reference tests during the initial cycles. With increasing cyclic loading, the nominal shear stress gradually decreased, resembling stress relaxation behavior. Damage progressed through cohesive cracking, leading to a gradual reduction in stiffness rather than sudden failure.

According to (DIN EN 1998-1), when determining the displacements of the primary structure, it should be ensured that the design seismic displacement $d_s$ is calculated from the displacement obtained from linear analysis based on the design response spectrum $d_e$ and the behavior factor $q$ as follows:

$$d_s = q \cdot d_e \tag{9.17}$$

This conversion ensures that the displacement of the primary structure used as an action in the verification is not reduced by the behavior factor, since $q$ serves only to simplify and economize the design of the primary structure itself.

In contrast to facade constructions, modern all-glass structures can be regarded as primary load-bearing systems. In such cases, the loading results primarily from inertial forces generated by the self-weight of the glass elements combined with the ground acceleration. This behavior was simulated in force controlled tests, where strain increased continuously with progressive cyclic loading, forming a plateau region similar in appearance to creep behavior. This was accompanied by progressive cohesive cracking within the adhesive layer. Once the remaining cross-section was unable to sustain the applied load, complete failure occurred, resulting in a sudden loss of load-bearing capacity.

For both types of constructions investigated in this thesis, the varying natural periods $T$ of the actual structures were approximated by different test frequencies $f$. Using this approach, the frequency-dependent load-bearing and failure behavior was analyzed. Lower test frequencies $f$ resulted in more critical failure behavior with a lower number of cycles to failure $N_f$, whereas higher test frequencies led to higher values of $N_f$. The classical Basquin model for the high-cycle fatigue range could be extended to frequency-dependent fatigue to describe this behavior with a high coefficient of determination.

For seismic verification, (DIN EN 1998-1) permits the use of linear-elastic analysis methods, such as the lateral force method or modal response spectrum analysis. In these methods, the seismic effects are determined using equivalent static forces derived from response spectra. The seismic action is determined from the codified ground acceleration values in combination with the corresponding response spectra, which inherently incorporate the prescribed safety level for seismic design.

The lateral force method and modal response spectrum analysis form the basis for the verification methods for SG joints under seismic loading presented below. Based on these principles, four different design approaches with increasing complexity were developed in the subsequent sections, which are summarized in Figure 9.2.

### 9.3.2 Method 1: Verification as a Variable Action

As the simplest method for the design of SG joints under seismic loading, the seismic action can be considered as a variable action. The loading is determined, depending on the type of glass or facade construction, using the response spectrum method according to (DIN EN 1998-1). The verification can be performed according to the provisions of (ETAG 002-1; FKG 01/2021), applying a method factor of $\gamma_{\text{meth,FKG}} = 4$. However, this approach is only

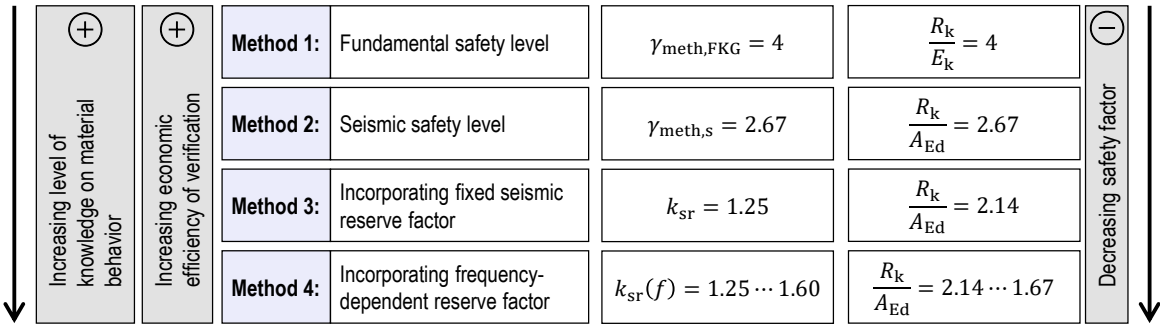


**Figure 9.2:** Schematic representation of the four verification methods for seismic design of SG joints, showing the relation between safety level, knowledge, and economic efficiency.

applicable when the simplified spring model defined in (FKG 01/2021) is used for the structural analysis.

The experimental investigations conducted in this work demonstrated that even at very high load levels, the SG joint was capable of sustaining multiple load cycles before failure under LCF loading. Across all tests, a consistent and reproducible load-bearing and failure behavior was observed.

Although this approach represents the most conservative verification, it may be sufficient for low seismic demands, eliminating the need for a more detailed analysis.

### 9.3.3 Method 2: Application of the Seismic Safety Level

As an alternative to the verification under variable actions, the application of the seismic safety level provides an approach that accounts for the different normative safety levels defined for fundamental and seismic design situations. This method does not explicitly consider the material- and load-specific load-bearing and failure behavior, but adopts the concept for determining the seismic method factor $\gamma_{\mathrm{meth,s}}$ introduced in section 9.2.2.

This approach is based on the fundamental safety level defined in (FKG 01/2021), which uses a method factor of $\gamma_{\mathrm{meth,FKG}} = 4$. For seismic design, this value is adapted to the seismic design situation according to (DIN EN 1990) by relating the safety levels of the limit state verifications for fundamental and seismic design situations. As a result, no partial safety factors are applied on the design seismic action $A_\mathrm{Ed}$ in the design, and a seismic method factor of $\gamma_{\mathrm{meth,s}} = 2.67$ is proposed. This adapted safety level forms the basis for the following methods, which additionally incorporate the material- and load-specific behavior of the SG joint.

### 9.3.4 Method 3: Application of a Global Seismic Material Overstrength

To account for the load-bearing and failure behavior of SG joints under seismic loading, as investigated in this work, the design parameters determined in section 8.5 were incorporated

into the verification. The results show a strong dependence of the design parameters on the test frequency $f$, representing different structures with varying natural periods $T$. Lower frequencies lead to more critical design parameters. Based on the findings from section 4.4, a critical minimum frequency of 0.5 Hz was defined, corresponding to the lower bound of the relevant frequency range for typical multi-storey building structures. By adopting this conservative value, a simplified and user-friendly design concept can be established.

Before applying the verification, it must be ensured that the lowest natural frequency $f$ of the respective structure is higher than the selected limit value. The findings of this study led to the introduction of the seismic reserve factor $k_{\mathrm{sr}}$, proposed in section 8.5.5, which describes the overstrength of SG joints under LCF loading compared to the strength under quasi-static loading. Since this factor was derived from normalized ground-motion histories, it can be directly transferred to the design concept.

Considering the two definitions of the seismic reserve factor $k_{\mathrm{sr}}$, based on the quasi-static reference properties of the experimental reference series $k_{\mathrm{sr,k}}$ and the approval documents $k_{\mathrm{sr,ETA}}$, the factor should conservatively be chosen as:

$$k_{\mathrm{sr}} = \min(k_{\mathrm{sr,k}}, k_{\mathrm{sr,ETA}}) \tag{9.18}$$

To differentiate between the two typical structural configurations, both force-controlled and displacement-controlled tests were carried out within the experimental program. When determining the seismic reserve factor $k_{\mathrm{sr}}$, only minimal differences were observed between the two test types. Therefore, for practical engineering design, the values obtained from the force-controlled series can be used. These results also formed the basis for the evaluation of the displacement-controlled tests when defining the number of cycles to failure $N_{\mathrm{f}}$, as presented in section 7.5.

Based on Eqs. (8.8), (8.9) and (8.11), the factor $k_{\mathrm{sr,k}}$ for the force-controlled test series can be expressed as shown in Eq. (9.19). $k_{\mathrm{sr,ETA}}$ can be determined analogously using $\tau_{\mathrm{k,ETA}}$ instead of $\tau_{\mathrm{k}}$.

$$k_{\mathrm{sr,k}}(f) = \frac{\tau_{\mathrm{ult,mean}}}{\tau_{\mathrm{k}}} \cdot \left( \frac{n_{\mathrm{eq}}}{D_{\mathrm{t}} \cdot a} \right)^{-\frac{1}{m}} \cdot f^{\frac{1}{m}} \tag{9.19}$$

Besides the parameters of the respective master curve, the result depends on the number of equivalent cycles $n_{\mathrm{eq}}$. As discussed in section 8.5.5, several approaches exist for the statistical evaluation. Since the seismic reserve factor $k_{\mathrm{sr}}$ characterizes a material property of the SG joint, the use of the 5 % and 95 % quantiles defined in section 9.2.1.4 and discussed in section 9.2.1.5 appears to be the most appropriate choice.

For the limit state of complete failure of the SG joint section, corresponding to a target damage of $D_{\mathrm{t}} = 1.0$ and a critical frequency of $f = 0.5$ Hz, the values of the seismic reserve factor $k_{\mathrm{sr}}$ are summarized in Table 9.1, which presents the 95 % quantile of $n_{\mathrm{eq}}$ evaluated for

both prediction master curves. Within the limitations of the underlying assumptions, the tabulated values may be regarded as conservative estimates suitable for use in engineering design.

**Table 9.1:** Summary of the seismic reserve factor $k_{sr}$ for both prediction master curves, evaluated for $D_t = 1.0$, $f = 0.5$ Hz, and the 95 % quantile of $n_{eq}$.

| Master curve | $k_{sr,ETA}$ [-] | $k_{sr,k}$ [-] |
|---|---|---|
| Force | 1.296 | 1.253 |
| Disp-$w_{cum}$ | 1.251 | 1.271 |

Since the seismic reserve factor $k_{sr}$ is defined as a multiplier relative to the characteristic quasi-static reference strength, it can be directly applied in the verification to modify this value. An approach analogous to the modification factor for load duration and moisture content $k_{mod}$ from (DIN EN 1995-1-1), which ensures a consistent treatment of time-dependent material effects within the Eurocode framework, is proposed. However, because the seismic reserve factor $k_{sr}$ considers only the seismic load case and not the entire range of load duration effects, a distinct notation was intentionally used. The design equation for the seismic verification given in Eq. (9.15) can therefore be extended as follows:

$$A_{Ed} \leq k_{sr} \cdot \frac{R_k}{\gamma_{meth,s}} \tag{9.20}$$

### 9.3.5 Method 4: Application of a Frequency-Dependent Seismic Material Overstrength

This method incorporates the load-bearing behavior of SG joints into the verification process with the highest level of detail. As described in section 8.5.5 and evident from the summarized representation of the seismic reserve factor $k_{sr}$ in Eq. (9.19), a significant influence of the frequency $f$ on the structural behavior of the SG joint is observed. At higher test frequencies, a higher load-bearing capacity under LCF loading is consistently identified.

By selecting a conservative frequency of 0.5 Hz, as adopted for Method 3 in section 9.3.4, the available strength reserves are not fully utilized. Therefore, the seismic reserve factor $k_{sr}$ can be adapted as a function of the frequency $f$ of the structure.

The frequency $f$ of the structure is generally determined during the seismic design process when deriving the seismic action from the response spectra (DIN EN 1998-1). Because the load-bearing capacity increases with rising frequency, the lowest natural frequency should be used to determine the seismic reserve factor $k_{sr}$. Natural frequencies outside the investigated range of 0.5 Hz to 5 Hz fall outside the scope of the present recommendations, as outlined in section 9.4. For the simplified response spectrum method, the fundamental period $T_1$ of the two principal directions can be applied, while for the modal response

spectrum method, the largest natural period $T_i$ among all considered modes should be used.

The remaining parameters required to determine the seismic reserve factor $k_{sr}$ using Eq. (9.19) can be taken from the relevant sections of this work: The number of equivalent cycles $n_{eq}$ is summarized in Table 8.1 for the different statistical evaluation intervals, the two joint geometries and for both master curves evaluated. The fitting parameters for the master curves $a$ and $m$ are summarized in Table 7.6. Finally, the quasi-static strength parameters of the reference series $\tau_{ult,mean}$ and $\tau_k$ are summarized in Table 6.2, $\tau_{k,ETA}$ of the manufacturer is shown in Table 3.1.

When evaluating $k_{sr}$, only minor differences were observed between the force and displacement master curves. Since the force master curve forms the basis for defining the number of cycles to failure $N_f$ and thereby serves as the foundation of the displacement master curve, the following recommendations are based solely on the force master curve. However, the differences in load-bearing and failure behavior between the two structural configurations, as discussed in section 9.3.1, should be considered in the design process.

Within the frequency range investigated in this work (0.5 Hz–5 Hz), the more conservative seismic reserve factor $k_{sr,k}$ varies between 1.253 and 1.603. Exemplary values of the seismic reserve factor $k_{sr}$ within the relevant frequency range are summarized in Table 9.2 for the force-controlled master curve. The seismic verification of the SG joint can subsequently be performed using Eq. (9.20) from section 9.3.4.

**Table 9.2:** Frequency-dependent seismic reserve factor $k_{sr}$ for the design of SG joints based on the prediction force master curve, evaluated for a target damage $D_t = 1.0$ and the 95 % quantile of $n_{eq}$.

| Frequency [Hz] | 0.5 | 0.6 | 0.8 | 1.1 | 1.4 | 1.8 | 2.3 | 3.0 | 3.9 | 5.0 |
|---|---|---|---|---|---|---|---|---|---|---|
| $k_{sr,ETA}$ | 1.296 | 1.322 | 1.363 | 1.410 | 1.447 | 1.486 | 1.526 | 1.570 | 1.614 | 1.658 |
| $k_{sr,k}$ | 1.253 | 1.278 | 1.318 | 1.363 | 1.399 | 1.437 | 1.475 | 1.518 | 1.561 | 1.603 |

Figure 9.2 summarizes the relationship between safety factor, economic efficiency, and the level of knowledge on material behavior, including the corresponding factors used in each method and the existing global safety level $\frac{R_k}{E_k}$.

## 9.4 Limitations

The proposed design recommendations for SG joints under seismic loading are subject to specific limitations that define their range of validity. The evaluation of the seismic reserve factor $k_{sr}$ and the related design parameters is restricted to a frequency range between 0.5 Hz and 5 Hz. This range represents typical natural frequencies of glass and facade structures subjected to seismic loading, as discussed in chapter 4, and corresponds to the frequencies

investigated in the experimental program in chapter 7. The extent to which the proposed design parameters can be extrapolated to frequencies outside this range requires further investigation.

The proposed methods are limited to shear loading of the SG joint. Other loading modes, such as tension or combined stress states, were not investigated and are therefore outside the scope of the present recommendations. The joint geometry corresponds to the geometrical limits specified in (ETAG 002-1). Application to geometries or aspect ratios outside these limits requires additional verification. All design parameters were determined using the DOWSIL 993 adhesive system. The transferability of the results to other batches, adhesive types, or manufacturers must be verified prior to practical application. In addition, the calculation of equivalent cycles is based on the linear damage accumulation hypothesis according to Miner's rule. The applicability of this assumption for SG joints under seismic LCF loading was not directly verified.

The failure limit applied in this work corresponds to the complete failure of the specimen in the force-controlled tests. When designing with the proposed seismic reserve factor, the formation of cracks within the 100 mm bonded length of the SG joint cannot be excluded. Such damage is acceptable in seismic design, as limited damage is generally accepted.

## 9.5 Summary of Design Recommendations

This chapter develops recommendations for the design and verification of SG joints in glass and facade structures subjected to seismic loading. The recommendations aim to ensure compatibility with existing safety concepts of (DIN EN 1998-1; DIN EN 1990) and (ETAG 002-1; FKG 01/2021).

The evaluation of SG joint design parameters developed in this work was therefore performed analogously to the treatment of material and product properties in (DIN EN 1990). Since the derived parameters represent material-related characteristics of the SG joint, the use of the 5 % and 95 % quantiles is proposed. This provides a consistent and traceable statistical basis for defining the global seismic safety level. The seismic safety level corresponding to the 475-year reference return period is already incorporated in the design spectra according to (DIN EN 1998-1) and therefore does not need to be accounted for again in the derivation of the design parameters.

By relating the global safety concept according to (ETAG 002-1; FKG 01/2021) with $\gamma_{\text{meth,FKG}} = 4$ to the Eurocode partial factor format with $\gamma_{\text{Q,1}} = 1.5$, a seismic method factor of $\gamma_{\text{meth,s}} = 2.67$ was derived. This proposed value represents a coherent global safety level for seismic design situations and aligns both design frameworks.

Four verification methods are introduced:

- Method 1: Seismic loading treated as a variable action using $\gamma_{\text{meth,FKG}} = 4$.

- Method 2: Application of the seismic safety level with $\gamma_{\text{meth,s}} = 2.67$.
- Method 3: Incorporation of a fixed seismic material overstrength using the experimentally derived seismic reserve factor $k_{\text{sr}} = 1.25$.
- Method 4: Extension of Method 3 by introducing a frequency-dependent $k_{\text{sr}}(f)$, reflecting the observed increase in load-bearing capacity with higher natural frequencies.

A general verification equation for the seismic design of SG joints is proposed. These recommendations are subject to the limitations outlined in the previous section and apply to shear-loaded SG joints for frequencies between 0.5 Hz and 5 Hz.

# 10 Conclusion and Outlook

## 10.1 Conclusion

The present work investigated the load-bearing and failure behavior of structural glazing (SG) joints under seismic loading, with the aim of establishing an engineering-oriented design approach. This objective was motivated by the lack of explicit design provisions for SG joints under seismic loading, despite their increasing use in modern facade construction and the documented vulnerability of facade systems to seismic effects.

The experimental investigations under low-cycle fatigue loading demonstrated that SG joints exhibited load-bearing behavior comparable to quasi-static loading during the initial load cycles. Significant differences were observed in the failure behavior of SG joints. In particular, a clear distinction between force-controlled and displacement-controlled loading conditions was identified, representing typical boundary conditions in all-glass constructions and conventional facade systems, respectively. Under force-controlled loading, the joints exhibited a progressive increase in deformation followed by sudden failure without residual load-bearing capacity. In contrast, displacement-controlled loading led to a gradual reduction in stress with remaining residual strength at the end of the test, without complete failure. As a result, conventional failure definitions were not directly applicable to displacement-controlled tests. To address this limitation, a consistent failure criterion based on the cumulative dissipated energy density was introduced and calibrated using the results from force-controlled tests. This approach enabled a consistent determination of the number of cycles to failure $N_f$ across different loading conditions.

Furthermore, the investigations revealed that the loading frequency has a governing influence on the low-cycle fatigue performance of SG joints. To account for this effect, the established Basquin approach was extended by incorporating a frequency-dependent term. The resulting model allowed the prediction of the number of cycles to failure as a function of both the stress level and the loading frequency, with a high degree of accuracy. This formulation was applicable to different loading conditions and joint geometries within the scope of the investigated parameter range and provided a unified description of the cyclic fatigue performance.

Based on these findings, a methodology for the characterization of seismic loading was developed. Real ground motion records were evaluated, and the structural response was determined using single-degree-of-freedom systems with varying natural periods covering the relevant range. The resulting response histories were transformed into equivalent load

cycles using the frequency-dependent extended Basquin model. This approach enabled the quantification of seismic actions in terms of equivalent cycles $n_{eq}$, providing a direct link between seismic loading and the experimentally derived fatigue behavior.

On this basis, engineering design parameters were derived through statistical evaluation of the equivalent cycles. The seismic demand was expressed in terms of damage accumulation $D$ and corresponding failure stress levels. These values were related to quasi-static reference strengths, resulting in the definition of seismic reserve factors $k_{sr}$ that quantify the overstrength of SG joints under cyclic–seismic loading.

Overall, the results demonstrated that the failure behavior of SG joints under seismic loading differs significantly from quasi-static conditions and can be consistently characterized through experimental and analytical approaches. The proposed frequency-dependent extended Basquin fatigue model, combined with the concept of equivalent load cycles $n_{eq}$, enabled the prediction of load-bearing performance under realistic seismic actions.

Building on this basis, a set of engineering-oriented design methods with increasing levels of complexity was developed, ranging from simplified approaches based on quasi-static design concepts to advanced concepts incorporating frequency-dependent seismic reserve factors. These methods enabled a consistent and application-oriented verification of SG joints under seismic loading. The present work therefore establishes a coherent and new framework that links material behavior, seismic loading, and engineering design, thereby providing a robust basis for the assessment and design of SG joints subjected to seismic actions.

Despite the comprehensive insights obtained, certain limitations remain, which define the scope for future research and are discussed in the following.

## 10.2 Outlook

Building on the findings of this work, several limitations are identified that define directions for future research. The investigations focused on short-term low-cycle fatigue loading representative of seismic events, while long-term effects such as creep, ageing, and temperature dependence were not considered. In particular, the influence of artificial ageing on the cyclic load-bearing and failure behavior represents an important aspect that should be addressed in future studies.

Furthermore, the experimental and analytical investigations were limited to a single SG adhesive. While the results provide consistent insights into the investigated material, the transferability to other SG adhesives and alternative low-modulus adhesive systems, such as one-component polyurethane adhesives, remains to be clarified. A broader experimental basis is therefore required to assess material-dependent effects and to generalize the proposed design approach.

The experimental program focused on shear loading, which represents the governing stress state for typical facade configurations based on the performed stress assessment. However, in specific structural situations, such as glass corners, combined stress states including tensile components may become relevant. Future investigations should therefore address tensile and combined loading conditions in order to extend the applicability of the proposed models.

In addition, the presented investigations were based on small-scale specimen tests and phenomenological models. The continuous crack propagation observed during cyclic loading indicates that a more detailed representation of the failure process could further improve the understanding of the underlying mechanisms. In this context, advanced finite element models incorporating damage evolution may enable a more accurate description of the load-bearing and failure behavior.

Moreover, the structural response of complete glass and facade systems was not explicitly considered in the present work. Research projects, such as the recently concluded project RISIKO (Müller et al. 2026b), aimed to address this aspect and to investigate the interaction between SG joints and the global structural behavior under seismic loading. Furthermore, the failure limit adopted for the derivation of the design parameters corresponds to complete failure of the 100 mm test specimen, which may be interpreted as a conservative assumption for the no-collapse requirement. For the damage limitation state or for the design of SG joints in large glass and facade constructions, alternative failure criteria may need to be defined. In addition, the calculation of equivalent cycles was based on the linear damage accumulation hypothesis according to Miner's rule. The applicability of this assumption for SG joints under seismic LCF loading was not directly verified and should be addressed in future experimental investigations.

From a design perspective, the proposed methods represent a first step towards a consistent verification concept for SG joints under seismic loading. Future work should focus on the integration of these approaches into existing standards, guidelines, and technical recommendations in order to enable their application in engineering practice. A fully probabilistic treatment could further refine the proposed verification concept and reduce its inherent conservatism.

# Declaration on the Use of Artificial Intelligence

The large language models (LLMs) ChatGPT (OpenAI) and Claude (Anthropic) were used via their standard chat interfaces between July 2025 and the completion of the publication version in October 2026, with the models current at the time. The LLMs were used to formulate, shorten, translate and polish text (initially supplemented by DeepL and DeepL Write), and occasionally for brainstorming on the detailed structure of individual sections. The overall structure, methodology, statements and conclusions originate from the author. In some cases, drafts were generated from the author's notes, preliminary work and provided source material. Passages from the author's cited prior publications were shortened and adapted, partly with LLM assistance. The LLMs were occasionally used to identify additional literature, which was verified against the original publications.

For proofreading, the thesis was reviewed using Claude for grammar, spelling, style and consistency. In this step, the author accepted, adapted or rejected each comment individually. No changes were made directly by the AI.

The LLMs were further used to write individual MATLAB functions for data evaluation and figures and to modify existing scripts according to the author's specifications. Agent-based coding tools (e.g. Codex, Claude Code) were not used. The code and its output were verified by plausibility checks, code review and manual calculation of individual steps. The LLMs also assisted with the LaTeX template.

All AI-generated output was critically reviewed and, where necessary, revised by the author, who bears full responsibility for the content of this thesis.

# References


Abeln, B. (2019). "Zur Bemessung struktureller Klebungen im Stahlbau". ger. Dissertation. Verlag Mainz and Rheinisch-Westfälische Technische Hochschule Aachen.

Aiello, C., N. Caterino, A. Bonati, and A. Occhiuzzi (2019). "The Role of Details for Seismic Performance of a Full Scale Glass Façade". In: *4th International Workshop on the Seismic Performance of Non-Structural Elements* (Pavia, Italy, May 22–23, 2019). SPONSE - International Association for the Seismic Performance of Non-Structural Elements.

Aiello, C., N. Caterino, G. Maddaloni, A. Bonati, A. Franco, and A. Occhiuzzi (2018a). "Experimental and numerical investigation of cyclic response of a glass curtain wall for seismic performance assessment". In: *Construction and Building Materials* 187, pp. 596–609. DOI: 10.1016/j.conbuildmat.2018.07.237.

Aiello, C., N. Caterino, G. Maddaloni, A. Bonati, and A. Occhiuzzi (2018b). "Lateral Cyclic Mechanical Response of a Glazed Curtain Wall: An Experimental Investigation". In: *16th European Conference on Earthquake Engineering (16ECEE)* (Thessaloniki, June 18–21, 2018).

Albiez, M. F. (2016). "Zur statischen Tragfähigkeit geklebter Kreishohlprofilverbindungen im Stahlbau". ger. Dissertation. Karlsruhe: Karlsruher Institut für Technologie (KIT).

Allen, R. M. (2007). "Earthquake Hazard Mitigation: New Directions and Opportunities". 4.21. In: *Treatise on geophysics*. Ed. by G. Schubert. Amsterdam u.a.: Elsevier, pp. 607–647. DOI: 10.1016/B978-044452748-6.00083-3.

Altenbach, H. (2018). *Kontinuumsmechanik. Einführung in die materialunabhängigen und materialabhängigen Gleichungen*. Berlin, Heidelberg: Springer Berlin Heidelberg. DOI: 10.1007/978-3-662-57504-8.

Ancheta, T. D., R. B. Darragh, J. P. Stewart, E. Seyhan, W. J. Silva, B. S. J. Chiou, K. E. Wooddell, R. W. Graves, A. R. Kottke, D. M. Boore, T. Kishida, and J. L. Donahue (2013). *PEER NGA-West2 Database. PEER Report 2013/03*.

Aucun, B., E. Carvalho, M. Fardis, and P. Pinto (2012). *Eurocode 8: Seismic design of buildings - Worked examples*. eng. In collab. with P. Bisch, E. Carvalho, H. Degee, P. Fajfar, M. Fardis, P. Franchin, M. Kreslin, A. Pecker, P. Pinto, A. Plumier, H. Somja, G. Tsionis, B. Aucun, and A. Athanasopoulou. Luxembourg: Publications Office. DOI: 10.2788/91658.

Bachmann, H. (1995). *Erdbebensicherung von Bauwerken*. Basel and Berlin: Birkhäuser. 292 pp.

Bachmann, H., P. Linde, and T. Wenk (1994). *Capacity design and nonlinear dynamic analysis of earthquake-resistant structures*. en. DOI: 10.3929/ethz-a-001436476.

Bahrampouri, M., A. Rodriguez-Marek, and R. A. Green (2021). "Ground motion prediction equations for significant duration using the KiK-net database". In: *Earthquake Spectra* 37.2, pp. 903–920. DOI: 10.1177/8755293020970971.

Baird, A., A. Palermo, and S. Pampanin (2011). "Facade damage assessment of multi-storey buildings in the 2011 Christchurch earthquake". In: *Bulletin of the New Zealand Society for Earthquake Engineering* 44.4, pp. 368–376. DOI: 10.5459/bnzsee.44.4.368-376.

BAM (1979). *Forschungsbericht 58 - Ermittlung des Bauteilwiderstandes aus Versuchsergebnissen bei vereinbartem Sicherheitsniveau*. Ed. by Bundesanstalt für Materialprüfung Berlin.

Basquin, O. (1910). "The Exponential Law of Endurance Tests". In: *Proceedings of the Thirteenth Annual Meeting* (Atlantic City, New Jersey, June 28–July 2, 1910). Ed. by American Society for Testing and Materials, pp. 625–630.

Bathias, C. and A. Pineau (2013). *Fatigue of materials and structures. Applications to design and damage*. [Place of publication not identified]: Wiley-ISTE. 368 pp.

Baumgartner, J., H. Schmidt, G. Rybar, T. Melz, L. Ernstberger, and D. Teutenberg (2016). *FAT 290 - Auslegung von geklebten Stahlblechstrukturen im Automobilbau für schwingende Last bei wechselnden Temperaturen unter Berücksichtigung des Versagensverhaltens*. ger. Vol. 290. FAT-Schriftenreihe. Berlin: FAT Forschungsvereinigung Automobiltechnik. 269 pp.

Bedon, Amadio, and Noé (2019). "Safety Issues in the Seismic Design of Secondary Frameless Glass Structures". In: *Safety* 5.4, p. 80. DOI: 10.3390/safety5040080.

Bedon, C. and C. Amadio (2017). "Enhancement of the seismic performance of multi-storey buildings by means of dissipative glazing curtain walls". In: *Engineering Structures* 152, pp. 320–334. DOI: 10.1016/j.engstruct.2017.09.028.

Beech, D. G. and D. B. Owen (1962). "Handbook of Statistical Tables". In: *Applied Statistics* 11.3, p. 211. DOI: 10.2307/2985368.

Behr, R. A., A. Belarbi, and J. H. Culp (1995). "Dynamic racking tests of curtain wall glass elements with in-plane and out-of-plane motions". en. In: *Earthquake Engineering & Structural Dynamics* 24.1, pp. 1–14. DOI: 10.1002/eqe.4290240102.

Behr, R. A. (1998). "Seismic Performance of Architectural Glass in Mid-Rise Curtain Wall". In: *Journal of Architectural Engineering* 4.3, pp. 94–98. DOI: 10.1061/(ASCE)1076-0431(1998)4:3(94).

– (2009). *Architectural glass to resist seismic and extreme climatic events*. eng. Woodhead Publishing in materials. Boca Raton, Fla and Oxford: CRC Press. 260 pp.

Behr, R. A. and A. Belarbi (1996). "Seismic Test Methods for Architectural Glazing Systems". In: *Earthquake Spectra* 12.1, pp. 129–143. DOI: 10.1193/1.1585871.

Benedix, R. (2020). *Bauchemie*. Wiesbaden: Springer Fachmedien Wiesbaden. DOI: 10.1007/978-3-658-26442-0.

Bianchi, S., J. Ciurlanti, D. Perrone, A. Filiatrault, A. C. Costa, P. X. Candeias, A. A. Correia, and S. Pampanin (2021). "Shake–table tests of innovative drift sensitive nonstructural elements in a low–damage structural system". In: *Earthquake Engineering & Structural Dynamics*. DOI: 10.1002/eqe.3452.

Bianchi, S., V. Hayez, G. Lori, M. Overend, and G. Manara (2024a). "Damage States of Structural Silicone Glazed Facades". In: *18th World Conference on Earthquake Engineering, WCEE2024* (Milan, Italy, June 30–July 5, 2024).

Bianchi, S., G. Lori, V. Hayez, G. Manara, R. Schipper, S. Pampanin, and M. Overend (2025). "Seismic Testing and Performance Evaluation of Unitized Curtain Walls". In: *Earthquake Engineering & Structural Dynamics*. DOI: 10.1002/eqe.70017.

Bianchi, S., G. Lori, V. Hayez, M. Overend, and G. Manara (2024b). "Influence of design variables on seismic performance of unitized curtain walls: a parametric experimental study". In: *Glass Structures & Engineering*. DOI: 10.1007/s40940-024-00255-2.

Bianchi, S., G. Lori, V. Hayez, R. Schipper, S. Pampanin, M. Overend, G. Manara, and T. Klein (2022). "Seismic testing and multi-performance evaluation of full-scale unitized curtain walls: research overview and preliminary results". In: *Fifth International Workshop on the Seismic Performance of Non-Structural Elements (SPONSE)*. Ed. by APPLIED TECHNOLOGY COUNCIL.

Blaß, H. J. and P. Schädle (2009). *Aussteifende Wandscheiben in Einzelelement-Bauweise*. ger. Vol. 13. Karlsruher Berichte zum Ingenieurholzbau. Karlsruhe: Univ.-Verl. Karlsruhe. 102 pp.

– (2011). *Verhalten einer Massivholzbauweise unter Erdbebenlasten*. ger. Vol. Bd. 18. Karlsruher Berichte zum Ingenieurholzbau. Hannover and Karlsruhe: Technische Informationsbibliothek u. Universitätsbibliothek and KIT Scientific Publishing. 166 pp. DOI: 10.5445/KSP/1000023972.

Bouwkamp, J. G. (1961). "Behavior of window panels under in-plane forces". In: *Bulletin of the Seismological Society of America* 51.1, pp. 85–109.

Bouwkamp, J. G. and J. F. Meehan (1960). "Drift limitations imposed by glass". In: *Proceedings of Second World Conference on Earthquake Engineering*. World Conference on Earthquake Engineering (Tokyo, Japan). Vol. 3.

Broker, K. A., S. Fisher, and A. M. Memari (2012). "Seismic Racking Test Evaluation of Silicone Used in a Four-Sided Structural Sealant Glazed Curtain Wall System". In: *Journal of ASTM International* 9.3, pp. 1–22. DOI: 10.1520/JAI104144.

Bueche, F. (1960). "Molecular basis for the mullins effect". In: *Journal of Applied Polymer Science* 4.10, pp. 107–114. DOI: 10.1002/app.1960.070041017.

– (1961). "Mullins Effect and Rubber-Filler Interaction". In: *Journal of Applied Polymer Science* 5.15, pp. 271–281. DOI: 10.5254/1.3539899.

Bues, M., C. Schuler, M. Albiez, T. Ummenhofer, H. Fricke, and T. Vallée (2019). "Load bearing and failure behaviour of adhesively bonded glass-metal joints in façade structures". In: *The Journal of Adhesion* 95.5-7, pp. 653–674. DOI: 10.1080/00218464.2019.1570158.

Bues, M. D. (2021). "Ein Beitrag zur Auslegung tragender Klebverbindungen im Fassadenbau". Versuchsanstalt für Stahl, Holz und Steine (VAKA). de. Dissertation. Karlsruhe: Karlsruher Institut für Technologie (KIT).

Calado, L. and J. Azevedo (1989). "A model for predicting the failure of structural steel elements". In: *Journal of Constructional Steel Research* 14.1, pp. 41–64. DOI: 10.1016/0143-974X(89)90069-2.

Campbell, K. W. and Y. Bozorgnia (2008). "NGA Ground Motion Model for the Geometric Mean Horizontal Component of PGA, PGV, PGD and 5% Damped Linear Elastic Response Spectra for Periods Ranging from 0.01 to 10 s". en. In: *Earthquake Spectra* 24.1, pp. 139–171. DOI: 10.1193/1.2857546.

– (2013). *NGA-West2 Campbell-Bozorgnia Ground Motion Model for the Horizontal Components of PGA, PGV, and 5%-Damped Elastic Pseudo-Acceleration Response Spectra for Periods Ranging*

*from 0.01 to 10 sec. PEER Report 2013-06*. Ed. by PEER Ground Motion Selection and Modification Working Group. Berkeley: Pacific Earthquake Engineering Research Center.

Campbell, K. W. and Y. Bozorgnia (2014). "NGA-West2 Ground Motion Model for the Average Horizontal Components of PGA, PGV, and 5% Damped Linear Acceleration Response Spectra". In: *Earthquake Spectra* 30.3, pp. 1087–1115. DOI: 10.1193/062913EQS175M.

Carbary, L. D., E. D. Bull, and S. S. Mishra (2007). "Development of a Practical Method to Evaluate the Fatigue Properties of Structural Silicone Glazing Adhesives". English. In: *Journal of ASTM International* 4.1, p. 100403. DOI: 10.1520/JAI100403.

Castiglioni, C. A., H. P. Mouzakis, and P. G. Carydis (2007). "Constant and Variable Amplitude Cyclic Behavior of Welded Steel Beam-to-Column Connections". In: *Journal of Earthquake Engineering* 11.6, pp. 876–902. DOI: 10.1080/13632460601188027.

Castiglioni, C. A. and R. Pucinotti (2009). "Failure criteria and cumulative damage models for steel components under cyclic loading". In: *Journal of Constructional Steel Research* 65.4, pp. 751–765. DOI: 10.1016/j.jcsr.2008.12.007.

Caterino, N., M. Del Zoppo, G. Maddaloni, A. Bonati, G. Cavanna, and A. Occhiuzzi (2017). "Seismic assessment and finite element modelling of glazed curtain walls". In: *Structural Engineering and Mechanics* 61.1, pp. 77–90. DOI: 10.12989/sem.2017.61.1.077.

Chopra, A. K. (2012). *Dynamics of structures. Theory and applications to earthquake engineering*. 4th ed. Upper Saddle River N.J.: Prentice Hall. xxxiii, 944.

Ciupack, Y., H. Pasternak, E. Stammen, and K. Dilger (2018). *Untersuchungen zum Tragverhalten und der Lebensdauer von Klebverbindungen im Stahlbau unter zyklischer Belastung - LebKleb. IGF-Vorhaben Nr. 18161 BG - FOSTA P 1005, Schlussbericht*. In collab. with Y. Ciupack and E. Stammen.

Coffin, L. F. (1954). "A Study of the Effects of Cyclic Thermal Stresses on a Ductile Metal". In: *Journal of Fluids Engineering* 76.6, pp. 931–949. DOI: 10.1115/1.4015020.

CRED (2021). *The Emergency Events Database*. Brussels, Belgium. Ed. by Centre for Research on the Epidemiology of Disasters - United Nations Office for Disaster Risk Reduction. UCLouvain. URL: www.emdat.be (visited on 06/11/2021).

D'Ayala, D., A. Meslem, D. Vamvatsikos, K. Porter, and T. Rossetto (2015). *Guidelines for Analytical Vulnerability Assessment of Low/Mid-Rise Buildings. Vulnerability Global Component Project*. DOI: 10.13117/GEM.VULN-MOD.TR2014.12.

da Silva, L. F. M., A. Öchsner, and R. D. Adams (2018a). *Handbook of Adhesion Technology*. Berlin, Heidelberg: Springer Berlin Heidelberg. DOI: 10.1007/978-3-642-01169-6.

– eds. (2018b). *Handbook of Adhesion Technology*. Cham: Springer International Publishing. DOI: 10.1007/978-3-319-55411-2.

Damm, J. (2023). *Zum Dämpfungsverhalten viskoelastischer Klebverbindungen im Stahlbau*. de. In collab. with T. Ummenhofer, G. Meschut, and L. Kärger. Karlsruher Institut für Technologie (KIT). DOI: 10.5445/IR/1000158830.

Dazio, A., T. Wenk, and H. Bachmann (1995). *Vorversuche an Stahlbetontragwänden unter zyklisch-statischer Einwirkung*. de. DOI: 10.3929/ethz-a-001557429.

Descamps, P. and V. Hayez (2018). "Silicone Joint Dimensioning Calculation Methods". 337-350 Pages / Challenging Glass Conference Proceedings, Vol. 6 (2018): Challenging Glass 6. en. In: DOI: 10.7480/CGC.6.2156.

Descamps, P., V. Hayez, and M. Chabih (2017). "Next generation calculation method for structural silicone joint dimensioning". En;en. In: *Glass Structures & Engineering* 2.2, pp. 169–182. DOI: 10.1007/s40940-017-0044-7.

Descamps, P., G. van Wassenhove, and V. Hayez (2020). "Simulating structural silicone glazing joint deformation with spring models". En;en. In: *Glass Structures & Engineering* 5.2, pp. 171–185. DOI: 10.1007/s40940-019-00105-6.

Dias, V., C. Odenbreit, O. Hechler, F. Scholzen, and T. Ben Zineb (2014). "Development of a constitutive hyperelastic material law for numerical simulations of adhesive steel–glass connections using structural silicone". In: *International Journal of Adhesion and Adhesives* 48, pp. 194–209. DOI: 10.1016/j.ijadhadh.2013.09.043.

Dilger, K., E. Stammen, and M. Feldmann (2022). *Mechanisches Verhalten von Silikonklebstoffen in Abhängigkeit der Belastungsdauer (Kurzzeit-, Langzeit- und Schwingbelastung) (NewMechsiko). IGF-Vorhaben 20602 N - DVS-Nr.: 08.3040, Schlussbericht*. Vol. 528. DVS Forschungsvereinigung.

Domininghaus, H., P. Elsner, P. Eyerer, and T. Hirth (2012). *Kunststoffe*. Berlin, Heidelberg: Springer Berlin Heidelberg. DOI: 10.1007/978-3-642-16173-5.

DOW Silicones Deutschland GmbH (2020). *Allowable compression and shear stress for DOWSIL™ 993 Structural Silicone. Project: The ONE Toranto, Canada (Internal document)*.

Drass, M. (2020). *Constitutive Modelling and Failure Prediction for Silicone Adhesives in Façade Design*. Vol. 55. Wiesbaden: Springer Fachmedien Wiesbaden. DOI: 10.1007/978-3-658-29255-3.

Drass, M. and M. A. Kraus (2020a). "Semi-Probabilistic Calibration of a Partial Material Safety Factor for Structural Silicone Adhesives - Part I: Derivation". In: *International Journal of Structural Glass and Advanced Materials Research* 4.1, pp. 56–68. DOI: 10.3844/sgamrsp.2020.56.68.

Drass, M. and M. A. Kraus (2020b). "Dimensioning of silicone adhesive joints: Eurocode-compliant, mesh-independent approach using the FEM". In: *Glass Structures & Engineering* 5.3, pp. 349–369. DOI: 10.1007/s40940-020-00128-4.

Drebenstedt, K. and M. Euler (2018). "Statistical Analysis of Fatigue Test Data according to Eurocode 3". In: *Maintenance, Safety, Risk, Management and Life-Cycle Performance of Bridges. Proceedings of the Ninth International Conference on Bridge Maintenance, Safety and Management (IABMAS 2018), 9-13 July 2018, Melbourne, Australia*. Ed. by N. Powers, D. M. Frangopol, R. Al-Mahaidi, and C. Caprani. First edition. Bridge maintenance, safety and management. Boca Raton, FL: CRC Press, pp. 2244–2251.

Feldmann, M., R. Kasper, B. Abeln, P. Cruz, J. Belis, J. Beyer, J. Colvin, F. Ensslen, M. Eliášová, L. Galuppi, A. Geßler, C. Grenier, A. Haese, H. Hoegner, R. Kruijs, K. Langosch, C. Louter, G. Manara, T. Morgan, J. Neugebauer, V. Rajčić, G. Royer-Carfagni, J. Schneider, S. Schula, G. Siebert, Z. Sulcova, F. Wellershoff, and R. Žarnić (2014). *Guidance for European structural design of glass components. Support to the implementation, harmonization and further development of the Eurocodes*. Ed. by S. Dimova. Vol. 26439 EN. EUR (Luxembourg. Online). Luxemburg: European Union. 196 str.

Feldmann, M., C. Richter, B. Abeln, and B. Schaaf (2017). "Zur Berechnung und Bemessung von Klebverbindungen aus der Sicht des Stahlbaus". In: *Stahlbau* 86.12, pp. 1106–1112. DOI: 10.1002/stab.201710554.

Feynman, R. P., R. B. Leighton, and M. L. Sands (2010). *Mainly electromagnetism and matter*. eng. New millenium edition. Vol. Volume 2. The Feynman lectures on physics / Feynman, Leighton, Sands. New York: Basic Books. 1 Band (verschiedene Seitenzählungen).

Flügge, W. (1975). *Viscoelasticity*. eng;ger. 2., rev. ed. Berlin, Heidelberg, New York: Springer. 194 pp.

Galli, U. (2011). "Seismic Behaviour of Curtain Wall Facades. A Comparison Between Experimental Mock-Up Test and Finite Element Method Analysis". Masterarbeit. POLITECNICO DI MILANO.

Geiß, P., C. Fritzsche, F. Kleiner, M. Peschka, M. Rauscher, H. C. Schmale, D. Vogt, A. Zanotti, C. Weber, and M. Wibbeke (2012). *Kleben von Stahl und Edelstahl Rostfrei*. Ausgabe 2012. Düsseldorf: Stahl-Informations-Zentrum.

Gent, A. N. (2012). *Engineering with Rubber. How to Design Rubber Components*. eng. 3rd Edition. s.l.: Carl Hanser Fachbuchverlag. 452 pp. DOI: 10.3139/9783446428713.

Giardini, D., G. Grünthal, K. M. Shedlock, and P. Zhang (1999). "The GSHAP Global Seismic Hazard Map". en. In: *Annals of Geophysics* 42.6. DOI: 10.4401/ag-3784.

– (2003). "The GSHAP Global Seismic Hazard Map". English. In: *International Handbook of Earthquake & Engineering Seismology*. Ed. by W. Lee, P. Jennings, and Kisslinger, Carl, Kanamori, Hiroo. International geophysics series v. 81A. Amsterdam and Boston: Academic Press, pp. 1233–1239.

Glinka, G., G. Wang, and A. Plumtree (1995). "Mean Stress Effects in Multiaxial Fatigue". In: *Fatigue & Fracture of Engineering Materials and Structures* 18.7-8, pp. 755–764. DOI: 10.1111/j.1460-2695.1995.tb00901.x.

Götz, S. and K.-G. Eulitz (2022). *Betriebsfestigkeit*. Wiesbaden: Springer Fachmedien Wiesbaden. DOI: 10.1007/978-3-658-38511-8.

Grambow, A. (2003). "Bestimmung der Materialparameter gefüllter Elastomere in Abhängigkeit von Zeit, Temperatur und Beanspruchungszustand". Dissertation. Aachen: RWTH Aachen.

Green, R. A. and G. A. Terri (2005). "Number of Equivalent Cycles Concept for Liquefaction Evaluations—Revisited". In: *Journal of Geotechnical and Geoenvironmental Engineering* 131.4, pp. 477–488. DOI: 10.1061/(ASCE)1090-0241(2005)131:4(477).

Grellmann, W. and S. Seidler (2025). *Kunststoffprüfung*. ger. 4., überarbeitete Auflage. München: Hanser. 739 pp.

Grünthal, G. (1998). *European macroseismic scale 1998. EMS-98*. eng. Vol. 15. Cahiers du Centre Européen de Géodynamique et de Séismologie. Luxembourg. 99 pp.

Gutenberg, B. and C. F. Richter (1956). "Earthquake magnitude, intensity, energy, and acceleration". In: *Bulletin of the Seismological Society of America* 46.2, pp. 105–145. DOI: 10.1785/BSSA0460020105.

Habenicht, G. (2009). *Kleben. Grundlagen, Technologien, Anwendungen*. Berlin, Heidelberg: Springer Berlin Heidelberg. DOI: 10.1007/978-3-540-85266-7.

– (2016). *Kleben - erfolgreich und fehlerfrei. Handwerk, Praktiker, Ausbildung, Industrie*. ger. 7. Aufl. 2016. SpringerLink Bücher. Wiesbaden: Springer Vieweg. 273 pp. DOI: 10.1007/978-3-658-14696-2.

Hagl, A. (2006). "Die Innovation – Kleben. Aktuelles aus der "Arbeitsgruppe Kleben" des Fachverbandes Konstruktiver Glasbau - FKG". In: *Stahlbau* 75.6, pp. 508–520. DOI: 10.1002/stab.200610054.

– (2007). "Bemessung von strukturellen Silikon-Klebungen". de;en. In: *Stahlbau* 76.8, pp. 569–581. DOI: 10.1002/stab.200710060.

Haibach, E. (2006). *Betriebsfestigkeit. Verfahren und Daten zur Bauteilberechnung*. ger. 3., korrigierte und ergänzte Auflage. VDI-Buch. Berlin: Springer. 759 pp.

Halford, G. R., B. A. Lerch, and M. A. McGaw (2000). *Fatigue, Creep-Fatigue, and Thermomechanical Fatigue Life Testing of Alloys*. ASM International, Materials.

Hanks, T. C. and H. Kanamori (1979). "A moment magnitude scale". In: *Journal of Geophysical Research* 84.B5, p. 2348. DOI: 10.1029/JB084iB05p02348.

Hayez, V., S. Bianchi, G. Lori, J. Feng, and J. Kimberlain (2023). "Performance of silicon bonded facades during seismic events". In: *Glass Performance Days 2023*. Glass Performance Days (Tempere, Finland, June 14–16, 2023).

Heinrich, G. and M. Klüppel (2000). "Recent Advances in the Theory of Filler Networking in Elastomers". en. In: *Filled Elastomers Drug Delivery Systems*. Ed. by A. Abe. 1st ed. Berlin/Heidelberg: Springer Berlin Heidelberg, pp. 1–44. DOI: 10.1007/3-540-45362-8_1.

Hennemann, O.-D., M. Brede, C. Nagel, O. Hahn, J. Jendrny, D. Teutenberg, M. Schlimmer, and K.-M. Mihm (2012). *Methodenentwicklung zur Berechnung und Auslegung geklebter Stahlbauteile im Fahrzeugbau bei schwingender Beanspruchung. = Development of a method for dimensioning and designing adhesive joint steel components in vehicle construction at cyclic loading*. In collab. with O.-D. Hennemann. Vol. 653. Forschung für die Praxis / Forschungsvereinigung Stahlanwendung e.V. im Stahl-Zentrum. Düsseldorf: Verl. und Vertriebsges. mbH. VI S., S. 7 - 476.

Holzapfel, G. A. (2010). *Nonlinear solid mechanics. A continuum approach for engineering*. eng. Repr. Chichester: Wiley. 455 pp.

Hosseini, M. (2005). "Behavior of Nonstructural Elements in the 2003 Bam, Iran, Earthquake". In: *Earthquake Spectra* 21.1, pp. 439–453. DOI: 10.1193/1.2098829.

Hou, C.-Y., Y.-F. Lee, and Y.-H. Peng (2019). "Fatigue damage analysis of steel components subjected to earthquake loadings". In: *International Journal of Structural Integrity* 10.1, pp. 25–40. DOI: 10.1108/IJSI-05-2018-0028.

Huang, B., S. Chen, W. Lu, and K. M. Mosalam (2017a). "Seismic demand and experimental evaluation of the nonstructural building curtain wall: A review". In: *Soil Dynamics and Earthquake Engineering* 100, pp. 16–33. DOI: 10.1016/j.soildyn.2017.05.025.

Huang, J., G. A. Fenton, L. Zhang, and D. V. Griffiths, eds. (2017b). *Geo-Risk 2017*. Geo-Risk 2017 (Denver, Colorado, June 4–7, 2017). Reston, VA: American Society of Civil Engineers. DOI: 10.1061/9780784480700.

Huveners, E. M. P., F. Herwijnen van, F. Soetens, and H. Hofmeyer (2007). "Glass panes acting as shear wall". In: *Heron* 52.1/2, pp. 5–29.

Huveners, E. M. P., F. Herwijnen van, F. Soetens, and H. Hofmeyer (2009). "Bracing Steel Frames with Adhesively Bonded Glass Panes - Mechanic Models". In: *Conference proceedings Glass Performance Days. 11th International Conference on Architectural and Automotive Glass*. Glass Performance Days (Tampere). Tampere, pp. 256–260.

Huveners, E., H. Hofmeyer, F. Herwijnen van, and F. Soetens (2008). "Numerical research on glass panes acting as a shear wall". In: *Challenging glass. Conference on Architectural and Structural Applications of Glass, Faculty of Architecture, Delft University of Technology, May 2008 ; [proceedings*. Ed. by F. Bos and C. Louter. Amsterdam: IOS Press Delft Univ. Press, pp. 359–368.

Iervolino, I., C. Galasso, and E. Cosenza (2010). "REXEL: computer aided record selection for code-based seismic structural analysis". In: *Bulletin of Earthquake Engineering* 8.2, pp. 339–362. DOI: 10.1007/s10518-009-9146-1.

Inca, E. (2019). "Seismic Behaviour of Point Fixed Glass Façade Systems: State of the Art Review". In: *European Journal of Engineering Science and Technology*. DOI: 10.33422/EJEST.2019.07.06.

Jalayer, F., R. de Risi, and G. Manfredi (2015). "Bayesian Cloud Analysis: efficient structural fragility assessment using linear regression". In: *Bulletin of Earthquake Engineering* 13.4, pp. 1183–1203. DOI: 10.1007/s10518-014-9692-z.

Jordi Alcaine, Ed Forwood, Pedro Gálvez, Peter Lenk, Ulli Mueller, and Viviana Nardini (2024). "Holistic Review of the Permanent Shear Deformation Effects on Structural Silicone Joints in SSG Façade Systems". en. In: *Challenging Glass Conference Proceedings* 9. DOI: 10.47982/cgc.9.546.

Kahraman, H. (2015). "Experimentelle Untersuchungen und Beschreibung des deformationsinduzierten anisotropen Werkstoffverhaltens von verstärkten Elastomeren". Dissertation. Aachen: RWTH Aachen.

Kaindl, S. (2014). "Simulation der Schwingfestigkeit von Elastomerbauteilen". Zentrums für Ingenieurwissenschaften. Dissertation. Halle-Wittenberg: Martin-Luther-Universität Halle-Wittenberg.

Kaiser, W. (2023). *Kunststoffchemie für Ingenieure*. München: Carl Hanser Verlag GmbH & Co. KG. DOI: 10.3139/9783446478077.

Kanamori, H. (1977). "The energy release in great earthquakes". In: *Journal of Geophysical Research* 82.20, pp. 2981–2987. DOI: 10.1029/JB082i020p02981.

Khoraskani, R. A. (2015). *Advanced Connection Systems for Architectural Glazing*. eng. SpringerBriefs in Applied Sciences and Technology. s.l.: Springer-Verlag. 125 pp. DOI: 10.1007/978-3-319-12997-6.

Kim, S.-W., B.-G. Jeon, D.-G. Hahm, and M.-K. Kim (2023). "Failure criteria evaluation of steel pipe elbows in nuclear power plant piping systems using cumulative damage models". In: *Thin-Walled Structures* 182, p. 110250. DOI: 10.1016/j.tws.2022.110250.

King, A. and K. Lim (1991). *The Behaviour of external glazing systems under seismic in-plan racking. Study Report SR 39*. Judgeford, New Zealand.

King, A. B. and S. J. Thurston (1992). "The racking behaviour of curtain wall galzing during simulated earthquake". In: *Proceedings of the Tenth World Conference on Earthquake*

*Engineering. 19-24 July 1992, Madrid, Spain*. World Conference on Earthquake Engineering and International Association for Earthquake Engineering. Rotterdam: Balkema.

Köhler, M., S. Jenne, K. Pötter, and H. Zenner (2012). *Zählverfahren und Lastannahme in der Betriebsfestigkeit*. Berlin, Heidelberg: Springer Berlin Heidelberg. DOI: 10.1007/978-3-642-13164-6.

Kraus, M. and M. Drass (2020a). "Semi-Probabilistic Calibration of a Partial Material Safety Factor for Structural Silicone Adhesives -Part II: Verification Concept". In: *International Journal of Structural Glass and Advanced Materials Research* 4.1, pp. 10–23. DOI: 10.3844/sgamrsp.2020.10.23.

– (2020b). "Semi-Probabilistic Design of Silicone Adhesive Joints: Eurocode-compliant and mesh-independent approach using Finite Elements". In: *GlassCon Global 2020*. GlassCon Global 2020 (Sept. 9–10, 2020).

Kuntsche, J. K. (2015). *Mechanisches Verhalten von Verbundglas unter zeitabhängiger Belastung und Explosionsbeanspruchung. Mechanical Behaviour of Laminated Glass under Time-Dependent and Explosion Loading*. ger. Vol. v. 46. Mechanik, Werkstoffe und Konstruktion im Bauwesen. [Place of publication not identified]: Springer Science and Business Media.

Lago, A. and T. J. Sullivan (2011). *A review of glass façade systems and research into the seismic design of frameless glass façades*. Vol. no. ROSE-2011/01. Research report. Pavia: IUSS. XIX, 166 str.

Landolfo, R. (2015). "Seismic Design of Steel Structures According to EN 1998-1". In: *Eurocodes: background & applications. Design of steel buildings : worked examples*. Ed. by M. Veljkovic, M. L. Sousa, S. Dimova, B. Nikolova, M. Poljanšek, and A. Pinto. JRC science and policy report 27346. Luxembourg: Publications Office of the European Union, pp. 291–336.

Lazan, B. J. (1968). *Damping of materials and members in structural mechanics*. en. Oxford: Pergamon Press.

Liu, A. H., J. P. Stewart, N. A. Abrahamson, and Y. Moriwaki (2001). "Equivalent Number of Uniform Stress Cycles for Soil Liquefaction Analysis". In: *Journal of Geotechnical and Geoenvironmental Engineering* 127.12, pp. 1017–1026. DOI: 10.1061/(ASCE)1090-0241(2001)127:12(1017).

Liu, L., X. Wang, Z. Wu, and T. Keller (2021). "Tension-tension fatigue behavior of ductile adhesively-bonded FRP joints". In: *Composite Structures* 268, p. 113925. DOI: 10.1016/j.compstruct.2021.113925.

Loch, M. (2014). "Beitrag zur Bestimmung von charakteristischen Werkstofffestigkeiten in Bestandstragwerken aus Stahlbeton". Kaiserslautern: Technische Universität Kaiserslautern.

MacRae, G., S. Pampanin, R. Dhakal, A. Palermo, A. Baird, and S. Tasligedik (2012). *Review of design and installation practices for non-structural components. Report prepared for the Engineering Advisory Group of the Department of Building and Housing by New Zealand Consultants, Industry and Related Experts*. New Zealand.

Mander, J. B., F. D. Panthaki, and A. Kasalanati (1994). "Low–Cycle Fatigue Behavior of Reinforcing Steel". en. In: *Journal of Materials in Civil Engineering* 6.4, pp. 453–468. DOI: 10.1061/(asce)0899-1561(1994)6:4(453).

Maniatis, I., G. Siebert, and G. Nehring (2015). "Dimensionierung von Klebefugen aus Silikon mit beliebiger Geometrie". de. In: *Stahlbau* 84.S1, pp. 293–302. DOI: 10.1002/stab.201590086.

Manson, S. S. (1965). "Fatigue: A complex subject—Some simple approximations". En;en. In: *Experimental Mechanics* 5.4, pp. 193–226. DOI: 10.1007/BF02321056.

Manson, S. S. and G. R. Halford (2006). *Fatigue and durability of structural materials*. English. Materials Park, Ohio: ASM International. 456 pp.

Martins, P. A. L. S., R. M. Natal Jorge, and A. J. M. Ferreira (2006). "A Comparative Study of Several Material Models for Prediction of Hyperelastic Properties: Application to Silicone-Rubber and Soft Tissues". In: *Strain* 42.3, pp. 135–147. DOI: 10.1111/j.1475-1305.2006.00257.x.

Mattei, S., M. Fasan, and C. Bedon (2021). "On the Use of Cloud Analysis for Structural Glass Members under Seismic Events". In: *Sustainability* 13.16, p. 9291. DOI: 10.3390/su13169291.

Mayer, B., C. Nagel, A. Fiedler, T. Melz, G. Rybar, G. Meschut, S. Çavdar, D. Teutenberg, A. Matzenmiller, and U. Kroll (2017). *Analyse der Schwingfestigkeit geklebter Stahlverbindungen unter mehrkanaliger Belastung. Schlussbericht zu IGF-Vorhaben Nr. 18107 N - FOSTA P1028 : Berichtszeitraum: 01.05.2014-31.10.2016, verlängert bis 30.04.2017 = Fatigue strength analysis of bonded steel joints under multiaxial loading conditions*. ger. In collab. with F.-J. Heise. Vol. 1028. Forschung für die Praxis / Forschungsvereinigung Stahlanwendung e.V P. Düsseldorf: Forschungsvereinigung Stahlanwendung e.V.

Mazzoni, S., T. Kishida, and Y. Bozorgnia (2023). "NGA-West2 Duration Metrics Dataset R230609". In: *The B. John Garrick Institute for the Risk Sciences*. DOI: 10.34948/N37G68.

Memari, A. M., X. Chen, P. A. Kremer, and R. A. Behr (2006a). "Development of Failure Prediction Models for Structural Sealant Glazing Systems under Cyclic Racking Displacement Conditions". In: *AEI 2006: Building Integration Solutions - Proceedings of the 2006 Architectural Engineering National Conference*. Architectural Engineering Conference (Omaha, Nebraska, United States, Mar. 29–Apr. 1, 2006). Ed. by American Society of Civil Engineers, pp. 1–15. DOI: 10.1061/40798(190)6.

– (2012a). "Prediction of Seismic Failure of Silicone Sealant in Two-Sided Structural Sealant Glazing Systems". In: *Journal of Architectural Engineering* 18.1, pp. 16–26. DOI: 10.1061/(ASCE)AE.1943-5568.0000061.

Memari, A. M., S. Fisher, C. Krumenacker, K. A. Broker, and R.-U. Modrich (2012b). "Evaluation of the Structural Sealant for Use in a Four-Sided Structural Sealant Glazing Curtain-Wall System for a Hospital Building". English. In: *Journal of ASTM International* 9.4, p. 104143. DOI: 10.1520/JAI104143.

Memari, A. M., A. Shirazi, and P. A. Kremer (2007). "Static finite element analysis of architectural glass curtain walls under in-plane loads and corresponding full-scale test". In: *Structural Engineering and Mechanics* 25.4, pp. 365–382. DOI: 10.12989/sem.2007.25.4.365.

Memari, A. M. (2013). "Design of Curtain Walls for Earthquake-Induced Loads and Drifts". English (US). In: *Curtain wall systems. A primer*. Ed. by A. M. Memari. ASCE manuals and reports on engineering practice no. 126. Reston, Virginia: American Society of Civil Engineers, pp. 105–128. DOI: 10.1061/9780784412701.ch08.

Memari, A. M., R. A. Behr, and P. A. Kremer (2003). "Seismic Behavior of Curtain Walls Containing Insulating Glass Units". In: *Journal of Architectural Engineering* 9.2, pp. 70–85. DOI: 10.1061/(ASCE)1076-0431(2003)9:2(70).

Memari, A. M., X. Chen, P. A. Kremer, and R. A. Behr (2006b). "Seismic Performance of Two-Side Structural Silicone Glazing Systems". In: *Journal of ASTM International* 3.10, pp. 40–49. DOI: 10.1520/JAI100407.

Memari, A. M. and A. Shirazi (2004). "Development of a Seismic Rating System for Architectural Glass in Existing Curtain Walls, Storefronts, and Windows. Paper No. 1541". In: *13th World Conference on Earthquake Engineering*. World Conference on Earthquake Engineering (Vancouver, B.C., Canada, Aug. 1–6, 2004). Vancouver, B.C., Canada.

Meskouris, K. (2011). *Bauwerke und Erdbeben. Grundlagen - Anwendung - Beispiele*. ger. 3., aktualisierte und erweiterte Auflage. Praxis. Wiesbaden: Vieweg+Teubner Verlag / Springer Fachmedien Wiesbaden GmbH Wiesbaden. 731 pp. DOI: 10.1007/978-3-8348-9856-2.

Meunier, L., G. Chagnon, D. Favier, L. Orgéas, and P. Vacher (2008). "Mechanical experimental characterisation and numerical modelling of an unfilled silicone rubber". In: *Polymer Testing* 27.6, pp. 765–777. DOI: 10.1016/j.polymertesting.2008.05.011.

Michigan Technological University (2021). *Earthquake Magnitude Scale and Classes*. Ed. by UPSeis - an educational site for budding seismologists. URL: http://www.geo.mtu.edu/UPSeis/magnitude.html (visited on 06/08/2021).

Miner, M. A. (1945). "Cumulative Damage in Fatigue". en. In: *Journal of Applied Mechanics* 12.3, A159–A164. DOI: 10.1115/1.4009458.

Miyauchi, H. and K. Tanaka (2000). "New shear fatigue test method for building sealants and some tests of sealant beads with various shapes". In: *3rd International Symposium on Durability of Building and Construction Sealants. Seneffe, Belgium, February 2 - 3, 2000*. Ed. by A. T. Wolf. RILEM proceedings PRO 10. Cachan, France: RILEM Publications, pp. 275–285.

Momeni, M. and C. Bedon (2024). "Review on Glass Curtain Walls under Different Dynamic Mechanical Loads: Regulations, Experimental Methods and Numerical Tools". In: *Facade Design - Challenges and Future Perspective [Working Title]*. IntechOpen. DOI: 10.5772/intechopen.113266.

Movahedi-Rad, A. V., G. Eslami, and T. Keller (2021). "A novel fatigue life prediction methodology based on energy dissipation in viscoelastic materials". In: *International Journal of Fatigue* 152, p. 106457. DOI: 10.1016/j.ijfatigue.2021.106457.

Müller, P. (2025). "Design of Structural-Glazing Joints under Seismic Loading". In: *Young Engineers Colloquium 2025*. Young Engineers Colloquium (München, Nov. 7, 2025). Ed. by International Association for Bridge and Structural Engineering.

Müller, P., T. Reisewitz, D. Offereins, and C. Schuler (2026a). "Kleben im konstruktiven Glasbau. Zum Tragverhalten unter Erdbebenbeanspruchung". In: *Stahlbau* 95.S2: *Sonderheft Glasbau & Fassade*, pp. 123–133. DOI: 10.1002/stab.70154.

Müller, P., C. Schuler, S. Koch, E. Stammen, K. Dilger, T. Reisewitz, and G. Siebert (2026b). *Bemessungsmodell für Dickschichtklebungen in Katastrophenszenarien (RISIKO). IGF-Vorhaben 01IF 22888 N / DVS-Nr. 08.3697; Laufzeit: 01.04.2023 - 31.03.2026; Abschlussbericht in Vorbereitung*.

Müller, P., C. Schuler, T. Reisewitz, G. Siebert, S. Koch, E. Stammen, and K. Dilger (2025a). "Bemessungsmodell für Dickschichtklebungen in Katastrophenszenarien". In: *25. Kolloquium Gemeinsame Forschung in der Klebtechnik*. Gemeinsame Forschung in der Klebtechnik (Köln, Feb. 18–19, 2025). Gemeinschaftsausschuss Klebtechnik.

– (2026c). "Bemessungsmodell für Dickschichtklebungen in Katastrophenszenarien". In: *26. Kolloquium Gemeinsame Forschung in der Klebtechnik*. Gemeinsame Forschung in der Klebtechnik (Köln, Feb. 10–11, 2026). Gemeinschaftsausschuss Klebtechnik.

Müller, P., C. Schuler, and G. Siebert (2023a). "Investigations on the influence of manufacturing and curing effects on the properties of structural-glazing adhesives subjected to tensile stresses". In: *Glass Structures & Engineering*. DOI: 10.1007/s40940-023-00226-z.

– (2024). "Experimental investigations on the cyclic load-bearing behavior of structural glazing joints under seismic load". En;en. In: *Glass Structures & Engineering*, pp. 1–25. DOI: 10.1007/s40940-024-00273-0.

– (2025b). "Analysis of the seismic ground motion loading on structural glazing connections in glass and facade constructions". En;en. In: *Bulletin of Earthquake Engineering*, pp. 1–40. DOI: 10.1007/s10518-025-02303-w.

– (2025c). "Discussion of failure criteria and low-cycle fatigue performance of structural glazing connections under various seismic loading scenarios". In: *Construction and Building Materials* 471, p. 140605. DOI: 10.1016/j.conbuildmat.2025.140605.

– (2025d). "Residual performance of structural glazing joints after seismic low-cycle fatigue loading". En;en. In: *Glass Structures & Engineering* 10.3, pp. 1–16. DOI: 10.1007/s40940-025-00303-5.

– (2025e). "Seismic Performance of Structural Glazing Connections Under Low Cycle Fatigue Loading: A Study on Alternative Joint Geometries". In: *IABSE Symposium: Environmentally Friendly Technologies and Structures: Focusing on Sustainable Approaches*. IABSE Symposium Tokyo (Tokyo, May 18–21, 2025). Ed. by T. Takeuchi, G. Siebert, and T. Nagayama. International Association for Bridge and Structural Engineering, pp. 1033–1042. DOI: 10.2749/tokyo.2025.1033.

Müller, P., G. Siebert, and C. Schuler (2023b). "Einfluss der Fertigung auf das Tragverhalten von SG-Klebungen". In: *Glas im konstruktiven Ingenieurbau 18 (GIKI18)*. Glas im konstruktiven Ingenieurbau (München, Mar. 2–3, 2023). Hochschule München.

– (2025f). "Strukturelle Klebverbindungen im Glas-und Fassadenbau unter seismischer Beanspruchung". In: *Glas im konstruktiven Ingenieurbau 19 (GIKI19)*. Glas im konstruktiven Ingenieurbau (München, May 22–23, 2025). Hochschule München.

Müller, P., E. Stammen, T. Reisewitz, S. Koch, C. Schuler, G. Siebert, and K. Dilger (2026d). "Vom Versuch zur Bemessung: Dickschichtklebungen unter hoher zyklischer Beanspruchung sicher nachweisen". In: *Joining Plastics* 20.3, pp. 40–51. DOI: 10.53192/JP20260340.

Mullins, L. (1948). "Effect of Stretching on the Properties of Rubber". In: *Rubber Chemistry and Technology* 21.2, pp. 281–300. DOI: 10.5254/1.3546914.

– (1969). "Softening of Rubber by Deformation". In: *Rubber Chemistry and Technology* 42.1, pp. 339–362. DOI: 10.5254/1.3539210.

Nardini, V. and F. Doebbel (2015). “Concept for Seismic Design of Structural Silicone Joints in Unitized Curtain Walling”. In: *Glass Performance Days 2015*. Glass Performance Days (Tempere, Finland, June 24–26, 2015), pp. 281–286.
– (2016). “Performance-Based Concept for Design of Structural Silicone Joints in Façades Exposed to Earthquake”. eng. In: *Challenge Glass 5 - Conference on Architectural and Structural Applications of Glass*. CGC 2016 (Ghent, June 16–17, 2016). Ed. by J. Belis, F. Bos, and C. Louter. Universiteit Gent. Ghent: Ghent University.
– (2020). “Influence of Performance and Design of Structural Silicone Joints on the Resilience of Curtain Wall Units Exposed to Seismic Impacts”. In: *Facade Tectonics 2020 World Congress*. Facade Tectonics (Aug. 5–27, 2020). Facade Tectonics Institute.
Norda, H. (2013). *Beitrag zum statischen nichtlinearen Erdbebennachweis von unbewehrten Mauerwerksbauten unter Berücksichtigung einer und höherer Modalformen*. Aachen, Techn. Hochsch., Diss., 2012. ger. Vol. 24. Mitteilungen des Lehrstuhls für Baustatik und Baudynamik. Aachen: Hochschulbibliothek der Rheinisch-Westfälischen Technischen Hochschule Aachen.
Nuñez Enriquez, D. (2022). “Seismic Performance of Glazed Curtain Walls. Connections: Experimental Testing and Finite Element Modelling”. Masterarbeit. Delft: TU Delft.
O’Brien JR., W. C., A. M. Memari, and M. Eeri (2015). “Prediction of seismic cracking capacity of glazing systems”. In: *Earthquakes and Structures* 8.1, pp. 101–132. DOI: 10.12989/eas.2015.8.1.101.
Oppe, M., R. Schieber, T. Fildhuth, and S. Grün (2021). “Transparente Gebäudehüllen in Gebieten mit hohen seismischen Anforderungen”. In: *GLASBAU 2021*. Ed. by B. WELLER. [S.l.]: WILHELM ERNST & SOHN VERL., pp. 103–115.
Oppe, M. and S. Grün (2020). “Uber – Mission Bay Campus, San Francisco”. In: *Stahlbau* 89.1, pp. 49–58. DOI: 10.1002/stab.201900099.
Palmgren, A. (1924). “Die Lebensdauer von Kugellagern”. In: *Zeitschrift des Vereins Deutscher Ingenieure* 68.14, pp. 339–341.
Palmieri, G., M. Sasso, G. Chiappini, and D. Amodio (2009). “Mullins effect characterization of elastomers by multi-axial cyclic tests and optical experimental methods”. In: *Mechanics of Materials* 41.9, pp. 1059–1067. DOI: 10.1016/j.mechmat.2009.05.002.
Pantelides, C. P. and R. A. Behr (1994). “Dynamic in-plane racking tests of curtain wall glass elements”. In: *Earthquake Engineering & Structural Dynamics* 23.2, pp. 211–228. DOI: 10.1002/eqe.4290230208.
Papazafeiropoulos, G. (2015). *Response Spectra. Dynamic response spectrum analysis, elastic and elastoplastic response spectra*. Ed. by MATLAB Central File Exchange. Version 1.7.
Payne, A. R. (1957). “Nonlinearity in the Dynamic Properties of Rubber”. In: *Rubber Chemistry and Technology* 30.1, pp. 218–241. DOI: 10.5254/1.3542666.
Payne, A. R., R. E. Whittaker, and J. F. Smith (1972). “Effect of vulcanization on the low–strain dynamic properties of filled rubbers”. In: *Journal of Applied Polymer Science* 16.5, pp. 1191–1212. DOI: 10.1002/app.1972.070160513.
Perrone, D., P. M. Calvi, R. Nascimbene, E. C. Fischer, and G. Magliulo (2019). “Seismic performance of non-structural elements during the 2016 Central Italy earthquake”. In: *Bulletin of Earthquake Engineering* 17.10, pp. 5655–5677. DOI: 10.1007/s10518-018-0361-5.

Petersen, C. and H. Werkle (2017). *Dynamik der Baukonstruktionen*. ger. 2. Aufl. 2017. Wiesbaden: Springer Fachmedien Wiesbaden. 1758 pp. DOI: 10.1007/978-3-8348-2109-6.

Radaj, D. and M. Vormwald (2007). *Ermüdungsfestigkeit. Grundlagen für Ingenieure*. 3., neubearbeitete und erw. Aufl. Berlin and New York: Springer. 688 pp.

Rasche, M. (2012). *Handbuch Klebtechnik*. ger. Hanser eLibrary. München: Hanser. 616 pp. DOI: 10.3139/9783446431980.

Richter, C., B. Abeln, B. Schaaf, and M. Feldmann (2021). "Vereinfachte rechnerische Last–Verformungsvorhersage von Klebfugen mit hyperelastischem Verhalten im Konstruktiven Glasbau". In: *ce/papers* 4.1, pp. 94–104. DOI: 10.1002/cepa.1245.

Richter, C. H. O. (2018). *Vereinfachte rechnerische Last-Verformungsvorhersage von Klebfugen mit hyperelastischem Verhalten im konstruktiven Glasbau*. Dissertation. [1. Auflage]. Vol. Heft 84. Schriftenreihe des Lehrstuhls für Stahlbau und Leichtmetallbau der RWTH Aachen. Aachen: Shaker Verlag. v, 159, X Seiten.

Richter, C. F. (1935). "An instrumental earthquake magnitude scale*". en. In: *Bulletin of the Seismological Society of America* 25.1, pp. 1–32. DOI: 10.1785/bssa0250010001.

Ristau, J. (2009). "Comparison of Magnitude Estimates for New Zealand Earthquakes: Moment Magnitude, Local Magnitude, and Teleseismic Body-Wave Magnitude". In: *Bulletin of the Seismological Society of America* 99.3, pp. 1841–1852. DOI: 10.1785/0120080237.

Rosendahl, P. L. (2020). "From bulk to structural failure: fracture of hyperelastic materials". UNSPECIFIED.

Rösler, J., H. Harders, and M. Bäker (2019). *Mechanisches Verhalten der Werkstoffe*. Wiesbaden: Springer Fachmedien Wiesbaden. DOI: 10.1007/978-3-658-26802-2.

Santarsiero, M. (2015). "Laminated Connections for Structural Glass Applications". Faculté de l'environnement naturel, architectural et construit. Dissertation. École Polytechnique Fédérale de Lausanne, 199 pp.

Santarsiero, M., C. Bedon, and K. Moupagitsoglou (2019). "Energy-based considerations for the seismic design of ductile and dissipative glass frames". In: *Soil Dynamics and Earthquake Engineering* 125, p. 105710. DOI: 10.1016/j.soildyn.2019.105710.

Sauer, J. A. and G. C. Richardson (1980). "Fatigue of polymers". En;en. In: *International Journal of Fracture* 16.6, pp. 499–532. DOI: 10.1007/BF02265215.

Scavino, G. (2014). "Curtain Wall Design: The Seismic Behaviour of Glazing Façades. Masterarbeit". Politecnico di Milano.

Schaaf, B., B. Abeln, C. Richter, M. Feldmann, E. Toups, J. Simon, S. Reese, R. Seewald, A. Schiebahn, and U. Reisgen (2021). "Bestimmung von Material- und Modellparametern hyperelastischer Silikonklebungen im konstruktiven Glasbau/Determination of material and model parameters of hyperelastic silicone bondings in structural glass construction". In: *Bauingenieur* 96.01-02, pp. 37–46. DOI: 10.37544/0005-6650-2021-01-02-63.

Schaaf, B. (2024). *Zum Tragverhalten hyperelastischer Klebverbindungen im konstruktiven Glasbau*. 1. Auflage. Vol. 97. Schriftenreihe des Instituts für Stahlbau. Aachen: Verlag Günter Mainz. 280 pp.

Schaaf, B. and M. Feldmann (2023). "Approach for the simulation of the load-deformation behaviour of hyperelastic bonded joints using strain and strain rate dependent tangent

moduli". In: *International Journal of Adhesion and Adhesives* 124, p. 103395. DOI: 10.1016/j.ijadhadh.2023.103395.

– (2024). "Time-dependent design of hyperelastic bonded joints in structural glass". In: *Glass Structures & Engineering*. DOI: 10.1007/s40940-024-00254-3.

Schröder, T. (2018). *Rheologie der Kunststoffe. Theorie und Praxis*. ger. München: Hanser. 364 pp.

Schuler, C., M. Albiez, M. Bues, H. Ehard, and T. Ummenhofer (2019). "Tragende Klebverbindungen im Stahl–, Glas– und Fassadenbau". In: *Stahlbau Kalender 2019*. Ed. by U. Kuhlmann. Wiley, pp. 587–642. DOI: 10.1002/9783433609873.ch9.

Schuler, C., F. Ilg, M. Feldmann, B. Abeln, K. Dilger, and E. Stammen (2022). *Klebtechnische Ertüchtigung von Ermüdungsschäden für Konstruktionen des Stahlbaus (StressPatches). IGF-Vorhaben Nr. 19963 N - FOSTA P 1296, Laufendes Forschungsvorhaben*.

Schuler, C., B. Mayer, T. Ummenhofer, M. Albiez, M. Bues, T. Vallée, and S. Fecht (2017). *Systematische Untersuchung des Trag- und Versagensverhaltens geklebter Stahl-Glas-Verbindungen (SG). IGF-Vorhaben 18211 N / FOSTA P 1052, Schlussbericht*.

Schuler, C., M. Teich, and P. Müller (2023). "Tragende Klebverbindungen im Glas– und Fassadenbau". In: *2023 Stahlbau Kalender*. Ed. by U. Kuhlmann. Wiley, pp. 781–838. DOI: 10.1002/9783433611302.ch10.

Schwarzl, F. R. (1990). *Polymermechanik. Struktur und mechanisches Verhalten von Polymeren*. ger. Berlin, Heidelberg: Springer Berlin Heidelberg. DOI: 10.1007/978-3-642-61506-1.

Seed, H. B. and I. M. Idriss (1970). *A Simplified Procedure for Evaluating Soil Liquefaction Potential. Earthquake Engineering Research Center Reports - Rep. No. UCB/EERC 70-9*.

Seed, H. B., I. M. Idriss, F. Makdisi, and N. Banerjee (1975). *Representation of irregular stress time histories by equivalent uniform stress series in liquefaction analyses. Earthquake Engineering Research Center Reports - Rep. No. EERC 75-29*. Ed. by University of California, Berkeley, Calif.

Shedlock, K. M. and J. G. Tanner (1999). "Seismic hazard map of the western hemisphere". English. In: *Annali Di Geofisica* 42, pp. 1199–1214.

Siebert, G. and A. Haese (2009). "Earthquake Tests of Glass Structures". In: *IABSE Symposium Report* 96.2, pp. 86–95. DOI: 10.2749/222137809796089016.

Simmons, N. C. (2011). "Analytical Evaluation of Racking Performance of Four-Sided Structural Silicone Glazing Curtain Wall Systems". Master Thesis. Pennsylvania: The Pennsylvania State University.

Simmons, N. C. and A. M. Memari (2013a). *Finite Element Modeling to Predict Racking Test Results and Performance of Four-Sided Structural Sealant Glazing Curtain Wall Systems*. EN. American Society of Civil Engineers. 735 pp. DOI: 10.1061/9780784412909.072.

– (2013b). *Racking Performance Analysis of Four-Sided Structural Sealant Glazing Curtain Wall Systems Through Video Capture Technique*. EN. American Society of Civil Engineers. 725 pp. DOI: 10.1061/9780784412909.071.

Sivanerupan, S., J. L. Wilson, E. F. Gad, and N. T. K. Lam (2014). "In-Plane Drift Capacity of Contemporary Point Fixed Glass Facade Systems". EN. In: *Journal of Architectural Engineering* 20.1, p. 04013002. DOI: 10.1061/(ASCE)AE.1943-5568.0000130.

Sivanerupan, S. (2011). "In-Plane Seismic Performance of Glass Façade Systems". Centre for Sustainable Infrastructure and Development, Faculty of Engineering and Industrial Sciences. Dissertation. Swinburne University of Technology, Melbourne, Australia.

Smith, K. N., P. Watson, and T. Topper (1970). "A Stress-Strain Function for the Fatigue of Metals". In: *Journal of Materials* 5.4, pp. 767–778.

Sousa, F., P. Zamani, A. Akhavan-Safar, and L. Da Silva (2024). "A comprehensive review of the S-N fatigue behaviour of adhesive joints". In: *Journal of Advanced Joining Processes* 9, p. 100178. DOI: 10.1016/j.jajp.2023.100178.

Spitz, M. (2012). "Modellbasierte Lebensdauerprognose für dynamisch beanspruchte Elastomerbauteile". Fakultät für Ingenieurwissenschaften, Abteilung Maschinenbau und Ver-fahrenstechnik. Dissertation. Duisburg-Essen: Universität Duisburg-Essen.

Staudt, Y., C. Odenbreit, and J. Schneider (2018). "Failure behaviour of silicone adhesive in bonded connections with simple geometry". In: *International Journal of Adhesion and Adhesives* 82, pp. 126–138. DOI: 10.1016/j.ijadhadh.2017.12.015.

Stelzer, R., B. Carlton, and S. Mazzoni (2020). "Comparison of Cycle Counting Methods for Potential Liquefaction and Structural Fatigue Assessment". In: *17th World Conference on Earthquake Engineering, 17WCEE* (Sendai, Japan, Sept. 13–18, 2020). Ed. by Japan Association for Earthquake Engineering.

Stommel, M., M. Stojek, and W. Korte (2018). *FEM zur Berechnung von Kunststoff- und Elastomerbauteilen*. ger. 2., neu bearbeitete und erweiterte Auflage. München: Hanser. 494 pp.

Sucuoğlu, H. and C. Vallabhan (1997). "Behaviour of window glass panels during earthquakes". In: *Engineering Structures* 19.8, pp. 685–694. DOI: 10.1016/S0141-0296(96)00130-7.

Sugiyama, S. (2000). "Fatigue resistance of structural glazing silicone sealants". In: *3rd International Symposium on Durability of Building and Construction Sealants. Seneffe, Belgium, February 2 - 3, 2000*. Ed. by A. T. Wolf. RILEM proceedings PRO 10. Cachan, France: RILEM Publications, pp. 97–111.

Tanaka, K. and M. Koike (1995). "Effect of Depth on Fatigue Resistance of Sealing Beads of Various Rectangular Cross Sections". In: *Durability of Building Sealants*. Ed. by J. C. Beech and A. T. Wolf. Routledge, pp. 27–36.

Tanaka, K. and H. Miyauchi (2000). "Effect of Cross-Sectional Size and Shape on the Fatigue Resistance of Sealed Joints to Shear Movement". In: *3rd International Symposium on Durability of Building and Construction Sealants. Seneffe, Belgium, February 2 - 3, 2000*. Ed. by A. T. Wolf. RILEM proceedings PRO 10. Cachan, France: RILEM Publications.

The Dow Chemical Company (2015). *Design Stress for DOW CORNING® Structural Silicones*. Wiesbaden: The Dow Chemical Company.

Thurston, S. and A. King (1992). *Two-Directional Cyclic Racking of Comer Curtain Wall Glazing. Study Report SR 44*. Judgeford, New Zealand.

– (1993). *Proposed Test and Evaluation Procedure for External Curtain Wall Glazing Systems to Simulate Seismic Loading. Technical Reccomendation 15*. Judgeford, New Zealand.

Treloar, L. R. G. (1975). *The Physics of Rubber Elasticity. By L. R. G. Treloar*. eng. 3rd ed. Oxford Classic Texts in the Physical Sciences Ser. Oxford: Oxford University Press. 323 pp.

U.S. Geological Survey (1997). *The severity of an earthquake*. Ed. by U.S. Government Printing Office. DOI: 10.3133/70039541.

Van Lancker, B., W. de Corte, and J. Belis (2020). "Calibration of hyperelastic material models for structural silicone and hybrid polymer adhesives for the application of bonded glass". In: *Construction and Building Materials* 254, p. 119204. DOI: 10.1016/j.conbuildmat.2020.119204.

Van Lancker, B., J. Dispersyn, W. de Corte, and J. Belis (2016). "Durability of adhesive glass-metal connections for structural applications". In: *Engineering Structures* 126, pp. 237–251. DOI: 10.1016/j.engstruct.2016.07.024.

Wald, D., L. Wald, B. Worden, and J. Goltz (2003). *ShakeMap, a tool for earthquake response. USGS Fact Sheet FS-087-03*. US Geological Survey. DOI: 10.3133/fs08703.

Wallau, W. (2023). "Reliability of structural sealant glazing systems - Potentials of performance-related durability testing". en. Dissertation. Berlin: Technische Universität Berlin.

Wallau, W., C. Recknagel, and G. J. Smales (2021). "Structural silicone sealants after exposure to laboratory test for durability assessment". In: *Journal of Applied Polymer Science* 138.35, p. 50881. DOI: 10.1002/app.50881.

Wallemacq, P., R. Below, and D. McClean. (2018). *Economic Losses, Poverty and Disasters 1998-2017*. en. DOI: 10.13140/RG.2.2.35610.08643.

Wesche, K., J. Hannawald, I. Hohberg, K. Littmann, B. Meng, E. Mikos, R. Rankers, B. Riecken, and J. W. Weber (1996). *Baustoffe Für Tragende Bauteile. Band 1: Grundlagen. Baustoffkenngrößen, Meß- und Prüftechnik, Statistik und Qualitätssicherung*. ger. In collab. with J. Hannawald, I. Hohberg, K. Littmann, B. Meng, E. Mikos, R. Rankers, B. Riecken, and J. W. Weber. 3rd ed. Wiesbaden: Springer Vieweg. in Springer Fachmedien Wiesbaden GmbH. 266 pp.

White, C. C., D. L. Hunston, K. T. Tan, J. J. Filliben, A. L. Pintar, and G. Schueneman (2012). "A Systematic Approach to the Study of Accelerated weathering of Building Joint Sealants". In: *Journal of ASTM International, Volume 9, Number 5; 2012* 9.5, pp. 1–17.

Wistuba, E. (1980). "Kleben und Klebstoffe". In: *Chemie in unserer Zeit* 14.4, pp. 124–133. DOI: 10.1002/ciuz.19800140404.

Wöhler, A. (1860). "Versuche zur Ermittlung der auf die Eisenbahnwagenachsen einwirkenden Kräfte und die Widerstandsfähigkeit der Wagen-Achsen". In: *Zeitschrift für Bauwesen* 10, pp. 583–614.

Wood, H. O. and F. Neumann (1931). "Modified Mercalli intensity scale of 1931". In: *Bulletin of the Seismological Society of America* 21.4, pp. 277–283. DOI: 10.1785/BSSA0210040277.

Yu, X., H. Sun, J. Liu, H. Zhao, and Y. Han (2024). "Experimental Study on Cyclic Simple Shear Test of Coastal Tidal Soft Soil". In: *Journal of Marine Science and Engineering* 12.7, p. 1066. DOI: 10.3390/jmse12071066.

Zarghamee, M. S., T. A. Schwartz, and M. Gladstone (1996). "Seismic Behavior of Structural Silicone Glazing". In: *Science and technology of building seals, sealants, glazing and waterproofing, sixth volume. Papers presented at the sixth annual symposium, held in Fort Lauderdale, Florida, 31 January 1996*. Ed. by J. C. Myers. ASTM-STP 1286. West Conshohocken, Pa.: ASTM, pp. 46-46–14. DOI: 10.1520/STP16294S.

Zhou, X. and K. K. Tamma (2004). “Design, analysis, and synthesis of generalized single step single solve and optimal algorithms for structural dynamics”. In: *International Journal for Numerical Methods in Engineering* 59.5, pp. 597–668. DOI: 10.1002/nme.873.

# Standards


AAMA 501.6 (2001). *Recommended Dynamic Test Method for Determining the Seismic Drift Causing Glass Fallout from Window Wall, Curtain Wall and Storefront Systems*. American Architectural Manufacturers Association.

ASTM C719 (1998). *Standard Test Method for Adhesion and Cohesion of Elastomeric Joint Sealants Under Cyclic Movement (Hockman Cycle)*. American Society for Testing and Materials.

ASTM C1401 (2014). *Standard Guide for Structural Sealant Glazing*. American Society for Testing and Materials: ASTM International.

ASCE/SEI 7-10 (2010). *Minimum Design Loads for Buildings and Other Structures*. American Society of Civil Engineers, Reston, Virginia 20191: American Society of Civil Engineers.

E1049-85 (2011). *Standard Practices for Cycle Counting in Fatigue Analysis*. ASTM International, West Conshohocken, PA: ASTM International.

AS 1170.4 (2024). *Structural design actions - Part 4: Earthquake actions in Australia*. Australian Standard.

IS 13935 (2009). *Seismic Evaluation, Repair and Strengthening of Masonry Buildings - Guidelines*. Bureau of Indian Standards.

IS 1893 (2016). *Criteria for Earthquake Resistant Design of Structures*. Bureau of Indian Standards.

DIN 18008 (2010). *Glas im Bauwesen - Teil 1 - 6*. Deutsches Institut für Normung.

DIN EN 16612 (2019). *Glas im Bauwesen - Bestimmung des Belastungswiderstandes von Glasscheiben durch Berechnung*. Deutsches Institut für Normung, Berlin: Beuth Verlag GmbH.

DIN 7724 (1993). *Polymere Werkstoffe Gruppierung polymerer Werkstoffe aufgrund ihres mechanischen Verhaltens*. DIN Deutsches Institut für Normung e. V., Berlin: Beuth Verlag GmbH.

DIN EN 1993-1-9 (2010). *Eurocode 3: Bemessung und Konstruktion von Stahlbauten – Teil 1-9: Ermüdung*. DIN Deutsches Institut für Normung e. V., Berlin: Beuth Verlag GmbH.

DIN EN 1998-1 (2010). *Eurocode 8: Auslegung von Bauwerken gegen Erdbeben – Teil 1: Grundlagen, Erdbebeneinwirkungen und Regeln für Hochbauten*. DIN Deutsches Institut für Normung e. V., Berlin: Beuth Verlag GmbH.

DIN EN 1998-1/NA (2011). *Nationaler Anhang – National festgelegte Parameter – Eurocode 8: Auslegung von Bauwerken gegen Erdbeben – Teil 1: Grundlagen, Erdbebeneinwirkungen und Regeln für Hochbau*. DIN Deutsches Institut für Normung e. V., Berlin: Beuth Verlag GmbH.

DIN EN 13022-1 (2014). *Glas im Bauwesen – Geklebte Verglasungen – Teil 1: Glasprodukte für Structural-Sealant-Glazing (SSG-) Glaskonstruktionen für Einfachverglasungen und Mehrfachverglasungen mit oder ohne Abtragung des Eigengewichtes;* DIN Deutsches Institut für Normung e. V., Berlin: Beuth Verlag GmbH.

DIN EN 923 (2016). *Klebstoffe – Benennungen und Definitionen*. DIN Deutsches Institut für Normung e. V., Berlin: Beuth Verlag GmbH.

DIN EN 13830 (2020). *Vorhangfassaden – Produktnorm*. DIN Deutsches Institut für Normung e. V., Berlin: Beuth Verlag GmbH.

DIN EN 1990 (2021). *Eurocode: Grundlagen der Tragwerksplanung*. DIN Deutsches Institut für Normung e. V., Berlin: Beuth Verlag GmbH.

E DIN EN 1998-1-1 (2022). *Eurocode 8 – Auslegung von Bauwerken gegen Erdbeben – Teil 1-1: Grundlagen und Erdbebeneinwirkung (Entwurf)*. DIN Deutsches Institut für Normung e. V., Berlin: Beuth Verlag GmbH.

DIN EN 1991-1-4 (2010). *Eurocode 1: Einwirkungen auf Tragwerke – Teil 1-4: Allgemeine Einwirkungen – Windlasten*. DIN Deutsches Institut für Normung e.V., Berlin: Beuth Verlag GmbH.

DIN EN 1995-1-1 (2010). *Eurocode 5: Bemessung und Konstruktion von Holzbauten – Teil 1-1: Allgemeines – Allgemeine Regeln und Regeln für den Hochbau*. DIN Deutsches Institut für Normung e.V., Berlin: Beuth Verlag GmbH.

DVS 3303 (2026). *Finaler Entwurf - Prinzipien zur Nachweisführung klebtechnischer Verbindungen (elastischer Dickschichtklebungen)*. DVS-Deutscher Verband für Schweißen und verwandte Verfahren e.V.

EN 1998-1 (2004). *Eurocode 8: Design of structures for earthquake resistance - Part 1 : General rules for buildings*. European Committee for Standardization.

ETAG 002-1 (2012). *GUIDELINE FOR EUROPEAN TECHNICAL APPROVAL FOR STRUCTURAL SEALANT GLAZING KITS (SSGK)*. European Organisation for Technical Approvals, Brussels: EOTA.

ETA-01/0005 (2017). *Sealant used in structural sealant glazing systems to bond glass onto metal*. European Organisation for Technical Approvals, Brussels: EOTA.

EAD 090010-00-0404 (2018). *Bonded glazing kits and bonding sealants*. European Organisation for Technical Approvals, Brussels: EOTA.

FKG 01/2021 (2021). *Technical Note - Structural Silicone Sealants in Structural Glass Systems*. Fachverband Konstruktiver Glasbau e.V., Köln: Fachverband Konstruktiver Glasbau e.V.

FEMA E-74 (2015). *Reducing the Risks of Nonstructural Earthquake Damage – A Practical Guide*. FEDERAL EMERGENCY MANAGEMENT AGENCY: APPLIED TECHNOLOGY COUNCIL.

FEMA 450 (2003). *Recommended Provisions for Seismic Regulations for New Buildings and Other Structures*. Federal Emergency Management Agency.

FEMA 356 (2000). *Prestandard and commentary for the seismic rehabilitation of buildings*. Federal Emergency Management Agency and American Society of Civil Engineers, Washington, D.C.

ISO 527-1 (2019). *Plastics – Determination of tensile properties – Part 1: General principles (ISO 5271:2019)*. International Organization for Standardization, Berlin: Beuth Verlag GmbH.

ISO 16269-6 (2014). *Statistical interpretation of data - Part 6: Determination of statistical tolerance intervals*. ISO Internationale Organisation für Normung: Beuth Verlag GmbH.

ISO 11003-2 (2019). *Adhesives - Determination of shear behaviour of structural adhesives - Part 2: Tensile test method using thick adherends*. ISO Internationale Organisation für Normung: ISO copyright office.

JASS 14 (2012). *Curtain Wall*. Japanese Architectural Standard Specification.

CNR-DT 210 (2013). *Istruzioni per la Progettazione, L'esecuzione ed il Controllo di Costruzioni con Elementi Strutturali di vetro*. National Research Council of Italy, Roma, Italy.

GB 50011 (2010). *Code for Seismic Design of Buildings*. National Standard of the Peoples's Republic of China.

NZS 1170.5 (2004). *Structural design actions - Part 5: Earthquake actions - New Zealand*. New Zealand Standards, Wellington, NZ.

# Appendix

# A Additional Data and Plots of Literature Data on Low-Cycle Fatigue of SG Joints

This appendix summarizes the literature data used for the qualitative evaluation of residual tensile strength after cyclic loading presented in section 3.4.4. The normalized ultimate tensile strength deviation is defined as:

$$\sigma_{\mathrm{Cycl,Norm}} = \frac{\sigma_{\mathrm{Cycl}}}{\sigma_{\mathrm{Ult}}} \tag{A.1}$$

where $\sigma_{\mathrm{Ult}}$ denotes the reference ultimate tensile strength and $\sigma_{\mathrm{Cycl}}$ the ultimate strength following cyclic loading. Table A.1 compiles the reported ultimate tensile stresses before and after cyclic loading, including the calculated normalized deviations. Figures A.1 and A.2 visualize the influence of fatigue cycles, load-control methods, and adhesive types on the tensile strength deviation.

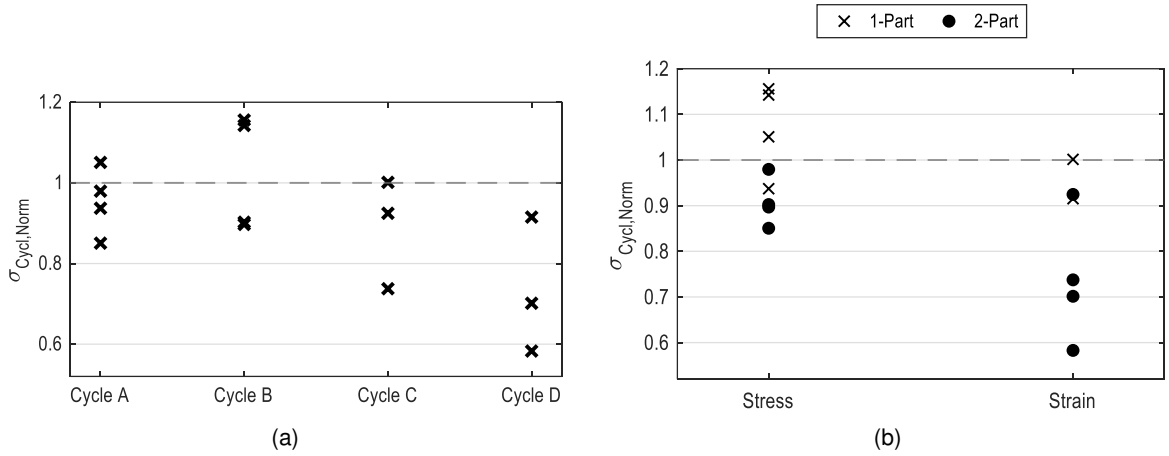


**Figure A.1:** Influence of fatigue cycles and load control on tensile strength deviation: (a) effect of fatigue cycle type; (b) effect of load control method.

**Table A.1:** Comparison of ultimate tensile stress for unaged and cyclic fatigued specimens

| Source | Fatigue cycle | Adhesive | | Joint geometry [mm$^2$] | Mean stress | | Deviation | |
|---|---|---|---|---|---|---|---|---|
| | | Type | Name | | $\sigma_{Ult}$ [MPa] | $\sigma_{Cycl}$ [MPa] | $\sigma_{Cycl,Norm}$ [-] | Perc [%] |
| (Zarghamee et al. 1996) | Cycle A | 1-Part | | 6.3 × 6.3 | 1.28 | 1.34 | 1.05 | 5.1% |
| | | | | 12.5 × 12.5 | 1.08 | 1.01 | 0.94 | -6.3% |
| | | 2-Part | | 6.3 × 6.3 | 1.41 | 1.20 | 0.85 | -14.9% |
| | | | | 12.5 × 12.5 | 0.98 | 0.96 | 0.98 | -2.0% |
| (Broker et al. 2012) | Cycle B | 1-Part | | 12.5 × 9.5 | 1.10 | 1.28 | 1.16 | 15.6% |
| | | 2-Part | | 12.5 × 9.5 | 1.15 | 1.03 | 0.90 | -10.3% |
| (Memari et al. 2012b) | Cycle B | 1-Part | DC 995 | 12.5 × 12.5 | 1.12 | 1.28 | 1.14 | 14.2% |
| | | 2-Part | DC 983 | 12.5 × 12.5 | 1.14 | 1.03 | 0.90 | -9.8% |
| (Nardini and Doebbel 2016) | Cycle C | 2-Part | SG-500 | 12 × 12 | 1.12 | 1.03 | 0.92 | -7.5% |
| | Cycle D | | | 12 × 12 | 1.12 | 0.78 | 0.70 | -29.9% |
| (Nardini and Doebbel 2020) | Cycle C | 1-Part | SG-20 CN | 12 × 12 | 1.22 | 1.22 | 1.00 | 0.1% |
| | | 2-Part | SG-500 CN | 12 × 12 | 1.13 | 0.83 | 0.74 | -26.2% |
| | Cycle D | 1-Part | SG-20 CN | 12 × 12 | 1.22 | 1.12 | 0.92 | -8.5% |
| | | 2-Part | SG-500 CN | 12 × 12 | 1.13 | 0.66 | 0.58 | -41.7% |

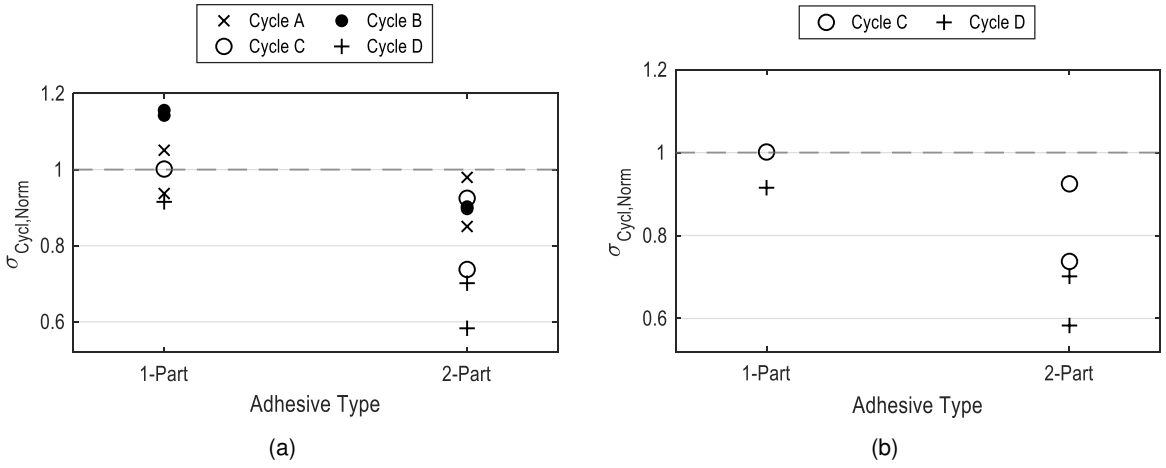


**Figure A.2:** Influence of adhesive type on tensile strength deviation: (a) comparison between adhesive systems; (b) results for Cycles C and D.

# B Results of the Statistical Evaluation of the Number of Equivalent Cycles

## B.1 Master Curves and Response Motion Types

**Table B.1:** Statistical evaluation of equivalent cycle numbers $n_{\mathrm{eq}}$ at $\mathrm{CSR}_{\mathrm{Ref}} = 100\%$ for different master curves and response motion types

| Master curve | Response motion | $Q_{25}$ | $Q_{50}$ | $Q_{75}$ | CV | Skewness | Count |
|---|---|---|---|---|---|---|---|
| [-] | [-] | [-] | [-] | [-] | [-] | [-] | [-] |
| Force | Acceleration | 0.516 | 0.789 | 1.198 | 0.609 | 1.205 | 1926 |
| Force | Displacement | 0.513 | 0.787 | 1.187 | 0.607 | 1.198 | 1926 |
| Disp-$w_{\mathrm{cum}}$ | Acceleration | 0.537 | 0.814 | 1.228 | 0.605 | 1.209 | 1926 |
| Disp-$w_{\mathrm{cum}}$ | Displacement | 0.538 | 0.811 | 1.221 | 0.603 | 1.203 | 1926 |

## B.2 Natural Period of the SDOF System

**Table B.2:** Statistical evaluation of the equivalent number of cycles $n_{\mathrm{eq}}$ at $\mathrm{CSR}_{\mathrm{Ref}} = 100\%$ as a function of the natural period $T_n$ of the SDOF system

| $T_n$ | $Q_{25}$ | $Q_{50}$ | $Q_{75}$ | CV | Skewness | Count |
|---|---|---|---|---|---|---|
| [s] | [-] | [-] | [-] | [-] | [-] | [-] |
| 0.1 | 0.508 | 0.783 | 1.250 | 0.630 | 1.071 | 321 |
| 0.2 | 0.563 | 0.854 | 1.289 | 0.611 | 1.312 | 321 |
| 0.3 | 0.563 | 0.827 | 1.294 | 0.577 | 0.945 | 321 |
| 0.6 | 0.576 | 0.842 | 1.187 | 0.528 | 0.893 | 321 |
| 1.0 | 0.465 | 0.777 | 1.115 | 0.613 | 1.117 | 321 |
| 2.0 | 0.419 | 0.692 | 1.019 | 0.664 | 1.770 | 321 |

## B.3 Ground Motion Magnitude

**Table B.3:** Statistical evaluation of the equivalent number of cycles $n_{\mathrm{eq}}$ at $\mathrm{CSR}_{\mathrm{Ref}} = 100\%$ as a function of earthquake magnitude

| Magnitude [-] | $Q_{25}$ [-] | $Q_{50}$ [-] | $Q_{75}$ [-] | CV [-] | Skewness [-] | Count [-] |
|---|---|---|---|---|---|---|
| 4 | 0.339 | 0.610 | 0.970 | 0.622 | 0.124 | 6 |
| 5 | 0.368 | 0.596 | 0.862 | 0.599 | 0.871 | 78 |
| 6 | 0.549 | 0.801 | 1.159 | 0.568 | 1.067 | 678 |
| 7 | 0.513 | 0.791 | 1.225 | 0.617 | 1.239 | 1020 |
| 8 | 0.472 | 0.809 | 1.282 | 0.657 | 1.138 | 144 |

## B.4 Joint Geometry

**Table B.4:** Statistical summary of the equivalent number of cycles $n_{\mathrm{eq}}$ at $\mathrm{CSR}_{\mathrm{Ref}} = 100\%$ as a function of the joint geometry and master curve

| Master curve [-] | Joint geometry [$\mathrm{mm}^2$] | $Q_{25}$ [-] | $Q_{50}$ [-] | $Q_{75}$ [-] | CV [-] | Skewness [-] | Count [-] |
|---|---|---|---|---|---|---|---|
| Force | 12 x 12 | 0.513 | 0.787 | 1.187 | 0.607 | 1.198 | 1926 |
| Force | 8 x 24 | 0.584 | 0.878 | 1.313 | 0.595 | 1.215 | 1926 |
| Disp-$w_{\mathrm{cum}}$ | 12 x 12 | 0.538 | 0.811 | 1.221 | 0.603 | 1.203 | 1926 |
| Disp-$w_{\mathrm{cum}}$ | 8 x 24 | 0.580 | 0.871 | 1.302 | 0.596 | 1.214 | 1926 |

## B.5 Parametric Study on the Influence of the Master Curve Slope

**Table B.5:** Statistical evaluation of the equivalent number of cycles $n_{\mathrm{eq}}$ at $\mathrm{CSR}_{\mathrm{Ref}} = 100\%$ as a function of the slope $m$ of the master curve

| Slope $m$ [-] | $Q_{25}$ [-] | $Q_{50}$ [-] | $Q_{75}$ [-] | $Q_{95}$ [-] | $Q_{98}$ [-] | CV [-] | Skewness [-] | Count [-] |
|---|---|---|---|---|---|---|---|---|
| 2 | 3.622 | 5.364 | 8.003 | 15.605 | 21.534 | 0.710 | 2.552 | 1926 |
| 4 | 1.524 | 2.204 | 3.175 | 5.491 | 6.865 | 0.591 | 1.772 | 1926 |
| 6 | 0.909 | 1.362 | 1.946 | 3.183 | 3.779 | 0.572 | 1.371 | 1926 |
| 8 | 0.635 | 0.954 | 1.420 | 2.321 | 2.740 | 0.588 | 1.233 | 1926 |
| 10 | 0.471 | 0.729 | 1.105 | 1.812 | 2.186 | 0.616 | 1.190 | 1926 |
| 12 | 0.360 | 0.595 | 0.916 | 1.513 | 1.841 | 0.648 | 1.184 | 1926 |
| 14 | 0.284 | 0.500 | 0.778 | 1.311 | 1.612 | 0.682 | 1.193 | 1926 |
| 16 | 0.226 | 0.432 | 0.682 | 1.164 | 1.453 | 0.717 | 1.211 | 1926 |
| 18 | 0.184 | 0.372 | 0.604 | 1.064 | 1.344 | 0.751 | 1.234 | 1926 |
| 20 | 0.153 | 0.327 | 0.552 | 0.978 | 1.232 | 0.786 | 1.260 | 1926 |
| 22 | 0.127 | 0.291 | 0.502 | 0.901 | 1.136 | 0.820 | 1.288 | 1926 |